Development and application of localization-based microscopy methods to study the structure and dynamics of chromatin through the process of cellular differentiation.

Pablo Gómez García

ICFO – The Institute of Photonic Sciences

UPC – Universitat Politècnica de Catalunya

Barcelona, November, 2019

Thesis supervisor:

Prof. Dr. Maria Pia Cosma
(CRG – Centre for Genomic Regulation, Spain)

Thesis co-supervisor:

Dr. Stefan Wieser
(ICFO – The Institute of Photonic Sciences, Spain)

Thesis committee members:

Prof. Dr. Marcelo Nollmann
(CBS – Center for Structural Biochemistry, CNRS/INSERM, France)

Prof. Dr. María García-Parajo
(ICFO – The Institute of Photonic Sciences, Spain)

Prof. Dr. Jérôme Solon
(Ikerbasque – Basque Foundation for Science, Spain)

Substitute thesis committee members:

Prof. Dr. Eran Meshorer
(ELSC – Edmond & Lily Safra Center for Brain Sciences, HUJI, Israel)

Prof. Dr. Michael Krieg
(ICFO – The Institute of Photonic Sciences, Spain)

Acknowledgements

I would like to acknowledge ICFO and CRG as research institutes that provided me the resources to develop my work and the environment to learn about what science means and how it functions in our time. In addition, I would like to acknowledge the support of my supervisors Melike Lakadamyali and Pia Cosma, who guided me through this tough venture that is the PhD. I am also very grateful to the postdocs that mentored me during the different stages: Joseph Borbely, Jason Otterstrom and Victoria Neguembor. I think that dedicated postdocs are the soul of a laboratory and, through their example, they have the capacity to shape the course of the academic life of its students. They clearly turned mine into a more pleasant, motivating and intelligent one. Finally, I appreciate the help and fellowship of the rest of my colleagues.

I have in mind all those persons who spent their time with me during the last years. Time is all we have and, sharing it, the best way to express our affection. I feel pleased and lucky for the families I belong to and for all the good friends that I have found along the way. I will just ask for your welfare and for many more chances to be together.

Abstract

Chromatin is a complex macromolecule composed by DNA, RNA and DNA-binding proteins. Its architecture changes dynamically inside the nucleus of live cells as a mechanism to regulate gene expression. Until recent years, the diffraction limit has kept the resolution of light microscopy methods in the order of magnitude of ~250 nm, so that the visualization of the chromatin fiber organization at the single nucleosome level (~11 nm) was not possible. The development of advanced light microscopy methods, such as localization-based microscopy has opened a new field by improving the spatial resolution up to 10 nm, providing us with the tools to visualize and analyze the spatial distribution and dynamics of single nucleosomes, which are the core elements of chromatin at the mesoscale level. In addition, when combined with computational methods, the potential of these localization-based microscopy techniques is upscaled. However, there are still major limitations, especially regarding to their extension to multi-color imaging, 3D imaging and their application in live cell imaging. Therefore, there is still need to improve the experimental procedures and the knowledge in data analysis to extract robust quantitative information from localization-based microscopy images which would lead us to the discovery of new biological insights.

In Chapter 1 of this thesis I give an introduction into the current knowledge on chromatin structure and dynamics and the state of the art of Single Molecule Localization Microscopy (SMLM) methods. Then, in chapters 2, 3 and 4 I present the main results obtained during my PhD. In particular, in chapter 2, I describe the development of a multi-color localization-based microscopy method that reduces significantly the experimental time investment of the available methods and achieves low crosstalk between color-channels while keeping the spatial resolution at 10 – 50 nm. In chapter 3, I describe the use of mesoscale chromatin computational modelling to study the structural conformation of an specific gene related with pluripotency (Oct4) in mouse embryonic stem cells (mESCs) and neural progenitor cells (mNPCs). In chapter 4, I describe the application of Single Molecule Tracking (SMT), which is another single-molecule localization-based microscopy method, to study chromatin dynamics at the single nucleosome level in the process of cell differentiation. Finally, in Chapter 5, I present a general discussion of the current state and the future of advanced light microscopy methods and their application in the quantitative study of chromatin.

Table of contents

Chapter 1: Introduction

1.1 Chromatin

The first scientific findings related with the chromatin fiber date back to the 19th century when F. Miescher and A. Kossel performed biochemical measurements that set the basis for the study of chromatin components. They already described the acidic "nuclein", which nowadays is known as nucleic acid, and the histone proteins. In those days, Fleming used the new light microscopes with low aberrations and observed for the first time the complex landscape that is present inside the cell nucleus. He proposed the term "chromatin" to name this heterogeneous substance inside the nucleus. This observation predates the discovery that DNA carries the genetic information. Since then, an intimate relation has connected microscopy and the study of chromatin. New developments in microscopy methods often lead to new insights about chromatin. During the 20th century, the field has grown extraordinarily and nowadays thousands of researchers are dedicated to studying multiple aspects of chromatin. This work has brought a deep knowledge about chromatin and its implications in multiple fields like genetics, bioengineering and cancer diagnosis. In addition, multiple chromatin components have been described during the past years **(Figure 1)**. However, there is still a large gap of knowledge about chromatin architecture at small (Kb-Mb) scales, its interactions with different proteins and how chromatin structure and dynamics relate cell physiology.

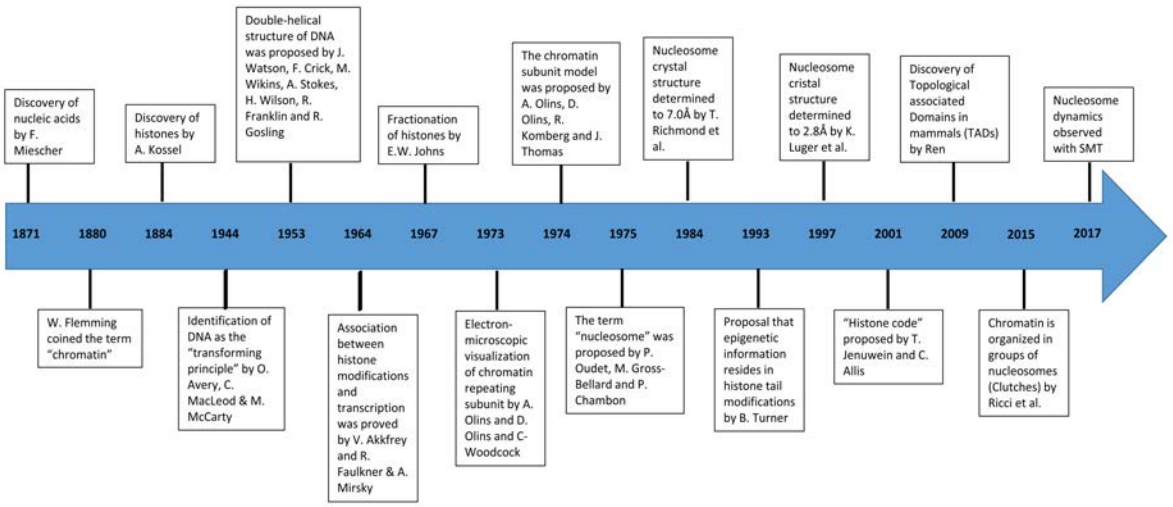

Figure 1. Milestones in the history of chromatin structure. Chromatin is a macromolecule composed of the DNA chain and a wide variety of proteins, present in the nucleus of eukaryotic cells.

The DNA chain, in the case of human cells, has 6.468.109 base pairs, encoding 20.000-25.000 different genes and, when stretched end-to-end, it measures two meters. One of the main purposes of chromatin is to help pack that very long chain of information (the DNA) into the cell nucleus that has a much smaller size (tens of microns). Nowadays we know that the fundamental unit of packaging is the nucleosome. Adapted from [1].

The discovery of nucleosome was a turning point in the field of chromatin structure. Instead of DNA coated by histone proteins, a new paradigm was established: the DNA chain is wrapped around a group of proteins, lately named histones, and both together form the nucleosomes, which are the fundamental unit of chromatin (**Figure 2**). Chromatin fiber can be seen as repetitive motifs of nucleosomes connected by open chains of DNA called linker DNA. The nucleosomes are formed by four pairs of histones proteins (H2a, H2b, H3, H4) and around 147bp of DNA wrapped around them in a left handed helical turn (this corresponds to 1.65 turns of DNA around the complex of histones (**Figure 2**). The nucleosomes have a shape close to a disc, with a diameter of around 11nm and a height of around 5nm. Without the neutralization of the electrostatic negative charged DNA chain by the positive charged nucleosomes, DNA cannot bend that sharply. Since the histones forming the nucleosomes are only capable of neutralizing around 60% of DNA negative charges, other factors such as the linker histone H1 or cations are required for further folding[2]. All those effects combined lead to an estimated sixfold-length compaction of the DNA. Apart from core and linker histones, the post-translational modifications on the histone protein tails also plays an important role in defining chromatin structure and function[3].

1.1.1 Chromatin fiber structure

Chromatin organization spans several length scales. We know that chromatin structure regulates and is, at the same time, regulated by gene expression, and that its conformation is dynamically changing over time. As explained above, the basic unit of chromatin is the nucleosome, which is formed by DNA wrapped around four pairs of histone proteins. Nucleosomes connected by linker DNA form the beads on a string structure which has been well characterized. However, at the mesoscale level, the chromatin fiber architecture remains unclear. Hundreds of nucleosome form gene elements and thousands of genes form entire chromosomes **(Figure 2)**.

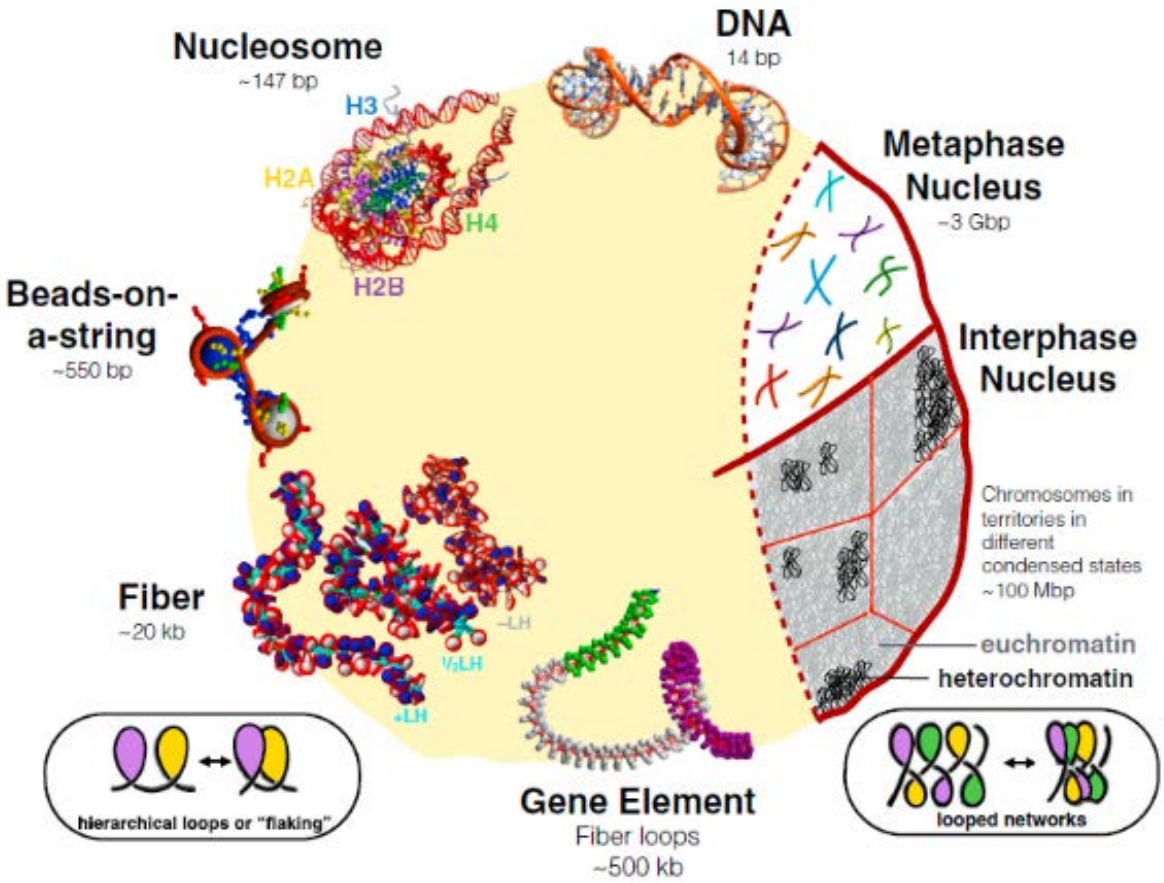

Figure 2. Coarse-grained computational model showing chromatin architecture at different scales. Adapted from [4].

Still, the 3D folding of the genome beyond the beads-on-a-string and its relation with gene regulation is nowadays one of the most relevant problems in biology. An important limitation has been the lack of tools that allow visualizing chromatin at the length scales between nucleosomes and chromosomes. Until very recently, it was thought that at the mesoscale, corresponding to tens of thousands of base pairs, in the order of magnitude of a single gene, chromatin was structured as a 30nm helix (**Figure 3a**), based on transmission electron microscopy images of in vitro reconstituted chromatin fibers[5–7] (**Figure 3c**). At that time two alternative models were proposed: one-start 30nm helix (or solenoid[5–7]) and two-start 30nm helix (or zig-zag[8]) (**Figure 3b**).

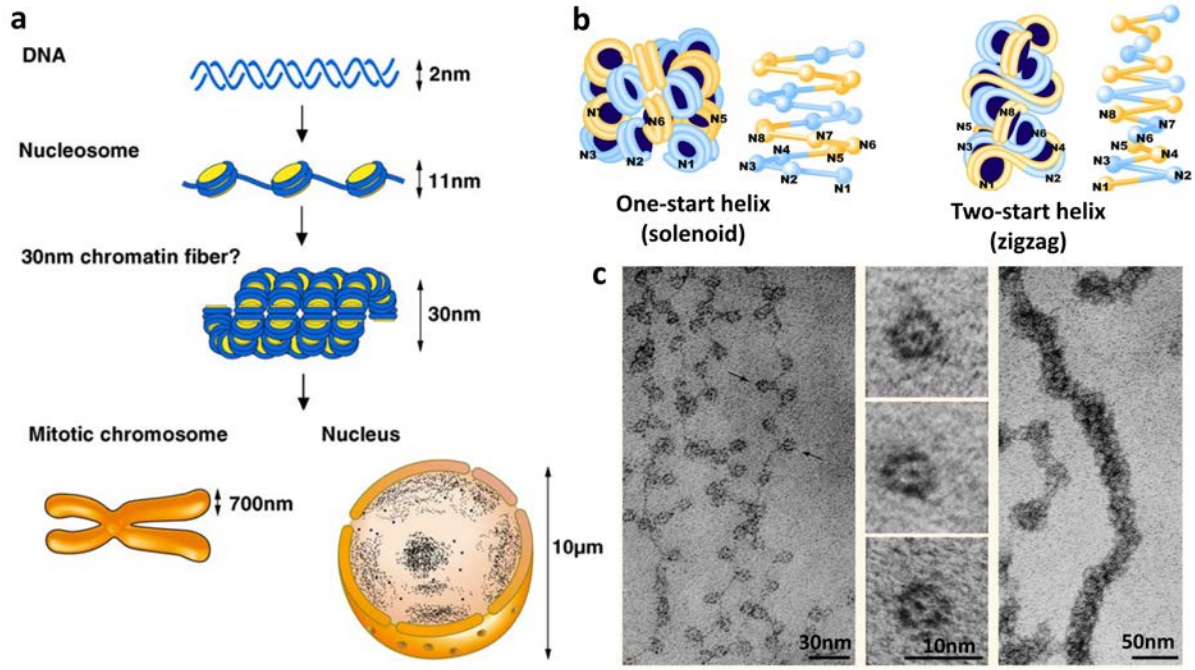

Figure 3. Classical view of chromatin architecture. a) Classical view of chromatin at different scales where the nucleosomes form a 30-nm fiber. **b)** Two options for the 30-nm chromatin fiber. With a single start, forming a helix or with two different starting points forming a zigzag structure. a) and b) adapted from [9]. **c)** Electron microscopy images of chromatin in vitro, showing the bead on a string structure on the left, isolated mononucleosomes on the middle and chromatin spread forming the 30nm fiber on the right. Adapted from [1].

But this helix was never seen in vivo and, since then, other models has been proposed like structures with disorganized regions[10], and lately the clutches model (**Figure 4a**), where the chromatin is formed by heterogeneous groups of nucleosomes that cluster together[11] (**Figure 4a** and **b**). In addition, nucleosome fibers as highly disordered structures resembling a 'polymer melt' has been proposed[9] (**Figure 9**).

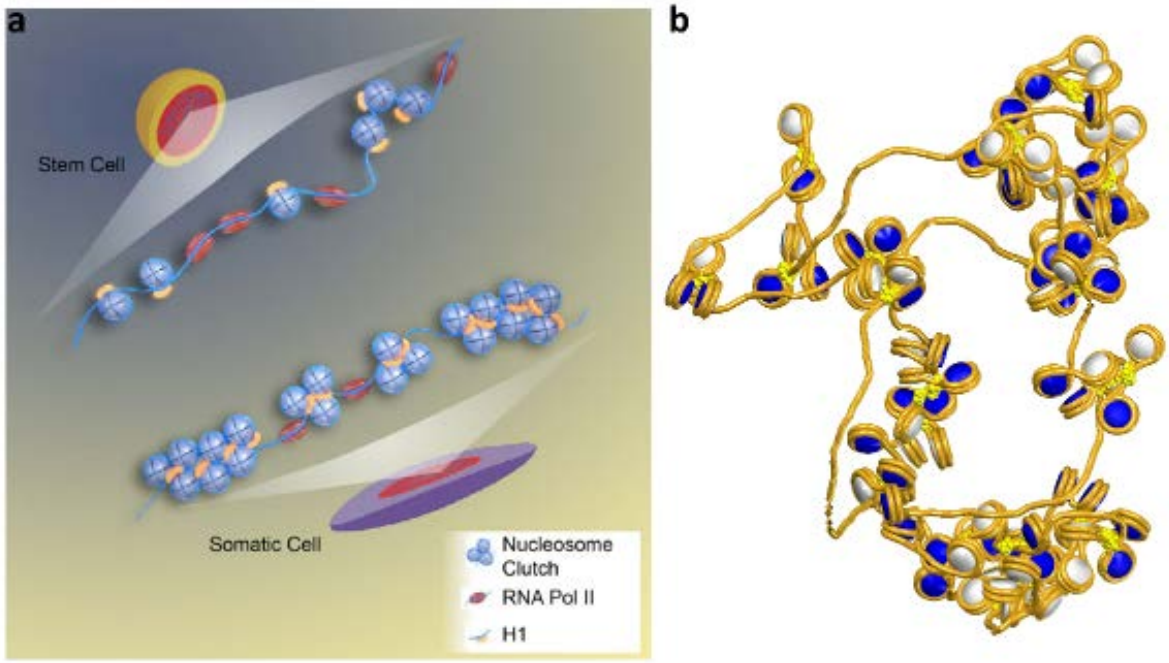

Figure 4. Nucleosomes arrange. a) Nucleosomes are arranged in heterogeneous clutches along the chromatin fiber. Larger and denser clutches form the "closed" heterochromatin. Nucleosome-depleted regions separate nucleosome clutches. Adapted from [11]. **b)** Our coarse-grained computational model of chromatin showing nucleosome clusters.

1.1.2 Chromatin and cell pluripotency

Cell potency is defined as the ability of a cell to differentiate into other cell types. It is correlated with the potential that the cell has to activate genes. Embryonic stem cells (ESC) are considered pluripotent, since they have the capacity to differentiate into multiple lineages. In their differentiation process, as they lose potency, they undergo dramatic morphological and molecular changes. One of the essential events during this process is the selective silencing and activation of specific subsets of genes. In addition, the genome undergoes a global reorganization via chromatin remodelling and epigenetic modifications[12]. All these changes are modulated both by the interaction of a wide variety of proteins with chromatin and the restructuring of chromatin architecture[12,13]. There are multiple mechanisms by which genome conformation influences cell fate (**Figure 5**).

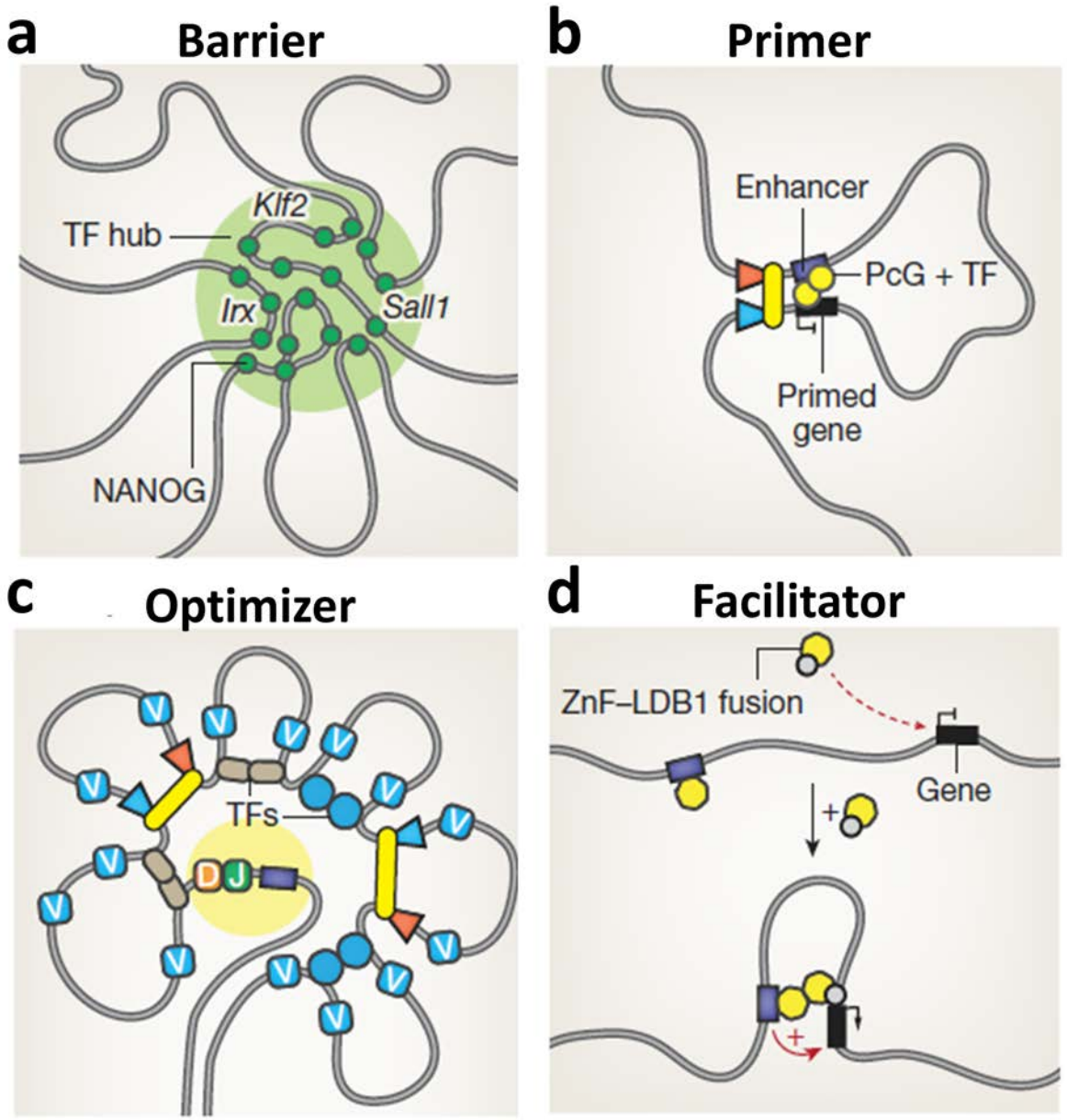

Figure 5. Four examples of how genome conformation helps to shape cell identity via transcription factor induced state transitions. Adapted from [14]. **a)** Acting as a barrier for phenotypic change: NANOG transcription factor forms a hub to cluster target genes like Klf2, Sall1 and Irx. This increases gene expression. **b)** Acting as a primer: groups of transcription factors acting together are able to generate chromatin loops. This has an influence in gene transcription. **c)** Acting as an optimizer: transcription factors induce locus contraction at a certain loci in order to achieve spatial proximity between the genes (indicated with V) and the enhancers (yellow region). This increase individual gene accessibility. **d)** Acting as a facilitator: tethering of a protein to a promoter generates a promoter–enhancer loop formation and activates gene transcription.

Apart from the previous examples, chromatin organization is involved in a huge number of different processes in order to regulate gene expression, so that it is an essential mechanism for the proper functioning of all eukaryotic cells. Moreover, it is involved in the cell fate determination of embryonic/adult stem cells and also in the reprogramming process of somatic cells undergoing its transition to pluripotent cells. Recently it was shown that chromatin is organized in groups of nucleosomes (**Figure 6a** and **b**) and that the size and compaction of these nucleosome groups is correlated with cell pluripotency[11] (**Figure 6b** and **c**).

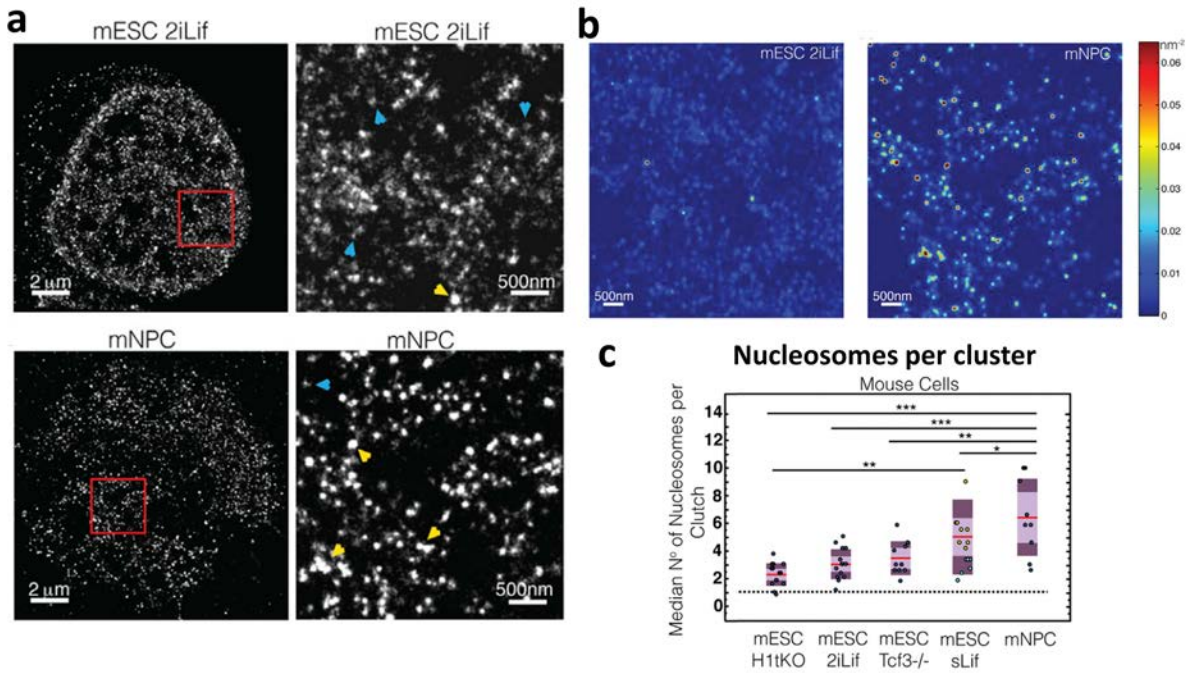

Figure 6. Nucleosomes are distributed in clusters of heterogeneous size and density and those properties correlate with pluripotency. **a)** Super resolution STORM microscopy images of histone H2B in mouse embryonic stem cells in 2iLif medium (upper panel) and mouse neural progenitor cells (lower panel) **b)** Density images showing the differences in cluster organization between mESC 2iLif and mNPC. Red color correspond to high-density regions and are more abundant in mNPC. **c)** Box plot displaying the median number of nucleosomes per cluster in different types of mouse-ESCs and mouse-NPCs. Adapted from [11].

1.1.3 Advanced methods to study chromatin structure

The lack of suitable tools has hindered progress in understanding chromatin structure. Microscopy has been an important tool in studying subcellular compartmentalization and organization, including the genome organization. However, until very recently, the diffraction limit of light has limited the microscope resolution to about 200-300 nm (depending on the wavelength), which is not sufficient to visualize the intermediate and small scales of

chromatin, since one single nucleosome is a disk with 11 nm of diameter and 5 nm of height. Conventional light microscopy has been used for many decades to study chromatin by labelling the DNA with a DAPI staining. Then, with the advent of more sophisticated methods like 3D Structure Illumination Microscopy (3D-SIM), there was a quantitative improvement in the resolution of the images, reaching around 100 nm, but still far from the size of a single nucleosome[15]. In such 3D-SIM images, two regions with lower and higher chromatin density appeared to be distinguishable (likely corresponding to euchromatin and heterochromatin), which are known to be related with active and inactive regions of chromatin, respectively[16] (**Figure 7a**). Another popular approach to study chromatin is electron microscopy, which showed the beads on string structure and can achieve a resolution of less than 1 nm, but it lacks labelling specificity, multi-color capability and is not suitable for live-cell imaging[5,6,8]. In particular Electron spectroscopic imaging (ESI) has been successfully applied to observe chromatin[17] (**Figure 7b**). In those images, more open and more close regions of chromatin can be clearly distinguished, likely corresponding to euchromatin and heterochromatin like in 3D-SIM images. In addition, due to the much higher resolution of this technique, the conformation of the chromatin fiber at the mesoscale level starts to appear, displaying a 10-nm fiber (**Figure 7b**).

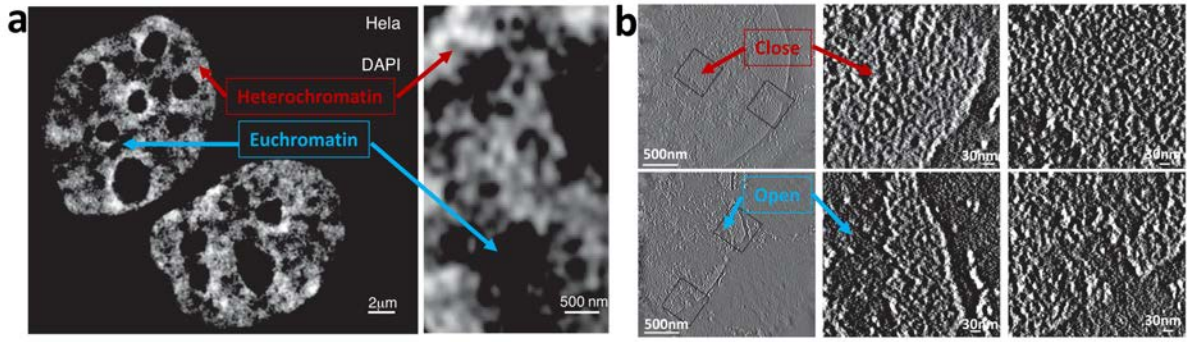

Figure 7. Chromatin observed with ESI and 3D-SIM. a adapted from [18], **b** adapted from [17]. **a)** Chromatin visualized with 3D-SIM with a DAPI staining displaying distinct chromatin density regions likely corresponding to euchromatin and heterochromatin. **b)** ESI images displaying open and closed chromatin domains corresponding to euchromatin and heterochromatin (left panels) and the 10-nm chromatin fibers in the zoomed regions (central and right panels).

In **Table 1** below there is a summary of the currently available microscopy methods used for the observation of chromatin.

Table 1. Advanced microscopy methods for visualizing chromatin and their different observed conformations. Adapted from [19]

Method	Sample	Staining	Observed structure	Reference
	Native chromatin	Negative stain, shadowing	One-start helix (solenoid)	5

Electron Microscopy	Native chromatin	Negative stain, shadowing, Non-stained	Two-start helical ribbon model	6
	Reconstituted nucleosome array	Negative stain	Two-start model	8
Electron Microscopy and Computation	Reconstituted nucleosome array	Positive stain, shadowing	Heteromorphic chromatin fibers	20
Cryo-Electron Microscopy	Native chromatin	-	Stem conformation of linker DNA segments formed by linker histones	21
	Reconstituted nucleosome array	-	Interdigitated solenoid model	22
	Reconstituted nucleosome array	-	Two-start zigzag model with tetra-nucleosomal unit	23
Electron spectroscopic image (ESI) with tomography	Native chromatin	-	Open and closed chromatin domains consisting of 10 nm fibres	17
Electron microscopy tomography	Native chromatin	Osmium ammine-B stain	Variable two-start helical ribbon model	24
	Native chromatin	Osmium staining of electron-dense precipitate produced by photoconverted DNA-bound fluorescent dye	Heterogeneous 5–24 nm chromatin fibre	25
Low-angle X-ray scattering (LAXS)	Isolated nuclei and chromatin	-	Two-start crossed-linker model	26
Small-angle X-ray scattering (SAXS)	Isolated nuclei and chromatin	-	Irregularly folded nucleosome fibres	27
X-ray crystallography	Reconstituted nucleosome	-	Nucleosome structure with angstrom-level resolution	28
	Reconstituted nucleosome array	-	Tetranucleosome folding unit	29

3D-SIM	Native chromatin	DAPI	Chromatin compartments with different density	[16]
Superresolution microscopy	Native chromatin	Fluorescent protein, fluorescent-tagged antibody	Nucleosome clutches along chromatin fibre	[11]

The development of new advanced methods, such as localization-based super resolution microscopy, has opened a new field, providing us with the tools to visualize and quantitatively analyze the spatial distribution of chromatin in fixed and live cells at the single molecule level. In addition, those microscopy methods can be used in conjunct with biochemical and sequencing methods like chromatin immunoprecipitation combined with massively parallel sequencing (Chip-Seq) (**Figure 8a**), Micrococcal Nuclease combined with sequencing (MNASE-Seq) (**Figure 8a**), Chromosome conformation capture methods like Hi-C (**Figure 8c**), or High-throughput DNA Sequencing (**Figure 8a**), as a correlative approach, to provide deeper insights about chromatin[30] (**Figure 8**). For instance, Hi-C has revealed that chromatin is organized in Topologically Associated Domains (TADs)[31,32] (**Figure 8b** and **c**), megabase regions in which the DNA within one domain preferentially interacts with itself rather than DNA in a neighbouring domain. However, these genomic methods work by averaging information over a large population of cells and unlike microscopy, they are not suitable for single cell analysis. Lately, TADs and the presence of cooperative DNA interactions[33] were confirmed by a new localization-based microscopy method called chromatin-tracing[34] but single cell information revealed that TAD boundaries are not fixed in single cells and these boundaries are emergent, statistical properties arising from population averaging. Hence, microscopy, due to its ability to probe single cells, is still a powerful tool that can reveal novel information not attainable by population based genomic methods. Development of new single cell based microscopy tools, thus, holds great promise for enhancing our understanding of genome organization.

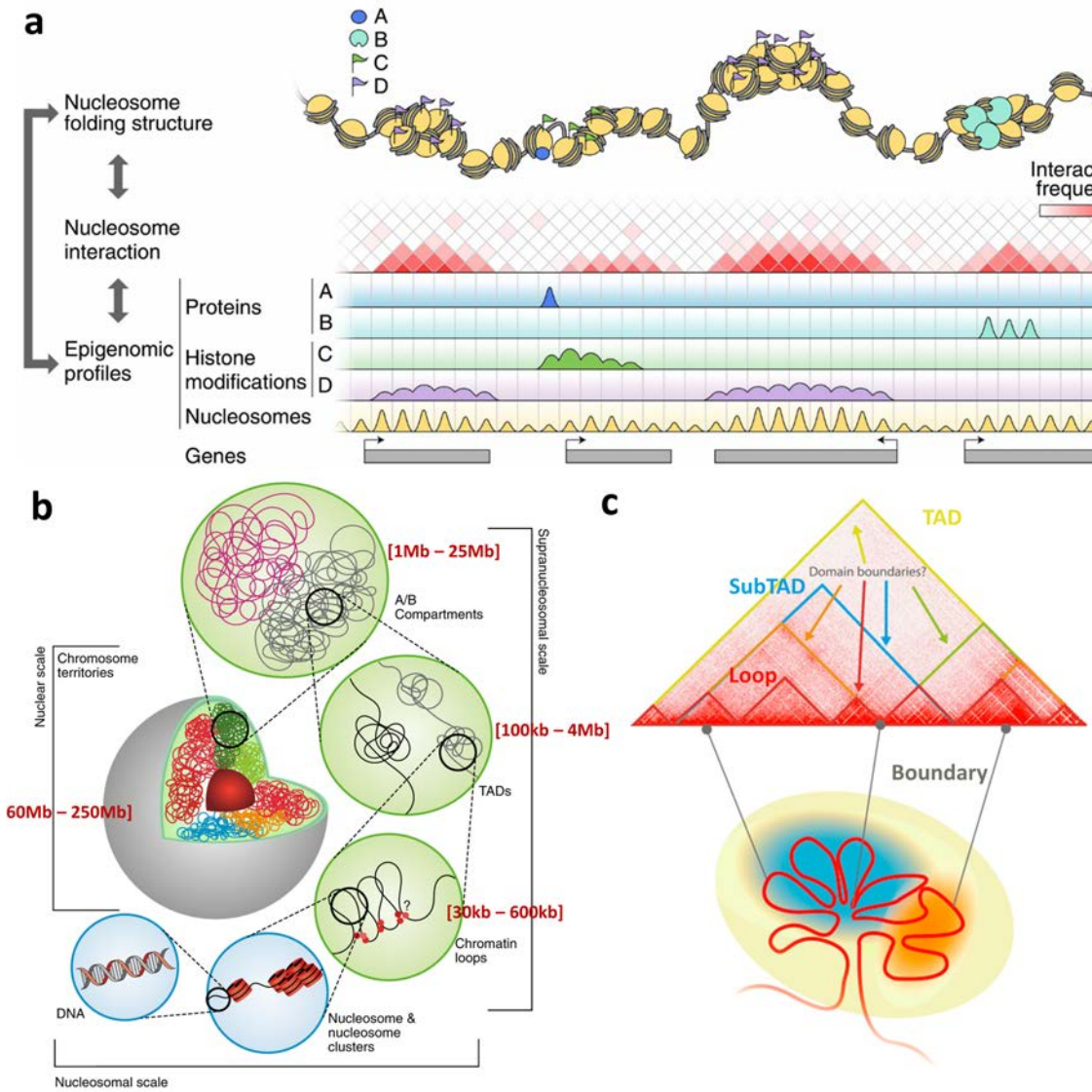

Figure 8. Chromatin structure at the nucleosome level measured with sequencing-based methods. a) Chromatin fiber obtained from computational modelling using Hi-C interaction data as an input (top panel). ChIP-seq can provide genome-wide positions of chromatin-binding proteins, histone modification and nucleosome occupancy. Adapted from [19]. **b)** A cartoon showing the vision of the different scales of chromatin as seen from Hi-C contact map measurements point of view. **c)** A cartoon showing the definition of TADs, subTADs and domain boundaries with an example of the corresponding Hi-C data. **b** and **c** adapted from [35].

1.1.4 Chromatin dynamics

Genome organization and dynamics play an important role in regulating gene expression. Several recent work including super-resolution imaging of nucleosomes and electron

tomography imaging of DNA showed that chromatin is a disordered chain formed of heterogeneous groups of nucleosomes with a varying range of nucleosome densities[11,25]. In super-resolution images, nucleosome groups (named clutches) were further clustered into larger domains (clutch domains) in the size range of hundreds of nanometers in length scale[11,36]. These results shed new light onto the organization of chromatin fiber at the 10-100 nm length scales. Assembly of nucleosomes into clutches, the compaction level of nucleosomes within the clutches as well as the assembly of clutches into clutch domains can limit accessibility of DNA to regulatory proteins and polymerases. Hence these structural features must be dynamically regulated in order to turn genes on and off in specific cell types.

Fluorescence Recovery After Photobleaching (FRAP) analysis and single molecule tracking (SMT) of histone proteins as well as tracking of individual genomic loci within the nucleus indeed showed that chromatin is highly dynamic. Individual genomic loci diffuse within a confined space in the nucleus[37,38] and this mobility correlates with the transcriptional activity of some genomic regions such as enhancers[37,39]. In some cases, genomic loci can dynamically change their positioning over large distances relocating from the nuclear periphery to the nuclear interior upon activation[40,41]. While FRAP analysis showed that nucleosomes are highly stable and turn over with slow dynamics[42], tracking of individual Halo-tagged histone proteins showed that histones also explore their local environment dynamically[43,44]. Live cell super-resolution imaging showed that groups of nucleosomes residing within nanodomains (similar in size to clutch domains) are also mobile[33,43,45]. However, currently how these dynamic measurements spanning multiple length scales, from individual nucleosomes to large genomic loci, relate to each other is not clear. The advent of these measurements in live-cells have introduced a new perspective with the proposal of new models that considers the chromatin fiber as a dynamic element like, for example, a liquid-like structure (**Figure 9**).

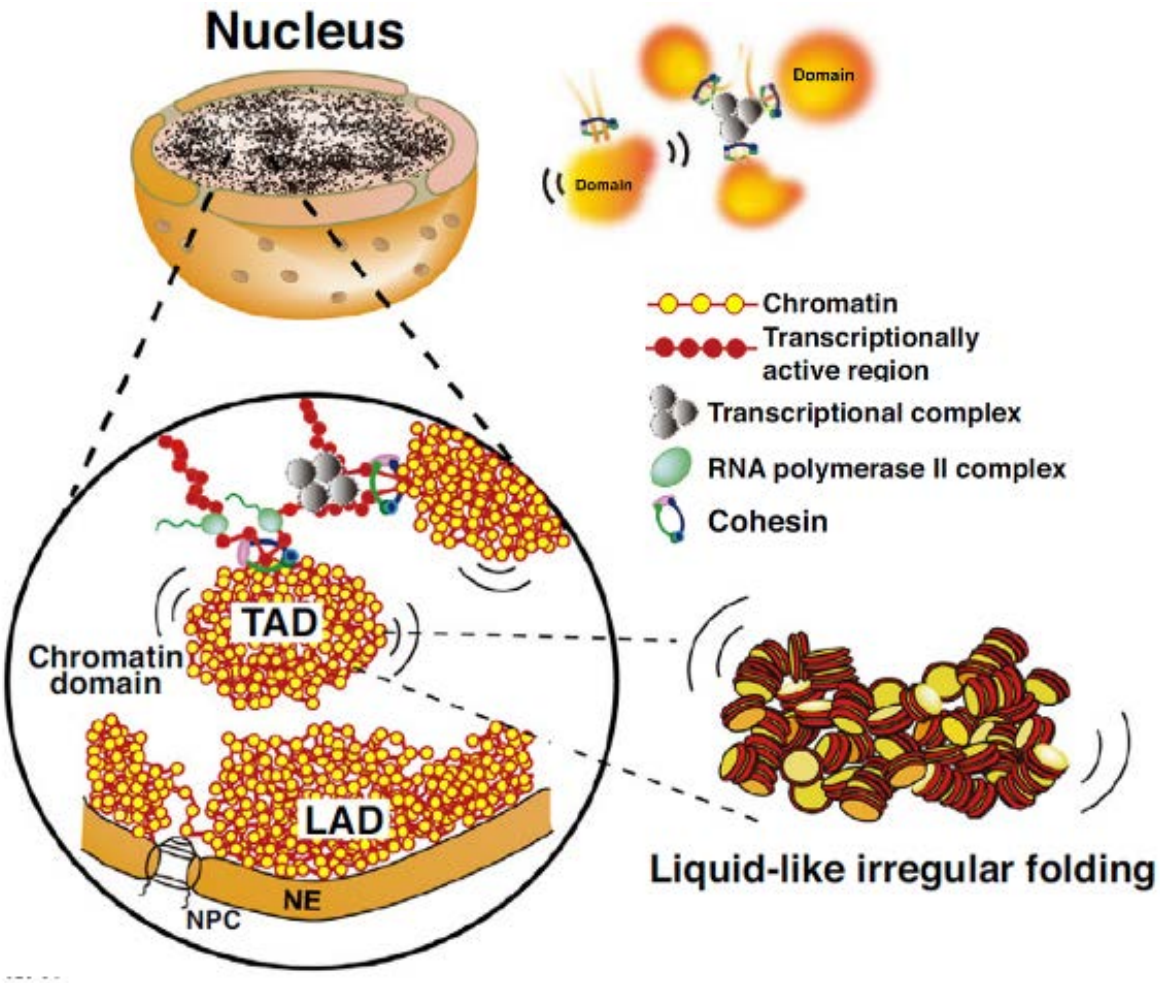

Figure 9. Cartoon showing the higher order structure of chromatin as 10-nm fibers forming domains like Topologically Associated Domains (TADs), loops and Lamin Associated Domains (LADs), hypothesizing that the compact domains could behave like a liquid drop with dynamic motion. TADs would be more mobile than LADs. In addition, it speculates that the binding of transcriptional protein complexes to chromatin during transcription might constrain nucleosome fluctuations. Adapted from [46].

In addition to chromatin being dynamic, several studies showed that architectural proteins are also highly dynamic inside the nucleus[47,48]. In particular, the dynamics of architectural proteins like H1 and HP1 increased in embryonic stem cells (ESCs) as shown by FRAP and SMT[12,49]. Partially based on these FRAP studies, it has been suggested that the ESC chromatin is hyperdynamic and devoid of heterochromatin. Super-resolution imaging showed that nucleosome clutch size is cell specific and ESCs have smaller, less compacted clutches compared to differentiated cells[11]. Nucleosome clutch size and compaction was further impacted by the amount of the linker histone H1 as well as the amount of acetylation on histone tails[36], suggesting that linker histones and histone post translational modifications

play a role in organizing nucleosomes into clutches. How the nucleosome clutch organization observed in fixed stem and somatic cells correlate with histone, H1, HP1 and locus dynamics measured in live cells is not clear. In addition, the mechanisms that regulate histone and chromatin dynamics in different cell types are poorly understood. Finally, it is not clear whether the folding of the chromatin fiber into nucleosome clutches is compatible with the polymer nature of DNA and the electrostatic interactions of histones, histone tails and linker histones with DNA.

1.2 Single Molecule Localization Microscopy

With the advent of super-resolution microscopy, diffraction limit is no longer an impenetrable barrier to light microscopy. In the last decade, several techniques have been developed that overcome the diffraction limit, extending the spatial resolution of light microscopy to length scales as small as 10–20 nm, an order of magnitude improvement over conventional fluorescence microscopy (**Figure 10**). Super-resolution microscopy methods can be broadly divided into two categories: those that are based on patterning the illumination light, such as Saturated Structured Illumination Microscopy – (S)SIM[50] or Stimulated Emission Depletion (STED)[51], and those that are based on single molecule localization, like Stochastic Optical Reconstruction Microscopy – STORM[52] and (Fluorescence) Photoactivation Localization Microscopy – PALM and fPALM[53]. A more recent method named Point Accumulation for Imaging in Nanoscale Topography (PAINT)[54,55] also belongs to this category but will be treated apart in an individual section below. Most of these methods have been applied to image chromatin and nuclear organization at high resolution[56,57].

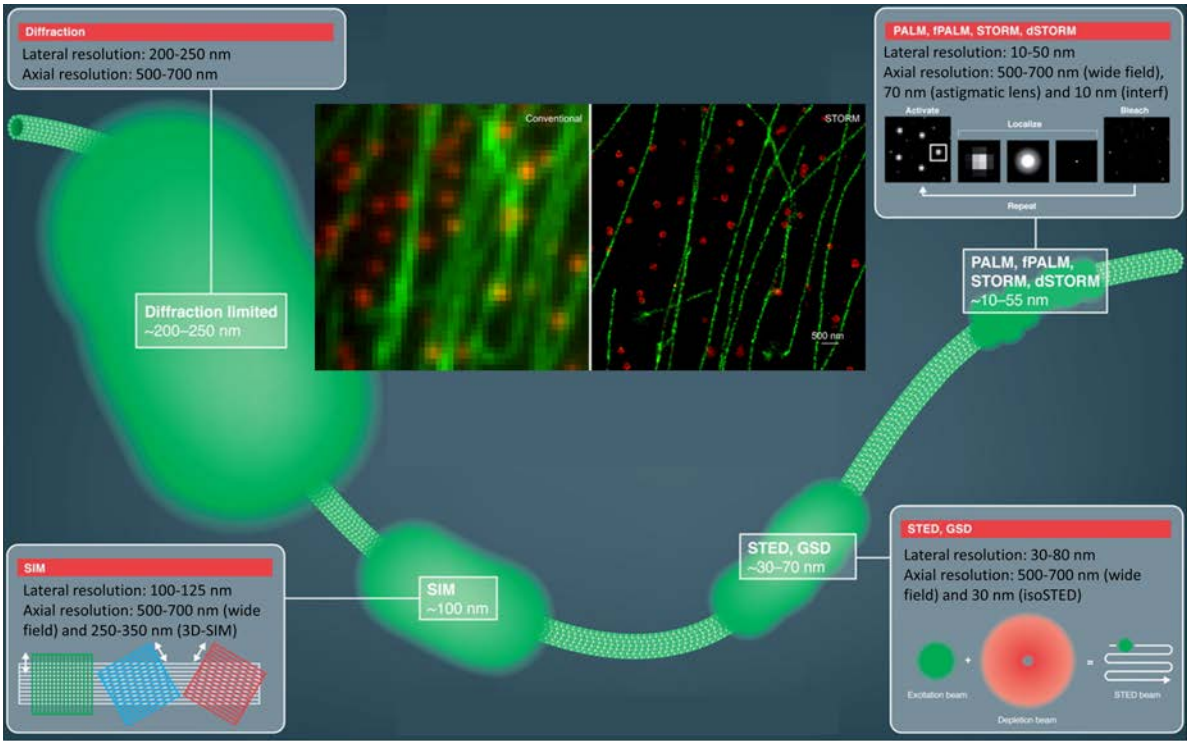

Figure 10. Super resolution microscopy at a glance. Four super resolution techniques and their corresponding resolution. The cartoon represents a microtubule with a diameter of 14nm and the different appearance under the microscopy methods. In addition, a two-color image of microtubules and clathrin-coated pits, comparing conventional and STORM images is shown. Adapted from [58,59].

1.2.1 Single Molecule Localization Microscopy Basis

Due to the diffraction phenomenon, an infinitesimal point source emitting fluorescence, after passing through an optical system (the microscope) and being projected into a detector (the camera) will have a shape that is characteristic of each system and is defined as Point Spread Function (PSF). This fact limits the spatial resolution of a microscope to:

Lateral (x, y) resolution: $r = \frac{\lambda}{2 \cdot NA}$

Axial (z) resolution: $r = \frac{2 \cdot \lambda \cdot n}{NA^2}$

Where λ is the wavelength of the light, n is the refraction index of the medium of propagation and NA is the numerical aperture of the objective piece.

In order to overcome this limit, SMLM methods localize each individual fluorophore separately by fitting a function to the intensity profile of each individual PSF (**Figure 11a**). The actual shape of a diffracted limited spot is better approximated by the airy function, but most of the localization algorithms work with a 2D Gaussian functions (**Figure 11b**), which is good enough to fit the PSF and find the center position (x,y) of the point emitter and the width of the Gaussian curve (**Figure 11b** and **c**).

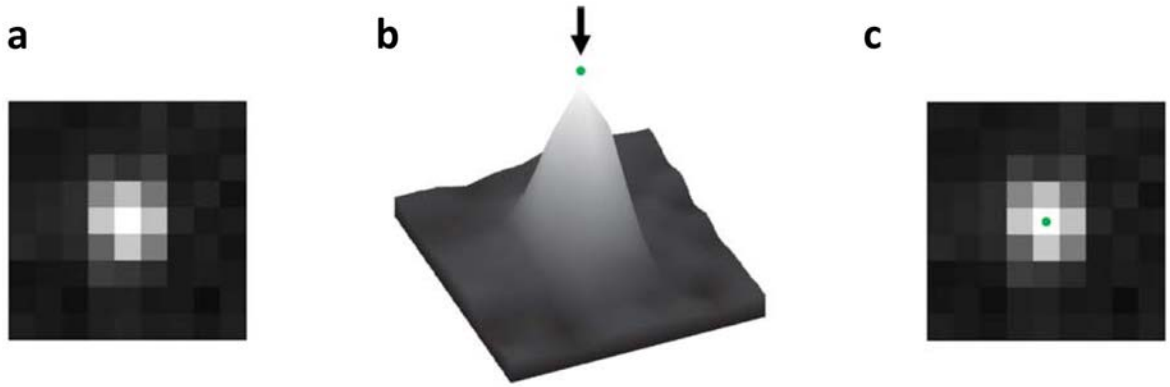

Figure 11. a) Point Spread Function (PSF). **b)** 2D Gaussian fitting on the fluorophore intensity profile detected by the camera. **c)** Localization position (x,y) of the fluorophore with high precision overlapped with the PSF. Adapted from [60].

Localization-based microscopy methods take advantage of single molecule detection and localization to break the diffraction limit[52,53]. The position of a single fluorescent probe can be localized with very high precision, depending on the number of photons collected from the spot[61]. However, this concept by itself is not sufficient to improve image resolution, since biological samples are labelled with a high number of fluorophores whose individual images overlap and cannot be distinguished. Therefore, in a densely labelled biological sample, it is necessary to separate the emission of many overlapping fluorescent probes in time. Then, if

one is able to localize the center position of hundreds of thousands of emitters with high precision and reconstruct an image will all those localizations, its resolution will be greater than any conventional microscopy method (**Figure 12**).

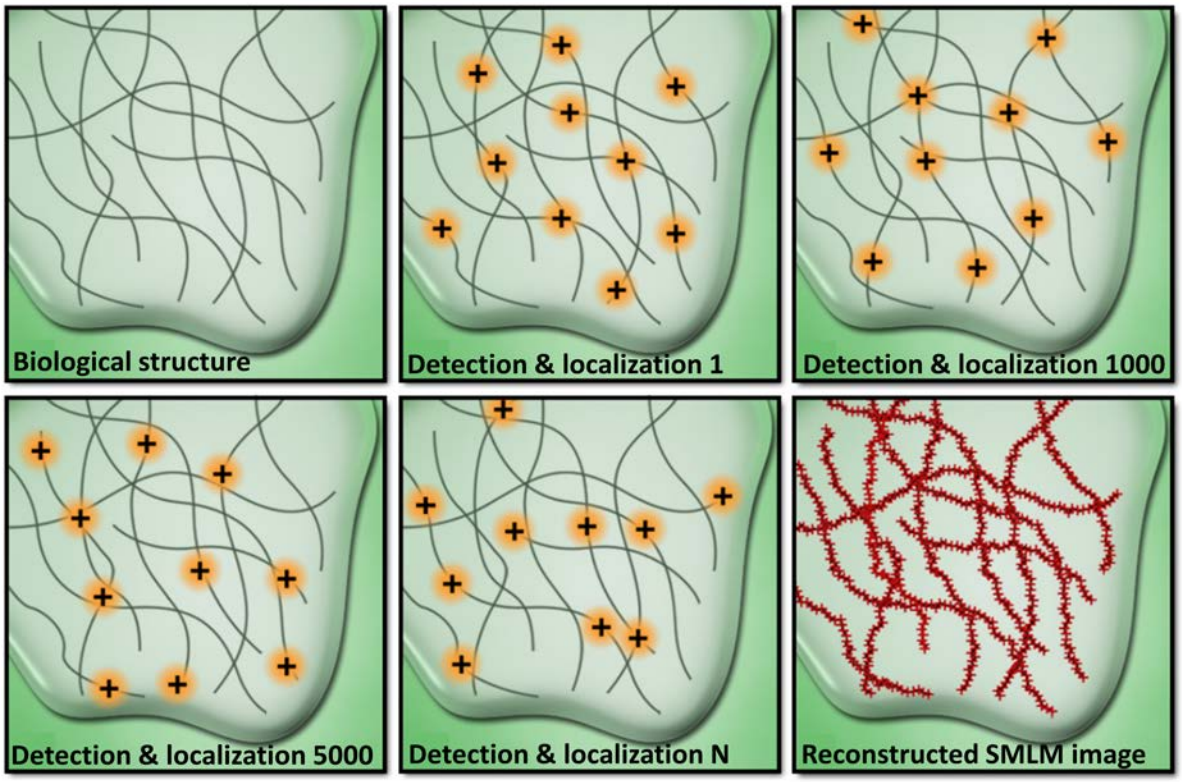

Figure 12. A cartoon showing the basic principle of single molecule localization based microscopy. Four acquisition and detection cycles are displayed. Adapted from MicroscopyU Single-Molecule Super-Resolution Imaging (https://www.microscopyu.com/techniques/super-resolution/single-molecule-super-resolution-imaging).

The resolution of this type of images is a complex concept and it is not trivial to determine. Of course, it depends on the localization precision (**Figure 11b** and **Figure 13a**), which ultimately depends on the number of collected photons (or the Signal to Noise ratio of the fluorophore), but also on the density of localizations (**Figure 13b**), the, the size of the labelling epitope or the drift of the microscope stage, among others. One experimental procedure to estimate the 2D localization precision is by computing the standard deviation (σ) of the distribution of multiple localizations of the same single fluorophore (**Figure 13a**). Analytically, the localization precision is given by the expression:

$$\sigma = \sqrt{\frac{s^2}{N} + \frac{a^2}{12N} + \frac{4\sqrt{\pi}s^3b^2}{a \cdot N^2}},$$

Where s is the standard deviation of a Gaussian function approximating the PSF of the fluorophore in a particular microscope, N the number of detected photons from the fluorophore by the camera, a is the pixel size of the camera and b is the standard deviation of the background. The first term is related with camera photon shot noise, the second with the effect of finite pixel size and the third with the background noise. In the case of very low background, the expression can be simplified to:

$$\sigma \approx \frac{s}{\sqrt{N}},$$

A localization precision of 10-20nm is typically achieved in a SMLM experiment with a state of the art microscope. The way to increase localization precision is to minimize the background signal while simultaneously maximizing photon output from the fluorophore. This can be achieved by selecting a bright fluorophore, using a sensible camera with low readout noise, reducing background fluorescence signal generated in the sample preparation or increasing the SNR by using HILO laser illumination[62]. There are other approaches to estimate the localization precision by obtaining the Cramér-Rao lower bound of the position estimation[63], and others to directly estimate the image resolution like Fourier ring correlation method[64].

The Nyquist criterion quantifies the effects of the localization density on the reconstructed image resolution[65]. It states that two structures separated less than twice the distance between localizations, is not resolvable:

$$\sigma_{Nyquist} = \frac{2}{\rho^{\frac{1}{D}}}$$

where ρ is the density of localizations and D is the imaging dimension (D=2 for 2D and D=3 for 3D). Following that criteria, another estimator for the image resolution can be obtained from the convolution of the two effects: localization precision and localization density.

$$\sigma_{effective} = \sqrt{\sigma_{Loc}^2 + \sigma_{Nyquist}^2}$$

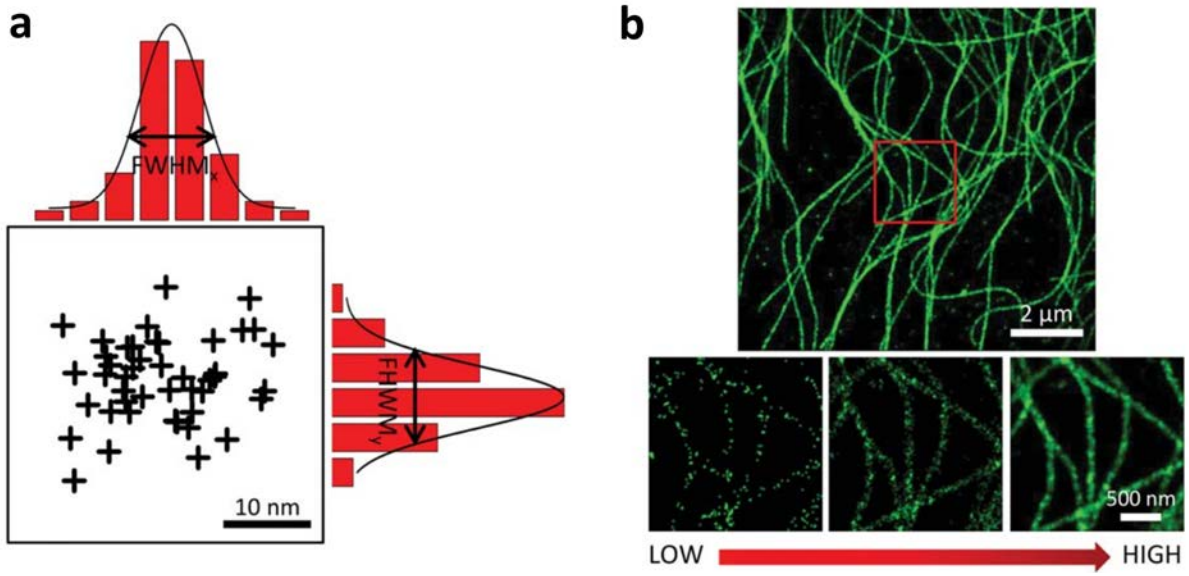

Figure 13. a) Example of the localization positions originated from a single fluorophores and their spatial distributions in x and y that can be fit fitted with a normal distribution. The full width at half maximum (FWHM=2.35·σ) can provide a quantitative measurement of the localization precision. **b)** Localization-based microscopy image of microtubules showing the effect of localization density on image quality. Adapted from [60].

In addition, it is also possible to improve the axial resolution. A typical way to extend localization-based imaging to the third dimension is by placing cylindrical lens in the imaging path[66]. Due to astigmatism, molecules that are above and below the focal plane will appear elliptical and the ellipticity will be either in the horizontal or vertical directions. This method can achieve an axial resolution of 50 nm over a range of 800 nm[67] (**Figure 14a**). Typically a calibration procedure is required to measure precisely the deformations of the PSF when a fluorophore moves up and down from the focal plane[67] (**Figure 14b**).

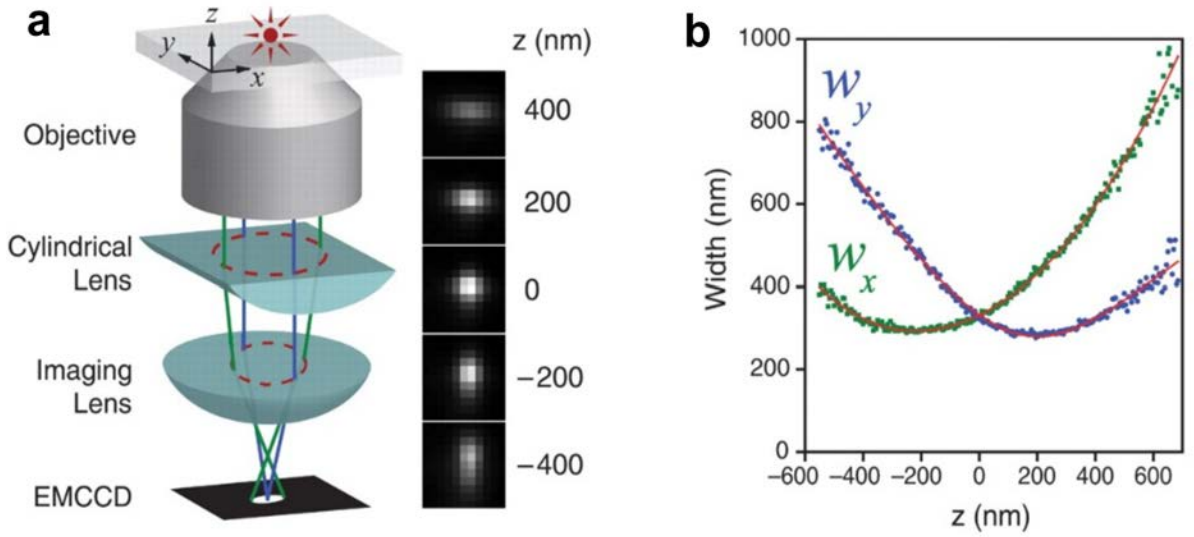

Figure 14. PSF engineering via astigmatic lens to perform 3D SMLM. a) The cylindrical lens elongates the shape of the PSFs in an elliptical way in x or y, depending on their relative position to the focal plane. **b)** This method needs a calibration step which will characterize the imaging system. This is typically performed with fluorescence beads. Adapted from [67].

1.2.2 STORM

One of the methods to achieve fluorophore fluorescence separation in time is the use of photoswitchable dyes typically associated with a sub-class of super-resolution microscopy method known as Stochastic Optical Reconstruction Microscopy or STORM[68]. These are probes whose fluorescence can be switched in a somewhat controlled fashion between bright and dark states using laser illumination. At any given frame, most of the fluorophores are in a long-lived dark state. Only a small subset of them is stochastically activated into the fluorescent state by excitation with the appropriate wavelength of light. As a result, the single molecule images of this small subset of molecules do not overlap and their positions can thus be determined precisely. By repeating the process of activation, imaging and de-activation over thousands of cycles, a super-resolution image can be built from molecule positions[69]. **Figure 15** shows a comparison between conventional and STORM microscopy for H2B (a histone protein that is constituent of the nucleosomes) imaging, and it shows a procedure to analyse the new information obtained with STORM. There is a wide choice of these fluorescent probes, ranging from photoactivatable, photoconvertible or photoswitchable fluorescent proteins to photoswitchable organic fluorophores[70]. The quality of the image will strongly depend on the fluorophore, specifically on the duty cycle (fraction of fluorophores in the on state at a given time), fluorophore brightness and the number of cycles before depletion. Depending on the fluorescent probe used, it is possible to achieve a spatial resolution in the order of 20–40 nm and a temporal resolution of 0.5–10 s (in live cell imaging)[71].

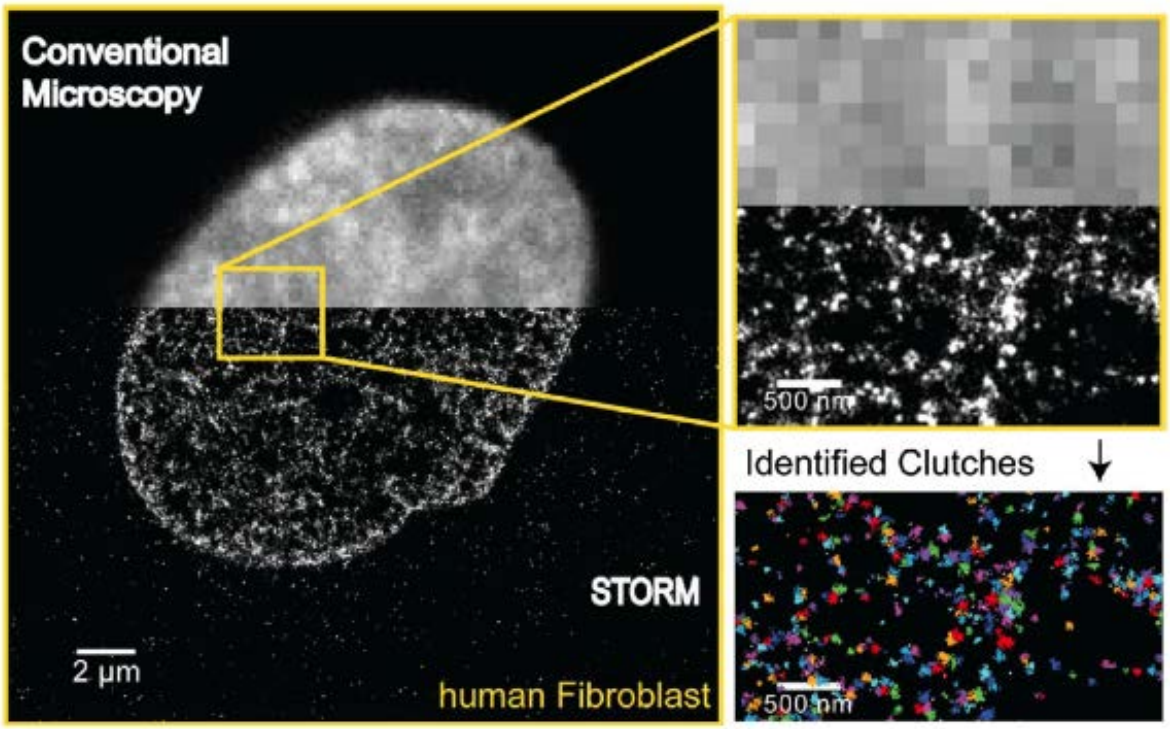

Figure 15. STORM image of nucleosome arrangement stained via H2B-Alexa647. Comparison of conventional fluorescence image (upper) and super-resolution (STORM) image (lower) of core histone H2B showing the arrangement of nucleosomes in a fibroblast nucleus. A zoom of the region inside the yellow rectangle is shown to the right. A cluster identification algorithm is used to automatically group localizations into clusters (colored crosses) and segment nucleosome clutches in the super resolution image. Adapted from [72].

1.2.3 PAINT

Point accumulation for imaging in nanoscale topography (PAINT)[73] is an alternative localization-based super-resolution microscopy method. In this approach, imaging is performed using diffusing fluorescent molecules that have a transient interaction with the protein of interest. This method does not rely on fluorophore photophysics or imaging buffer conditions and more importantly does not suffer from fluorophore depletion due to irreversible photobleaching. Initially, PAINT was applied to obtain super-resolved images of cell membranes and artificial lipid vesicles. Recently, DNA-PAINT was developed[73,74]. It achieves programmable dye interactions with the biological structure of interest and increases the labelling specificity and the number of utilizable fluorophores. Here, stochastic switching between bright and dark states is achieved via repetitive, transient binding of fluorescently labelled oligonucleotides to complementary docking strands (**Figure 16a**). In the unbound state, only background fluorescence from partially quenched imager strands is observed (**Figure 16a**), because they are diffusing faster than the long exposure time (typically 100ms).

However, when binding and immobilization of an imager strand occurs, fluorescence emission is detected (**Figure 16a**). No high laser power is required for this technique, since the long exposure times and the typical residence times of the oligos is around 100ms. It is also possible to control the dark and bright times, by tuning the binding strength and concentration of the imager strand (**Figure 16a**). DNA-PAINT is highly quantitative[75] and does not suffer from photobleaching as there is continuous replenishment of imager strands from solution. A 2D spatial resolution of less than 10nm can be obtained as shown with labelled DNA Origami (**Figure 16b**). This technology can be used in conjunct with primary and secondary antibody labelling making it useful for most fluorescence microscopy applications (**Figure 16c**). **Figure 16b, d** and **e** show a comparison between conventional and DNA-PAINT localization-based microscopy images.

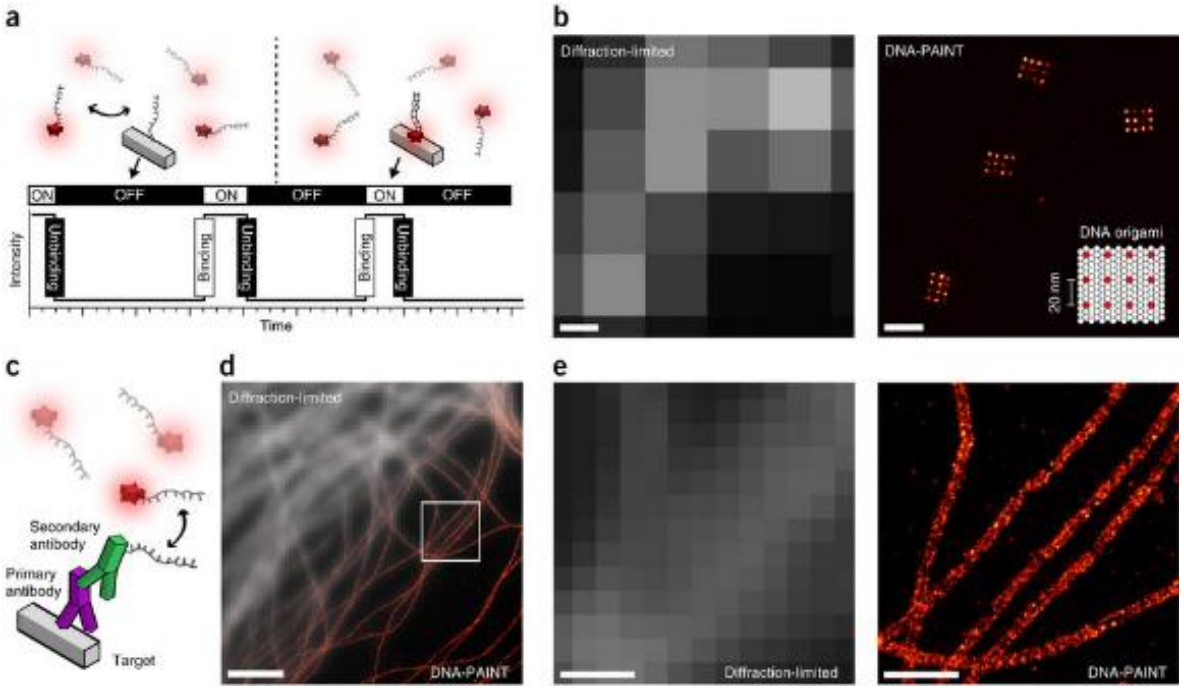

Figure 16. DNA-Paint concept. **a)** Transient binding of dye-labeled DNA strands (imagers) to their complementary target sequence (docking site) attached to a molecule. **b)** DNA Origami imaged with DNA-Paint. **c)** DNA-Paint labelling strategy. **d)** and **e)** Tubulins image comparing conventional and DNA-Paint imaging. Adapted from [73].

1.2.5 Single Molecule Tracking (SMT)

Several experimental techniques have been developed recently for measuring dynamic processes in living cells. One of the most used techniques by biologists in last decades is fluorescence recovery after photobleaching (FRAP)[76]. It can be used to study the mobility of lipids and proteins in the cell membrane and also in the cell cytoplasm and cell nucleus[76,77]. Other methods to obtain information on the dynamics of molecules in living cells are fluorescence correlation spectroscopy (FCS)[77], and image correlation spectroscopy (ICS)[78].

All these techniques provide an ensemble time average of the dynamics of the molecules under study. Heterogeneities within the cell that affect the diffusion of the molecules, short-lived molecular interaction events and molecules that play different roles and thus have different type of motion, are in general not accessible with these methods. A different approach that combines high spatial and temporal resolution is single molecule tracking (SMT). As a localization-based microscopy method, SMT localizes each individual particle with a precision of tens of nanometers and one can extract dynamic information of the single molecule's motion. The spatial resolution is given by the localization precision of the diffraction limited spots (10-50nm, depending on the imaging conditions) and the temporal resolution is given by the camera frame rate.

The advent of new membrane permeable dyes of less than 2nm of diameter than can penetrate in a cell nucleus of a living cell[79] and its conjugation with Tag technologies, like Halo Tag[80], provide a non-invasive labelling system that ensures high molecular specificity and the possibility of capturing dynamic processes in live cells. With this technology, we are able to study both chromatin assembly (with super resolution microscopy) and dynamics (with SMT). In addition, single particle tracking has also been used to follow the movement of fluorescent tracers such as quantum dots[81] (**Figure 17a**). Apart from the appropriate fluorophore, a method to target the protein of interest is needed. This can be achieved via different labelling modules, like antibodies (**Figure 17b**) or recently HaloTAG or SnapTAG systems[80,82]. The movement of these tracers mostly occurs via diffusion and can be hindered by the presence of obstacles created by highly compact chromatin structures and nuclear crowding. The selection of the probe with the appropriate characteristics is crucial for any SMT experiment (**Figure 17a** and **b**).

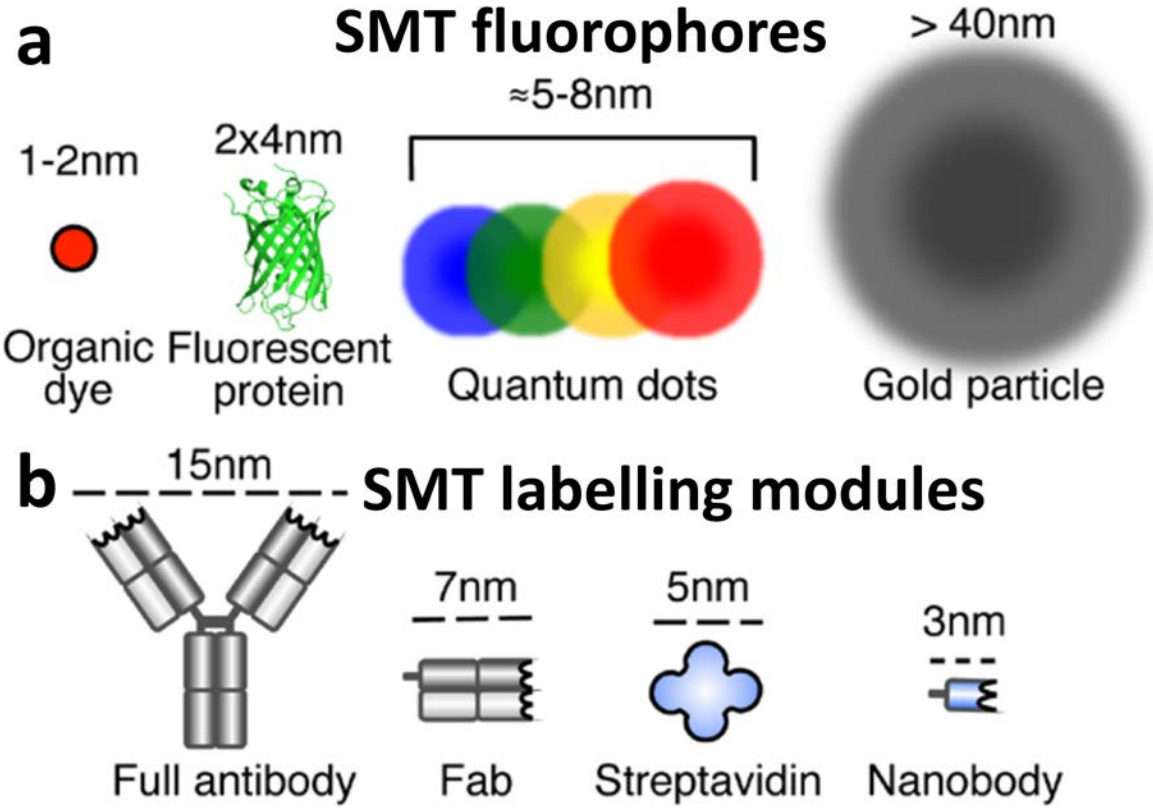

Figure 17. Labelling strategies for SMT. **a)** List of available fluorescent particles. **b)** List of specific labelling modules for biological molecules. Note that with the Halo-Tag system no labelling module is required. Adapted from [83].

There are three main steps to follow in order to perform a SMT experiment. The first one is to record a video on the microscope capturing the motion of the molecules of interest. Here the most important parameters are the laser power (that determines SNR, photobleaching and photoswitching) and the camera exposure time (that determines time resolution). For studying diffusion (or fast) dynamics, short exposure times are required, in the order of tens of milliseconds. Temporal resolution is limited by the maximum camera frame rate and the length of the traces by photobleaching. On the other hand, for studying slow dynamics (like chromatin unbinding events or residence times) long exposure times are used, in the order of hundreds of milliseconds to seconds. The second step is the localization, which is similar to SMLM methods and finally the tracking, when the localizations corresponding to the same molecule are connected (**Figure 18**). The algorithms to perform the localization and link the tracks are evolving significantly in the last years, and the approaches range from a simple nearest neighbour approach[84] to more complex ones based on Bayesian inference or assuming an a priori motion type for the tracks[83]. Still all the available techniques are prone to make mistakes when connecting the tracks, so there is room for improvement. For biological applications, scientist normally choose the simplest option, like nearest neighbour connection with certain spatial threshold, like a maximum frame-to-frame jump, avoiding prior assumptions and discarding tracks with merging and splitting events.

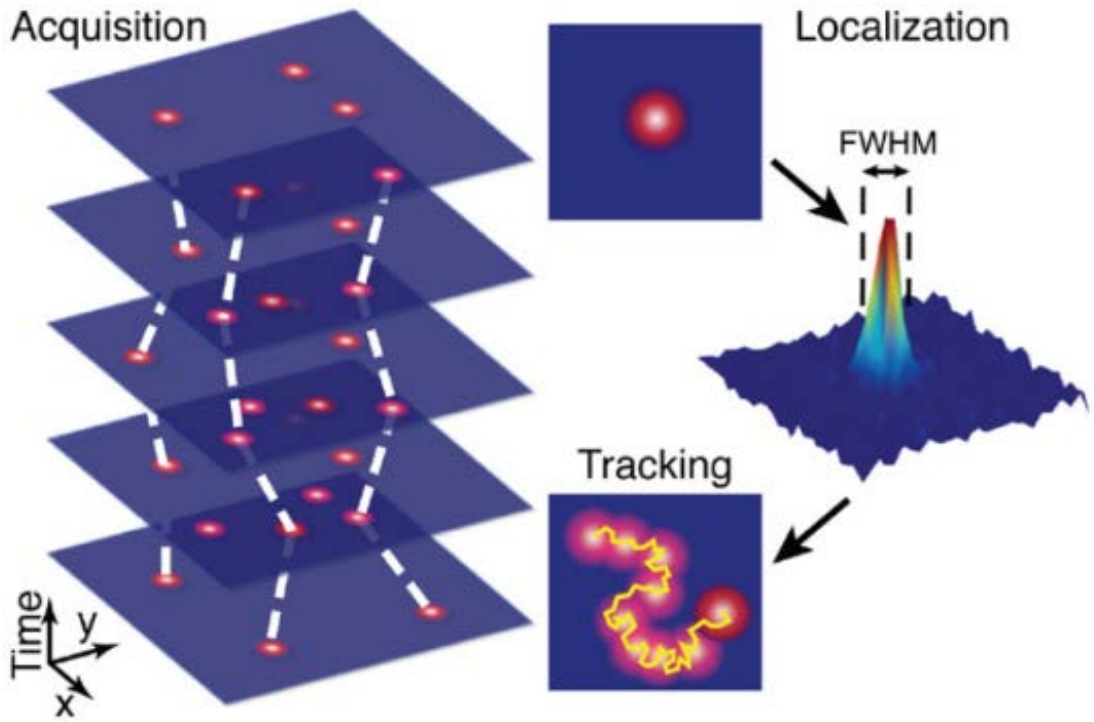

Figure 18. Schematic representation of SMT. Figure shows the acquisition over consecutive camera frames, localization of the molecule positions by fitting a 2D Gaussian and tracking step which connects the positions in order to generate a trajectory. Adapted from [83].

The length of the trajectory is important as it determines the amount of available information for performing downstream analysis. SMT suffers from photobleaching as well as from photoswitching of the fluorophores. The perfect SMT fluorophore will be a very bright and very stable one, so that it can be tracked ad infinitum with enough laser power to acquire high SNR. Reversible photoswitching can be partially amended on the processing step by allowing the tracking algorithm to connect the gaps of the trajectories with a certain threshold value, like a maximum spatial distance between the PSF and a maximum number of frames without localizations.

Once the trajectories are built one needs to analyse them in order to extract quantitative information. In this case, the analysis is different from the super resolution microscopy images of fixed structures, where the study is focused just on the spatial distribution. Here, time plays a crucial role and so the required analytical tools need to be adapted. SMT data analysis is still an immature field. Many new algorithms are continuously appearing, with the disadvantage that almost each scientific group uses their own analytical methods, so that there is a lack of standardization and it is sometimes difficult to compare the results. Still, there are some widely used methods. Mean Square Displacement (MSD) is probably the most relevant

one (**Figure 19a, b** and **c**). It is based on the analysis of the size of the frame-to-frame jumps of single molecules at different time lags (**Figure 19a**).

When dealing with thousands of trajectories, there are two common versions of the MSD. The Time-MSD (T-MSD) performs a time average of the trajectories assuming that the displacements at different times are equivalent (fulfilling the ergodic principle[85]):

$$TMSD(t_{lag} = m \cdot \Delta t) = \frac{1}{N-m} \cdot \sum_{i=1}^{N-m} \left(\boldsymbol{x_j}(t_i + m \cdot \Delta t) - \boldsymbol{x_j}(t_i) \right)^2,$$

where N is the number of positions of the tracks, $m \cdot \Delta t$ the discrete temporal sampling of the recorded image stack and x_j the 2D or 3D positions at each time point. Alternatively, the Time-Ensemble average of the MSD (TE-MSD) is the average of the T-MSD computed on all the trajectories for a particular condition:

$$TEMSD(t_{lag} = m \cdot \Delta t) = \frac{1}{J} \frac{1}{N-m} \cdot \sum_{j=1}^{T} \sum_{i=1}^{N-m} \left(x_j(t_i + m \cdot \Delta t) - x_j(t_i) \right)^2,$$

where J is the total number of trajectories. For the case of Brownian motion (or perfect random diffusion), the MSD can be simplified just by computing the variance of the solution of the diffusion equation[86] and the MSD scales linearly with the t_{lag} (**Figure 19b**):

$$MSD = 4 \cdot D \cdot t_{lag}$$

This is the MSD for Brownian motion of a 2D trajectory, where D is the diffusion coefficient. Note that normally the curve does not start at the origin due to the localization precision limit inherent to SMT technique. The localization error (σ) can be estimated from the point where the MSD curve intersects the y-axis as $MSD(tlag=0) = 4 \cdot \sigma^2$ (**Figure 19b**).

The crowded and heterogeneous environment of most of the biological systems introduces a new level of complexity in the analysis of SMT data, since molecules can freely diffuse, interact with other molecules and experiment molecular crowding or electrostatic barriers[87,88]. Molecules often perform what is defined as anomalous diffusion, better described by a power-law distribution:

$$MSD\left(t_{lag}\right) = 4 \cdot K \cdot t_{lag}^{\alpha},$$

where K is a generalized diffusion constant and α is the anomalous exponent, which characterize the motion type of the trajectory. α=1 is considered free diffusion or Brownian motion, α<1 sub-diffusion or confined motion and α>1 super-diffusion or directed motion (**Figure 19c**). This last motion type, which was extensively observed for active intracellular transport along microtubules[89], is also better modelled as a ballistic movement[87]:

$$MSD\left(t_{lag}\right) = 4 \cdot D \cdot t_{lag} + \left(v \cdot t_{lag}\right)^2,$$

where v is the speed of transport.

Confined motion can be modelled as a molecule constrained by physical or other types of compartments that can present several geometries at different scales. This behaviour is frequently found in molecules diffusing in the complex environment that is the cell nucleus of live cells. **Figure 19d** shows four examples of diffusing molecules that can be found in cells presenting different behaviours depending on the geometry of their local environment. One example that will be used for the analysis of the trajectories presented in **Chapter 4** of this thesis is the circle confined diffusion model[88], where a particle is confined to an static circular region with radius of confinement R and diffusion coefficient that represents the short-term mobility D_{micro}:

$$TEMSD = R^2 \cdot \left(1 - e^{\frac{-4 \cdot D_{micro} \cdot t_{lag}}{R^2}}\right)$$

This equation corresponds to the motion illustrated in **Figure 19d** but when the circle is not moving, so that D_{macro} doesn't play a role.

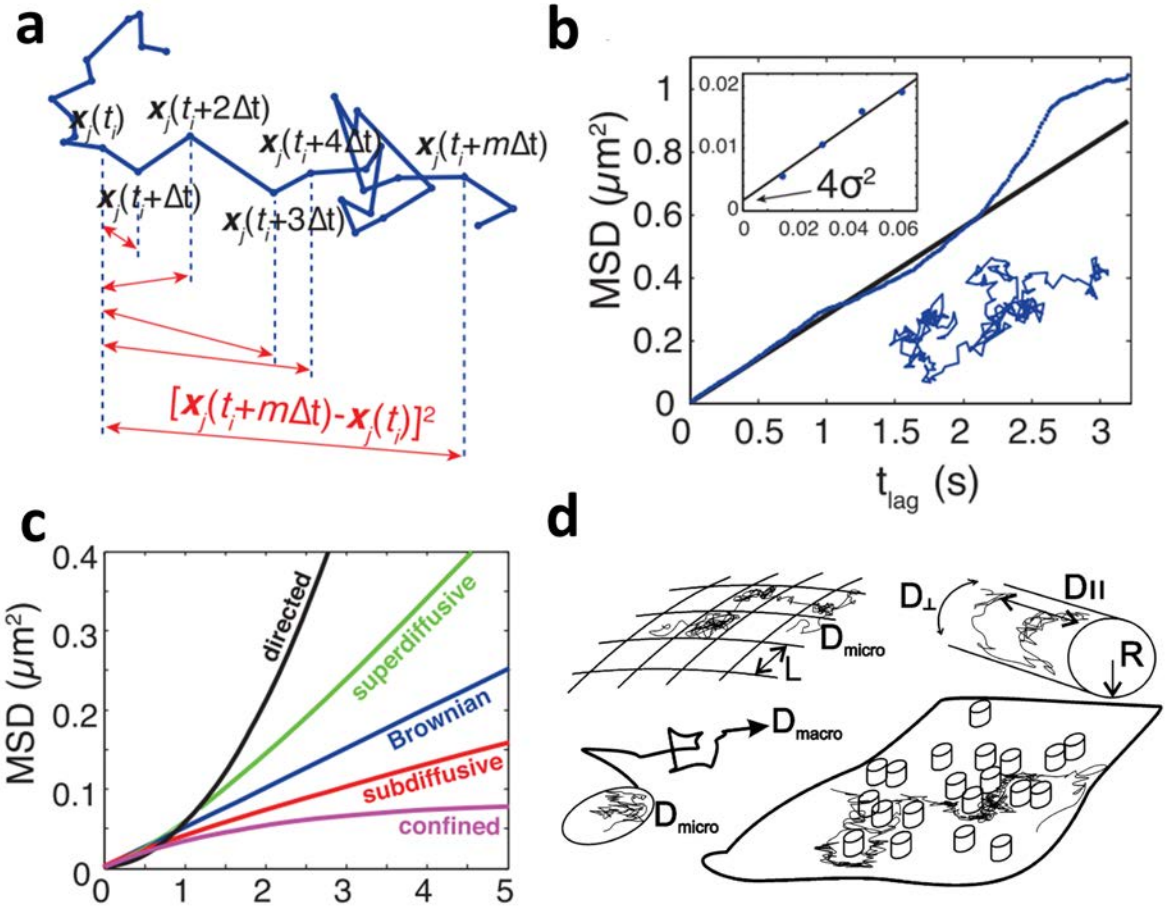

Figure 19. Mean Square Displacement (MSD). a) One trajectory showing the frame to frame jumps

at the different time lags. **b)** MSD curve of a random diffusing molecule (blue points) fitted with a linear distribution (black line). **c)** Theoretical definitions of different motion types based on their MSD curves. **d)** Cartoon showing four different subdiffusion behaviours of molecules that can take place in the cell nucleus. Clockwise and starting from the top left corner: hop diffusion, alternating between microscopic and macroscopic diffusion. Diffusion on cellular nanotubules, like microtubules or actin filaments, diffusion in a membrane containing static obstacles and confined diffusion (D_{micro}) within a moving circle (D_{macro}). Adapted from [83,88].

As it was mentioned before, the nucleus of eukaryotic cells is a very complex environment. Until very recently, SMT experiments were performed outside the nucleus, in the cytoplasm, mainly because of the difficulty to label target proteins inside the nucleus without harming the live cell. In addition, previous labelling probes were too big in comparison with the size of the target proteins, such that the labels could affect protein motion. With the advent of new developments in the field of probes, we are now able to perform SMT on a wide variety of targets inside the cell nucleus. HaloTag technology combined with cell permeable dyes is a good example of how these technologies have revolutionized the field (**Figure 20a**). Some advances also recently arised from the technical point of view in the imaging procedure. In order to image physiological processes in live cells, one needs to be as less invasive as possible to not perturb their normal function. On the other hand, the localization precision (or resolution) of localization-based microscopy methods is proportional to the amount of photons collected from the fluorescent probes. Thus, imaging approaches to achieve high enough signal to noise while maintaining the laser power low enough to not stress the biological samples are required. This is the main advantage of highly inclined thin illumination (HILO)[62], that enhances the signal to noise ratio by not illuminating the fluorophores that are out of the focal plane (**Figure 20b**). Some examples of what can be achieved when combining HILO and HaloTag technologies are shown in **Figure 20a** and **b** for different target proteins and imaging conditions.

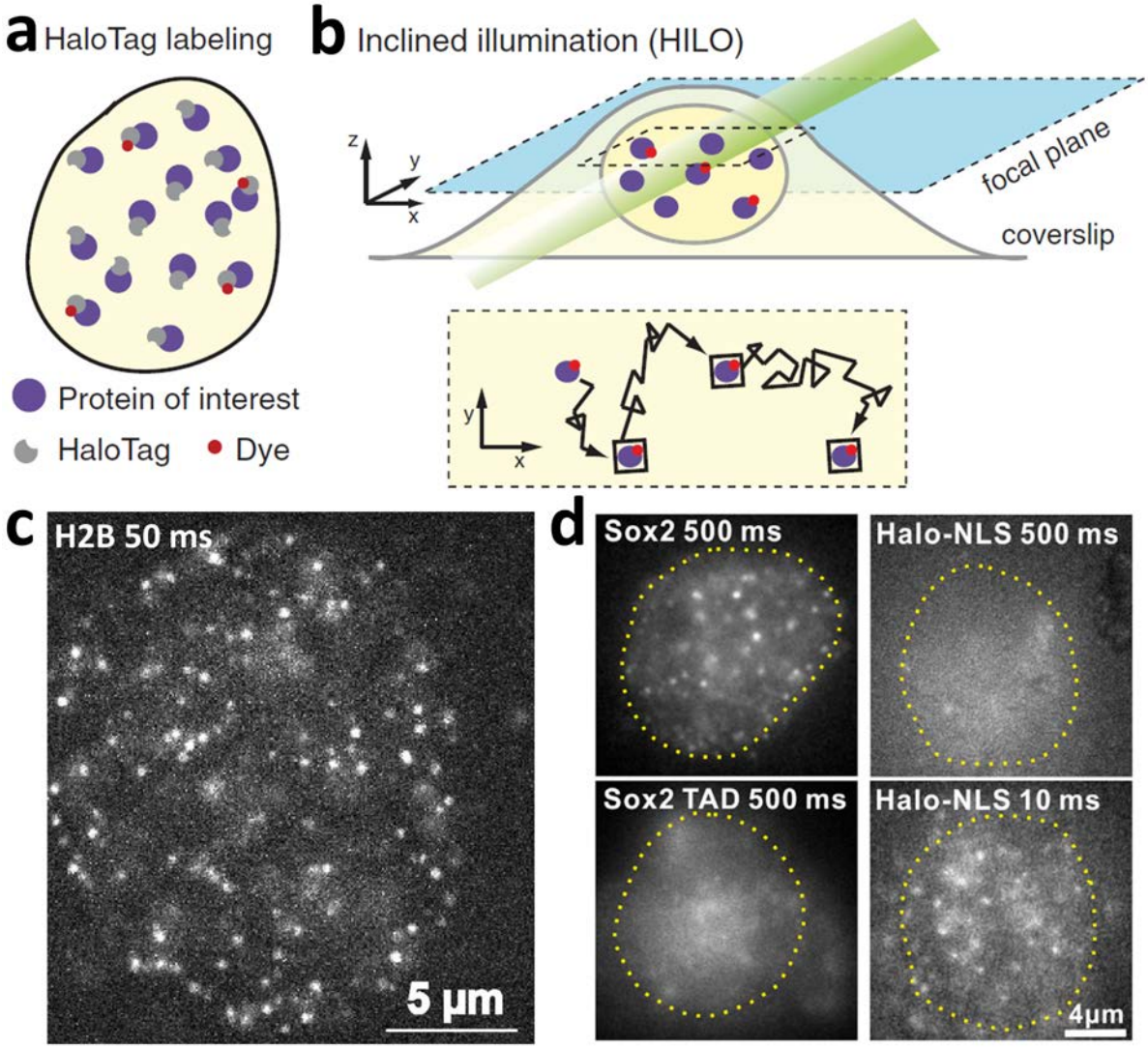

Figure 20. SMT in the cell nucleus. a) Scheme showing the HaloTag labelling technique. **b)** HILO illumination used in SMT experiments (top panel) and an example trajectory of a protein interacting with chromatin at specific sites. Transcription factors interacting with chromatin (lower panel). Adapted from [90]. **b)** One example frame of a SMT image stack of H2B taken at 50ms of exposure time, where single molecules are displayed. Adapted from [91]. **c)** Various examples of proteins and image conditions imaged in the cell nucleus of live cells. At 500 ms of camera exposure time, only Sox2 proteins bounded to chromatin are seen. When removing the Sox2 binding domain or imaging nuclear localization signal, no single spots are detected. But at 10 ms of exposure time, free diffusing NLS is detected. Adapted from [92].

Chapter 2: Frequency-multiplexed Super Resolution Microscopy

The content of this chapter is part of *P. A. Gómez-García et al., Excitation-multiplexed multicolor superresolution imaging with fm-STORM and fm-DNA-PAINT. Proceedings of the National Academy of Sciences 115-51, 2018.* (see **List of publications**).

2.1 Abstract

Recent advancements in single-molecule localization-based microscopy have made it possible to visualize biological structures and dynamic processes within the cell with unprecedented spatial resolution. Determining the spatial co-organization of these complex structures, like chromatin, under physiological and pathological conditions is an important biological goal. For example, in the context of visualizing the organization of the genome, it is important to visualize not only the DNA but also the architectural proteins that shape genome organization, including histones, as well as the epigenetic modifications of these histones that determine whether a specific region is active or silenced. Hence, visualizing genome organization requires tools that can achieve nanoscale spatial resolution in multiple colors in a multiplexed manner. Currently, one of the main limitations of this family of techniques is the difficulty to extend them to multiple colors, so that multiple target molecules can be imaged simultaneously. We developed an approach for simultaneous multi-color super resolution imaging which relies solely on fluorophore excitation, rather than fluorescence emission properties. By modulating the intensity of the excitation lasers at different frequencies, we show that the color channel can be determined based on the fluorophore's response to the modulated excitation. We use this frequency multiplexing to reduce the image acquisition time of multi-color super resolution DNA points accumulation in nanoscale topography (DNA-PAINT) while maintaining all its advantages: minimal color cross-talk, minimal photobleaching, maximal signal throughput, ability to maintain the fluorophore density per imaged color, and ability to use the full camera field of view. We refer to this imaging modality as "frequency multiplexed DNA-PAINT" or fm-DNA-PAINT. We also show that frequency multiplexing is fully compatible with Stochastic optical reconstruction microscopy (STORM) super resolution imaging, which we term fm-STORM. Unlike fm-DNA-PAINT, fm-STORM is prone to color cross-talk. To overcome this caveat, we further develop a machine-learning algorithm to correct for color cross-talk with more than 95% accuracy, without the need for prior information about the imaged structure. We expect fm-DNA-Paint to have several applications in visualizing the co-organization of multi-protein complexes, sub-cellular structures and organelles with high throughput.

2.2 Introduction

Multi-color localization-based microscopy is important for determining the relationship among the spatial distribution and sub-cellular localization of multiple proteins. However, existing multi-color implementations for super-resolution microscopy have important caveats including color cross-talk, unavailability of well-performing spectrally distinct photoswitchable fluorophores and long acquisition times. One approach for multi-color super-resolution microscopy uses fluorophore pairs in which the same reporter is coupled to different activators[59]. In this case, the color is determined based on the wavelength of the activation laser. Typically, a cycle of 3-4 camera frames is used in which a short pulse of activation laser light is followed by the imaging laser. In each cycle a different activation laser is used and the fluorophore localizations are color-coded based on which cycle the fluorophore turned on[59]. This approach is free from chromatic aberrations and the need for image registration. In addition, the full camera field-of-view is maintained over multiple colors. However, this is a sequential imaging approach, in which the time investment scales with the number of colors needed and it is prone to color cross-talk[93], since fluorophores can also undergo spontaneous blinking or can be activated by the "wrong" activation laser. A second approach uses spectrally-distinct photoswitchable reporter dyes[94] such that color cross-talk can be reduced or eliminated. However, chromatic aberrations can be difficult to correct at the nanoscale level[95]. In addition, there is a limited availability of spectrally distinct photoswitchable fluorophores with favorable photophysical properties. An alternative, third approach, which also reduces color cross-talk, is the use of spectrally-distinct photoswitchable reporter dyes[94,96–99]. While the multiple colors can be imaged simultaneously to reduce time investment, it comes at the expense of a reduced FOV since it requires splitting the camera FOV into smaller sub-regions, one for each color to be detected, hence decreasing experimental throughput. In addition, there is a limited availability of spectrally distinct photoswitchable fluorophores that minimize spectral cross-talk while simultaneously maintaining favorable photoswitching properties in the same imaging buffer. As a result, sequential imaging approaches are often preferred at the expense of increased image acquisition time.

PAINT is particularly amenable to multi-color super-resolution imaging since the on/off "blinking" solely depends on the oligo binding properties such that conventional fluorophores can be used. However, these advantages come with the major shortcoming of requiring long image acquisition times (tens of minutes up to several hours per color). This drawback arises because the unbound diffusing imager strands contribute to background[100]. The image acquisition time is related to the number of detected events per camera frame, which is proportional to the imager strand concentration [100]. Since increasing the imager strand concentration leads to increased background, there is a practical limit to how fast images can be acquired with conventional DNA-Paint[100]. Typically, multi-color DNA-

PAINT is performed sequentially by using imager strands labeled with the same fluorophore and with the target species labeled with orthogonal docking strands[74]. Therefore, the time investment scales linearly with the number of colors in sequential multi-color DNA-PAINT.

Finally, fluorescent molecules can also be discriminated based on their emission spectra in a fourth class of multi-color methods that use spectral information[101,102]. In general, these approaches necessitate increasing molecular sparseness to avoid spatio-spectral overlapping and in some cases splitting of the camera FOV into sub-regions, lengthening the acquisition time or reducing the available FOV. Importantly, spectral fluctuations inherent to single molecules[103] can limit the applicability of spectrally-resolved super-resolution approaches. All these caveats combined together limit the practical application of multi-color super-resolution imaging in biology.

2.3 Methodology

The method relies on the fact that individual fluorophores emit fluorescence directly proportional to their absorption cross-section at a given excitation wavelength. Thus, by modulating multiple excitation lasers at distinct frequencies, fluorophores with different excitation spectra will be excited to a varying degree according to their absorption cross-section at each given excitation wavelength. The total fluorescence emission from different fluorophores is collected on a single detector, in a color-blind fashion, and it is then demodulated using Fourier analysis in the frequency domain to retrieve the magnitude of the individual fluorophore signals for each color channel. For frequency multiplexing, the intensities of all of the excitation lasers were sinewave modulated independently at their own unique frequencies using acousto-optic modulators (AOM) (**Figure 21a**). A frequency range of 50-10Hz was used depending on the specific experimental configuration (**Detailed Methods DM1.1**). The different wavelengths were combined and coupled into the microscope objective through dichroic mirrors. The emitted fluorescence light was collected by the same objective and directed through a set of notch filters to solely reject the laser excitation wavelengths used in the experiment (**Figure 21a**). This configuration yielded maximum signal throughput to the EM-CCD detector.

The fluorophores emitted light proportionally to their absorption cross-sections at each excitation wavelength. For demodulation, the intensity evolution of the fluorophore within a given frame window (*m*), ranging from 4-6 frames, was transformed to the frequency domain (**Detailed Methods DM1.1**). For a given frame window, *m*, the Discrete Fourier Transform generates *m*/2 frequency bins and therefore *m*/2 available color-channels. Hence, a 6 frame window enables 3-color imaging (**Figure 21b**).

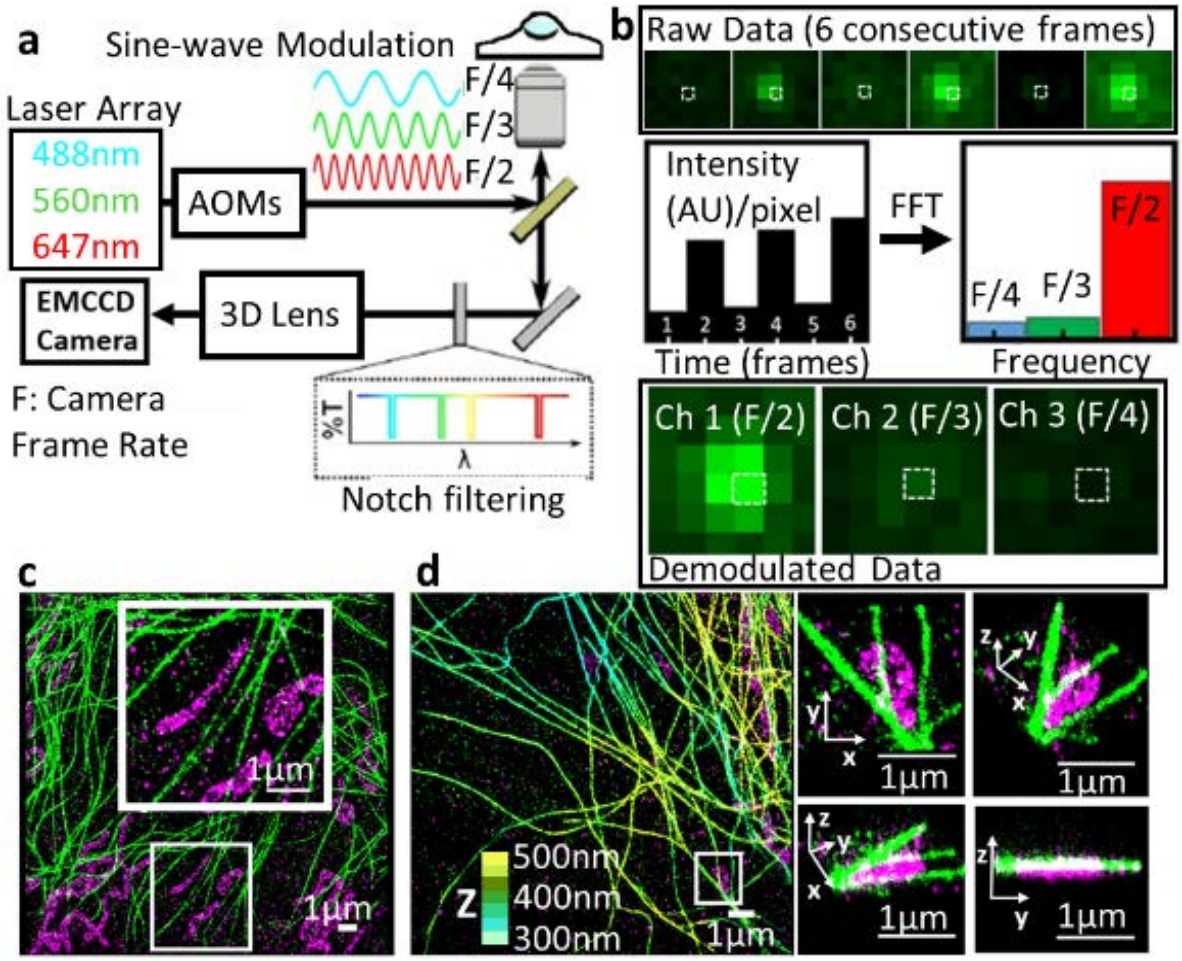

Figure 21: Frequency multiplexed concept. (a) Schematic of the microscope setup and imaging method. An example case of three illumination lasers are shown as sinewave modulated at three different frequencies, *F*/2, *F*/3 and *F*/4, where *F* is the camera frame rate. (**b)** Representative example of data processing. Upper panel: subROI of 6 consecutive frames with one fluorophore present. Middle panels: intensity evolution of the selected pixel (white box) in the time domain and amplitudes in the frequency domain after a FFT over the 6 frames. Bottom panel: resulting demodulated data split into the three different channels. **(c)** 2-Color, 2D fm-DNA-PAINT image of mitochondria (magenta) and microtubules (green). **(d)** 2-Color 3D fm-DNA-PAINT image of mitochondria and microtubules. Zooms on the right show 3D views of the white boxed region. Mitochondria is represented in magenta. For the microtubules, the color-coding indicates *z*-position (from 300 nm in light blue to 500 nm in yellow).

Experiments were performed using a custom microscope based on a Nikon Eclipse Ti body (Nikon Instruments). The optical system on the excitation path is formed by a set of dichroic mirrors and individual AOM for each laser line. This configuration allows modulating each laser independently and combining all of them together to simultaneously illuminate the sample. We used HiLo illumination[62] for all fm modalities. Just for demonstration of the

method, we used fixed and live BSC1 cells where we labelled microtubules, mitochondria and/or lysosomes. The data processing was performed by a combination of Insight3 localization software and custom Python scripts (freely available at Github: https://github.com/PabloAu/Excitation-multiplexed-multicolor-super-resolution-imaging-with-fm-DNA-PAINT-and-fm-STORM).

For more detailed explanation about the experimental procedures carried on for imaging, biological sample preparation, data processing and optical equipment see the **Appendix 1: Detailed Methods, section DM1.1**.

2.4 Results

2.4.1 fm-PAINT

For frequency multiplexed (fm) DNA-PAINT, the intensity evolution of each pixel in the time domain, corresponding to 6 consecutive frames acquired at a camera exposure time t = 16 ms per frame (F=60 Hz), was converted into amplitudes in the frequency domain by performing a Fast Fourier Transform (FFT). Those values were then assigned to the corresponding pixels on the demodulated images (one value per channel) (**Figure 21b**). After demodulation, fluorophores were localized in their corresponding color channel, in which they were already separated spatially and spectrally. The demodulated image stack had an effective exposure time of $m*t$, with m = 6 and t = 16 ms, fulfilling the long exposure conditions of DNA-PAINT (i.e., ~ 100 ms corresponding to an effective frame rate of 10 Hz). DNA-PAINT is particularly amenable to frequency multiplexing, since the fluorophore functionalized oligo stays bound to its complimentary oligo for a few hundred milliseconds. Hence, the bound fluorophore can be detected over multiple frames when imaged at the rate of 16 ms per frame, whereas the diffusing molecules are too dim after demodulation to be localized (**Detailed Methods DM1.1**, **Figure 22**). As a result, the color assignment becomes unambiguous. Accordingly, 2-color 2D and 2-color 3D images of microtubules and mitochondria, using Cy5-equivalent and Cy3-equivalent as fluorophores, respectively and imaged with fm-DNA-PAINT (**Figure 21c, d**) produced minimal color crosstalk (2.8% crosstalk from Cy5 into Cy3 channel and 0.8% crosstalk from Cy3 into Cy5 channel, **Detailed Methods DM1.1**, **Figure 23**). If desired, the color cross-talk could be further reduced using a simple correction approach without compromising the overall detected number of localizations (**Detailed Methods DM1.1**, **Figure 23**).

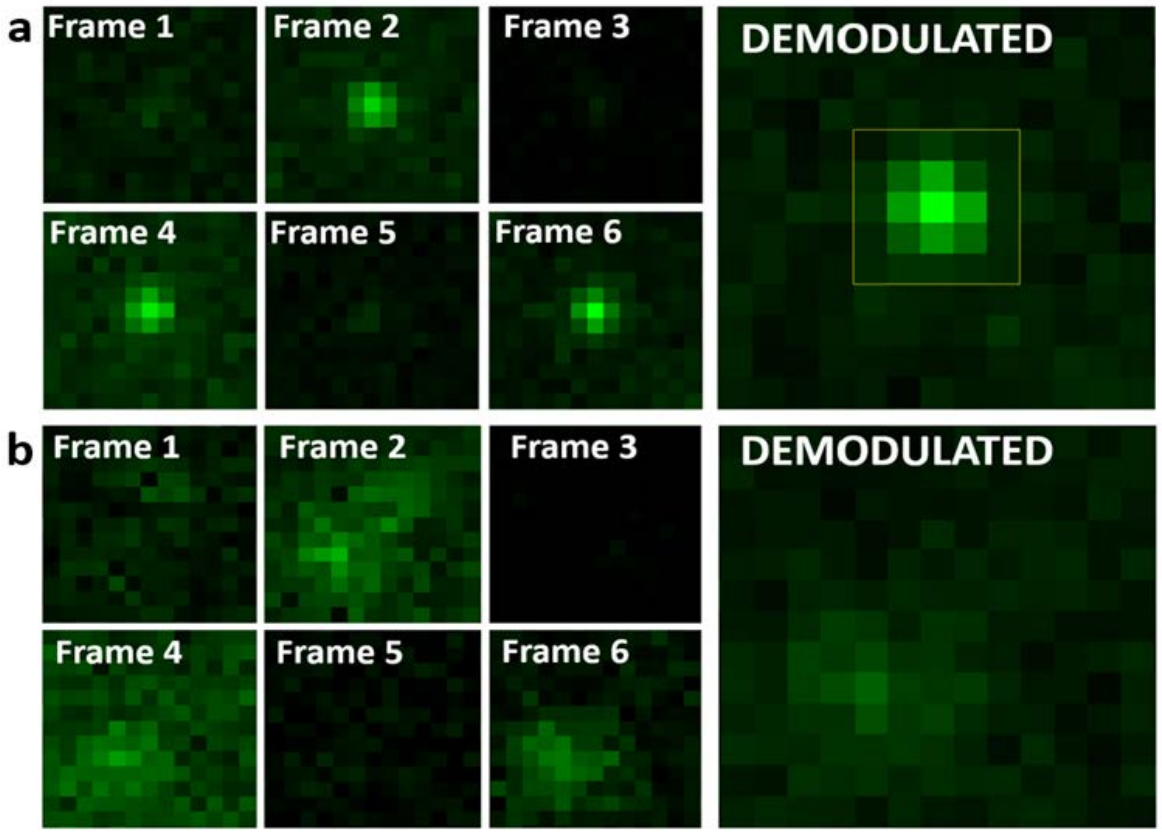

Figure 22: Effect of diffusing molecules on fm-DNA-PAINT: (**a**) Individual frames corresponding to a bound molecule in fm-DNA-PAINT (left) and the corresponding point spread function (PSF) of the molecule after demodulation (right). The PSF is bright enough to be localized by the localization algorithm (yellow square). (**b**) Individual frames corresponding to a diffusing molecule in fm- DNA-PAINT (left) and the corresponding point spread function (PSF) of the molecule after demodulation (right). The PSF is too dim to be localized by the localization algorithm.

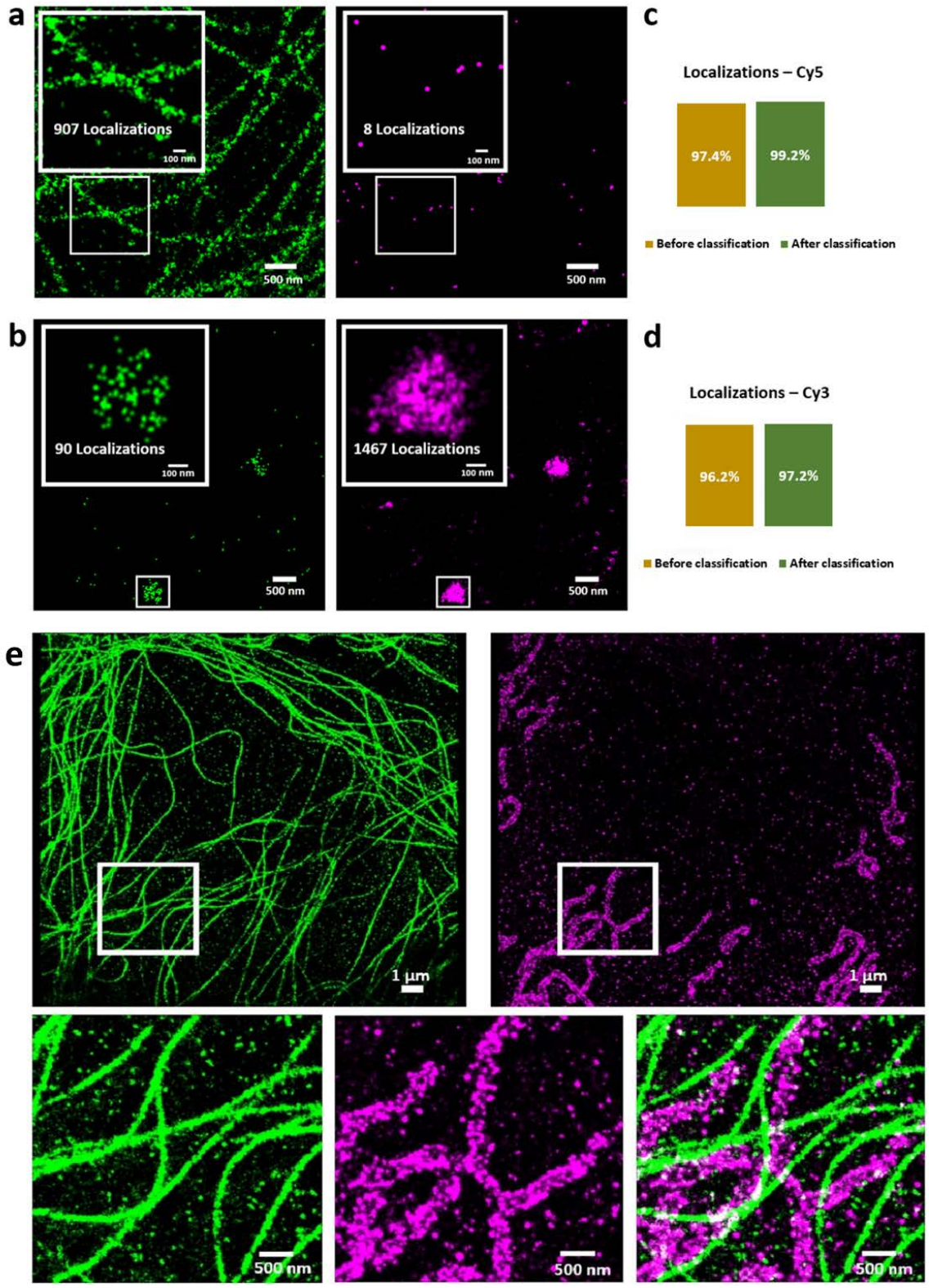
a
907 Localizations
100 nm
500 nm
8 Localizations
100 nm
500 nm
c
Localizations – Cy5
97.4%
99.2%
Before classification
After classification
b
90 Localizations
100 nm
500 nm
1467 Localizations
100 nm
500 nm
d
Localizations – Cy3
96.2%
97.2%
Before classification
After classification
e
1 µm
1 µm
500 nm
500 nm
500 nm

Figure 23: Color cross-talk quantification and correction in fm-DNA-PAINT. (**a-b**) Microtubules (green) (**a**) and lysosomes (magenta) (**b**) labeled with Cy5-equivalent and Cy3-equivalent dyes alone, respectively and imaged in two colors using fm-DNA-PAINT. Images show the results before crosstalk correction. The green localizations correspond to the Cy5 channel and the magenta localizations correspond to the Cy3 channel. Localizations in a region of interest around the imaged structure were quantified in the two channels (white boxes and insets). (**c-d**) Percentage of localizations belonging to the Cy5 (**c**) or Cy3 (**d**) channels before color cross-talk correction (yellow bars) and after color cross-talk correction (green bars). (**e**) Two-color super-resolution image of microtubules and mitochondria imaged using fm-DNA-PAINT, after crosstalk correction (same image shown in main Fig. 1c with the display split into two channels). Upper left panel shows microtubule channel only and upper right panel shows mitochondria channel only. Lower panel shows a zoom region (highlighted with a white box) of the microtubules, mitochondria and the overlay.

Localization precision determines the final resolution in single molecule based localization microscopy. We thus compared the localization precision of fm-DNA-PAINT to conventional DNA-PAINT using two different methods[52,63,67] (**Detailed Methods DM1.1**, **Figure 24**). Both methods showed that the localization precision of fm-DNA-PAINT was somewhat decreased (by a factor of ~1.4-2) compared to conventional DNA-PAINT. This decrease is merely due to the fact that by modulating the excitation lasers, fluorophores are excited only half of the duration of a single frame, and thus emit roughly half of the photons compared to continuous excitation. The modest decrease in localization precision of fm-DNA-PAINT is largely compensated by its gain in image acquisition times. Nonetheless, the fm-DNA-PAINT localization precisions were close to the reported values for other single molecule localization microscopy methods[63,104,105]. The localization precision can be improved by increasing the excitation laser powers so that the effective excitation is similar to that of conventional DNA-PAINT.

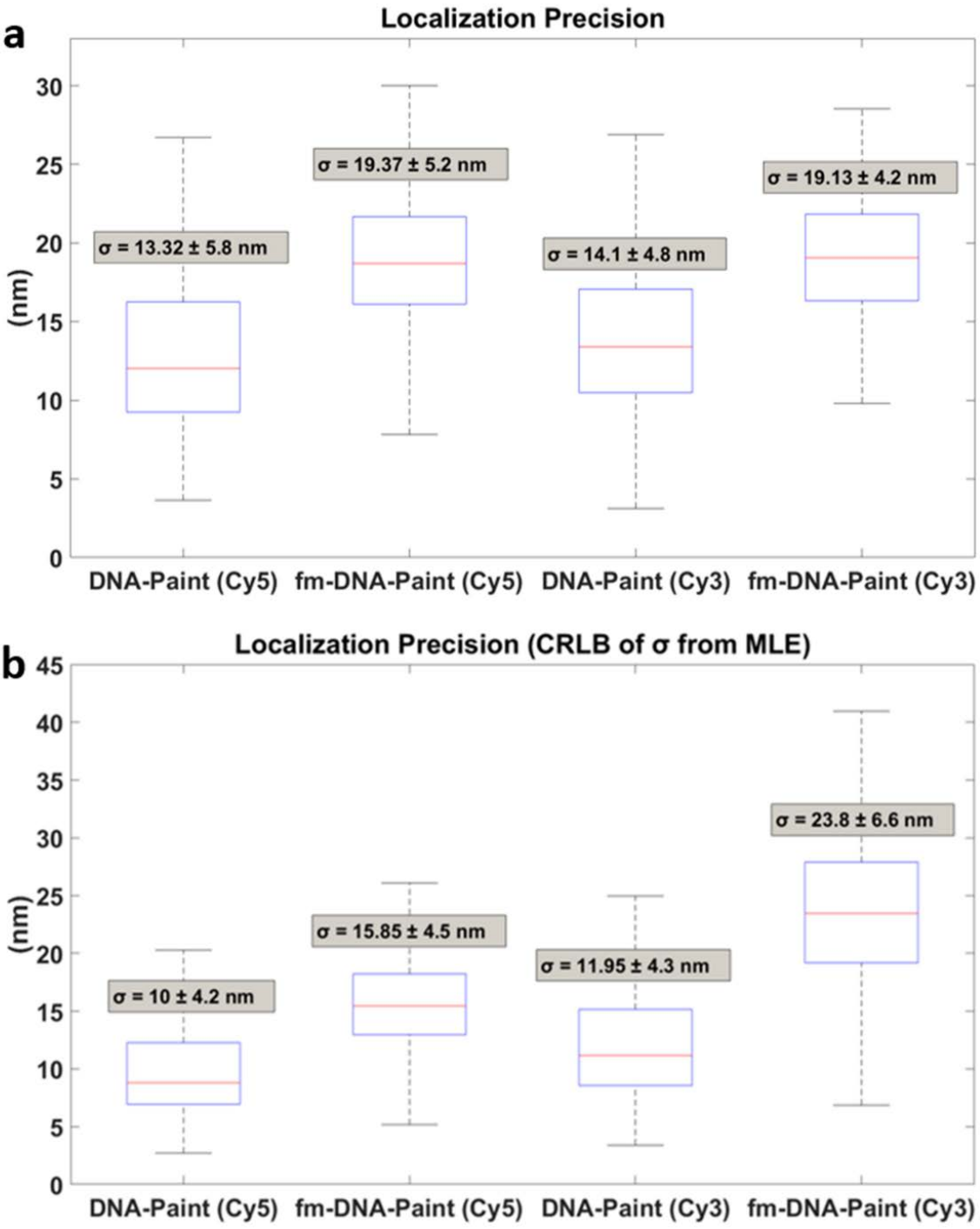

Figure 24: Localization precision comparison between conventional and fm-DNA-PAINT. (a) Localization precision calculated by localizing the same fluorophore in multiple frames and compared between conventional DNA-PAINT with 100 ms exposure time and fm-DNA-PAINT with 16 ms exposure time and 6 frame window size, for Cy5 and Cy3 fluorophores. **(b)** Comparison of the localization precision obtained from Cramer-Rao Lower Bound of the MLE Gaussian fitting.

For both (a) and (b) the mean σ ± the standard deviation are indicated in the box plots. Laser excitation powers were identical for conventional DNA-PAINT and fm-DNA-PAINT, i.e., 300W/cm^2. The box indicates the 25th (q_1) and 75th (q_3) percentiles. The whiskers extend to the most extreme data value that was not considered an outlier. Outliers are values bigger than $[q_3 + 1.5\cdot(q_3 - q_1)]$ or smaller than $[q_1 - 1.5\cdot(q_3 - q_1)]$. Around 99.3% (or ±2.7σ) of the data lies within these whiskers values.

fm-DNA-PAINT is particularly powerful as it is much faster in terms of experimental time investment compared to conventional multi-color DNA-PAINT. Multi-color DNA-PAINT is typically performed sequentially and requires exchanging the imager oligo strands with orthogonal ones [74], which can be cumbersome, introduces drift and adds additional time to the experiment. In fm-DNA-PAINT, multiple colors are obtained simultaneously and with an effective image acquisition time that is similar to that of one-color DNA-PAINT. There are some practical limits that determine the image acquisition time and the available number of color channels, such as the separation between the centers of the frequency bins used for modulation, the camera frame rate, the signal-to-noise ratio and the overlap between the excitation spectra of fluorophores. The number of frequency bins f_n (and hence the number of color channels) depends on the frame window size used for demodulation (m) (**Figure 25a**). For example, a modest estimate of f_n=3 can be fit inside a demodulation frame window of m=6 frames (**Figure 25a**), which will maintain a good separation between the frequency bins. The effective frame rate depends on the camera frame rate F and the demodulation frame window m (**Figure 25a**). For a frame rate of 60 Hz (used here), it is thus possible to image three colors with an effective frame rate of 10 Hz. This frame rate is equivalent to the one typically needed for acquiring a single color conventional DNA-PAINT image, improving the imaging throughput by three-fold (**Figure 25b**). Since these acquisition settings do not reach the lower limit of photon collection for high localization precision (**Figure 24**), the number of channels can further be increased, while maintaining the same effective frame rate, by increasing F and m (**Figure 25b**).

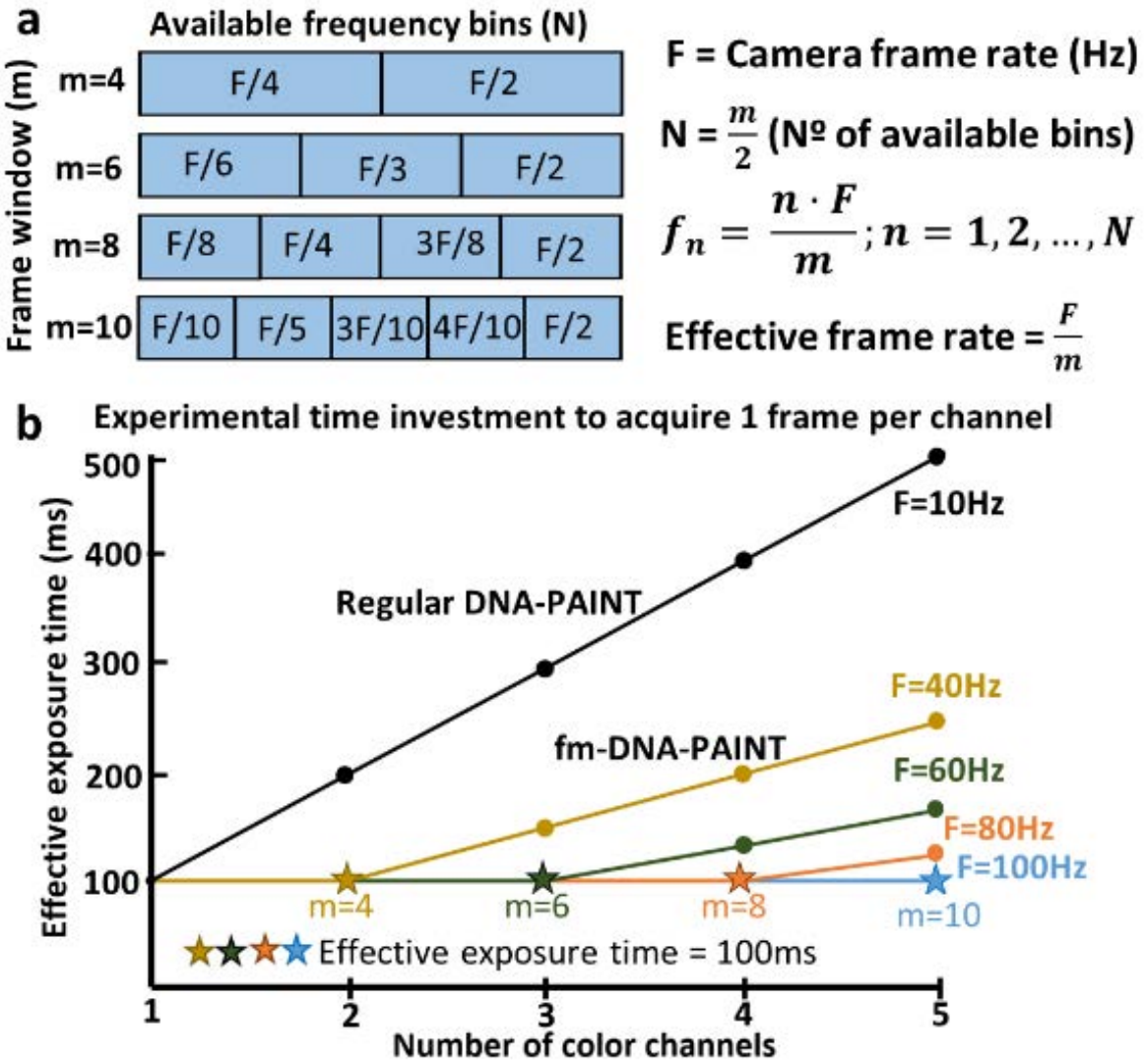

Figure 25: Multi-color fm-DNA-PAINT dramatically improves experimental time investment compared to sequential multi-color DNA-PAINT: (a) Scheme showing the available frequency bins *fn* (and thus number of colors) for a given demodulation frame window size *m* **(b)** Effective exposure time versus the number of color channels for different camera frame rates *F*. The black line shows conventional DNA-PAINT where multi-color imaging is performed sequentially, assuming an exposure time of 100 ms per color (i.e., *F*=10Hz).

The image acquisition time in DNA-PAINT depends on both the camera frame rate and the time needed to collect a sufficient number of localizations to satisfy the Nyquist criterion for high image resolution[106]. DNA-PAINT does not suffer from photobleaching as there is continuous replenishment of imager strands from the solution. As a result, the number of localizations per frame is constant and hence the cumulative number of localizations increases linearly with the number of frames acquired. We experimentally verified that the cumulative number of localizations over time was similar for single-color fm-DNA-PAINT

(16ms exposure time, *m*=6) and single-color conventional DNA-PAINT (100 ms exposure time) (**Figure 26**). Therefore, no additional time is needed in fm-DNA-PAINT to accumulate equal number localizations as compared to conventional DNA-PAINT.

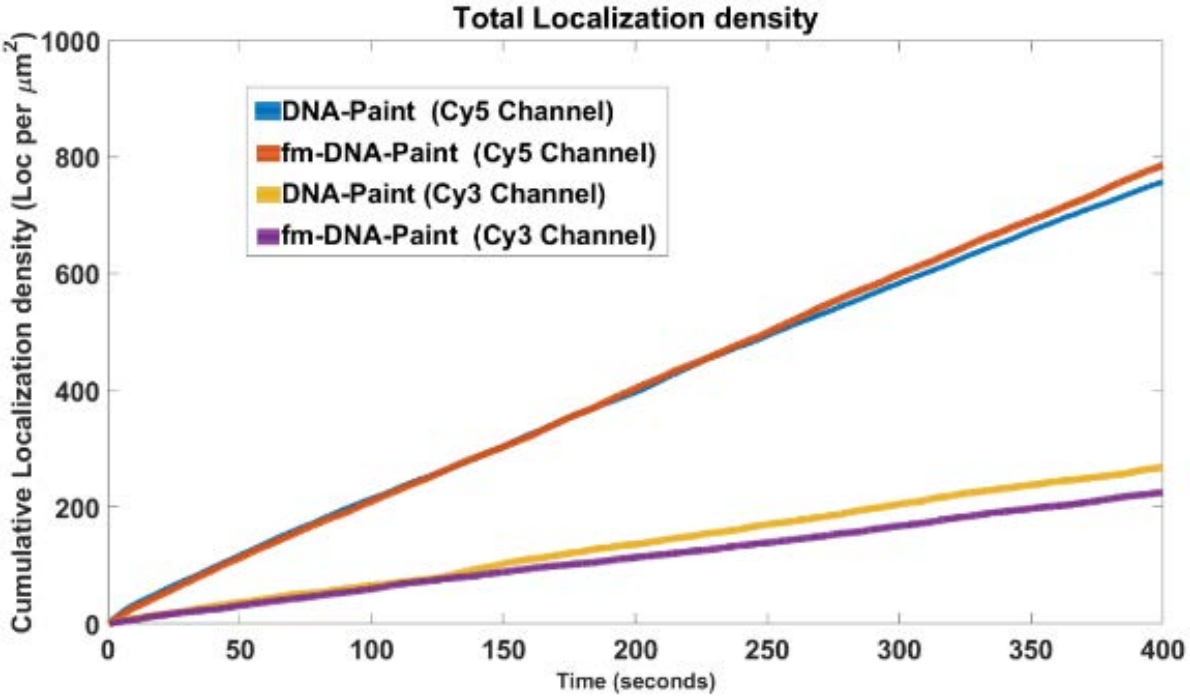

Figure 26: Cumulative localization density as a function of time. Number of localizations per frame in both DNA-PAINT and fm-DNA-PAINT grow linearly with the number of frames, since in both cases there is inexhaustible amount of fluorophores. No differences are measured in terms of the total localization density as a function of time between conventional and fm-DNA-PAINT. The difference in the slopes between the Cy5 and Cy3 channels is only due differences in the concentrations of the fluorophores used for the experiments, being higher in the Cy5, 647 nm channel than in the Cy3, 561 nm channel.

To assess any potential limits in extending fm-DNA-PAINT to more colors, we first estimated the percentage of spatially overlapping PSFs as the number of colors is increased. This control is needed since acquiring multiple colors simultaneously on a single detector can lead to crowding and spatial overlap between the fluorophores. Reducing the fluorophore density to minimize spatial overlap would jeopardize the advantages of the method, as it would result in longer image acquisition times to fully reconstruct a super-resolution image. As expected, the probability of spatial overlap became significant for more than three colors (**Figure 27**). To then assess the capability of our method to distinguish spectrally distinct fluorophores having full spatial overlap, we simulated three sinewave modulated signals and combined them so that they spatially overlap on the same pixel, and followed their time evolution (**Figure 27**). In the frequency domain the amplitudes at the different modulation

frequencies are fully distinguished and separated into each different component to retrieve their unique color (**Figure 27**).

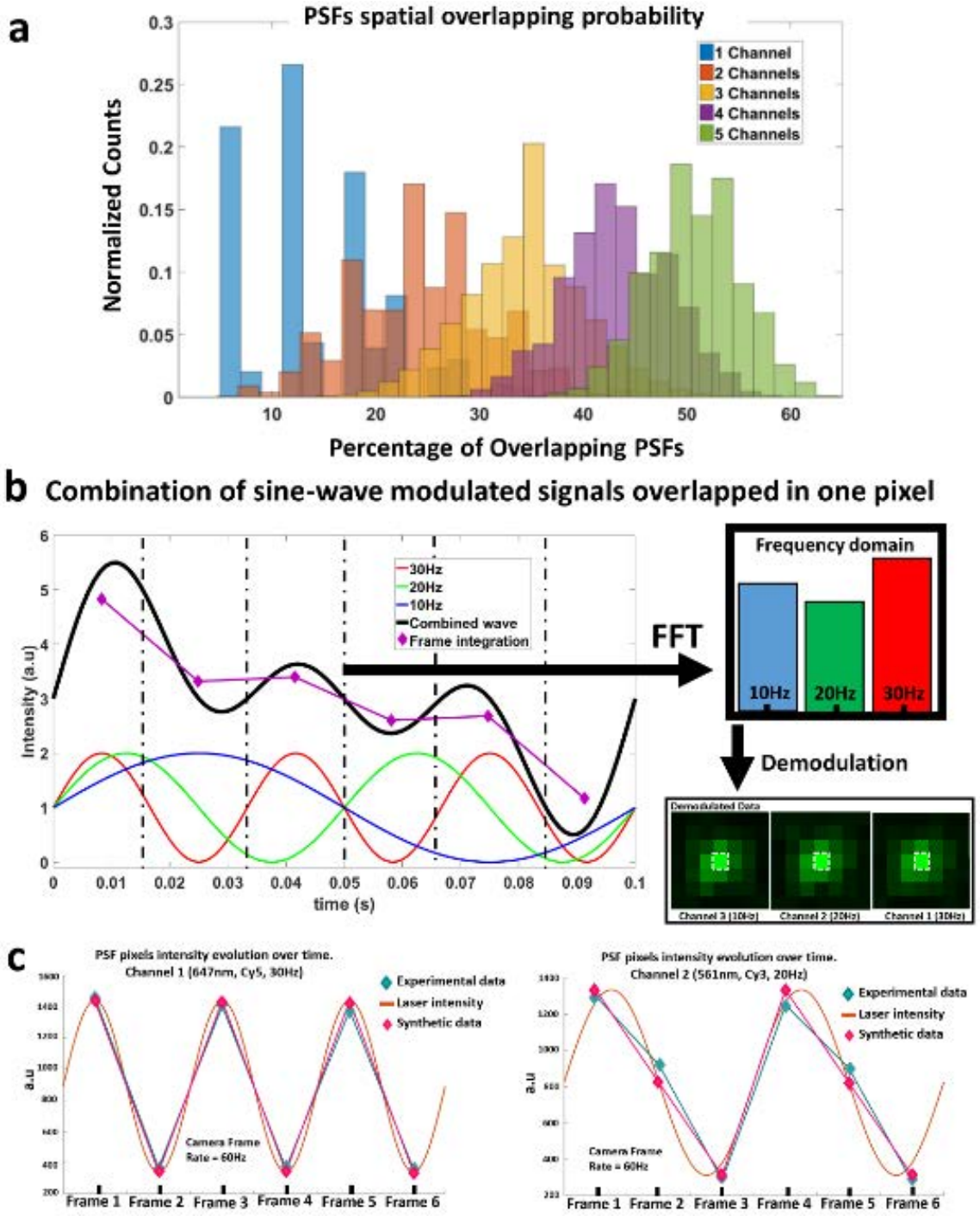

Figure 27: Effect of the spatial overlap between spectrally distinct fluorophores (Cy5-equivalent and Cy3-equivalente) in fm-DNA-PAINT. (a) Histogram showing the probability of

spatial overlap between randomly distributed fluorophores with a PSF of 5x5 pixels (800x800nm) and a constant PSF density per frame of 0.1 localization/μm^2. The probability of spatial overlap is shown for one-to-five color channels. **(b)** Example of one pixel intensity evolution in time domain when three spectrally distinct fluorophores overlap spatially. The three fluorophores are modulated with excitation laser frequencies of 10 Hz, 20 Hz and 30 Hz. The red, green and blue lines correspond to the sinewave modulation of the three lasers. The black line is the combination of these individual sinewaves. The magenta line is the integration of the combined sinewave over each frame (16 ms in this case), which is proportional to the pixel intensity signal, due to the response of the three overlapping fluorophores to the three sinewave modulations. Note that a 6 frame window size (m=6) is used, and thus 6 pixel values are calculated. In the frequency domain the pixel can be properly demodulated into the three different color channels. The white square in the demodulated data shows the demodulated pixel in the three corresponding channels. The intensity of the pixel on the reconstructed (demodulated) image is proportional to the amplitude in that particular frequency in the frequency domain. **(c)** The response of fluorophores to sinewave modulated laser excitation obtained from experimental data. The orange line shows the modulated sinewave excitation. The blue diamonds are the measured intensity of the fluorophore over 6 frames in response to the sine wave excitation. The magenta diamonds are the generated intensity of the fluorophore in the synthetic data over 6 frames. The blue and magenta lines are guides to the eye.

Since currently there are only two different types of commercially available DNA-PAINT antibodies, we generated synthetic data to further determine the ability of fm-DNA-PAINT to acquire more than two-colors. The synthetic data was generated by taking as input a 5x5 pixel sub-region of interest (subROI) of a PSF from one frame of the single color experimental data (**Detailed Methods DM1.1**). We created multiple PSFs over several consecutive frames to simulate the emission of a fluorophore under sinewave modulated illumination. We first confirmed that the synthetic data generated for two different fluorophores faithfully represented our experimental data (**Figure 27**). Having validated our approach, we next generated 5-color synthetic data in which all 5 different fluorophores were spatially mixed together in a color-blind fashion and with spatial overlap (**Detailed Methods DM1.1**, **Figure 28**). The synthetic data was then demodulated and separated into 5 different channels (**Figure 29**). The fluorophores were correctly assigned to the corresponding channels, further demonstrating the capability of the method to separate spectrally distinct fluorophores in the presence of spatial overlap (**Figure 29**)**.** Importantly, these results also show that the increased fluorophore density resulting from multiple different fluorophores does not affect color discrimination of fm-DNA-PAINT, thus maintaining its advantages in terms of image acquisition speed.

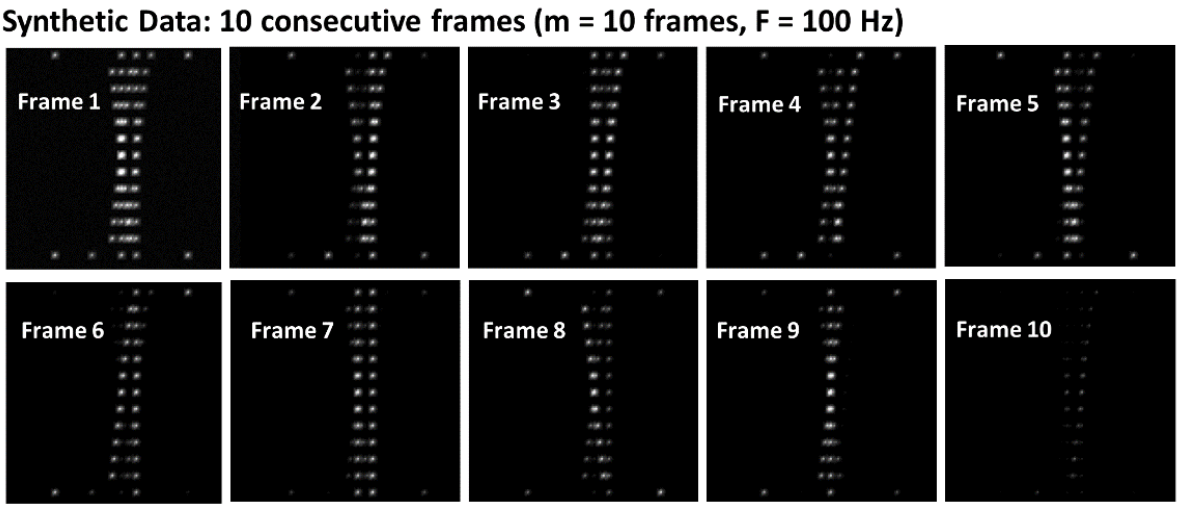

Figure 28: Synthetic raw data for 5-color fm-DNA-PAINT. 5-color synthetic image generated with camera frame rate F=100Hz and f_i of 50Hz, 40Hz, 30Hz, 20Hz and 10Hz, assuming that the fluorophores have minimal spectral overlap (similar to the 2-color experimental data with Cy5 and Cy3). Ten consecutive frames from the synthetic raw data are shown. The brightness of the pixels in each frame reflects the integrated intensity of the modulated excitation. The corresponding demodulated frames for each channel are shown in **Figure 29** below

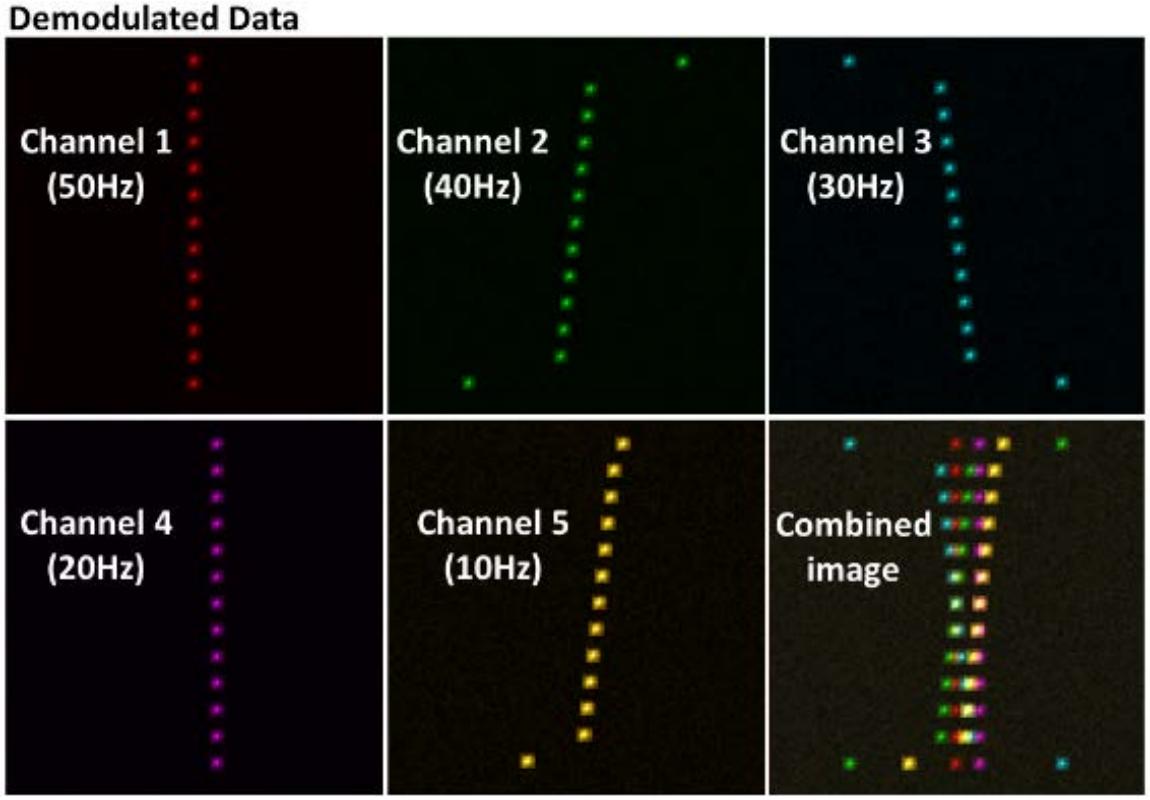

Figure 29: Simulations demonstrate the extendibility of multi-color fm-DNA-PAINT to 5-

color channels. Demodulated frames for each channel from a 5-color synthetic image generated with camera frame rate F=100Hz and f_i of 50Hz, 40Hz, 30Hz, 20Hz and 10Hz, assuming that the fluorophores have minimal spectral overlap (similar to the 2-color experimental data with Cy5 and Cy3). The overlapped (combined) image is shown on the lower right panel.

Despite correct color discrimination, the spatial overlap between fluorophores could still distort the reconstructed PSF on the demodulated data if there is partial spectral overlap between the fluorophores. For instance, in our experiments, Cy5 absorbs ~10% of the 561nm laser. This additional amplitude in the "wrong" modulation frequency will perturb the reconstructed PSF, affecting the accuracy of the corresponding localization. To determine the magnitude of this effect, we generated semi-synthetic stacks of images taking as input the experimental PSFs obtained from the two color fluorophores (**Detailed Methods DM1.1**). In these image stacks, we kept the spatial positions of the PSFs belonging to one-fluorophore constant and shifted the PSFs of the second fluorophore (D_{shift}) allowing for spatial overlap (**Figure 30 and Figure 31a**). The semi-synthetic stacks were demodulated and the centers of the PSFs of the shifted fluorophores were localized. We then computed the distances from the localized x and y positions to their actual simulated positions ($D_{relative}$) (**Figure 31a**). $D_{relative}$ was only slightly affected (**Figure 31b,c, *inset***) with an overall effect for Cy5 of 10.6 nm and 5.9 nm for spatial overlapping and non-overlapping fluorophores, respectively, and 6.8 nm and 2.1 nm for Cy3. Thus, overall the distortions due to spatial overlap led to a localization error of ~ 5 nm for both channels, which was smaller than the average localization precision (**Figure 24)**. We also determined if changes in the relative brightness of one fluorophore with respect to the other fluorophore has an impact on the localization error in the presence of spatial overlap (**Detailed Methods DM1.1**, **Figure 32a, b**). Again, the error in localization was minor compared to spatially non-overlapping fluorophores for all relative intensity values.

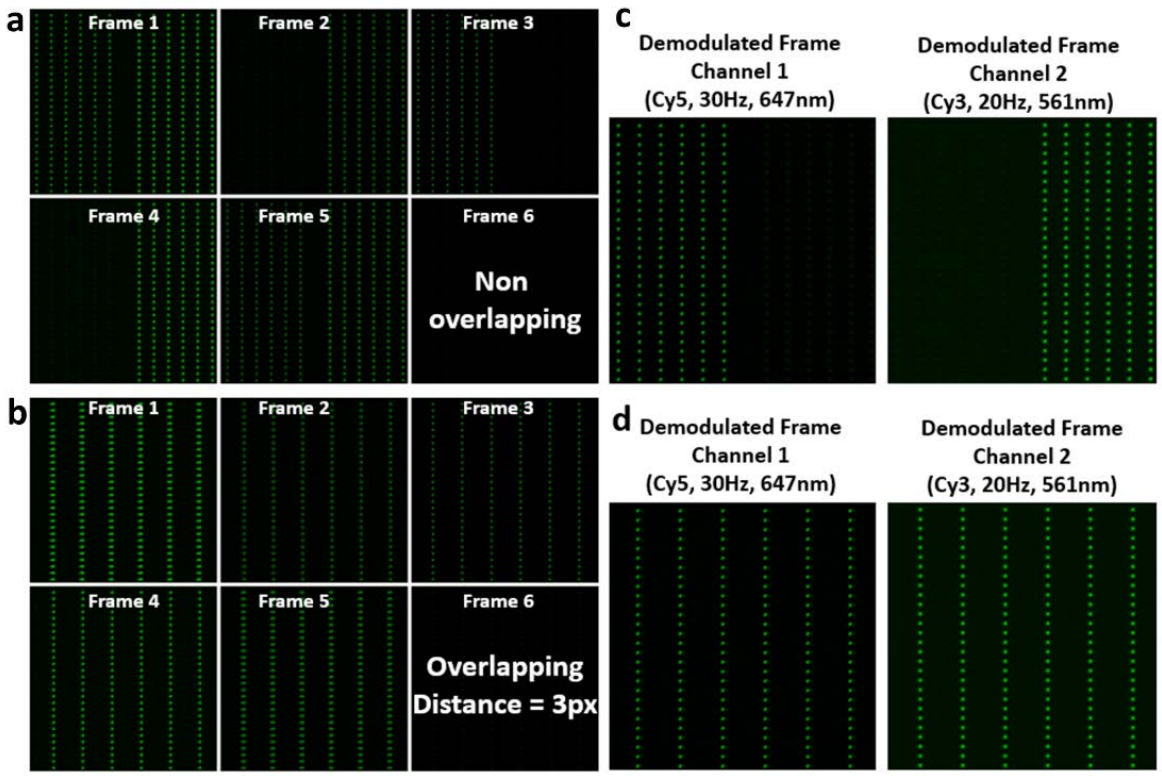

Figure 30: Semi-synthetic data to assess the effect of spatial overlap on the localization precision of fm-DNA-PAINT. (a) 6 consecutive frames of the semi-synthetic dataset in the absence of spatial overlap between the two spectrally distinct fluorophores (Cy5-equivalent, left 6 stripes and Cy3-equivalent, right 6 stripes) illuminated with lasers at different modulation frequencies (30Hz and 20Hz respectively). The camera frame rate is F=60Hz. 168 PSFs per channel were generated. The difference in brightness in the frames reflects the integrated excitation intensity for the different modulated lasers. **(b)** Similar as (a) but with an overlapping of 3 pixels between the two color channels. **(c)** Corresponding demodulated frame of the image stack in **a** for both channels. **(d)** Corresponding demodulated frame of the image stack with spatially overlapping fluorophores in **b** for both channels.

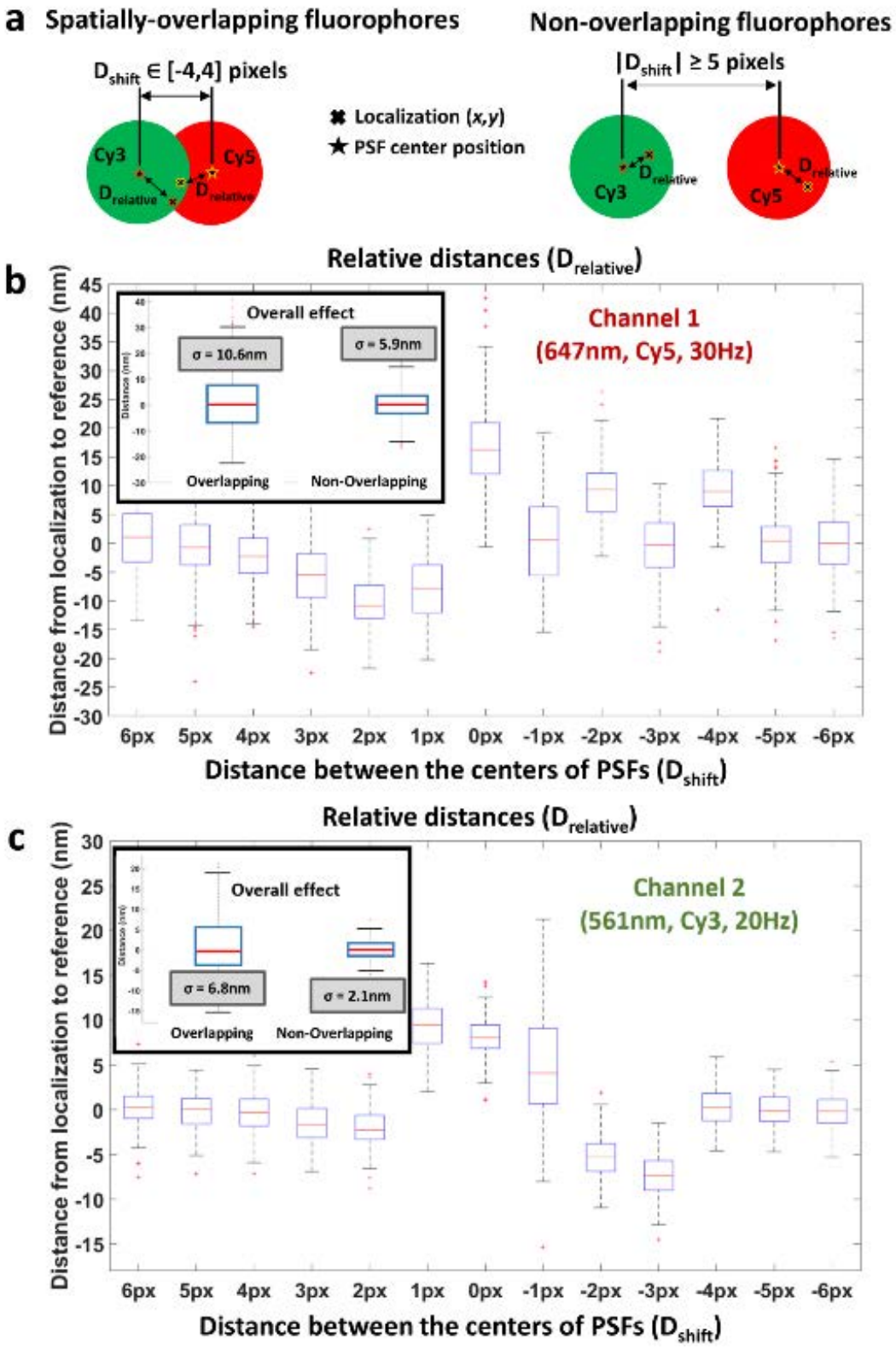
a
Spatially-overlapping fluorophores
Non-overlapping fluorophores
$D_{shift} \in [-4,4]$ pixels
$|D_{shift}| \geq 5$ pixels
Localization (x,y)
PSF center position
Cy3
Cy5
$D_{relative}$
b
Relative distances ($D_{relative}$)
Distance from localization to reference (nm)
Overall effect
σ = 10.6nm
σ = 5.9nm
Overlapping
Non-Overlapping
Channel 1
(647nm, Cy5, 30Hz)
6px 5px 4px 3px 2px 1px 0px -1px -2px -3px -4px -5px -6px
Distance between the centers of PSFs (D_{shift})
c
Relative distances ($D_{relative}$)
Distance from localization to reference (nm)
Overall effect
σ = 6.8nm
σ = 2.1nm
Overlapping
Non-Overlapping
Channel 2
(561nm, Cy3, 20Hz)
6px 5px 4px 3px 2px 1px 0px -1px -2px -3px -4px -5px -6px
Distance between the centers of PSFs (D_{shift})

Figure 31: Effect of the spatial overlap between spectrally distinct fluorophores (Cy5-equivalent and Cy3-equivalente) on localization accuracy in fm-DNA-PAINT. (a) Cartoon showing the method used for estimating the perturbation on the localization position produced by the spatial overlap of spectrally distinct fluorophores, for overlapping (left) and non-overlapping (right) conditions. The green and red circles denote the two different fluorophores, with their real center positions marked by the star symbol. D_{shift} corresponds to the spatial shift between the different colored PSFs in the semi-synthetic data. After demodulation, the *x,y* positions are determined (cross symbols) and $D_{relative}$ (distance between the localized positions and the real positions) is measured. Thus, $D_{relative}$ is a measure of the spatial overlap influence that one color-fluorophore has on the localization position of the other color-fluorophore after demodulation. **(b)** Effect of Cy3 spatial overlap on the localization position of the Cy5 channel, for different degrees of spatial overlap, i.e., D_{shift}. The inset shows the combined distribution for all overlapping pixels and all non-overlapping pixels. **(c)** Effect of Cy5 spatial overlap on the localization position of the Cy3 channel, for different degrees of spatial overlap, i.e., D_{shift}. The inset shows the combined distribution for all overlapping pixels and all non-overlapping pixels. Although in principle one would expect $D_{relative}$ to be zero in the complete absence of spatial overlap, $D_{relative}$ is also influenced by the difference in brightness and background of the fluorophores. This is because our generated semi-synthetic data uses experimental input data including background. Therefore slight variations in the fluorophore brightness and/or background will lead to small deviations in the demodulated localization positions. For the generated *in-silico* data, this effective localization error is around 5.9 nm for Cy5 and 2.1 nm for Cy3. Notice that the influence of spatial overlap in the localization position of the fluorophores is larger for Cy3 than for Cy5, i.e., a factor of 3 for the influence of Cy5 in the position of Cy3 and only a factor of 1.8 for the influence of Cy3 in the position of Cy5. This result is entirely consistent with the fact that Cy5 absorbs about 10% of the Cy3 excitation wavelength (561nm) and thus it would induce a larger perturbation on the Cy3 channel. In (b) and (c) the box indicates the 25th (q_1) and 75th (q_3) percentiles. The whiskers extend to the most extreme data value that was not considered an outlier. Outliers are values bigger than $[q_3 + 1.5\cdot(q_3 - q_1)]$ or smaller than $[q_1 - 1.5\cdot(q_3 - q_1)]$.

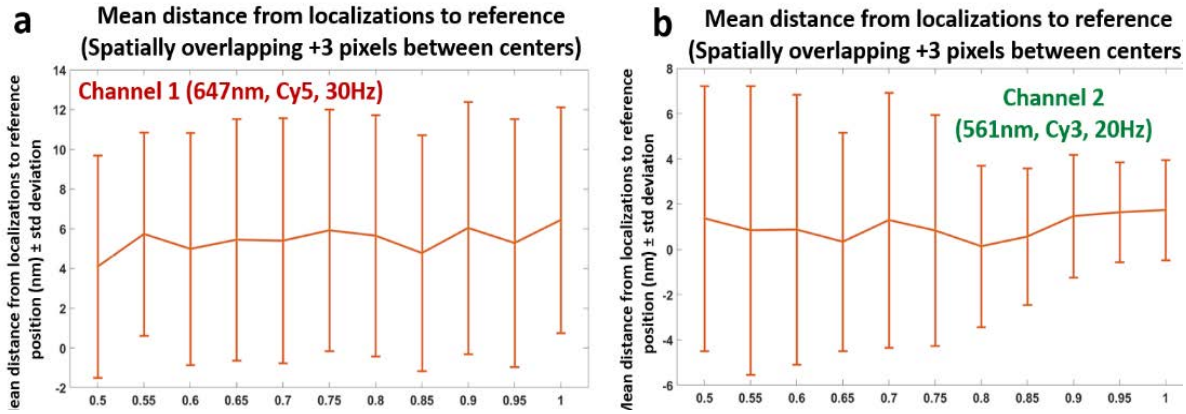

Figure 32: (a) and **(b)** Effect of the relative signal between fluorophores on localization accuracy in the presence of spatial overlap. In this case, a constant relative distance of +3 pixels between the centers of the PSFs was set, such that there is spatial overlap. The relative signal between the PSFs

was set by generating semi-synthetic data, in which the Cy5 intensity was kept constant and all pixels of Cy3 PSF in the 6 consecutive frames were multiplied by a relative intensity factor (ranging from 1 to 0.5). The vertical bars are the standard deviation.

2.4.2 fm-STORM

STORM is another commonly used single molecule localization microscopy method, which relies on the use of buffers containing reducing agents and oxygen scavengers in order to induce photoswitching in organic fluorophores[52]. We next set out to implement frequency multiplexing in STORM (fm-STORM) using a 4 frame window for the demodulation. In this case, unlike fm-DNA-PAINT, the demodulation was performed after the fluorophores were localized in each frame. We determined the localization precision of fm-STORM from the standard deviation of the localized positions of the same fluorophore over consecutive frames. The average localization precision was around 18 nm for both fluorophores, close to typical values reported for conventional STORM[104] (**Figure 33**).

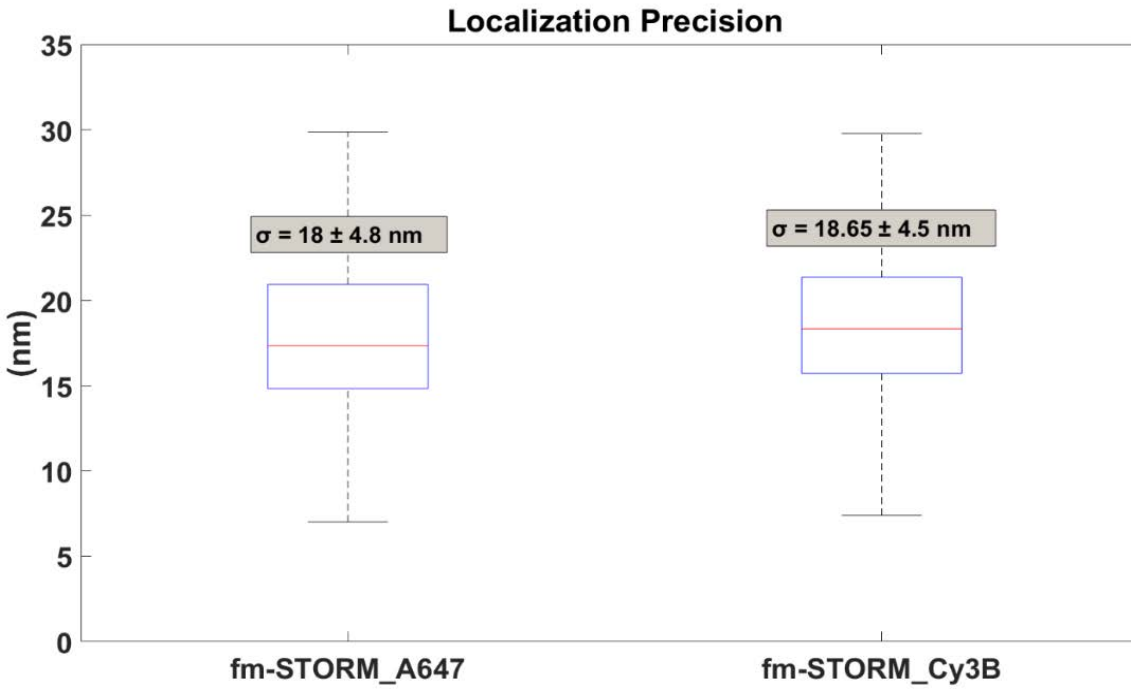

Figure 33: Localization precision in fm-STORM for A647 and Cy3B fluorophores. Box plot showing the experimental localization precisions obtained for 1-Color fm-STORM, for both channels, corresponding to A647 and Cy3B. The localization precisions have been calculated from the training data sets with camera frame rate F=90Hz, 647nm laser sinewave modulated at f_1=45Hz and the 561nm laser modulated at f_2=22.5Hz. The localization precisions have been determined by obtaining the standard deviation of the localizations over multiple consecutive frames of the same fluorophore. The box indicates the 25th (q_1) and 75th (q_3) percentiles. The whiskers extend to the most extreme data value that was not considered an outlier. Outliers are values bigger than $[q_3 + 1.5 \cdot (q_3 -$

q_1)] or smaller than [$q_1 - 1.5 \cdot (q_3 - q_1)$]. Around 99.3% (or ±2.7σ) of the data lies within these whiskers values.

The stochastic nature of photoswitching in organic fluorophores led to more ambiguity in assigning a unique color to each fluorophore in fm-STORM compared to fm-DNA-PAINT, giving rise to higher cross-talk between color channels. This ambiguity is due to the broad on-off blinking dynamics of the fluorophores, which is difficult to control and leads to fluorophores often being detected in less than 4 consecutive frames. Indeed, color cross-talk quantification showed that around 12% of A647 localizations and 10% of Cy3B localizations were miss-assigned to the wrong color channel (**Figure 34**).

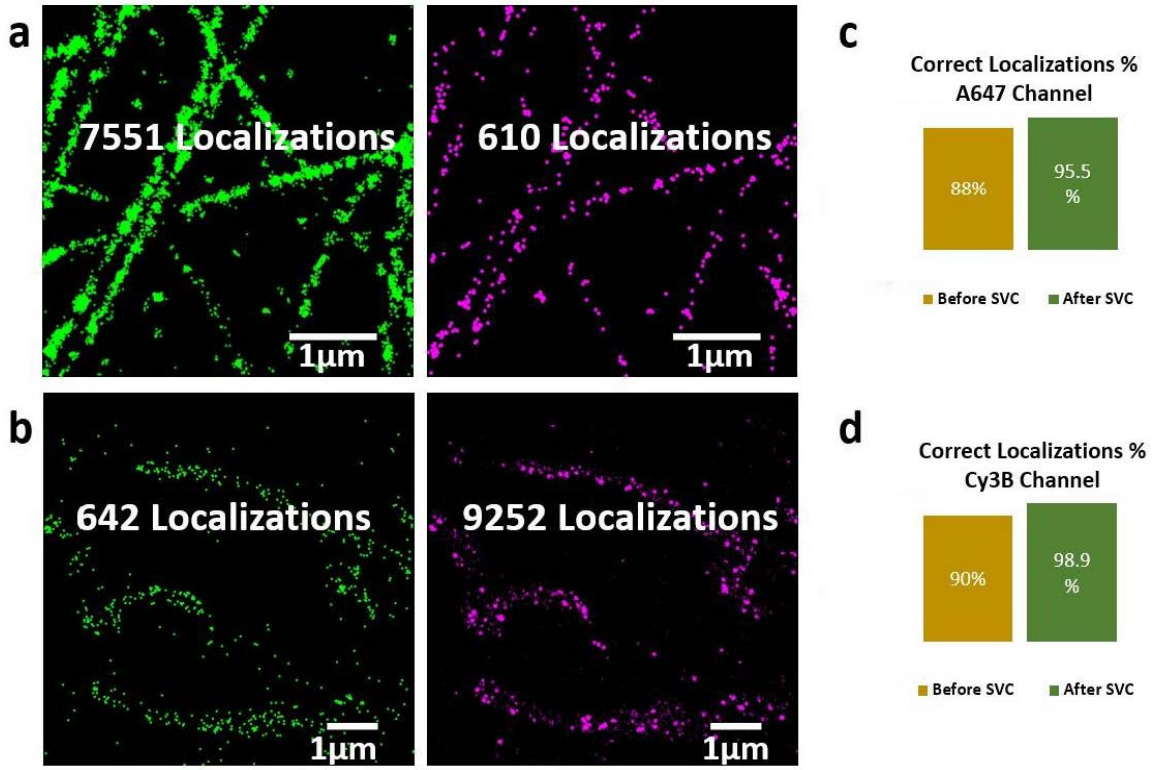

Figure 34: Color cross-talk quantification in fm-STORM. (**a, b**) Microtubules (green) and mitochondria (magenta) labeled with AlexaFluor647 (AF647) alone and Cy3B alone, respectively and imaged in two colors using fm-STORM. Images show the two channels before cross-talk correction. The green localizations correspond to the AF647 channel and the magenta localizations correspond to the Cy3B channel. Localizations in the displayed region of interest were quantified in the two channels. (**c, d**) Percentage of localizations belonging to the AF647 (**c**) or Cy3B (**d**) channels before color cross-talk correction (yellow bars) and after color cross-talk correction (green bars) using the machine learning algorithm.

In order to correct for the fm-STORM associated cross-talk between color channels, we developed a machine learning algorithm. The algorithm relies on the use of training data consisting of biological samples labeled with a single fluorophore and imaged with fm-STORM (**Figure 35**). The *x-y* positions of fluorophores in the training data were first determined and localizations were classified as single or multi-frame localizations depending on whether they appeared only in one frame or multiple subsequent frames (**Figure 35**). Around 50% of localizations were initially characterized as single frame localizations. The localized *x-y* position of each fluorophore was then used to define a subROI of 4 by 4 pixels and the FFT was performed for this subROI to determine the amplitudes belonging to each different frequency bin. This data was used to train the support vector classifier (SVC) to build decision boundaries separating the multiple color channels (**Figure 35, Detailed Methods DM1.1**, **Figure 36**). In practice, a percentage of single frame localizations (30-40%) was in fact multi-frame localizations that failed to be localized in one or more frames by the localization algorithm. Hence, these localizations could correctly be classified after the FFT as they appeared with higher intensity in one frequency bin (**Figure 36a**). The true single frame localizations (~30% of all localizations) were rejected, as they could not be accurately classified (SI Appendix, Methods). Once the decision boundaries were built we used them to classify the fluorophores in a multi-color experiment.

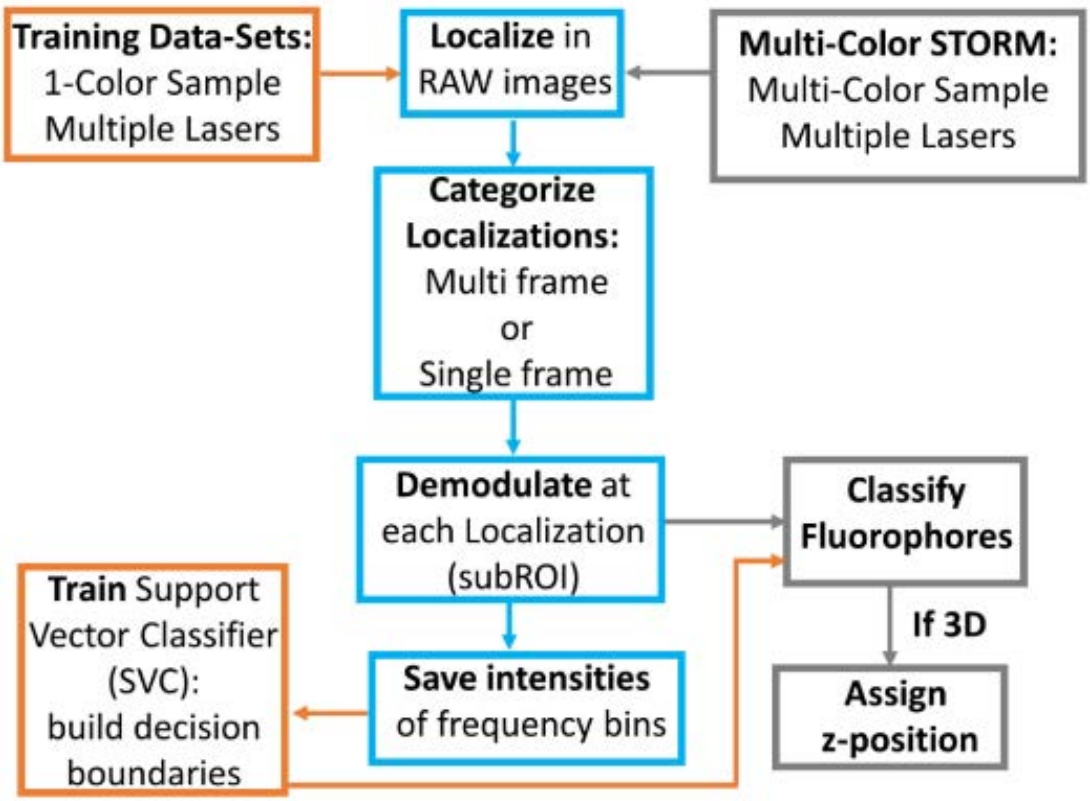

Figure 35: Workflow of the machine learning algorithm for fluorophore classification in fm-STORM. The algorithm requires training data sets for each fluorophore and imaging condition, in order to build the decision boundary regions for fluorophore classification. Localizations that appear in only a single frame and those that appear in multiple frames are categorized in order to be processed separately.

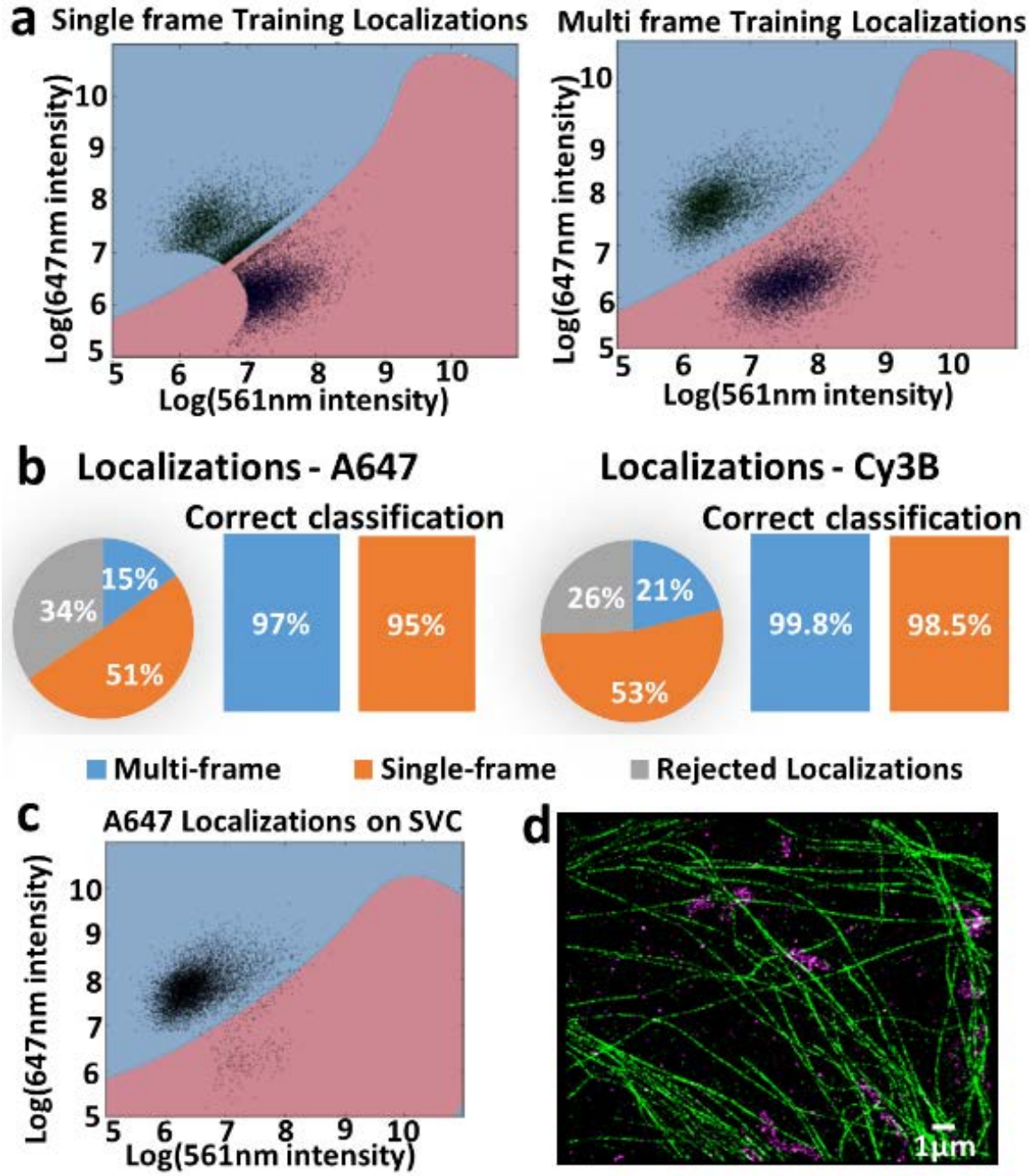

Figure 36: Machine learning algorithm effectively corrects for color cross-talk in fm-STORM.

(a) Training data set plots with decision boundaries, localized in one frame (left plot) and in multiple frames (right plot). **(b)** Pie chart shows percentage of single, multi-frame and rejected localizations for Alexa Fluor 647 and Cy3B. Bar plots show percentage of correctly assigned single and multi-frame localizations. **(c)** Alexa Fluor 647 localizations on SVC decision boundary plot. **(d)** Two-color image of microtubules (green) and mitochondria (magenta) labeled with Cy3B and Alexa Fluor 647, respectively.

To validate the algorithm for two-color fm-STORM, we labeled individual structures (mitochondria or microtubules) in single color with the photoswitchable fluorophores Cy3B and/or A647, and imaged them with fm-STORM with the two laser intensities modulated at different frequencies (647nm at 45Hz and 561nm at 22.5Hz). After classification using the decision boundary, 97% of localizations from multi-frames were correctly classified for the A647 channel and this number increased up to nearly 100% in the case of the Cy3B channel (**Figure 36b-d**). The decision boundaries could also be generated using training data from three different fluorophores (ATTO488, Cy3B and A647), demonstrating that this approach can be readily extended to more than two colors (**Figure 37**). Overall, the image acquisition times of fm-STORM are comparable to or even faster than sequential multicolor imaging with activator-reporter pairs (see Discussion) while the cross-talk correction can be performed with better accuracy using the machine learning algorithm. Typically, 10-30% of crosstalk is present in the standard activator-reporter approaches, depending on the fluorophores used and the labeling density[107,108] (**Figure 38**). In order to correct for this cross-talk, statistical methods have been developed[109], but their performance often depends on the amount of cross-talk and the spatial separation between the different structures in the image. For the structures imaged here, standard cross-talk correction could correctly classify up to only 88% of localizations (**Figure 38**).

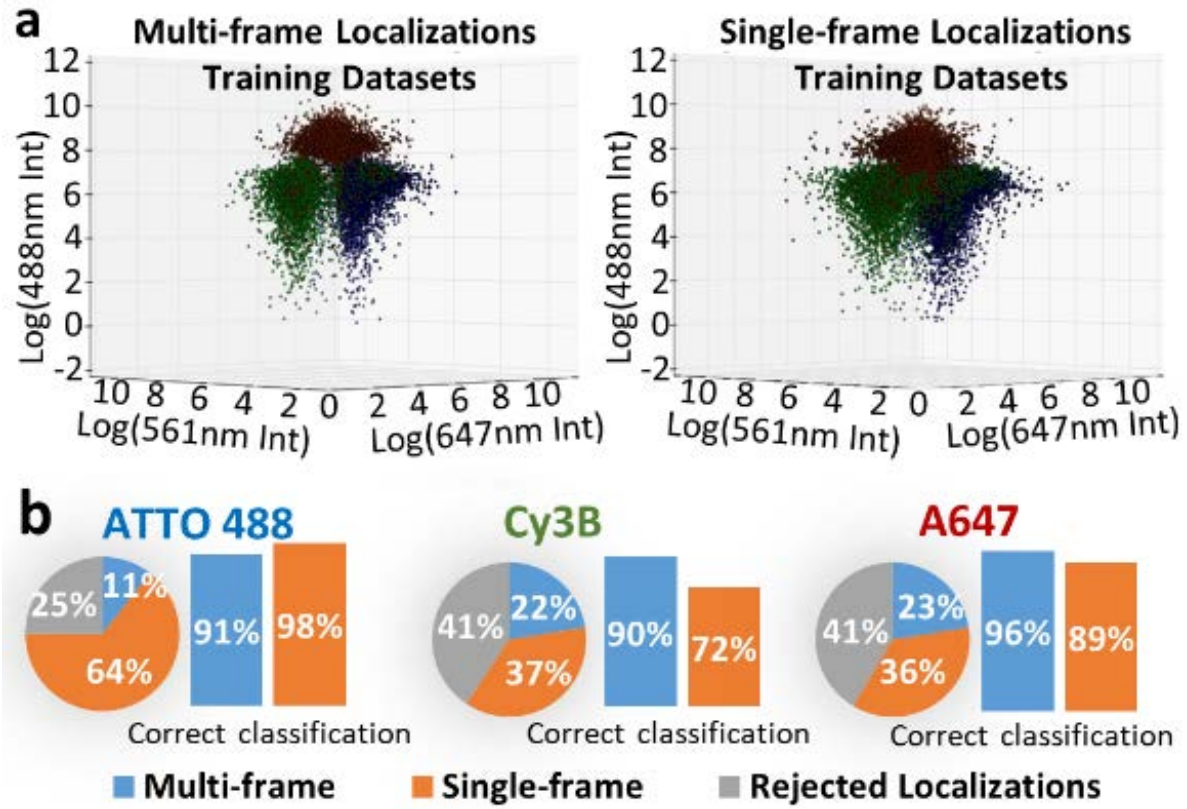

Figure 37: Training data for cross-talk correction of three color fm-STORM. (a) Multi- and single- frame localizations obtained from a training dataset using ATTO488, Cy3B and AF647 fluorophores, showing the color-separation in the three channels. **(b)** Percentage of single-frame, multi-frame and rejected localizations for the three fluorophores (pie charts) and the correctly classified single- and multi- frame localizations for three fluorophores (bar charts) calculated from a sub-set of localizations used for the training data

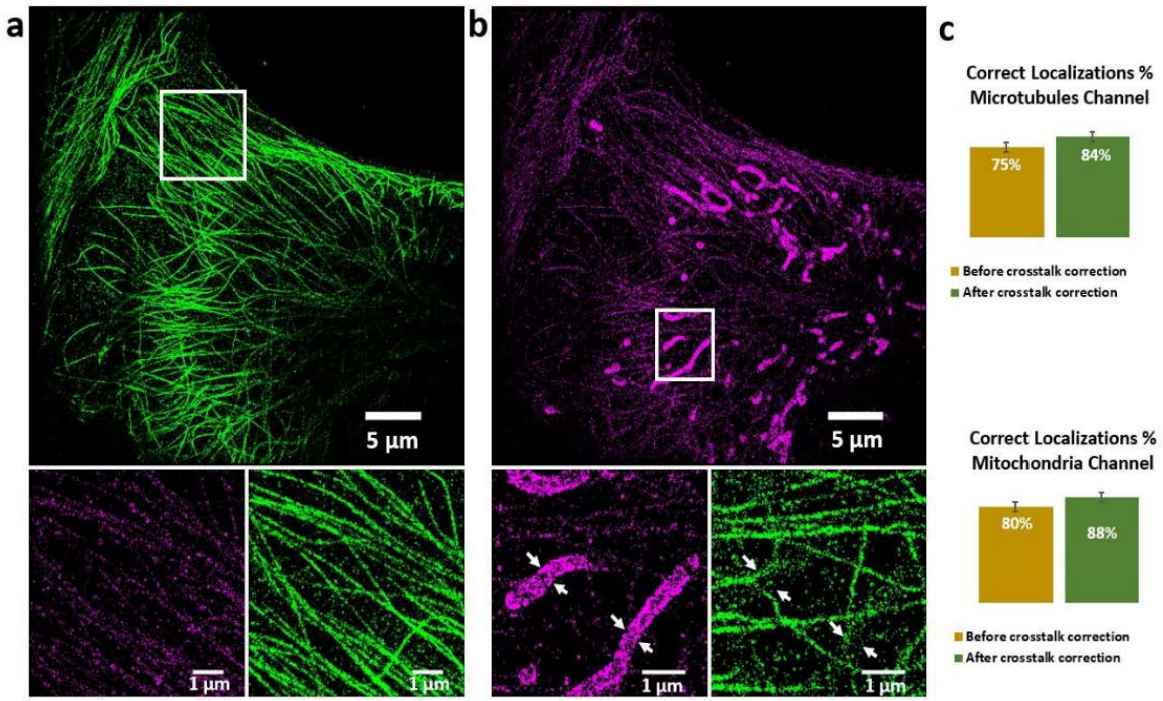

Figure 38: Two-color STORM image of microtubules and mitochondria imaged using the activator/reporter approach. Microtubules and mitochondria were labeled with AF405/AF647 and Cy3/AF647 activator-reporter pairs, respectively. Images are shown after standard cross-talk correction. **(a)** Microtubule channel (green) and a zoom-in of the white boxed region where there are microtubules only, displaying both channels (green and magenta). **(b)** Mitochondria channel (magenta) and zoom in of the white-boxed region where mitochondria can be identified (white arrows), displaying both channels (green and magenta). **(c)** Percentage of correct localizations assigned to each channel. Since the two structures are clearly defined and separated, the cross-talk calculation can be performed by counting the number of localizations from the two channels in regions where only one structure is present (i.e. mitochondria-only or microtubules-only regions). Yellow bars shows the values before cross-talk correction and green bars after cross-talk correction using statistical approaches.

2.4.3 fm-live

Finally, to demonstrate the versatility of the frequency multiplexed method, we performed three-color live-cell imaging. We prepared live BS-C-1 green monkey kidney epithelial cells that were stably expressing eGFP-α-tubulin (microtubules) and mCherry-LAMP1 (lysosomes), labeled mitochondria with MitoTracker Deep Red FM, and imaged them with three excitation wavelengths (488, 561, and 640 nm). With N=3 excitation lasers we selected a frame window size m=6 and demodulated the data on a pixel-by-pixel basis as for the fm-DNA-PAINT approach. The three resulting images from each demodulated image block have a temporal resolution of 1/6 the camera hardware frame rate, which is only a factor of two slower than the limit using sequential excitation. However, the advantages gained by this

frequency-domain approach are that motion discretization artefacts are limited because the data is acquired continuously—motion blurring is still present for rapidly-moving objects—and there is a factor of $\sqrt{2N}/2$ less noise than an equivalent time-interleaved excitation. Representative demodulated wide-field images of the microtubules, lysosomes, and mitochondria (**Figure 39a-c)**. The indicated sub-region is shown at various time points across a span of 70 seconds for all three channels, demonstrating full compatibility of this technique for imaging living cells with high temporal, spatial, and spectral resolution over long periods of time.

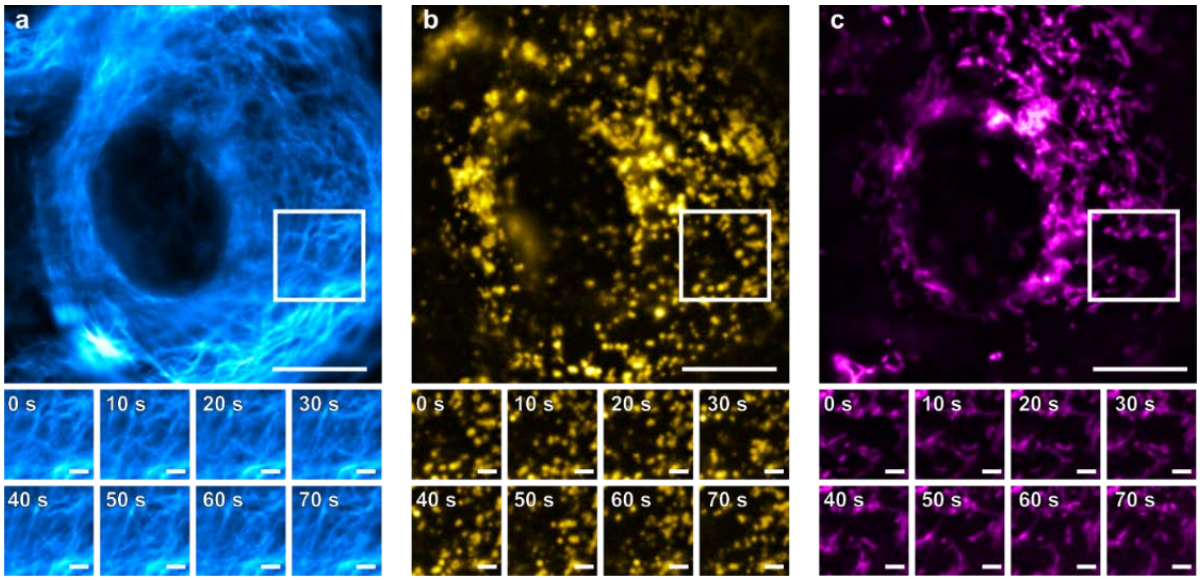

Figure 39. **fm-live images**. **Simultaneous three-color microscopy of live BS-C-1 cells**. **a)** Microtubules stained by the stable expression of eGFP-α-tubulin. **b)** Lysosomes via the stable expression of mCherry-LAMP2. **c)** Mitochondria labeled with Mitotracker Deep Red FM. Scale bars are 10 μm in the main images and 2 μm in the sub-images. Images shown are averages of 10 sequential demodulated frames acquired with an effective frame rate of 20 Hz.

2.5 Discussion

We have developed a new multi-color super-resolution method that relies entirely on the excitation rather than emission properties of fluorophores and implemented it in two modalities of single molecule based super-resolution microscopy: fm-DNA-PAINT and fm-STORM. DNA-PAINT offers multiple advantages in terms of increased localization precision, minimal photobleaching, image quantification and multi-color capabilities compared to other single molecule super-resolution approaches[74,75]. However, these advantages come at the expense of image acquisition time, making conventional DNA-PAINT extremely slow for multi-color super-resolution or for multiplexed, high-throughput applications[110]. The temporal bottleneck arises because of the need of detecting true binding events in a background of diffusing molecules. Faster camera speeds, or increased concentration of imager strands in the imaging buffer will lead to an effective increase in background and/or false localizations[100]. Recently, the background problem was addressed by combining fluorescence resonance energy transfer (FRET) with DNA-PAINT[100]. This approach significantly increases the image acquisition speed, but it also makes DNA-PAINT prone to photobleaching and dependent on the photophysics of donor-acceptor dyes. Our approach of fm-DNA-PAINT preserves all the advantages of conventional DNA-PAINT, and importantly, it can acquire multiple colors in the same amount of time needed to acquire a single color conventional DNA-PAINT image.

Importantly, fm-DNA-PAINT does not require color cross-talk correction or the rejection of localizations due to color mis-assignment since the long binding times (hundreds of milliseconds) of the imager oligos makes color discrimination much less ambiguous. In our current implementation, the number of colors was only limited by the commercially available oligo-coupled antibodies and as such, there is no fundamental limit to extend this approach to more colors with the only requirement that the fluorophores are preferentially excited at one unique excitation wavelength. Indeed, our simulations show that even in the case of substantial spatial overlap among fluorophores for a five-color acquisition, the demodulation step properly assigns each fluorophore to the correct color channel, with minimal distortion to the PSF from the spatial overlap and minimal error in localization.

There are some practical limits that determine the acquisition speed and the number of color channels such as the separation between the center of the frequency bins used for modulation, the overlap between the excitation spectrum of fluorophores, camera frame rate and the signal to noise ratio. The number of frequency bins (n) (and hence the number of color channels) depends on the number of frames used for demodulation (m). For example, a modest estimate of 2 frequency bins (and hence 2 colors) can be fit inside a demodulation frame window of m=4 frames, which will maintain a good separation between the frequency bins (**Figure 25**). The effective frame rate depends on the camera frame rate (F) and the demodulation frame window (m). For a frame rate of 60 Hz (used here), it is hence possible in practice to image

3 colors with an effective frame rate of 10 Hz. This frame rate is equivalent to the frame rate typically needed for acquiring 1 color using conventional DNA-Paint, decreasing the acquisition time and improving the imaging throughput by 3-fold. The effective frame rate can further be improved by increasing the camera frame rate.

Our calculations for spatial overlap errors were based on experimental data of Cy3- and Cy5-equivalent fluorophores, which have some spectral overlap (**Figure 40**). Fluorophores with greater overlap in their excitation spectra can be used in fm-DNA-PAINT, but as the spectral overlap increases their discrimination in the frequency domain becomes more challenging, especially when spatial overlap is also present, in which case PSF distortions may become significant. Spectral overlap will ultimately lead to an increase in color cross-talk, necessitating correction algorithms like the machine learning algorithm developed here or advanced unmixing algorithms[111]. The need to correct for color cross-talk also has an impact on the total imaging time, since cross-talk algorithms typically discard a portion of localizations and more localizations must be accumulated to get to the same final Nyquist resolution. That being said, since DNA-PAINT uses conventional fluorophores, it is possible to choose up to five different fluorophores with spectral separations comparable to those between Cy3 and Cy5 (**Figure 40)**. As a result, we expect that fm-DNA-PAINT can easily multiplex five different colors in one shot, dramatically enhancing the throughput of this method. This enhanced throughput should not only improve multi-color super-resolution imaging but also other single molecule based techniques that depend on multiplexing, including bar-coding approaches such as MERFISH[112] or Oligo-PAINT[113].

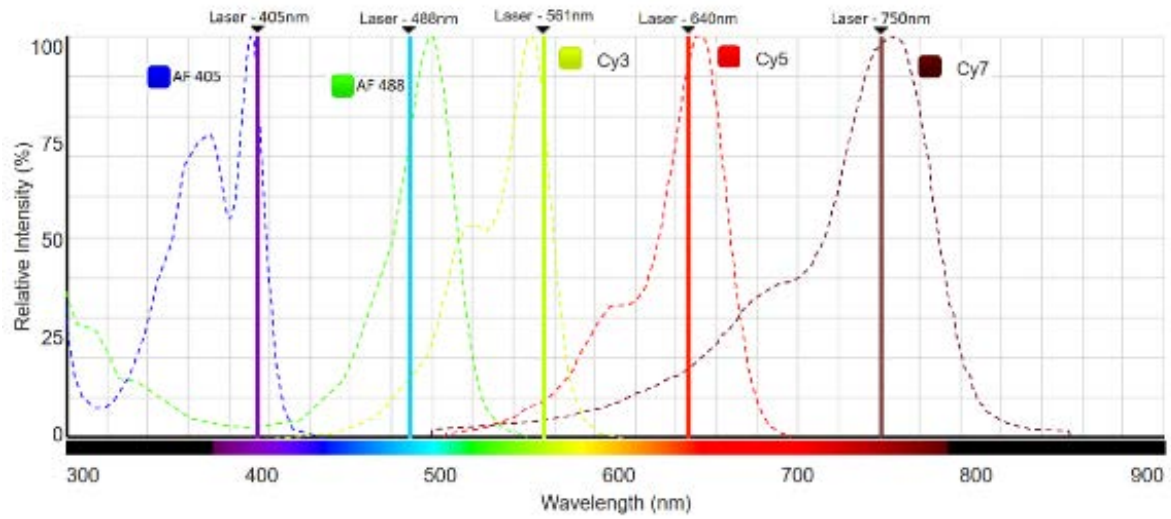

Figure 40. Absorption spectra of 5 different standard fluorophores for implementation in fm-DNA-PAINT. Example of 5 different fluorophores with relatively little spectral overlap in their absorption spectra. The suitable lasers for differential excitation of each of the fluorophores is included in the figure. Notice that there is negligible overlap between AF405, AF488, Cy3 and Cy5,

and thus, in principle fm-DNA-PAINT of four colors with minimal color crosstalk and in the presence of spatially overlapping fluorophores should be easily obtainable. A somewhat larger spectral overlap exists between Cy5 and Cy7, so that excitation of Cy5 by the 640nm laser line would also marginally excite Cy7, leading to an additional amplitude of Cy7 in the frequency bin of the Cy5 channel. (Adapted from The Spectra Viewer, www.thermofisher.com)

We also showed that our frequency multiplexing scheme can be implemented for multi-color STORM. fm-STORM was prone to color cross-talk due to the stochasticity of fluorophore photoswitching. The machine learning algorithm we developed could correct for color cross-talk with high accuracy (>95% correctly classified fluorophores). This algorithm should be applicable to correct for color cross- talk that arises in emission based super-resolution microscopy when fluorophores with overlapping emission spectra are used[114,115], as long as the training dataset is generated using the specific experimental configuration, making it a versatile approach for correcting color cross-talk in super- resolution imaging.

The speed of fm-STORM is an improvement over the sequential, activator-reporter scheme of multi-color STORM imaging[94,107]. The latter also uses a frame window of 4-6 frames to ensure that fluorophores belonging to one activator-reporter pair fully switch off before the fluorophores belonging to the next activator-reporter pair are switched on. This approach is needed to reduce color cross-talk. However, in the activator-reporter multi-color STORM case the colors are acquired sequentially (4-6 frame window per color channel), whereas in fm-STORM multiple colors can be acquired simultaneously within the same frame window. Both methods lead to similar levels of color cross-talk and require correction algorithms that discard a similar percentage of localizations. Although from the technical point of view frequency multiplexing can be readily implemented in both DNA-PAINT and STORM, controlling the photophysical properties of multiple fluorophores under a single buffer solution remains a challenge. The working principle of DNA-PAINT makes this technique much more amenable to frequency multiplexing and thus we expect fm-DNA-PAINT to become highly useful to the community.

Chapter 3: Mesoscale modelling of chromatin

The content of this chapter is part of a manuscript under preparation (see **List of publications**).

3.1 Abstract

Recent experimental data suggest that chromatin structure is complex and highly heterogeneous within the nucleus of individual cells. Advanced microscopy methods, like localization-based microscopy have been proved powerful and quantitative tools to understand a wide variety of features of chromatin structure. STORM was used to observe that nucleosomes form heterogeneous groups in vivo, named clutches. Clutches are smaller and less dense in mouse embryonic stem cells (mESCs) compared to neuronal progenitor cells (mNPCs). Here, using coarse-grained modeling of a 30kb region around the pluripotency gene Oct4, we show that the previously observed clutch differences between mESCs and mNPCs genome wide can be reproduced at a single gene locus. The reorganization of clutches in differentiation is associated with substantial changes in the compaction and inter-nucleosome contact probability of the Oct4 fiber that correlate with Oct4's activity in mESCs and mNPCs. In addition, the coarse-grained models of chromatin fibers corresponding to specific genomic loci including Oct4 are fully compatible with the nucleosome clutches observed in super-resolution images

3.2 Introduction

Genome organization plays an important role in regulating gene expression. Several recent works, including super-resolution imaging of nucleosomes and electron tomography imaging of DNA, highlighted that chromatin is disordered and heterogeneous groups of nucleosomes with a varying range of nucleosome densities are present in folded chromatin[25,116]. In super-resolution images, nucleosome groups (named clutches) were further clustered into larger domains (clutch domains) in the size range of hundreds of nanometers in length scale[36,116]. These results shed new light onto the organization of chromatin fiber at the 10-100 nm length scales. Assembly of nucleosomes into clutches, the compaction level of nucleosomes within clutches, as well as the assembly of clutches into clutch domains can limit accessibility of DNA to regulatory proteins and polymerases. Hence, these structural features must be dynamically regulated as genes turn on and off in specific cell types.

Here, to address these questions and analyze the organizational patterns of nucleosomes within clutches in mouse ESCs and NPCs, we used coarse-grained mesoscale models of Kb-range nucleosome fibers. Mesoscale models of chromatin fibers of the pluripotency gene Oct4 revealed the presence of nucleosome clusters compatible with the nucleosome clutches previously observed genome wide in super-resolution images. The previously observed global changes in clutch size and compaction upon differentiation were reproduced in the models at the level of a single pluripotency gene locus[36,116]. These modeling results further suggest that the Oct4 fiber undergoes overall compaction in NPCs, especially in regions surrounding the Oct4 gene and its super enhancer. Hierarchical looping, corresponding to stacks in space of hairpin loop structures[117], is further enhanced in NPC Oct4 fibers, explaining the formation of larger clutches. The nucleosomes within clutches maintain a configuration most compatible with zigzag geometry in both ESCs and NPCs irrespective of clutch size.

3.3 Methodology

For studying the chromatin structure and relate it with chromatin dynamics and with the previous clutches quantifications obtained from STORM images[11,36], we make use of a coarse-grained computational model. Our mesoscale chromatin model combines nucleosomes, histone core tails, linker DNA, and linker histone by coarse-grained units at different levels of resolution to create oligonucleosome fibers[118,119] (**Figure 41**). The nucleosome core with wrapped DNA and without tails is treated as an electrostatic charged object; flexible histone core tails are coarse grained to mimic their atomistic behavior; linker DNA connecting nucleosomes is modeled by the Stigler worm-like chain model; and linker histones are coarse grained with charged beads for the C-terminal and globular domains (**Detailed Methods DM1.2**). The fiber energy consists of bending, twisting, electrostatic, and excluded volume terms. Fiber configurations are sampled by Monte Carlo (MC) simulations that survey and approach equilibrium conformations[4,118,119] (**Detailed Methods DM1.2** and **Figure 41**).

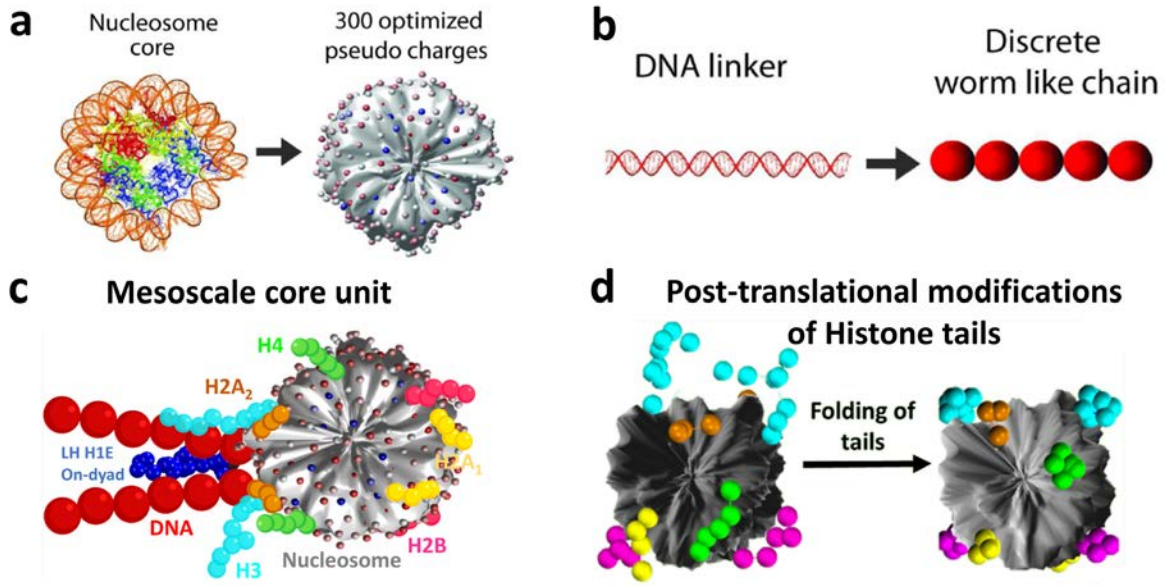

Figure 41. Mesoscale coarse-grained chromatin computational model. a) Modeling of the nucleosome core as a rigid body with 300 pseudo charges. **b)** The linker DNA connecting two nucleosomes is modelled as a discrete chain of beads with electrostatic and mechanic properties. **c)** Basic building block for the chromatin mesoscale model. **d)** Modeling of post-translational modifications like histone tail acetylation**.** Adapted from [119,120].

Our nucleosome-resolution chromatin mesoscale model has been already applied to the study of many biological problems including gene folding[121], combines nucleosomes, histone core tails, linker DNA, and linker histones by coarse-grained units at different levels of resolution

to create oligo-nucleosome fibers[118,119] (**Figure 41**). Fiber configurations are sampled by Monte Carlo (MC) simulations that survey and approach equilibrium conformations[4,118,119] (**Detailed Methods DM1.2**).

For more detailed explanation about the coarse-grained chromatin model, see **Detailed Methods,** section **DM1.2**.

3.4 Results

3.4.1 Mesoscale modeling of Oct4 reveals a chromatin conformation composed of nucleosome clusters whose organization and compaction change upon differentiation

Recently, using super-resolution microscopy we showed that nucleosome clutches contain a median number of around 6 nucleosomes in somatic cells[116] corresponding to a genomic length scale of a few kilobases. We further showed that the size of the nucleosome clutches inversely correlates with the pluripotency level of mouse embryonic stem cells (mESCs), as well as human induced pluripotent stem cells (hiPSCs)[116]. In particular, upon in vitro differentiation of mESCs into mNPCs, clutch size increases[116]. In addition, mutant mESCs lacking three isoforms of the linker histone H1 (H1tKO)[122] have smaller nucleosome clutches compared to wild type mESCs[116]. These results suggest that nucleosome clutches correlate well with the open or closed state of the chromatin fiber and they are remodeled in cellular reprograming and differentiation.

To gain further insights into the chromatin remodeling of mESCs during differentiation[36,116], we simulated chromatin fibers typical of mESC and mNPC (**Figure 42** and **Figure 43**). To define chromatin fibers relevant to stem cell pluripotency and differentiation, we selected a specific genomic region of ~30 Kbp that includes an important pluripotency gene, Oct4, active in mESCs but silenced in mNPCs[123]. We sought to capture this gene expression activity by differences in clutch patterns and overall compaction. We expected mESC fibers to form smaller clutches compared to mNPC fibers based on previous super-resolution data. We used publicly available MNase-Seq data of mESCs and mNPCs[124] to position the nucleosomes (**Figure 43b**), define the H1 to nucleosome ratio[125], and specify the amount of histone tail acetylation in the two cell types[12] (**Detailed Methods DM1.2** and **Figure 43b, c**). We expect these parameters to be important for organizing gene structure[4,121,126], clutch organization, and DNA compaction[36,116] based on previous modeling and experimental results from super-resolution. Specially, the nucleosome positions obtained from the MNase-Seq data[124] determine the DNA linker lengths and the nucleosome free regions (NFR) (**Figure 43b**), key factors affecting chromatin. To incorporate realistic linker histone H1 densities, we used linker histone to nucleosome ratios of 0.5 and 0.8 for mESC and mNPC, respectively, as reported previously[125]. Histone tail acetylation patterns were asigned as determined previously[12,127] with overall levels of 15% and 10% for mESC and mNPC, respectively, based on immunofluorescence measurements (**Detailed Methods DM1.2** and **Figure 43c**).

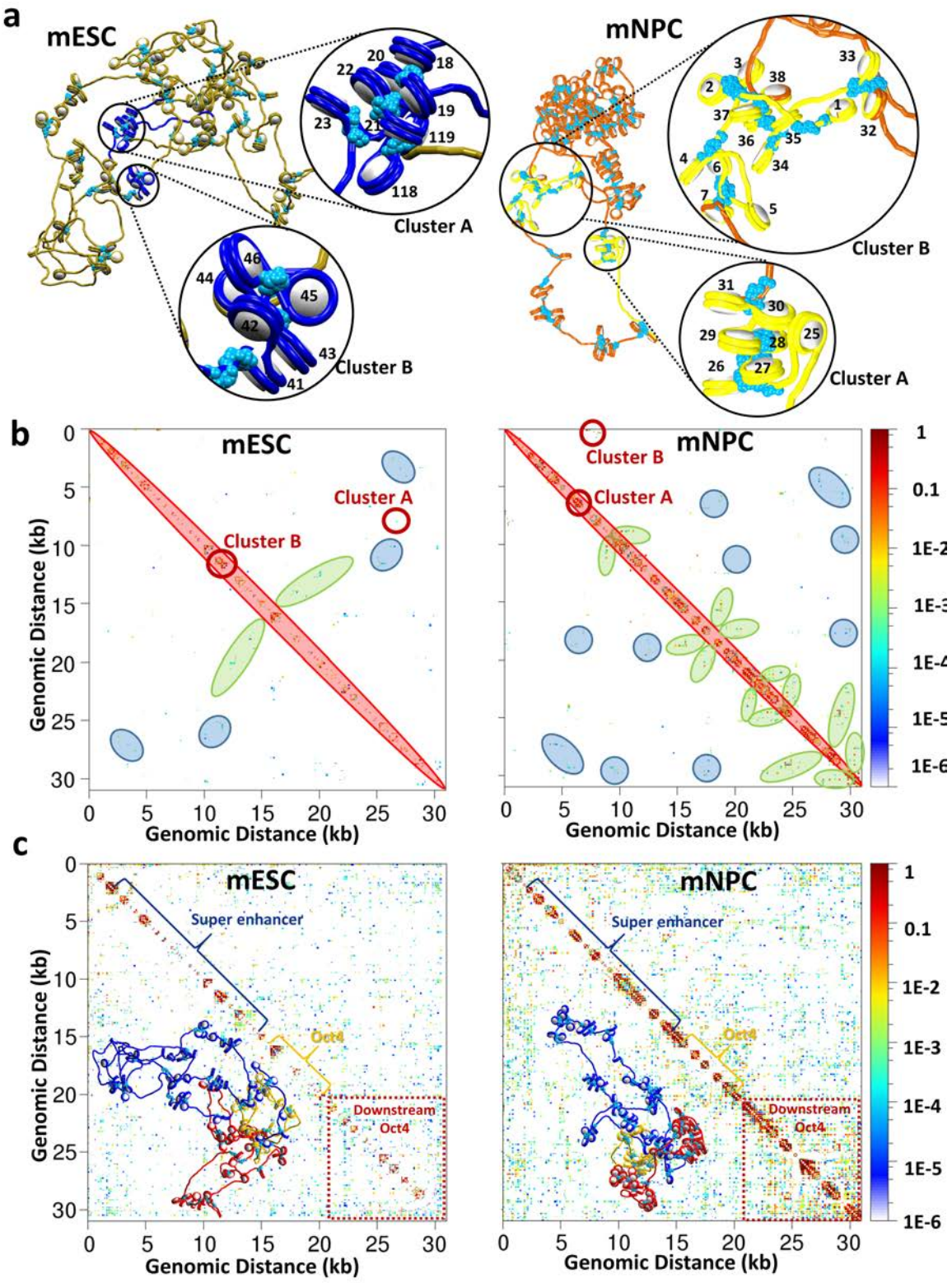
a
mESC
mNPC
Cluster A
Cluster B
Cluster B
Cluster A
b
mESC
mNPC
Cluster A
Cluster B
Cluster B
Cluster A
Genomic Distance (kb)
Genomic Distance (kb)
Genomic Distance (kb)
Genomic Distance (kb)
1
0.1
1E-2
1E-3
1E-4
1E-5
1E-6
c
mESC
mNPC
Super enhancer
Super enhancer
Oct4
Oct4
Downstream Oct4
Downstream Oct4
Genomic Distance (kb)
Genomic Distance (kb)
Genomic Distance (kb)
Genomic Distance (kb)
1
0.1
1E-2
1E-3
1E-4
1E-5
1E-6

Figure 42. Nucleosome architecture of the Oct4 pluripotency region revealed by computational modeling. a) Representative equilibrated structures of chromatin fibers corresponding to the Oct4 pluripotency region in mESCs (left) and mNPCs (right) obtained from mesoscale modeling are shown. Zooms show the nucleosome clusters obtained from DBSCAN analysis of the 3D chromatin fibers. The numbers correspond to the identity of the nucleosomes based on their linear sequence along the Oct4 region. **b)** Inter-nucleosome contact probability maps for the fibers shown in panel (a). Hierarchical folding (indicated in blue) and hairpin folding (indicated in green) revealed in the inter-nucleosome contact matrices for representative mESC and mNPC chromatin fibers. These structural features were previously defined[117] and are determined based on the shape of the nucleosome contact density in the map (Methods). In addition to these previously defined features, density corresponding to nucleosome clusters are also detected in the maps (red circles). Matrices are normalized by the maximal number of contacts seen throughout the trajectory. The matrix densities are 0.007 and 0.024 for mESC and mNPC, respectively. **c)** Inter-nucleosome contact probability matrices for the 30 trajectory ensemble per condition. Contact probability matrices were obtained by normalizing contact maps by the maximum number of contacts across each trajectory, for each system, and summing all contacts. One representative fiber for each system is shown with yellow nucleosome perimeters for the Oct4 region, blue for the super enhancer region, and red for the downstream Oct4 region. The dashed red box in the mNPC matrix corresponds to the region downstream of Oct4. The matrix densities are 0.0546 and 0.1322 for the ensemble of mESCs and mNPCs, respectively.

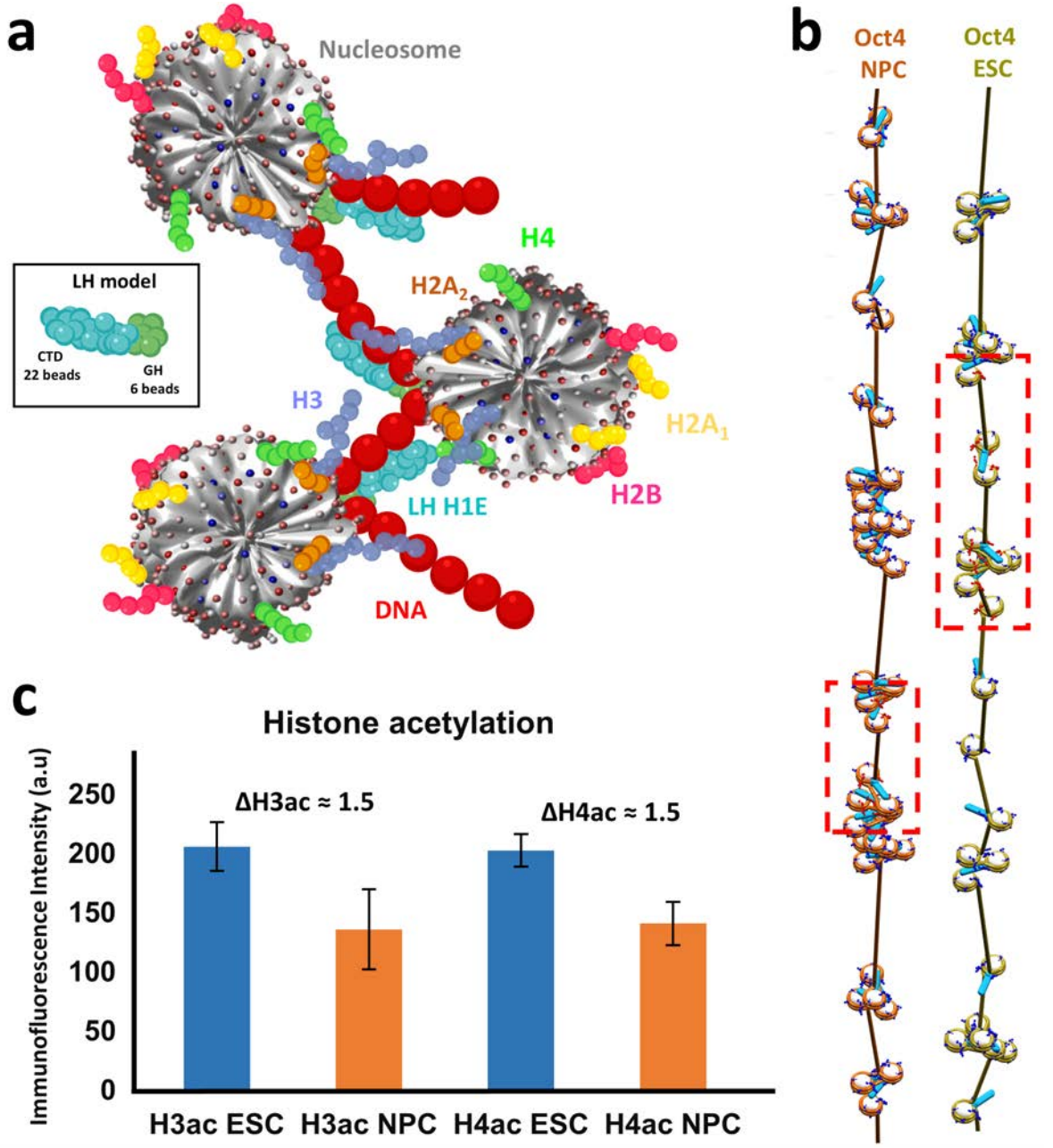

Figure 43. Computational modeling of chromatin fibers typical of mESC and mNPC. a) Scheme of our chromatin mesoscale model for a three-nucleosome system. Each nucleosome core particle is modeled by 300 pseudo charges, and coarse grained beads are used for N-terminal tails of the core histones H4, H3, H2A, and H2B (5 amino acids per bead), C-terminal tail of the core histone H2A (5 amino acids per bead), linker histones (6 beads for the globular head and 22 beads for the C-terminal domain), and linker DNA (~9 bp resolution), treated with a worm-like chain model**. b)** Initial configurations of the chromatin fibers (with linker histone, H1 shown in cyan, native histone tails in blue, and acetylated histone tails in red), displaying 30kbp around the Oct4 gene in mESC and mNPC.

Nucleosome positions were obtained from MNase-Seq data analysis[124] (Methods). We used a linker histone (H1) per nucleosome ratio of 0.5 for mESC and 0.8 for mNPC as reported previously[122,128] and acetylation levels of 10% for mNPC and 15% for mESC located in two islands (indicated with red dashed rectangles) based on immunofluorescence results (panel c) and experimental evidence of histone acetylation spatial distribution[127]. **c)** Quantification plots of H3 and H4 acetylation in mESC and mNPC obtained by immunofluorescence[12]. Bars represent the mean fluorescence intensity values with standard deviations. 206 ± 20.5 a.u for H3ac in mESCs, N = 29. 136.1 ± 33.8 a.u for H3ac in mNPCs, N = 25. 202.8 ± 13.7 a.u for H4ac in mESCs, N = 33. 141.1 ± 18.3 a.u for H3ac in mNPCs, N = 28.

Both the mESC and mNPC systems were simulated by 30 independent trajectories of 80 million MC steps each. Visual inspection of the resulting chromatin fibers revealed a significant difference in global fiber shape for the different cell types: mNPC fibers were more compact than mESC fibers (**Figure 42a**). Quantitative analysis (**Detailed Methods DM1.2**) confirmed higher sedimentation coefficients (**Figure 44a**), smaller radii of gyration (**Figure 44b**) and volume (**Figure 44c**) for the mNPC compared to the mESC. These quantitative results are consistent with the visually more compact mNPC fibers. Visual inspection of the fibers further revealed nucleosomes grouped together into heterogeneous clusters resembling nucleosome clutches previously described in super-resolution images. To confirm the visual inspection quantitatively and gain a detailed understanding of nucleosome patterns inside the clusters, we further analyzed the 3D fibers using density based spatial clustering of applications with noise (DBSCAN)[129]. This analysis revealed nucleosome clusters consisting on average of 6 and 18 nucleosomes per cluster in mESCs and mNPCs, respectively (**Figure 44d**). The nucleosome packing ratio within the clusters was also significantly higher in mNPCs compared to mESCs (**Figure 44e**). Finally, mNPC fibers contained fewer nucleosome clusters compared to mESC fibers (**Figure 44f**), consistent with the nucleosome clusters becoming larger in mNPCs.

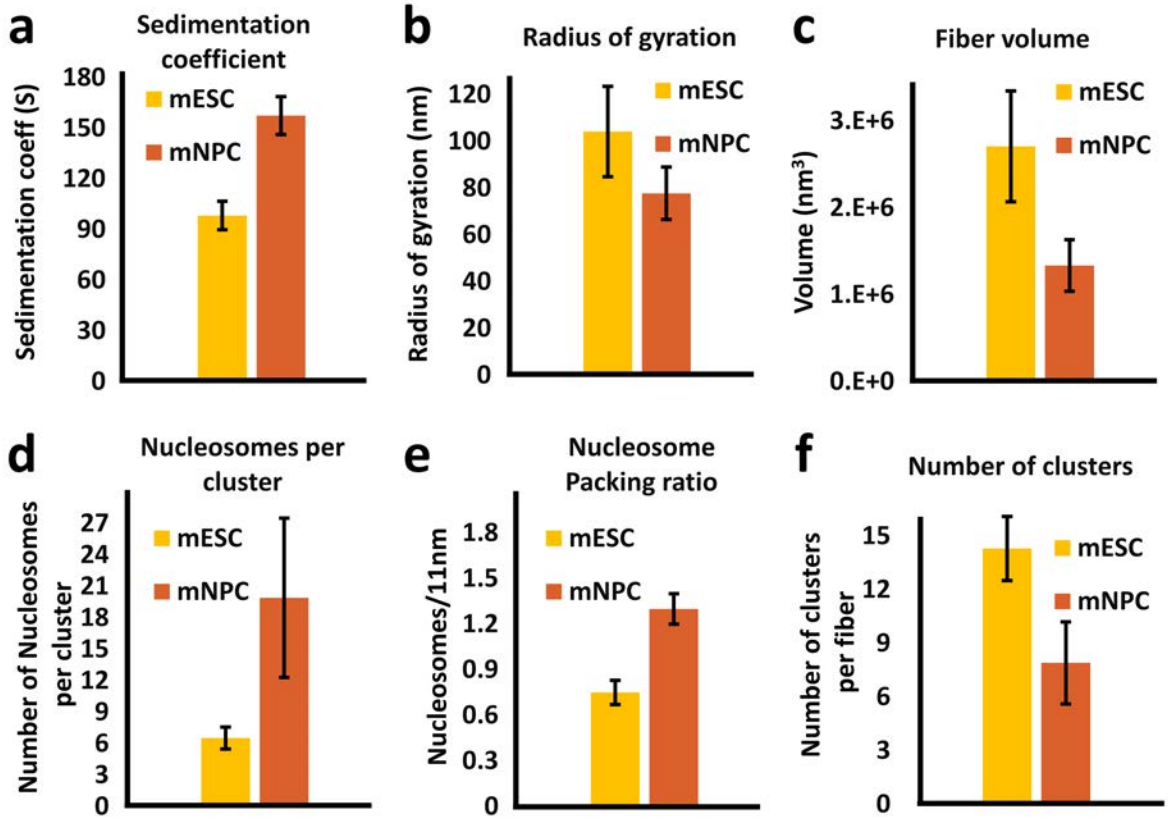

Figure 44. **Chromatin fibers undergo compaction upon the process of cell differentiation.** The bar plots display the results obtained from the analysis of the ensemble of 3000 configurations obtained from the mesoscale models of chromatin fibers corresponding to 30kbp around the Oct4 gene for mESC and mNPC. For all the plots, mean and standard deviation are plotted. **a)** Sedimentation coefficient of fibers. **b)** Radius of gyration of the fibers. **c)** 3D volume of the fibers. **d)** Average number of nucleosomes per cluster (see methods for details about the calculation). **e)** Packing ratio is the number of nucleosome per unit length of 11nm. **f)** Number of clusters per fiber.

Inter-nucleosome contact probability matrices for the two selected fibers shown in Figure 1a further revealed increased nucleosome contact in mNPCs compared to mESCs (average matrix density of 0.007 and 0.024 for mESC and mNPC, respectively) (**Figure 42b**), consistent with the increased fiber compaction and larger nucleosome clusters of mNPCs. Interestingly, distant nucleosomes appear to interact within the larger clusters (see cluster A of mESCs and cluster B of mNPCs in **Figure 42a**). Features corresponding to nucleosome clusters, hairpin looping and hierarchical looping corresponding to stacks of hairpin loops[117] (**Detailed Methods DM1.2**) were also evident in the nucleosome contact matrices (**Figure 42b**). Hierarchical looping and hairpin features were enhanced in mNPCs compared to mESCs. These hierarchical loops and hairpin structures likely explain the formation of larger clutches through the contact of distant nucleosomes upon differentiation. By further generating inter-nucleosome contact probability matrices for all the 30 fibers per condition

(**Figure 42c**), we further confirmed the presence of enhanced nucleosome contact frequency in mNPC fibers (average matrix density of 0.0546 and 0.1322 for the ensemble of mESCs and mNPCs, respectively). Interestingly, the highest enhancement in contact probability was observed in the region downstream of the Oct4 gene/super-enhancer region (dashed red box in **Figure 42c**), corresponding to a higher-level of compaction for this downstream region. Finally, the distance between nucleosomes dimers as well as the triplet and dihedral angle of bonded (i.e. consecutive) nucleosomes (**Figure 45a-c**) were most consistent with a zigzag geometry in both cell types. This feature underscores the prevalence of the zigzag secondary structure topology[117].

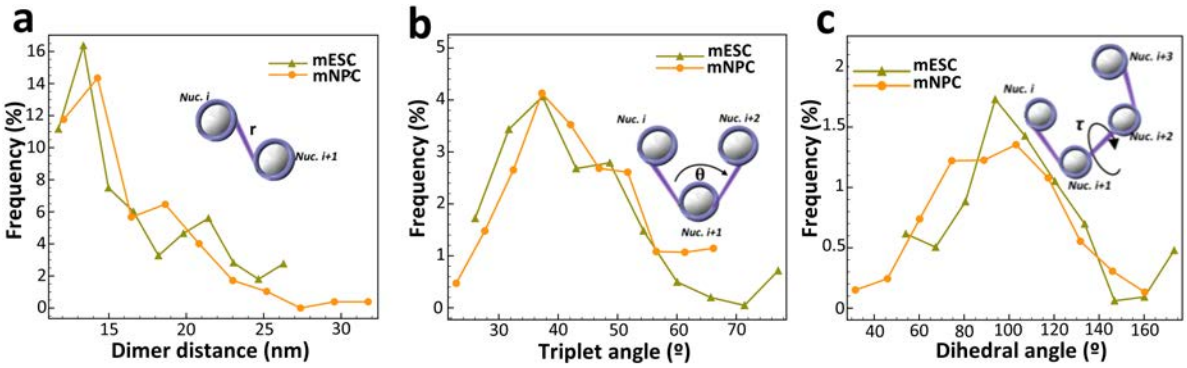

Figure 45. **Nucleosome cluster geometry analysis for mESC and mNPC.** Probability distributions in mESC (green) and mNPC (orange) of nucleosome dimer distance **(a)**, triplet angle **(b)**, and dihedral angle **(c)** measured for consecutive (bonded) nucleosomes belonging to the same nucleosome cluster over all nucleosome clusters of a single trajectory.

3.4.2 Nucleosome clusters in the Oct4 modeled fibers are compatible with nucleosome clutches observed genome-wide with super-resolution imaging

The DBSCAN analysis of the modeled 3D fibers is consistent with previous super-resolution data that revealed that nucleosomes form heterogeneous clutches in vivo. However, given that the super-resolution images have lower resolution and are genome-wide with no sequence specificity compared to the modeled fibers, to directly relate the model fiber configurations to previous experimental super-resolution data, we simulated super-resolution images from the modeled fibers using the simulation package SuReSim[130] (**Detailed Methods DM1.2** and **Figure 46a**). Since the chromatin fiber generated by the model is 3D but our super-resolution images are 2D, we performed 1000 2D random projections on each resulting super-resolution localization list (**Detailed Methods DM1.2** and **Figure 46a**). We applied a distance based clustering algorithm[116] to group the fluorophore positions in the simulated super-resolution images and segment nucleosome clutches as previously described (**Detailed Methods DM1.2** and **Figure 46a**). This analysis confirmed the presence of nucleosome clutches in the 2D projections of the simulated super-resolution images from the

3D model (**Figure 46a** and **Figure 47a-b**). We compared the identity of the nucleosomes in the segmented clutches to that of 3D clusters determined by DBSCAN analysis for Clusters A and B in the example simulated fiber shown in Figure 1a. As expected, depending on the 2D projection, the clutches contained all or only a subset of the nucleosomes in the 3D clusters (**Figure 47a-c**). Similarly, in some 2D projections, nucleosomes found within different 3D clusters could merge into the same clutch (**Figure 47c**).

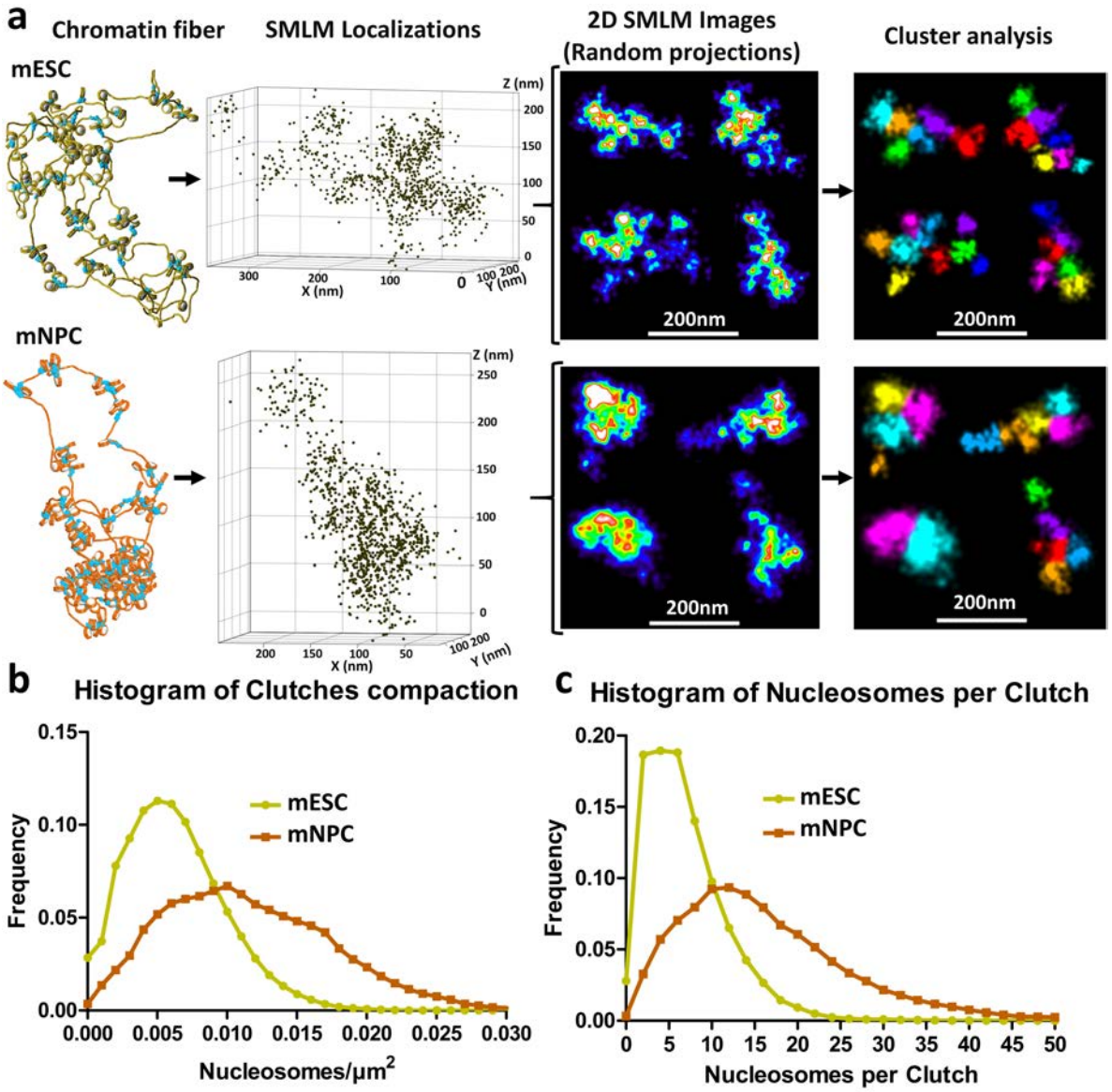

Figure 46. Mesoscale modeling of chromatin fibers recapitulates super-resolution images of nucleosomes. a) Workflow showing the procedure for generating super-resolution images from a given computational chromatin fiber. First, the nucleosome positions within the 3D fibers (chromatin fiber) are converted into localized x, y, z positions of nucleosomes (referred to as SMLM localizations, SMLM: Single Molecule Localization Microscopy) with SuReSim. Then the localizations are rotated

1000 times in 3D by randomly picking an angle and axis of rotation to obtain random 2D projections. Finally, the 3D coordinates of the localizations are projected in a 2D slice with a maximum depth of 400 nm. The 2D localizations are then rendered as a super-resolution image (SMLM image) by representing each localization as a Gaussian with a fixed width of 9 nm. The color coding corresponds to the density of localizations. Finally, cluster analysis is performed to segment the localizations based on their spatial proximity. Each cluster is pseudo color-coded with a different color. **b-c)** Histogram of nucleosome packing density (i.e. number of nucleosomes per clutch area) **(b)** and histogram of the number of nucleosomes per clutch **(c)** computed from the cluster analysis of the simulated super-resolution images of Oct 4 in mESCs (yellow) and mNPCs (orange).

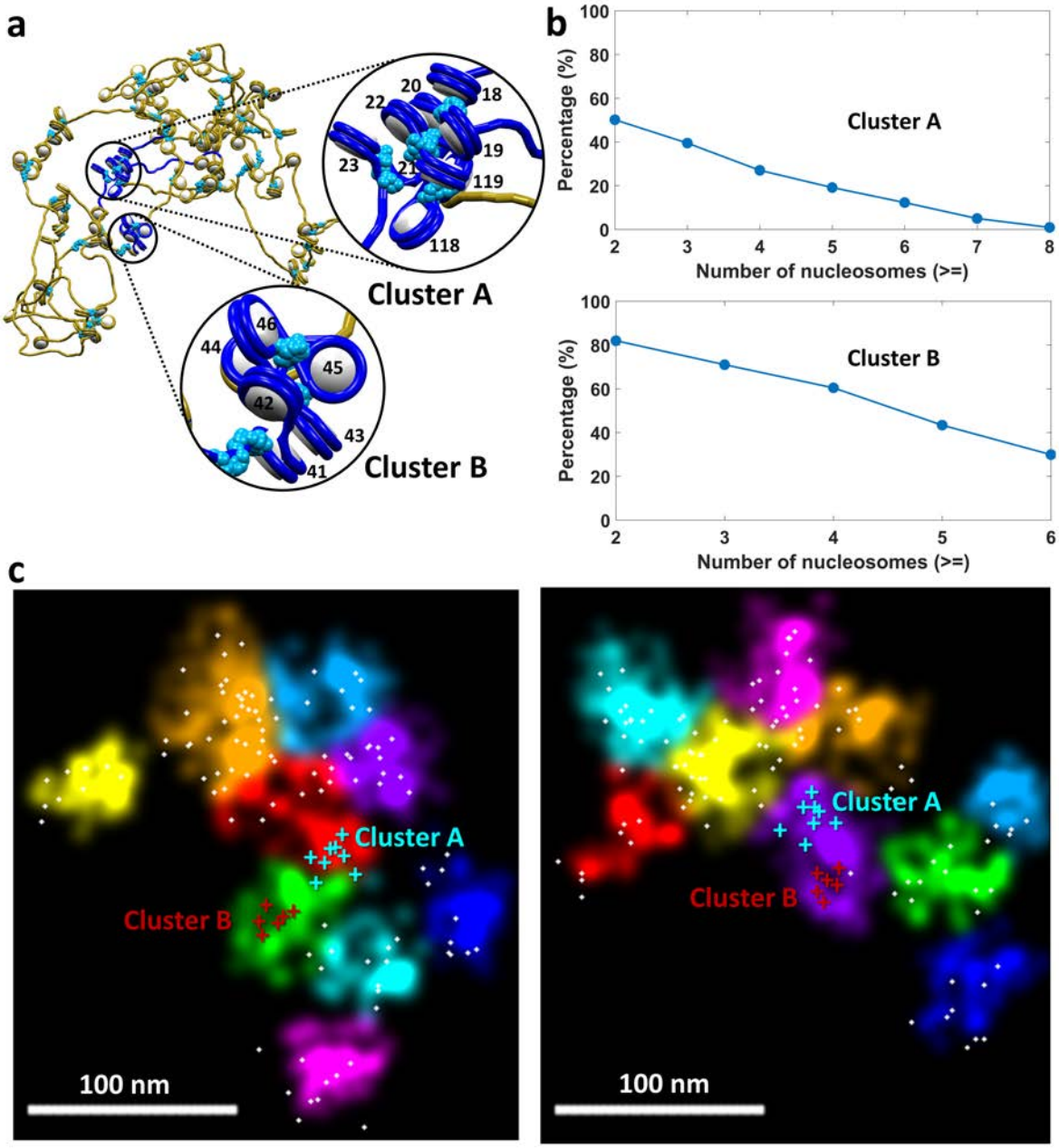

Figure 47. Comparison of nucleosome cluster analysis in 3D fibers by DBSCAN and nucleosome clutch analysis in simulated super-resolution images: (a) Example mESC Oct4 fiber from the mesoscale model shown in Figure 1. Two nucleosome clusters identified in the DBSCAN analysis are shown in the zoom: Cluster A containing 8 nucleosomes and Cluster B containing 6 nucleosomes. **(b)** Percentage of simulated super-resolution images in which a subset of the nucleosomes identified in Cluster A (top) or Cluster B (bottom) are also found within the same segmented nucleosome clutch. **(c)** Two example simulated super-resolution images in which nucleosome clutches are segmented and pseudo color coded. The white dots represent the true positions of all nucleosomes from which the super-resolution images were simulated. The cyan and red crosses correspond to the nucleosomes

identified in Cluster A and Cluster B, respectively. In the left example, Cluster A and Cluster B nucleosomes appear in separate clutches whereas in the right example they appear in the same clutch due to 2D projection effects and the lower spatial resolution of the super-resolution images.

The compaction level of nucleosomes within clutches ($6.2 \cdot 10^{-3} \pm 3.5 \cdot 10^{-3}$ Nucleosomes/μm^2 for mESCs and $11.5 \cdot 10^{-3} \pm 6 \cdot 10^{-3}$ Nucleosomes/μm^2 for mNPCs) (**Figure 42b**), and the number of nucleosomes per clutch (6.4 ± 4.7 Nucleosomes/clutch in mESCs compared to 16.4 ± 11.3 Nucleosomes/clutch in mNPCs) (**Figure 46c**) were higher in mNPCs compared to mESCs[36,116]. Despite the above mentioned differences between the 3D model and the simulated images, remarkably, the number of nucleosomes per clutch in the two cell types was in close agreement with the DBSCAN results obtained from directly analyzing the 3D fibers at higher resolution (**Figure 44d**). Previous super-resolution experimental data showed a median number of ~3 and ~6 nucleosomes per clutch averaged globally over the entire chromatin of mESCs and mNPCs, respectively. The number of nucleosomes per clutch is lower in the experimental data compared to the model, which may reflect differences in the global clutch configuration versus the local Oct4 gene clutch configuration. The experimental data may also potentially underestimate the number of nucleosomes per clutch due to labeling inefficiencies particularly in more compact regions. Nonetheless, the comparison of experimental data and simulated images to the model revealed that the global changes in clutch conformation of mESCs and mNPCs are representative of specific changes to the clutch conformation of a model pluripotency gene like Oct4. In fact, these differences in clutch conformation are likely even more prominent in specific genomic regions that change their expression level upon differentiation compared to genome-wide differences in clutches. In addition to differences in the number and compaction of nucleosomes in clutches, significant differences were also observed for the number of clutches per fiber (**Figure 48a**), the clutch area (**Figure 48b**), and the nearest neighbor distance between clutches (**Figure 48c**) in the two cell types.

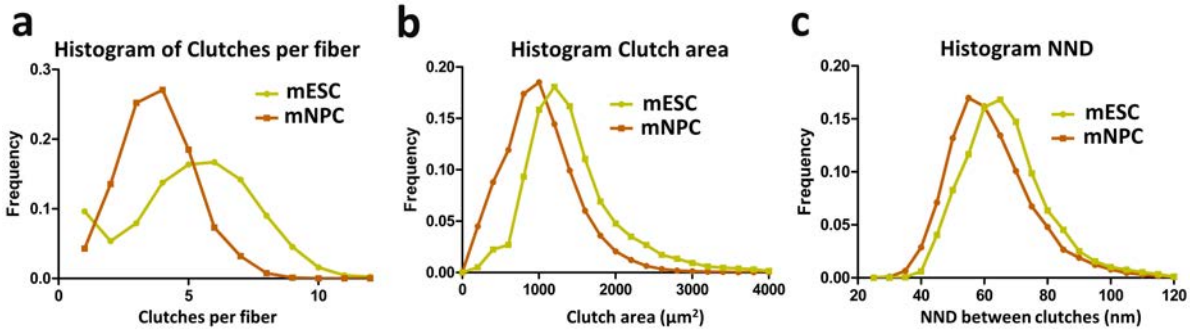

Figure 48. Analysis of the simulated super-resolution images of Oct4 locus in mESCs and mNPCs. a) Histogram of the number of clutches per fiber. **b)** Histogram of clutch area. **c)** Histogram of nearest neighbor distance between clutches.

Overall, our results show a heterogeneous chromatin fiber conformation both globally and at the level of specific pluripotency genes, manifested as heterogeneous groups of nucleosome

clutches. In addition, we reveal the presence of folding motifs like hierarchical looping, which are cell-type specific and dynamically change upon cell differentiation.

3.5 Discussion

Recent high-resolution imaging experiments including super-resolution fluorescence microscopy and electron tomography have revealed a complex picture of chromatin structure, in which chromatin is composed of 10-nm fibers that form nucleosome clusters (or clutches) of different levels of nucleosome density[17,36,116]. The level of chromatin fiber compaction likely influence the activation or repression of key lineage and pluripotency genes during development. For this reason, it is paramount to study these chromatin fiber features in somatic and stem cells. We showed that chromatin structure can be directly measured and modelled using complementary techniques: super resolution imaging and coarse-grained computation. Specifically, using mesoscale modeling of large nucleosome assemblies incorporating realistic nucleosome positions based on MNase-Seq data with experimentally measured linker histone and acetylation densities, we showed that the nucleosome cluster differences of a model pluripotency gene (Oct4) correlate with the global state of clutch conformation seen in mESCs and mNPCs by super-resolution experiments. Furthermore, the enhanced chromatin compaction during differentiation is directly related to changes in nucleosome positioning, amount of linker histones, and acetylation patterns. Each one of these physical parameters can be independently varied in the mesoscale model to generate experimentally testable hypotheses about the most important mechanisms responsible for nucleosome clutch formation and reorganization in differentiation. Ongoing work, for example, is showing that nucleosome positions, in particular, are a dominant factor in determining cluster patterns. The model further revealed that the changes to cluster size upon differentiation are likely due to increased hairpin and hierarchical looping, which ultimately might contribute to the silencing of Oct4 in mNPCs. Despite dramatic reorganization of the clutches upon differentiation, the nucleosome geometry within clutches is unaffected and most consistent with zigzag secondary-structure fiber topology.

Chapter 4: Single Molecule Tracking of single nucleosomes

The content of this chapter is part of a manuscript under preparation (see **List of publications**).

4.1 Abstract

We recently showed that nucleosomes in folded chromatin fibers in vivo form heterogeneous groups, named nucleosome clutches. Nucleosome clutches are smaller and less densely compacted in embryonic stem cells (ESCs) compared to neuronal progenitor cells (NPCs), in correlation with the more open chromatin state of ESCs. Here, we use Single Molecule Tracking (SMT) to measure the local nucleosome dynamics and correlate them with the super resolution images of chromatin in ESCs and NPCs[11,36]. We use Slow (500ms of exposure time)- and Fast-SMT (15ms of exposure time) to show that nucleosome turn over and local dynamics within the chromatin fiber correlate with the structural features observed in super-resolution data and the mesoscale models. Nucleosomes are less stable, turn over faster, and explore larger areas in mESCs compared to mNPCs. The local dynamics correspond to the motion of individual nucleosomes within chromatin rather than the motion of large chromatin domains. Finally, the amount of linker histone H1 places the largest constraint on the local motion of nucleosomes whereas it is less important for nucleosome turn over at longer time scales. These results give a detailed picture of nucleosome dynamics in different cell types and link nucleosome dynamics to structural differences in nucleosome organization in different cell types as observed by super-resolution microscopy and further corroborated by coarse-grained modeling.

4.2 Introduction

One outstanding biological question that will benefit from the development and application of advanced imaging technologies is the relationship between chromatin structure, dynamics and gene activity. Chromatin is a complex of DNA and histone proteins, which helps compact and spatially organize the genetic code within the small space of the nucleus. Applying super resolution microscopy, previous work in the lab showed that nucleosomes within folded chromatin fibers are organized in heterogeneous groups named nucleosome clutches, unlike the textbook model that suggested a much more ordered and hierarchical folding of nucleosomes. Nucleosome clutches are smaller and less densely compacted in embryonic stem cells (ESCs) compared to neuronal progenitor cells (NPCs), in correlation with the more open chromatin state of ESCs. We also applied modelling of the Oct4 region (**Chapter 3**) showing a correlation between chromatin structure and cell pluripotency. Here we use Single Molecule Tracking (SMT) to compare the chromatin structure and local nucleosome dynamics with the super resolution images of chromatin fiber in ESCs and NPCs.

Fluorescence Recovery After Photobleaching (FRAP) analysis and single molecule tracking (SMT) of histone proteins, as well as tracking of individual genomic loci within the nucleus demonstrated that chromatin is highly dynamic. Individual genomic loci diffuse within a confined space in the nucleus[37,38,131] and this mobility correlates with the transcriptional activity of some genomic regions such as enhancers[37,39]. In some cases, genomic loci dynamically reposition over large distances, for example by relocating from the nuclear periphery to the nuclear interior upon activation[40,41]. While FRAP analysis showed that nucleosomes are highly stable and turn over slowly[42], tracking of individual Halo-tagged histone proteins showed that histones also explore their local environment dynamically[43,44]. Live cell super-resolution imaging showed that chromatin domains that are hundreds of nanometers in size are also mobile[33,43,45]. However, how these dynamic entities spanning multiple length scales, from individual nucleosomes to large genomic loci, relate to each other and what are the associated mechanisms of their folding and dynamics, remain unknown.

In addition to chromatin fluidity, several studies showed that architectural proteins are also highly dynamic inside the nucleus[47,48]. In particular, the dynamics of architectural proteins like H1 and HP1 increase in embryonic stem cells (ESCs) as shown by FRAP and SMT[12,49]. Based in part on these FRAP studies, it has been suggested that the ESC chromatin is hyperdynamic and depleted of heterochromatin[132]. Super-resolution imaging showed that nucleosome clutch size is cell-type specific, and that ESCs have smaller, less compact clutches compared to differentiated Neuronal Progenitor Cells (NPCs)[116]. We further noted that nucleosome clutch size and compaction depends on the amount of linker histone H1[116], as well as the amount of acetylation on histone tails[36], suggesting that linker histones and histone post translational modifications play a role in organizing nucleosomes into clutches.

How the nucleosome clutch organization in fixed stem and somatic cells correlate with nucleosome dynamics in live cells remains unclear. In addition, the mechanisms that regulate nucleosome and chromatin dynamics in different cell types are poorly understood.

Fast- and Slow-SMT revealed that histone H2B is dynamic in vivo and explores its local environment within the chromatin fiber. The smaller and more open clutches of ESCs compared to the larger and more compacted clutches of NPCs correlate with different histone dynamics observed in the two cell types. Histone residence times within chromatin are only weakly dependent on the amount of linker histone H1. The extent of the local histone mobility within the chromatin fiber, on the other hand, mainly depends on the amount of H1. These results offer a rich picture of nucleosome dynamics and link nucleosome dynamics to structural differences in nucleosome organization in different cell types.

4.3 Methodology

Single Molecule Tracking experiments consist on four main steps: the labeling, the imaging, the single molecule localization and track reconstruction and the quantitative analysis of the trajectories. The selected experimental conditions for each of those steps have a significant impact on the measurements, so for each specific objective, in our case the study of chromatin dynamics at different time scales, one needs to choose different experimental designs.

We generated mESC or mESCs- H1tKO (triple knock out of the linker histone H1) [133] cell lines stably expressing H2B fused to Halo-tag at low levels and used 10 picomolar concentration of Janelia Fluor 549 (JF549)-tagged Halo ligand to sparsely label H2B molecules within the nucleus (**Figure 49a, b**). NPCs were obtained from the differentiation of mESC with retinoic acid treatment. Importantly, for the SMT experiments we used low light illumination levels throughout the experiments (**Detailed Methods DM1.3**) and avoided a pre-photobleaching step typically used in SMT [92] to not compromise cell viability. Further, by labeling DNA with Hoechst and taking a snapshot of the nuclei before and after SMT, we ensured that the nuclei were stable during the imaging process. In addition, for the 2-Color SMT experiments, we combined this Halo-Tag-H2B-JF549 labeling strategy with Telomeres or Centromeres fused to GFP.

We performed the SMT experiments on a N-STORM 4 microscope (Nikon Instruments) equipped with an incubator (Okolab) for maintaining live cells at 37ºC and 5%-CO_2 conditions. For the case of 2-color experiments, we used a Dual-view system that uses a dichroic mirror for splitting the camera field of view into two, one for each channel. In order to capture the fast and slow dynamics of chromatin, we performed experiments with short (15 ms) and long (500 ms) camera exposure time, respectively. For both conditions, we maintained the laser power as low as possible to not stress the cells, while still having good enough 2D localization precision of the single molecules (around 40 nm).

First, using slow-SMT (at 500 ms of exposure time), we determined the residence times of H2B in mESCs, mESCs- H1tKO, and mNPCs (**Detailed Methods DM1.3**). As a control, we also measured residence times in fixed cells to determine experimental limitations in measuring residence times, which is mainly limited by photobleaching and tracking errors. Positions of tracked molecules were distributed randomly within the nuclei and hence there was no spatial bias in the sampling of H2B molecules (**Figure 49b**).

Then, to characterize H2B mobility at short time scales, we carried out fast-SMT (at 15 ms of exposure time) (**Detailed Methods DM1.3**) and detected three different motion types in the H2B trajectories (**Figure 49c** and **Figure 50b**): i) confined motion, likely corresponding to H2B stably incorporated into nucleosomes, ii) Brownian diffusion, likely corresponding to free H2B not incorporated into nucleosomes, and (iii) switching behavior between confined

motion and Brownian diffusion (butterfly motion), likely corresponding to transient destabilization of the nucleosomes[134–136] (see **Detailed Methods DM1.3**).

For the localization and tracking we used TrackMate[84], which is an open-source plugin for Fiji[137]. The localization was performed by 2D Gaussian fitting on the diffraction limited spots of the single molecules, and the tracking, using the simplest approach, just by connecting the nearest neighbor localizations with a certain maximum jump threshold from frame to frame, depending on the imaging conditions (**Figure 49b** and **c**).

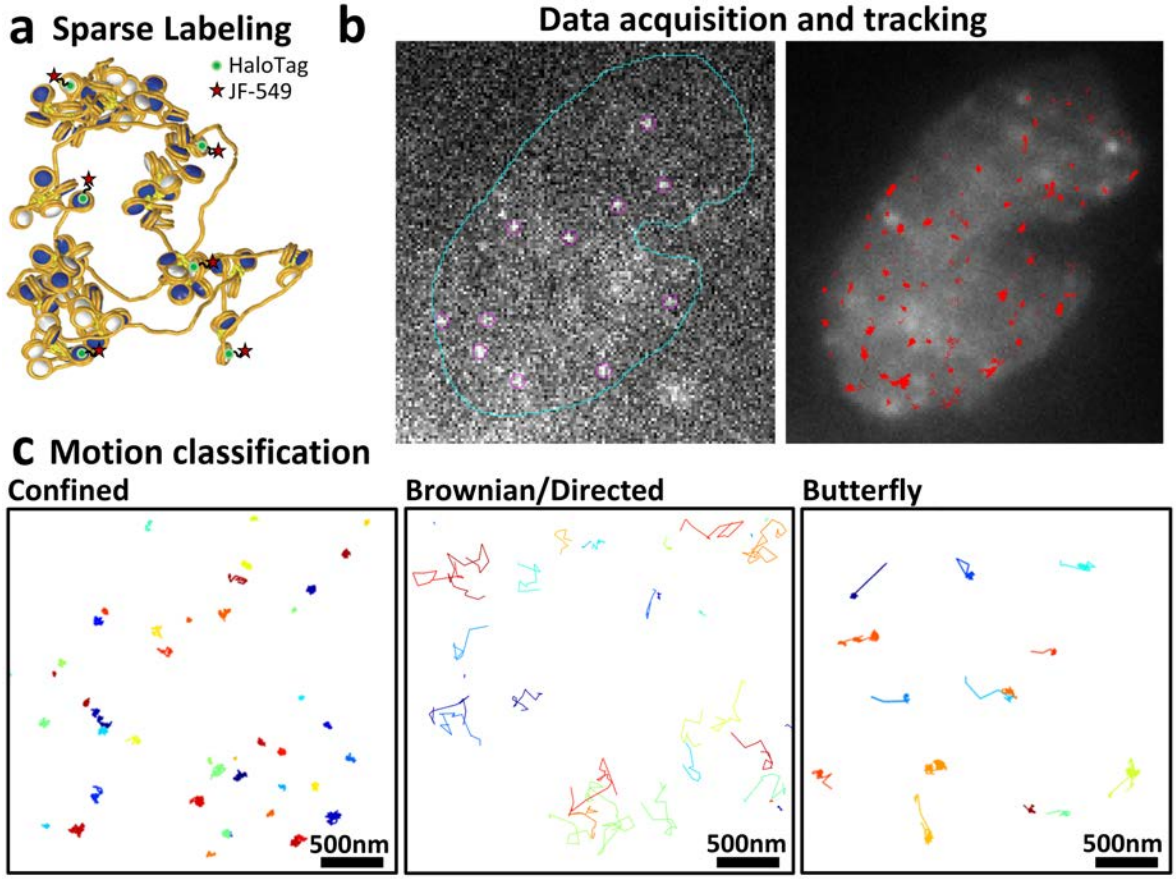

Figure 49. Workflow for the fast-SMT experiments and analysis. a) Cartoon showing the tagging and labeling strategy for SMT. Histone H2B was tagged with Halo-tag and sparsely labeled using Halo ligand conjugated to Janelia Fluor (JF)-549 dye. **b)** Data is acquired with 15 ms exposure time, single molecules are identified in each frame (magenta circles, left panel), their position determined by fitting to a Gaussian and molecules are connected from one frame to the next frame to generate trajectories (red, right panel) using TrackMate[84] plugin in ImageJ. **c)** Trajectories are classified into three different motion types (confined, Brownian/directed and butterfly) based on the alpha coefficient of the power law fit to the MSD versus time curve. Colors are just used to represent the different trajectories.

We developed our custom software for track analysis. It is a Matlab code (available at https://github.com/PabloAu/Single-Molecule-Tracking-Analysis), that makes use of some functions of @msdanalyzer[138]. In short, first we classify each trajectory based on their motion type (**Figure 49c**). Then, from the ensemble of the confined trajectories, which correspond to H2B histone incorporated into nucleosomes constituting the chromatin structure, we compute the radius of confinement by fitting the circle confined diffusion model to the TE-MSD[88]. For the estimation of the diffusion coefficient, we used the first 3 points of each T-MSD curve corresponding to each individual trajectory and fitted them with a linear distribution[139,140]. Finally, the residence time of the unbinding (or turn over) dynamics was computed by fitting a double exponential decay function to the survival H2B fraction on the long exposure dataset.

For more detailed explanation about the experimental and analytical procedures carried on for studying chromatin dynamics, see **Detailed Methods DM1.3**.

4.4 Results

4.4.1 Nucleosome residence time within chromatin increases in differentiation

Given our super-resolution and modeling results that reveal dramatic structural reorganization of the chromatin fiber both globally and at specific genes during differentiation, we wanted to explore how the local dynamics of individual nucleosomes within clutches change upon differentiation and how these dynamics relate to the structural changes observed. Using SMT, we measured H2B dynamics in mESCs, mESCs-H1tKO and mNPCs that were obtained upon differentiation of the Halo-H2B expressing mESCs using retinoic acid treatment (**Detailed Methods DM1.3**).

H2B residence time was lower in all three cell types compared to fixed cells, suggesting that H2B is dynamic and likely turns over in vivo (**Figure 50a**). H2B residence time was shortest in mESCs-H1tKO and progressively increased in wild type mESCs and mNPCs, suggesting that H2B is more stable in differentiated cells (**Figure 50a**). The H1 to H2B ratio is higher in mNPCs compared to mESCs[125], as a result H1 may play a role in stabilizing H2B and increasing its residence time within chromatin. However, interestingly, knocking out three isoforms of the linker histone had a significant but subtle effect on H2B residence time (25.8 ± 1 seconds for mESCs and 16.2 ± 0.7 seconds for mESCs-H1tKO, **Figure 50a**), pointing to factors besides H1 in increasing H2B's residence time. These results are consistent with previous FRAP analysis of H2B turnover in wild type and mESC-H1tKO[141].

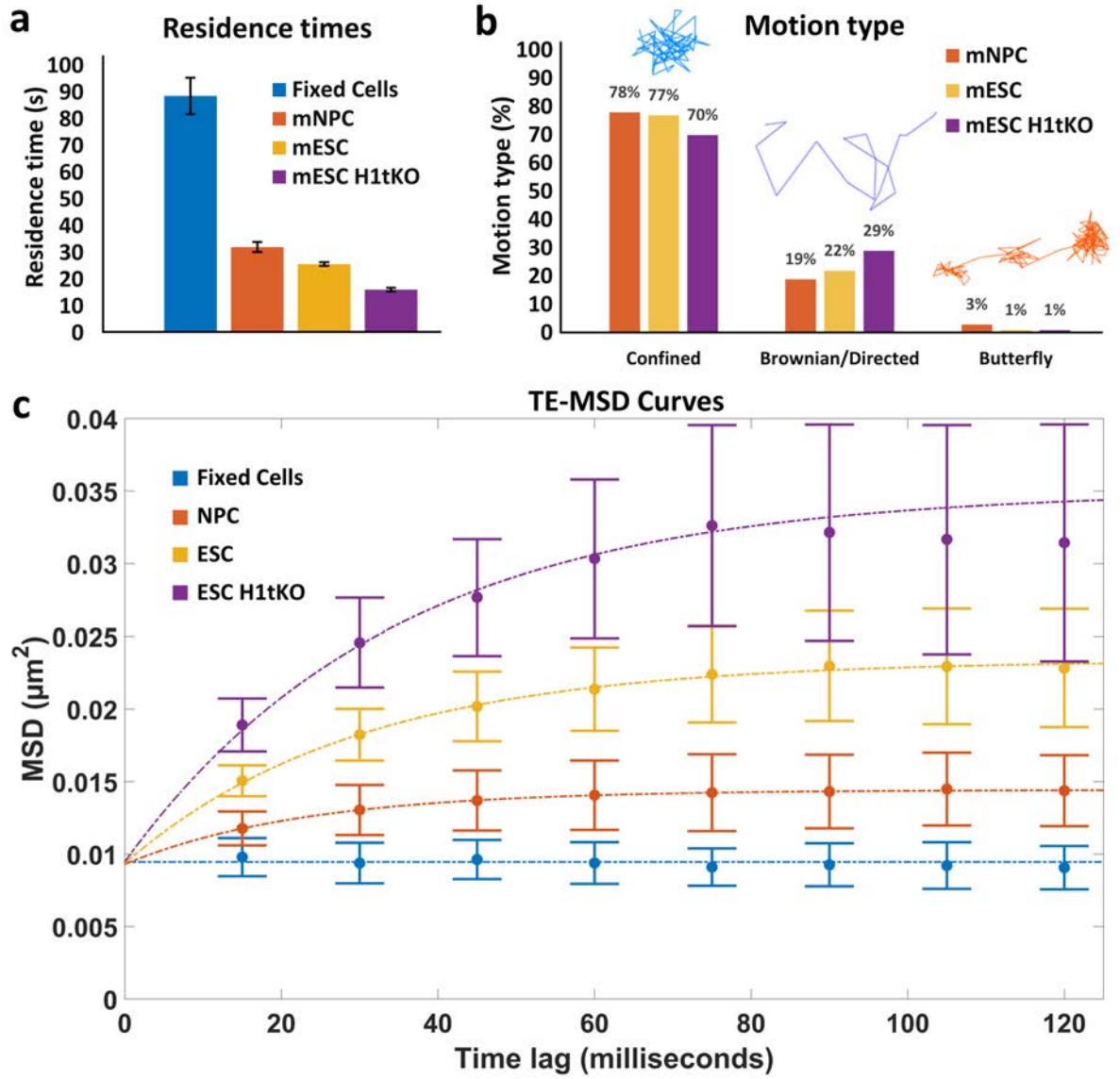

Figure 50. Nucleosomes have shorter residence time and move more dynamically within chromatin in mESCs compared to mNPCs. a) Residence times measured using Slow-SPT (500ms exposure time) in fixed cells (cyan), mNPCs (orange), mESCs (yellow) and mESC-H1tKO (mESCs in which three isoforms of H1 has been knocked out) (purple). Values were obtained from the double exponential decay function fitting of the survival fraction distribution of the trajectories over time. Mean and 95% Confidence Interval values are plotted. N= 245, 3200, 2593 and 887 trajectories were used for the analysis for fixed cells, mNPC, mESC and mESC-H1tKO, respectively. **b)** Proportion of trajectories showing confined, Brownian/directed or a mixture of confined and Brownian/directed (butterfly) motion. N=4021, 5295 and 2436 trajectories for mNPC, mESC and mESC-H1tKO were used, respectively. **c)** Mean Square Displacement (MSD) versus time plot for the different cell types. The ensemble MSD average of all the displacements for each time lag and the standard deviation are displayed. A circle confined diffusion model was used to fit the Time Ensemble (TE)-MSD (dashed

lines) and the average diffusion coefficient and radius of confinement were obtained for each cell type. For fixed cells, all the tracks were used without filtering (N=284 trajectories). For the rest, only the confined trajectories were used (N=543, 860 and 370 trajectories for mNPC, mESC and mESC-H1tKO, respectively).

4.4.2 Nucleosomes exhibit more confined mobility within chromatin upon differentiation

Our fast-SMT experiments allowed us to characterize H2B mobility at short time scales. The majority of H2B trajectories belonged to the confined motion category in all three cell types (**Figure 50b**). As a control, we also tracked transcription factors including Oct4 and CTCF and as expected find them to be more dynamic compared to H2B (**Figure 51**). To determine the extent of local nucleosome mobility, we analyzed the radius of confinement of H2B from the sub-population of H2B molecules that exhibited confined motion. This analysis showed a radius of confinement of 50 nm in fixed cells, which corresponds to the localization precision of our measurements (**Figure 50c**). In living cells, the radius of confinement was larger compared to fixed cells for all cell types (**Figure 50c**), underscoring the dynamic nature of nucleosomes during their residence time within chromatin. The radius of confinement was largest in mESCs-H1tKO (157 ± 6 nm), lacking linker histone, and progressively decreased in mESCs (115 ± 3 nm) and mNPCs (82 ± 1.5 nm) (**Figure 50c**). We observed large differences in the radius of confinement between mESCs-H1tKO and wild type mESCs (**Figure 50c**), suggesting that the local dynamics of chromatin bound H2B is mostly constrained by the presence of linker histone H1.

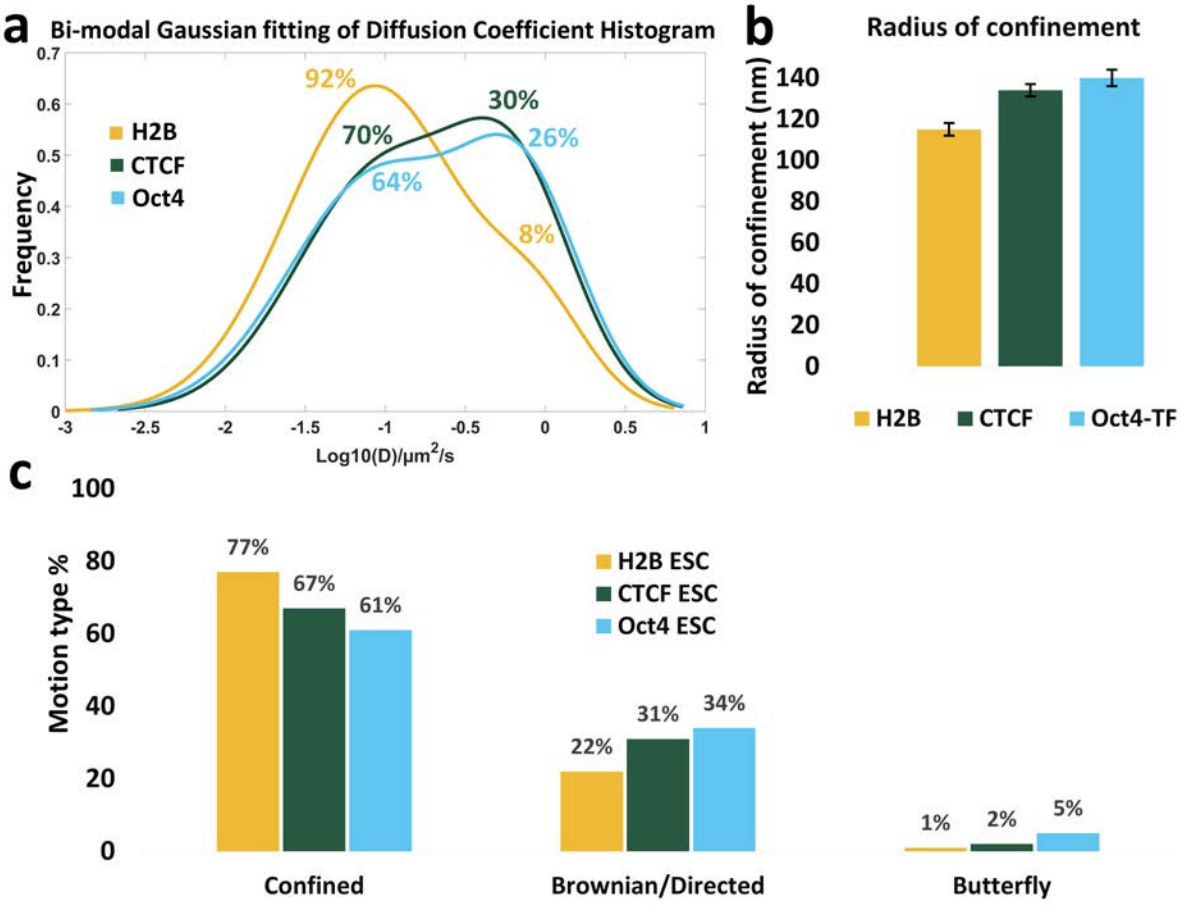

Figure 51. Transcription factors are more dynamic than H2B. Mobility of transcription factors compared to H2B analyzed in mESCs. **a)** Histogram of diffusion coefficients for the different proteins fitted with a bi-modal Gaussian distribution. All the tracks from all the motion types were used. N= 5355, 2247 and 1219 trajectories for H2B, CTCF and Oct4 were analyzed, respectively. **b)** Radius of confinement obtained by fitting the circle confined diffusion model to the TE-MSD curves of confined tracks for each protein. Mean and 95% confidence interval values are plotted. N= 860, 464 and 269 trajectories were used for H2B, CTCF and Oct4, respectively. **c)** Percentage of different motion types present for the different proteins. N= 5355, 2247 and 1219 trajectories for H2B, CTCF and Oct4 were analyzed, respectively.

To further confirm that these dynamics correspond to local motions of nucleosomes within the chromatin fiber, rather than the motion of large chromatin domains, we tracked telomeres and centromeres using SMT (**Figure 52**). Telomeres are at the ends of chromosomes and can likely move more freely than other chromatin domains embedded within chromosomes. In mouse, their length varies between 50–150 kbp[142] (or 100–750 nucleosomes) and their volume correlates with their length[143]. These measurements showed that at these short time scales (i.e. tens of milliseconds), telomere and centromere mobility was much smaller than H2B and comparable to the mobility measured in fixed cells (**Figure 52b, c**). While the

mobility of telomeric H2B (i.e. H2B overlapping with telomeres) was slightly lower than non-telomeric H2B, even telomeric H2B mobility was substantially higher than the mobility of large telomeric regions (**Figure 53**). At longer time scales (i.e. tens of seconds), telomeres and centromeres showed dynamic behavior, exploring areas ranging from 0.5x0.5 μm^2 to 1.5x1.5 μm^2, consistent with previous studies[131,144]. Hence, large chromatin domains are relatively immobile at short time scales compared to H2B and the latter likely corresponds to the mobility of individual nucleosomes themselves or small groups of nucleosomes within the chromatin fiber.

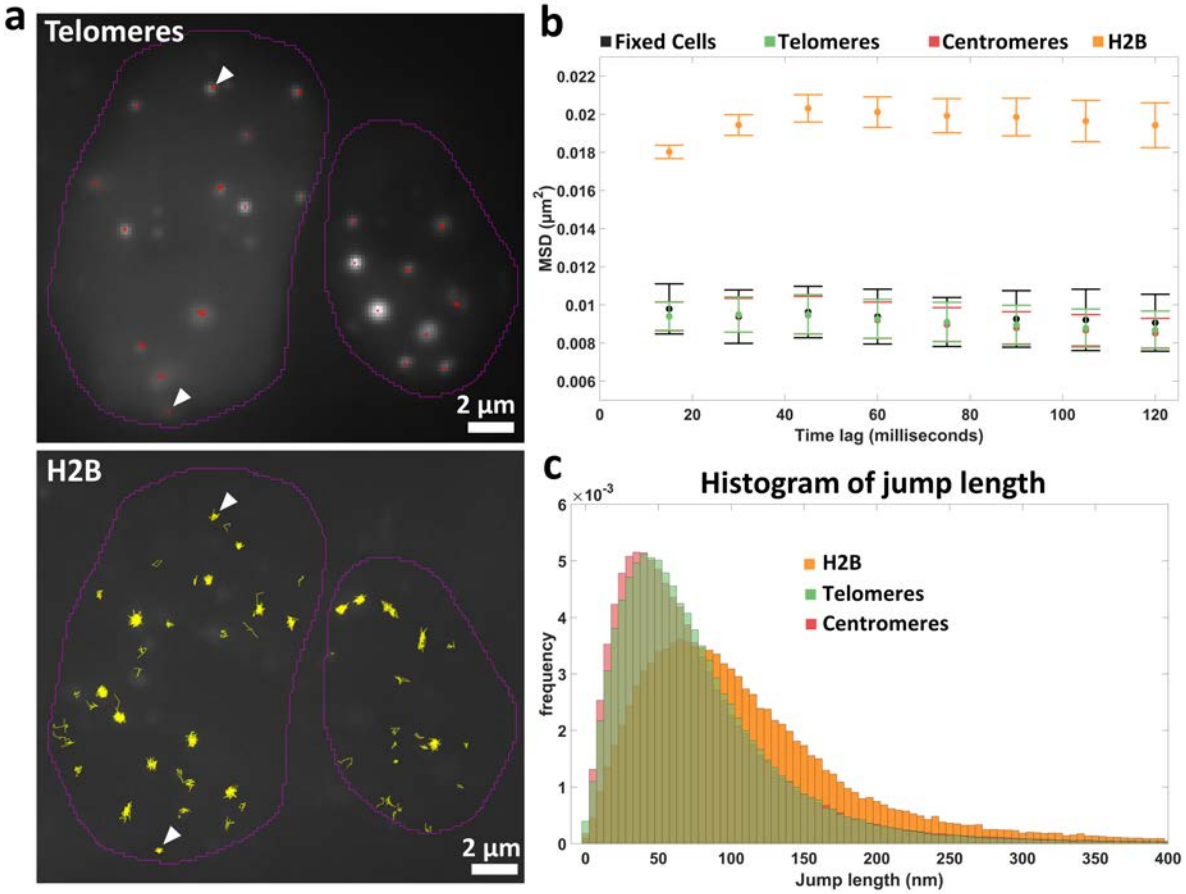

Figure 52. Telomere motion takes place at much slower timescales compared to nucleosome motion. a) Upper panel shows telomere trajectories (red) overlapped on a maximal projection image of telomeres. The tracks were cropped so that their track length is in the same scale as for H2B trajectories for visualization purposes. Lower panel shows the corresponding H2B trajectories from the 2-color SMT experiment. White arrows indicate example trajectories where telomeres and nucleosomes overlap. A maximum spatial threshold of 250nm between the telomere trajectory and the H2B trajectory position was imposed in order to assign a nucleosome trajectory to a telomeric region. **b)** TE-MSD curves comparing H2B in live cells to telomeres, centromeres and H2B in fixed cells. Telomere and centromere MSD curves overlap with MSD curve of H2B in fixed cells, whereas

H2B in live cells is more dynamic. N=284, 9135, 10660 and 11752 trajectories were used for fixed cells, telomeres, centromeres and H2B respectively. **c)** Histogram of frame to frame jump distribution for telomeres (orange), centromeres (green) and H2B in live cells (cyan). N=11752, 9135 and 10660 trajectories were analyzed for H2B, telomeres and centromeres, respectively.

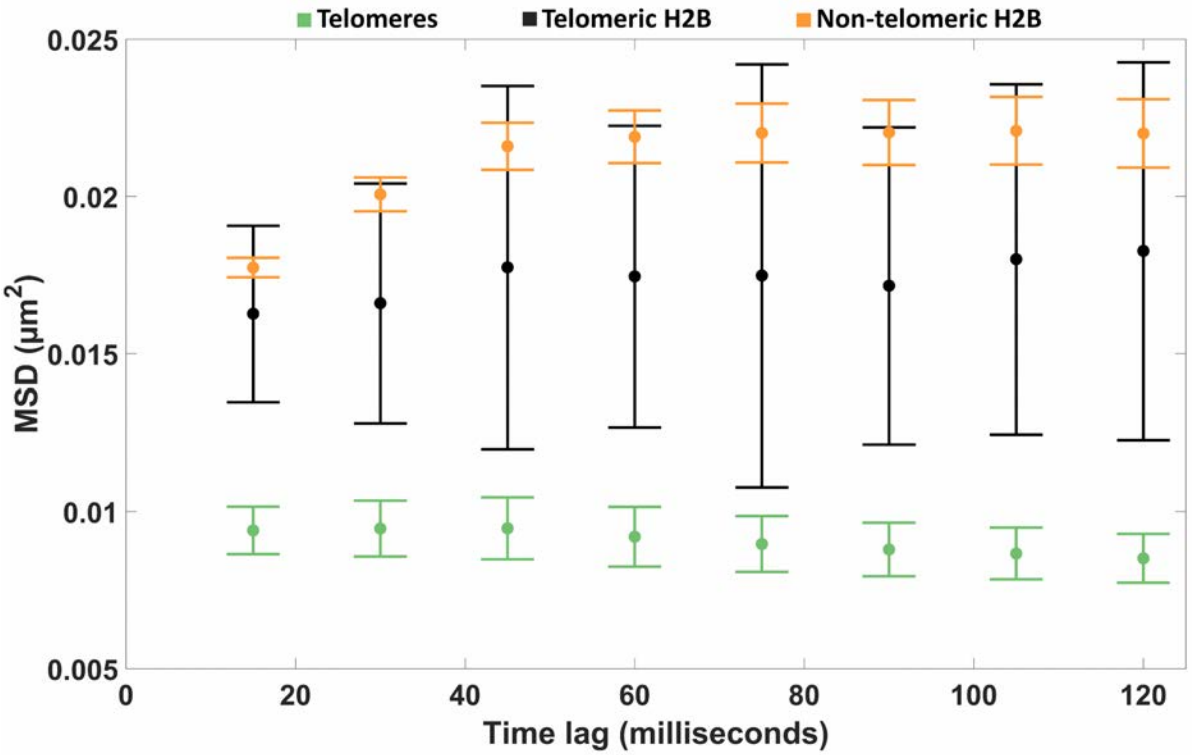

Figure 53. TE-MSD curves for telomeres, telomeric H2B and non-telomeric H2B. N= 9135, 87 and 9312 trajectories for telomeres, telomeric H2B (H2B tracks overlapping with a telomeric region) and non-telomeric H2B (H2B tracks not overlapping with a telomeric region) were analyzed, respectively.

4.4.3 Dynamics of both heterochromatic and euchromatic nucleosomes are affected by the process of differentiation

Overlaying the H2B motion trajectories on Hoechst images of DNA allowed us to further explore the differences in the local nucleosome dynamics between heterochromatic and euchromatic regions of the different cell types (**Figure 54a**). We sub-categorized the H2B trajectories based on their overlap with high or low intensity regions in the Hoescht images, corresponding to more heterochromatic or more euchromatic regions, respectively (**Figure 54a**). This analysis showed that the nucleosomes in heterochromatic regions were more confined than those in euchromatic regions in all three cell types (**Figure 54b**). The more

confined mobility of heterochromatic nucleosomes was further confirmed by tracking H2B that overlapped with telomeres. H2B tracks overlapping with telomeres showed on average more confined mobility compared to those trajectories that did not overlap with telomeres (**Figure 53**). Interestingly, there were significant differences between the radius of confinement of both heterochromatic and euchromatic nucleosomes among the three cell types: euchromatic nucleosomes of mESCs-H1tKO were the least confined and the heterochromatic nucleosomes of mNPCs were the most confined (**Figure 54b**). Hence, our results demonstrate that the mobility of both the heterochromatic and euchromatic nucleosomes are affected by differentiation (**Figure 54b**).

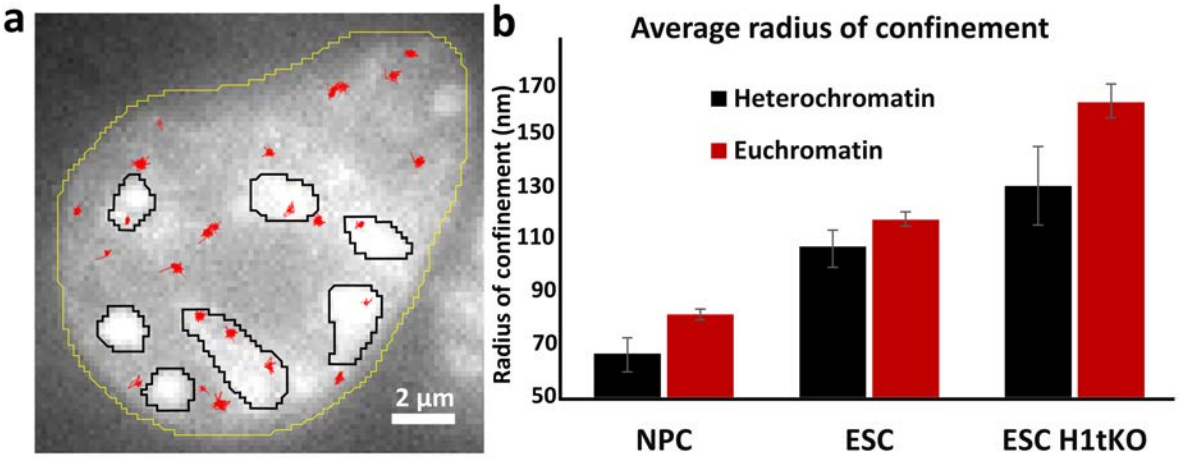

Figure 54. Mobility of both euchromatic and heterochromatic nucleosomes change upon cell differentiation. a) Image of a mESC labeled with Hoestch33342 showing the cell nucleus (yellow region of interest, ROI). Euchromatin (low intensity) and heterochromatin (high intensity, black ROIs) regions and the corresponding H2B trajectories within each region (red) are shown. **b)** Bar plot showing the radius of confinement estimation from circle confined diffusion model for H2B moving within euchromatic (red) and heterochromatic (black) regions in the different cell types. Mean and 95% Confidence Intervals are plotted. Only confined trajectories were used (N= 543, 860 and 370 trajectories for mNPC, mESC and mESC-H1tKO, respectively).

4.4 Discussion

To determine how the changes in nucleosome clutch organization in the process of cell differentiation impacts nucleosome dynamics in living cells, we used SMT to measure the dynamics of individual nucleosomes in mESCs, H1TKO-mESCs and mNPCs and compared these dynamics to those of larger genomic regions. Our experiments showed profound changes in nucleosome residence times and local nucleosome motion in mESCs, mESCs-H1tKO, and mNPCs consistent with the measured structural changes. Nucleosome motion was more constrained within heterochromatic regions composed of large, compacted nucleosome clutches compared to euchromatic regions. The residence time and local mobility of both hetero- and euchromatic nucleosomes also depended on cell type as nucleosomes of differentiated cells containing larger and more compacted nucleosome clutches were more stable than nucleosomes of mESCs. The measured dynamics likely correspond to movement of individual nucleosomes within their local chromatin fiber as larger genomic regions like telomeres and centromeres were immobile at these short time scales. The measured nucleosome dynamics may correspond to nucleosome sliding as well as other types of nucleosome destabilization within chromatin. Interestingly, the local, confined motion of nucleosomes within the chromatin fiber was most affected by knock-out of the linker histone H1. The mESCs-H1tKO also had the smallest nucleosome clutches as measured using super-resolution microscopy[116]. Hence, the presence of a large number of tightly compacted nucleosomes within clutches, which are likely stabilized by the linker histone, can potentially constrain nucleosome motion. The residence time of nucleosomes, on the other hand, was affected by factors other than linker histone since the residence time was moderately affected in mESCs-H1tKO. It will be interesting to further probe the molecular mechanisms responsible for nucleosome stability and local motion. Measuring the impact of these dynamics on transcription factors binding to chromatin and gene activation will further help unravel the relation between genome organization and function.

Chapter 5: Conclusions and perspectives

5.1 Advanced microscopy methods and computational modelling to study biological multi-component structures

Since the appearance of localization-based microscopy methods in the first decade of the 21st century, new developments to improve or extend their performance has been constantly arising[145]. Those new advancements were focused on: increasing the spatial resolution[146–149], extending the SMLM techniques to 3D imaging[66,150], imaging thick samples[151,152], applying them to live-cell imaging[65,71], increasing the number of targets to be imaged simultaneously[74,94,108], reducing the acquisition time[153–155] and reducing the cost of the equipment required for these type of experiments[156,157]. Nowadays, a huge amount of different methods belongs to the localization-based microscopy family each with their corresponding pluses and minuses. One of the most important features of any microscopy method is its 2D and 3D spatial resolution. **Figure 55** below shows a representation of the resolution of some of most used advanced microscopy methods at the present.

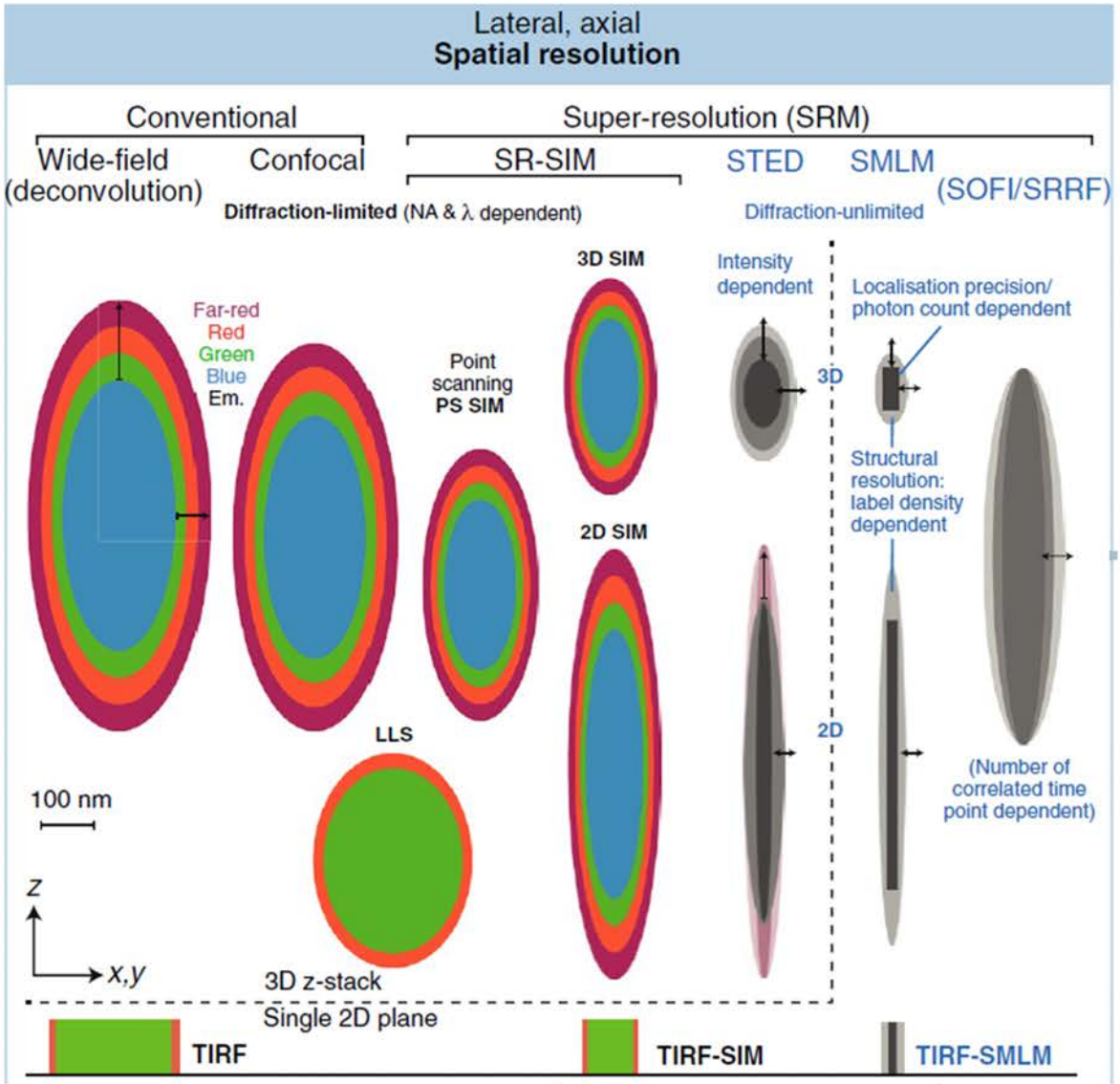

Figure 55. Diagram representing the spatial resolution of the available advanced light microscopy methods. The diagram displays the x-y and z resolution of the most used advanced microscopy techniques at the present. Adapted from [145].

The suitability of a particular SMLM method depends on the specific biological problem to be studied. For example, sometimes it is not necessary to use SMLM if the structural information at the nanoscale level is not required. **Figure 56** below show the main features, divided into three important characteristics: imaging depth, temporal resolution, and light intensity, (with advantages and limitations) of the most used advanced microscopy methods at the present.

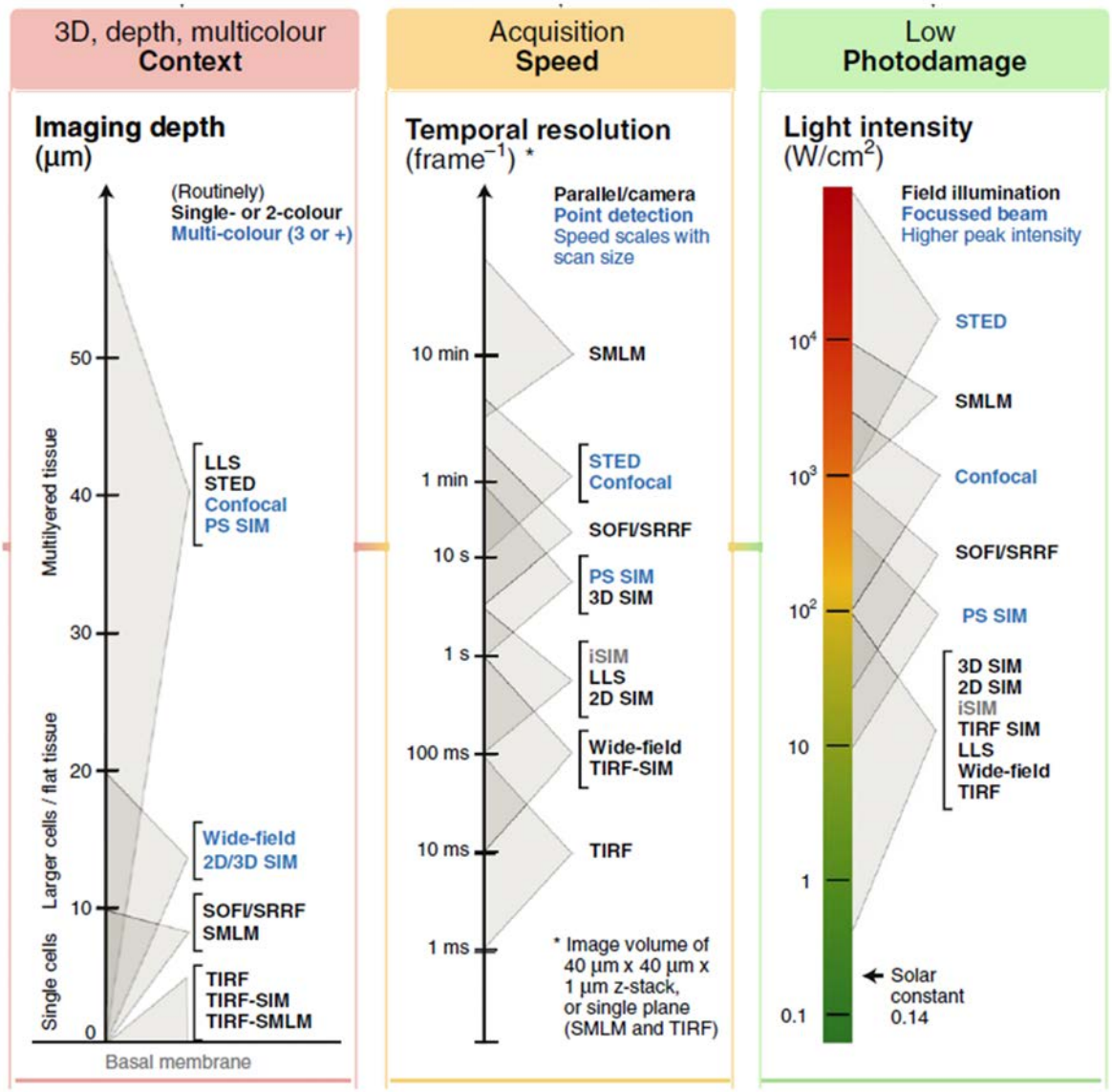

Figure 56. Technical overview of the available advanced light microscopy methods. The diagram displays the most used advanced microscopy techniques at the present. Left panel is arranged based on the imaging depth (z) of each technique. Center panel, is arranged depending on the acquisition speed (or temporal resolution). In right panel, the methods are sorted according to the required illumination intensity that is correlated with photo-damage, limiting the live-cell possibilities of certain techniques. Note that there is often a compromise between the different features of the performance of the presented methods. Adapted from [145].

In our project, we tackled two of these common objectives of the field by presenting a multi-color approach with low cross-talk between channels (less than 5%), that reduces significantly the experimental time of imaging. While we demonstrated the proof-of-concept of this

method with two colors, our simulations show that it can be easily extended to 5 (if not more) colors. Experimental implementation of 5-color fm-DNA-PAINT is an important next goal. In addition, fm-DNA-PAINT can be further multiplexed by sequential imaging of 5-colors at one time, opening the door to imaging tens or hundreds of targets in a short period of time. Furthermore, the combination of our method with other multiplexed approached like Exchange-PAINT[74], which has been demonstrated to be capable of imaging up to ten different targets but at the cost of being very time demanding, would increase the multiplexing ability of fm-PAINT and decrease the acquisition time of Exchange-PAINT, potentially allowing to image several tens of channels.

We believe that fm-DNA-PAINT will be very valuable for several biological applications that require high-throughput multi-color imaging, including discerning the spatial organization of multi-protein complexes, organelle-organelle contacts and chromatin structure-function relationship. The application of this methodology to study chromatin is particularly attractive. Chromatin consists of multiple components including DNA, histone proteins, and histone epigenetic modifications. Ability to simultaneously image all these components in one shot in high-throughput will open the door for understanding how epigenetic modifications shape chromatin structure in several cell types, as well as how these spatial organization is remodelled in physiological (differentiation, cellular reprograming) or pathological (cancer, neurological disorders) processes.

The improvement in the throughput of multi-color super-resolution imaging will open the door for high-content screening experiments using super-resolution microscopy[110], enabling to address questions related with chromatin structure and its cell-to-cell heterogeneity by imaging and analysing multiple components of a population of hundreds to thousands of cells. In the future, fm-DNA-PAINT, in combination with these improved imager oligos can potentially enable 5-color, live-cell super-resolution microscopy.

Another compelling application of our technique would be in image-based "spatial transcriptomics" methods like MERFISH[112,158], which measure both the gene expression and spatial distribution of the corresponding RNAs within the cell context. Introducing excitation-based frequency multiplexing can extend the throughput while maintaining the full camera field of view and leaving aside the use of systems based on dichroic mirrors to split fluorescence emission light into multiple paths. In that line, we envision our method to be applicable to spatial genomics and proteomics measurements where a large-scale study of the whole genome activity or all the proteins produced or modified in a biological system are studied. One family of widely used methods for genomics and proteomics experiments consist on performing immunoassays, where the target biomolecules are labelled with antibodies tagged with fluorescent probes[159]. Lately, these measurements were also applied to pharmacology and molecular diagnosis of diseases[160]. While several decades ago they used to be done sequentially, nowadays the field is going towards multiplexed approaches able to

detect multiple targets simultaneosly[159,161,162]. The modern version of these approaches is based on the new optical labelling reagents, like microbeads or nanoparticles, that can be engineered with different fluorescent coats that absorb light at a wide wave length spectrum and emit a specific fluorescence signal on each wavelength to be recognized as a particular antigen[159,161]. Typically, probes are excited one at a time, while different lasers provide different intensities of light to identify the probe. In that way, more than 10 different targets can be measured in the same biological sample[159,161,162]. Our method can help to extend the maximum number of targets of these methods by introducing excitation frequency modulation, which provides information about the absorption of each probe, giving another layer of barcoding. Finally, the fm-live and fm-DNA-PAINT can be combined in a correlative approach to visualize both dynamics and structure of cellular components, like the cargo transport of lysosomes in microtubules[163] or collagen export from the endoplasmic reticulum[164].

Since the publication of our work[165], some other solutions came up to deal with the main limitation of DNA-PAINT SMLM imaging technique, which is the very long experimental time consumption (typically between 20 to 60 minutes of acquisition per image). In one approach, Wade et al., presented an alternative for multi-color DNA-PAINT which is also based on multiplexing the channels on frequency, but instead of modulating the illumination source, they introduced different sizes of the binding domains of the DNA strands (imager strands), so that the different probes have their own characteristic affinity with their specific conjugated strands (docking strands). This produces a unique binding-unbinding rate for each probe that can be decoupled in the frequency domain by post-processing of the data[154]. This method has been used to image 4 colors in vitro with DNA Origami samples or 2 colors in situ with Hela cells. In addition, the length of the docking oligo was varied, therefore changing the binding duration of the imager oligo and give an additional dimension of barcoding. The combination of frequency and temporal barcoding could image 124 colors in vitro using DNA-origami. While this method is an attractive approach for multi-color imaging, its cellular implementation has significant limitations. Controlling the precise number of docking oligos on the DNA-origami structures is straight forward, however, achieving the same precise control for labelling antibodies with docking strands is much more challenging since the antibody conjugation is highly stochastic. In addition, since reducing the binding time of an imager oligo is not desirable as it introduces background by making it difficult to discriminate bound versus unbound, freely diffusing oligos, the temporal barcoding approach favors longer acquisition times. As such, the demonstration of this freguency/time barcoding approach was limited to only 2 colors in cells. Fm-DNA-PAINT does not suffer from these limitations and we believe it can be readily expanded to more colors in cells than the current state-of-the art of 2 colors.

In another recent work, Schueder et al. presented an improvement for conventional DNA-PAINT, which they called Speed-optimized DNA-PAINT[155]. It is based on the optimization of the DNA strands to speed up the hybridization of the imager oligo to the docking oligo for shortening the apparent blinking time of the fluorophores and hence reducing the total time needed for imaging. They claim to reduce the acquisition by an order of magnitude[155], but in order to achieve this, a specific (optimum) DNA strand is required, so it is limited to one-color imaging or a sequential approach for multi-color imaging. Its performance regarding the experimental time reduction of one order of magnitude has been shown in vitro with DNA Origami structures. Whereas for in situ, they just demonstrate an improvement in volumetric imaging, meaning 2D imaging of targets that are few micrometers away from the coverslip[155]. They claim that the improved imaging conditions of the method allows to obtain the data in the same acquisition time as in the classical DNA-PAINT case, but with a reduced background signal, increasing SNR and thus the localization precision. It is straightforward to combine this new Speed-optimized DNA-PAINT approach with our fm-DNA-PAINT, to exploit the benefits of both methods: simultaneous multi-color acquisition with low crosstalk and fast DNA-PAINT imaging with an increase in the localization precision of the single molecules. In the future, such a combination can potentially enable multi-color live-cell super-resolution imaging.

In my view, the knowledge in molecular biology will continue progressing in parallel with new developments in advanced light microscopy methods[166]. Another important trend in the field is the use of correlative approaches, where light microscopy is combined with genome sequencing[167–169], electron microscopy imaging[170,171], chromatin conformation capture methods like Hi-C[168] or other biochemical measurements[172] (**Figure 57**). These methods will help to determine the structure of chromatin at its different scales and tackle one of the core and most difficult questions in the field that is the connection between structure and physiological function. In particular, the correlative super resolution electron microscopy techniques (CSREM) provide structural information with sub-nanometer resolution and specificity at the protein level (**Figure 57c**). For the case of light microscopy and biochemical methods, one of the main advantages is the connection between single cell and population-based measurements. Furthermore, SMLM, contact maps and computational methods can be used together[167,173] (**Figure 57a, b** and **d**). In addition, other correlative approaches has been recently developed like SMLM and Atomic Force Microscopy (AFM)[174], which measures the precise spatial localization of single molecules together with high-resolution AFM images in a biologically relevant context, establishing a connection between the structure at the nanoscale level and the physiological function. Our fm-STORM and fm-DNA-PAINT approaches could be also combined with the methods described above, to increment the number of specific biological targets.

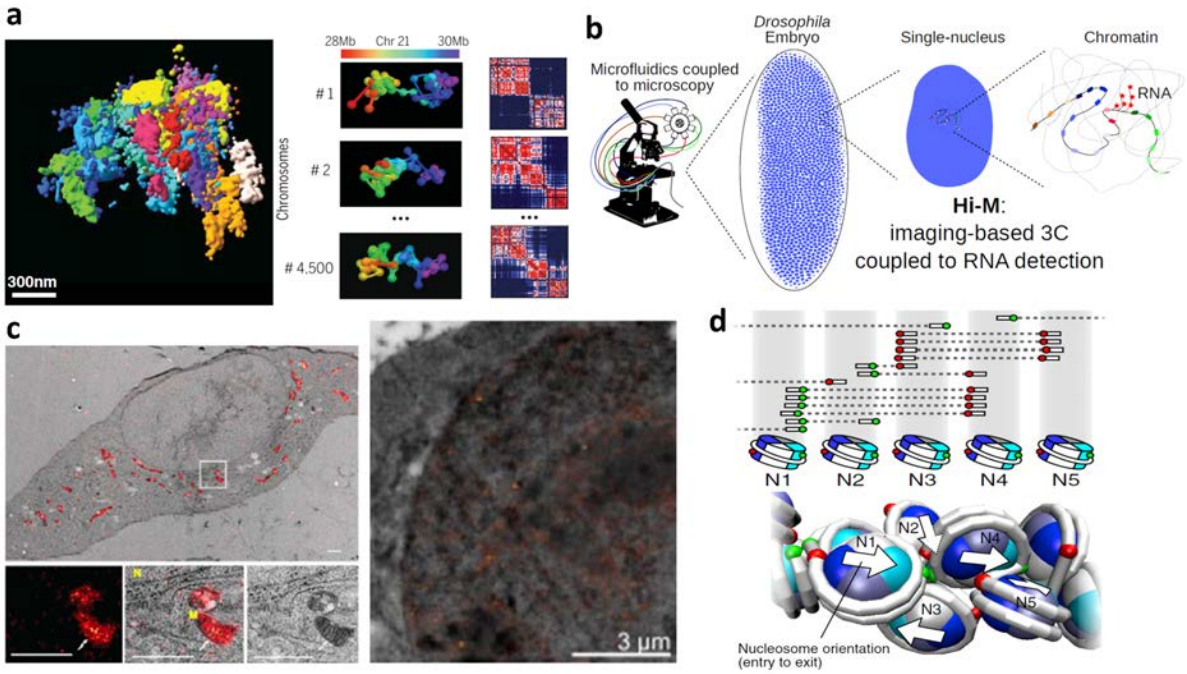

Figure 57. An overview of light microscopy correlative approaches to study chromatin. a) Chromatin Tracing is a method to image a piece of the chromosome of 30Mbp by sequentially imaging segments of 30kbp with localization-based microscopy. It allows single-cell measurements and population-based. The information of the distance maps is directly comparable with contact maps, showing chromatin domains at different scales. Instead of measuring the interactions, chromatin tracing measures the spatial distance. Adapted from [169]. **b)** Hi-M is another localization-based microscopy approach able to measure both gene expression and chromatin conformation at an specific locus. Adapted from [168]. **c)** Correlative approaches of super resolution and electron microscopy provide sub-nanometer resolution and specificity. On the left, EM image of the nucleus overlapped with SR image of mitochondria. On the right, EM image of the nucleus overlapped with SR image of H2B histone to study chromatin structure. Adapted from [171,175]. **d)** Hi-CO genome mapping combines modeling with biochemical measurements to study the hierarchical chromatin architecture at the nucleosome scale. It revealed distinct nucleosome folding motifs in the yeast genome like α-tetrahedron, β-rhombus and other motifs related with epigenetic modifications. Adapted from [172].

Finally, SMLM has been demonstrated to be a powerful tool for the visualization of cellular structures with unprecedented spatial resolution (typically 10-20nm for 2D imaging). But, in order to further extract quantitative information, cutting-edge data analysis for each cellular context must be applied to process the super resolved images[11,36,176–178]. The future of SMLM also goes through the development of new computational methods for the analysis of SMLM data. In that context, turning super resolution microscopy into a more quantitative method, with the ability to precise counting of molecules is a main objective of the field[179,180].

In summary, the new technical developments in microscopy and the new approaches that combine them with other techniques coming from biochemistry or computation will shed light into a large number of unknowns of molecular biology. They will allow scientist to connect the different scales and decipher the whole picture of hierarchical mechanisms that govern the function of a cell. In particular, I envision advanced microscopy methods to be essential quantitative tools for a complete understanding of one of the most important remaining question in the field: how gene regulation works.

5.2 Single Molecule Tracking (SMT) for studying transcription and chromatin dynamics

Single Molecule Tracking of proteins in the nucleus of live cells with high spatiotemporal resolution was not possible until very recently[83]. It came with the advent of new fluorescent dyes that are bright and small enough, and permeable to the cell membrane and with the development localization-based microscopy methods. It has revolutionized the field of molecular biology, since for the first time, researchers are able to observe and quantify dynamics at the single molecule level, without restraining to ensemble measurements of populations with methods like FRAP. Another recent alternative techniques capable of monitoring chromatin dynamics are FLIM-FRET Microscopy[181], where the level of chromatin compaction at different chromosomal regions can be measured and monitored dynamically with high precision and nanoscale resolution, but the 3D motion of chromatin is not captures, or Hi-D[38], that is able to reconstruct a map of chromatin movement as an optical flow field from a series of confocal fluorescence images, but is not able to measure single nucleosome dynamics.

Still, given its single protein and highly quantitative capabilities, nowadays a growing number of scientist are using SMT for a wide variety of distinct applications. It has been proven that in the case of sparsely labeled scenarios, SMT outperforms the rest of the available methods[38]. Transcription, for example, is regulated at multiple levels, including the structure of chromatin and the dynamic binding of transcription factors to their target promoters. Thanks to the quick technological progress of SMT methods, we are gaining profound insights into the mechanisms of gene regulation via chromatin structure and transcription factor dynamics[182]. With the ability to label and track specific proteins and gene locus simultaneously in live cells, we can observe and measure the physiological events that happens before, during and after transcription at the single molecule level.

In these recent years, SMT allowed to characterize the behavior and elucidate important mechanisms related with chromatin organization and gene transcription. It is important to note that a detailed characterization of chromatin dynamics is required as a benchmark in order to study its interactions with DNA-Binding proteins, which ultimately regulate the entire gene transcription machinery. Recently, it has been shown that chromatin domains are dynamic and its mobility correlates with the relative position of each specific region inside the cell nucleus and with the chromatin state[43] (**Figure 58**).

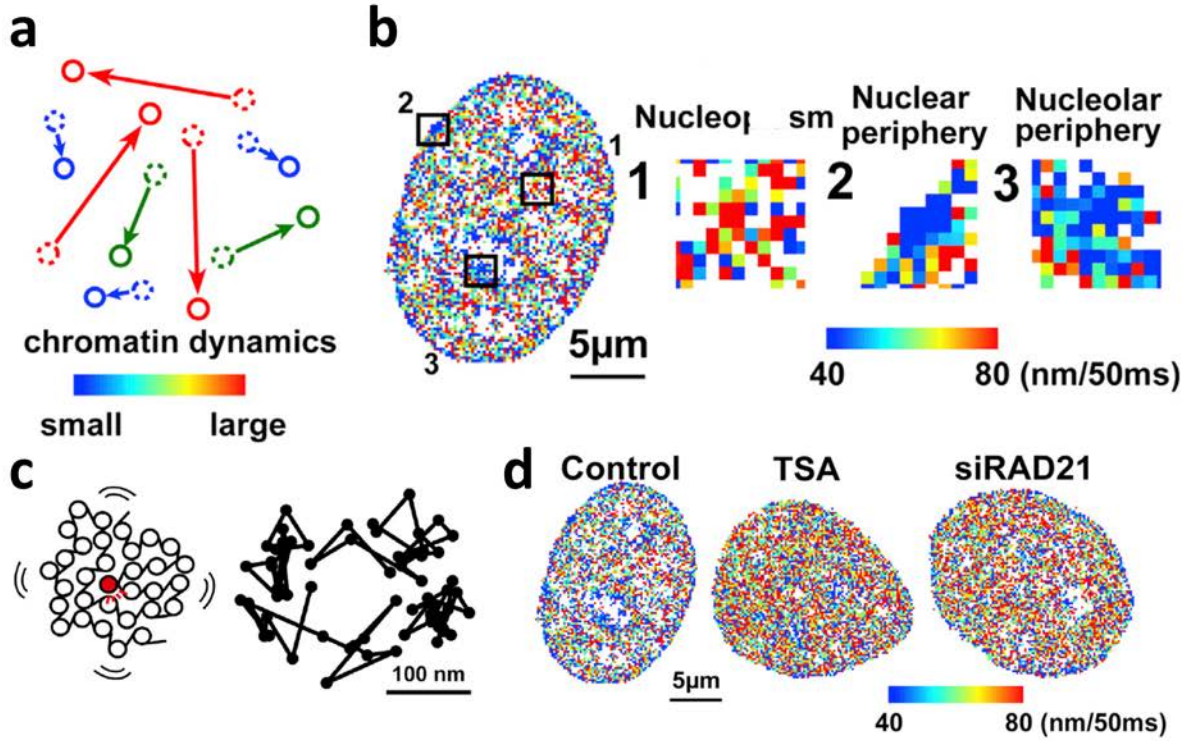

Figure 58. Chromatin domain dynamics measured with SMT. a) Chromatin dynamics at the single nucleosome level are defined by measuring the frame to frame jump size of individual nucleosomes. **b)** A scheme for the calculation of heat maps of chromatin dynamics and an example nucleus. **c)** A cartoon representing the mobility of chromatin domains and the trajectories obtained from SMT of single nucleosomes. **d)** Chromatin mobility heatmaps for HeLa (control), TSA-treated, and RAD21-KD cells. Adapted from [43].

In addition, the interaction of transcription factors with chromatin at the single molecule level was recently reported. The nuclear exploration of Tet repressors (TetRs) was measured with SMT (**Figure 59a**). It was found that their target search mechanism is based on 3D diffusion interspersed with transient interactions with non-cognate sites of chromatin (**Figure 59b**). The distribution of the residence times of nonspecific interactions is broad, so that the distinction between specific and nonspecific protein-chromatin interactions in terms of duration is not apparent. In addition, it is thought that the searching process is determined by the low association rate to nonspecific sites, rather than free diffusion[183] (**Figure 59a** and **b**). Multifocus SMT comes with the ability of imaging 9 focal planes simultaneously at the expense of photon flux per fluorophore reduction, since an optical grating splits the emission fluorescence signal into 9 different paths[92,184]. The combination of this method and ChIP-exo mapping was used to study the association of Sox2 and Oct4 to their enhancer in ESCs (**Figure 59c**). They found that there is a hierarchy in the process of enhanceosome assembly where Sox2 is favored to engage the target chromatin site first, followed by assisted binding

of Oct4[92]. In addition, they confirmed that Sox2 target search consist on both 3D diffusion and 1D sliding along open chromatin (facilitated diffusion)[92] (**Figure 59d**).

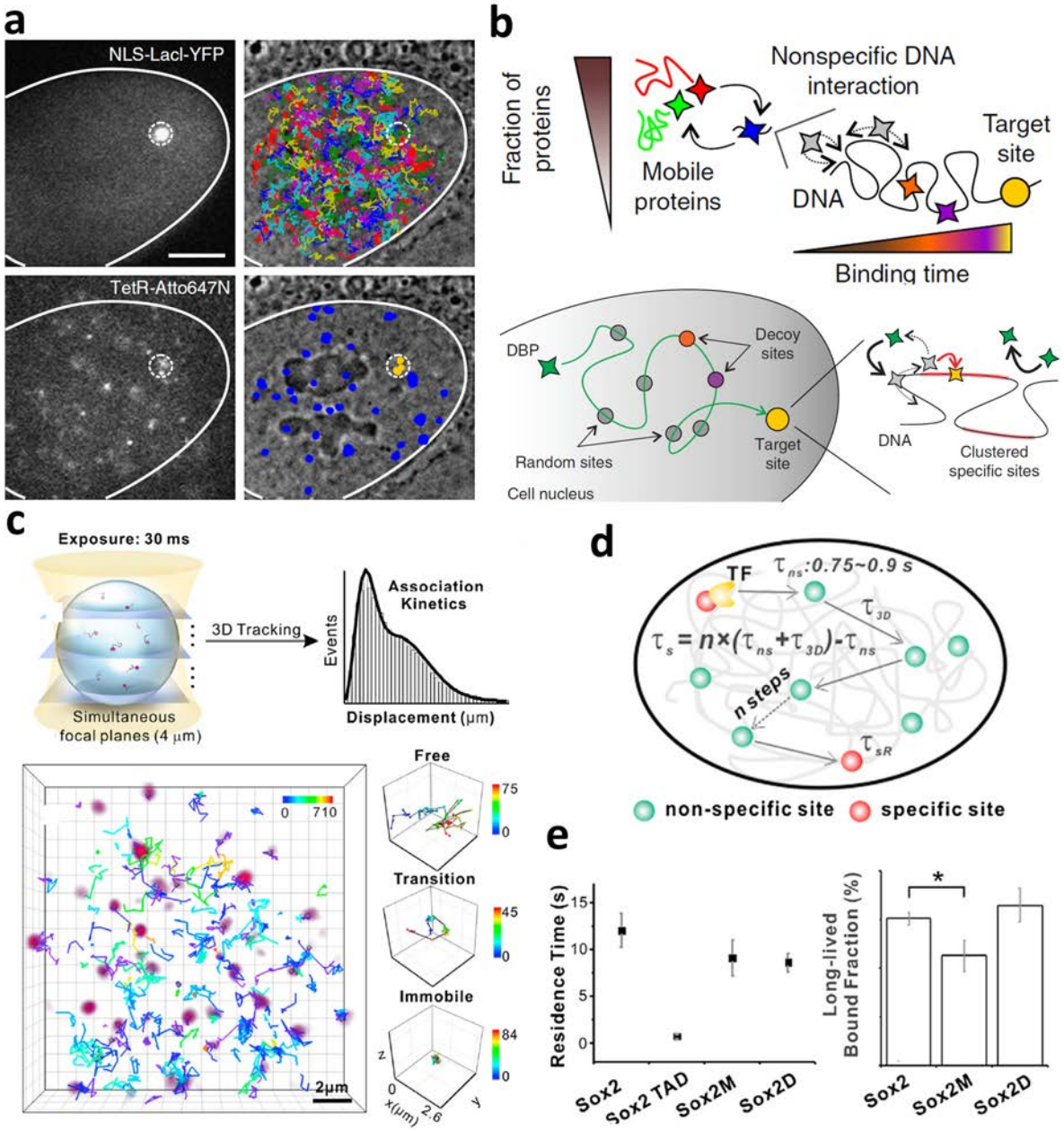

Figure 59. Nuclear exploration and interaction with their binding sites of TetR and Sox2 transcription factors measured with SMT. a) Images of LacI locus and Tet repressor protein (TetR) nuclear exploration. In the bottom right subpanel, blue dots represent unspecific binding sites and the yellow, specific interactions of TetR with chromatin. **b)** Top panel shows a scheme of TetR target search strategy, where the fraction of protein behaving in a certain manner and the binding time (or

chromatin affinity) are represented. Bottom panel shows a scheme with the general DNA Binding Protein (DBP) target search mechanism, alternating between free 3D diffusion in the nucleus and unspecific binding to chromatin and sliding motion. Adapted from [183]. **c)** Sox2 transcription factor association to chromatin kinetics measured with 3D multifocus SMT. Top left panel shows a scheme with the experimental microscopy approach for the association kinetics. Bottom panel shows a rendering of a nucleus with the Sox2 3D trajectories and three examples of different behaviors presented in the motion of the TF. The frame to frame jump histogram was computed for the ensemble of each population and fitted with a mathematical model to extract quantitative information about association kinetics (searching time, searching efficiency, diffusion coefficients, etc) (top right panel). **d)** A drawing with a representative model of TF target search that sustains the measurements. **e)** Results obtained from 2D SMT at long exposure times to measure the dissociation kinetics by fitting a double exponential decay curve to the survival distribution of the tracks. Sox2 and different Sox2 constructs with mutations on the DNA-binding surface (Sox2-TAD, Sox2M, Sox2D), have different residence times and stable binding percentage. Adapted from [92].

Finally, with 2D SMT assays and new analytical methods for SMT data analysis based on asymmetry coefficient of the angles of the protein trajectories, it was found that different DNA-binding proteins present different target search strategies[136] (**Figure 60**). While c-Myc behaves like a global explorer, P-TEFb behaves like a local explorer[136] (**Figure 60a**). That implies that c-Myc would be equally distributed around every chromatin site, while P-TEFb would present a heterogeneous spatial distribution in the nucleus, so for each P-TEFb protein, the efficiency of the chromatin target search depends on its initial position[136] (**Figure 60b** and **c**). They propose a model in which the local environment (the local chromatin structure) influence on the dynamics of TFs[136] (**Figure 60b**).

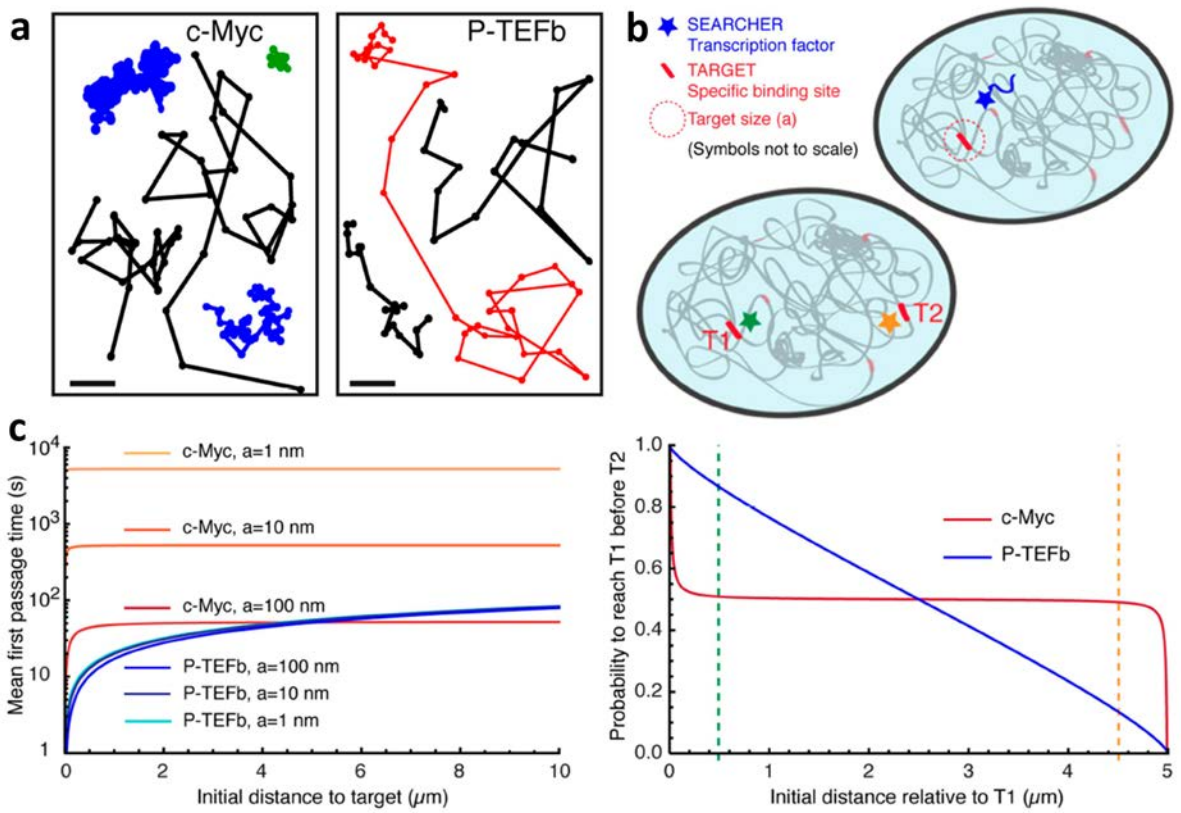

Figure 60. SMT reveals that two DNA-Binding Proteins (c-Myc and P-TEFb) present distinct target search strategies in the nucleus. a) Some examples of trajectories of c-Myc (local explorer) and PTEF-b (global explorer). **b)** A drawing representing the global explorer and its target (right) and the local explorer with two target (left). **c)** Two graphs representing the Mean first passage time (MFPT) as a function of the initial distance to the target, and the Probability of interaction with target 1 before interacting with target 2, as a function to the relative distance between the searcher and the targets, for both c-Myc and P-TEFb transcription factors. Adapted from [136].

However, how to integrate all those measurements related with chromatin and gene transcription into one single picture is not clear. Even some of the main results and conclusions arising from SMT experiments are partially discrepant[44], especially those ones regarding the binding-unbinding rates and the bound-to-unbound fraction of TFs[44,48,92,185–187], the TFs strategy to efficiently reach their specific target site[81,92,136,188–190], or the chromatin physical state that determines its structure and behavior[191,192]. In my view, a full characterization of chromatin dynamics at its different scales will serve as a benchmark to make the SMT measurements of TFs more meaningful. In addition, it will allow to relate those in vivo findings from SMT with modeling of chromatin and TFs dynamics[193] and with the new models of chromatin organization, like the recently proposed liquid-liquid phase separation structure (LLPS)[194]. In our project, we provided new measurements and quantifications to characterize and correlate chromatin dynamics and structural properties at

the single nucleosome level (**Figures 42, 46, 50, 52** and **54**). We observed that TFs like Oct4 and CTCF present a more mobile motion than H2B and a bigger proportion of tracks combining confined and Brownian/directed motion, which we called "butterfly" motion. Those trajectories could correspond to TFs interacting with chromatin while searching for their target site and therefore they should be analyze deeply in future works. Furthermore, we measured the dynamics of single nucleosomes during the process of cell differentiation, showing that this motion corresponds to local nucleosome dynamics rather than large chromatin domain motion, since large regions of chromatin, like Telomeres or Centromeres, composed of 100-750 nucleosomes, present slower mobility than single nucleosomes at the millisecond time scale. This suggest that, like chromatin structure, chromatin dynamics also happen at multiple scales. In order to fully connect chromatin structure, dynamics and function, those relations, from the single nucleosome level to the whole chromosome, passing by the mesoscale level and the gene level, must be bridged.

Another current limitation of the SMT field is the lack of robust and standardized analytical methods to extract quantitative information from the experiments. The guidelines for the experimental side of the SMT field are well established and the technical limitations are well known. Short track length, irreversible photo bleaching, reversible photo switching, drift of the microscope stage, limited SNR due to background or low fluorophore signal or an excessive number of molecules on the field of view that hinders the precise localization of the diffraction limited spots. I expect all those to be progressively overcome by the design of better probes, the improvement of microscope set-ups, the increase in camera sensitivity, the establishment of new labelling strategies and the appearance of new experimental procedures[186]. However, how to extract quantitative information from the recorded data is still under revision. Nowadays, it is a common practice that each group develop their own algorithms and codes to tackle each specific biological problem. This scenario hinders the comparison of the results coming from different researchers and the connection between SMT and other measurements from other fields. There is a necessity to standardize robust analytical methods so that quantitative results arising from SMT experiments are more meaningful. There are already some basic tools, like the Mean Square Displacement (MSD) that were established during the late 20th for the study of solid particles diffusing in liquid mediums[87,195–199], and that can be directly applied to study protein motion in the cell nucleus. However, this new context requires new solutions, since the nucleus is a complex environment where anomalous diffusion and interactions of different nature, like electrostatic, mechanical, chemical or volume exclusion interactions, are constantly happening between biomolecules. To resolve this issue, new computational models of chromatin (**Figure 61a** and **b**) and their relation with the dynamics of chromatin loci and transcription factors[200], new algorithms to analyze the data[201], like Bayesian approaches for connecting the dots of the trajectories[202] or new analytical tools to study molecules motion under weak ergodic conditions[85] (**Figure 61c**), are being developed.

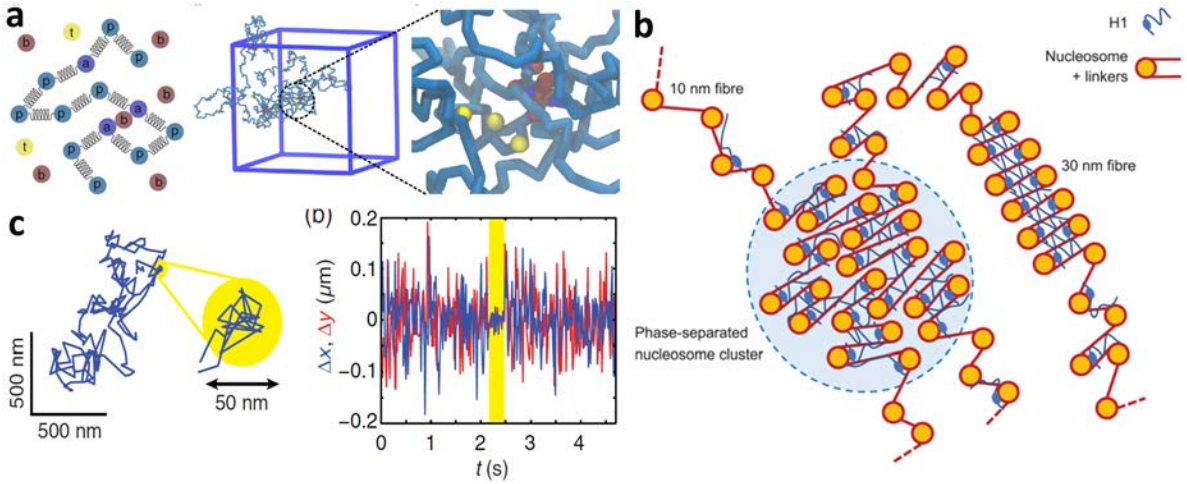

Figure 61. Perspectives of computational modeling and SMT data analysis methods for the quantitative study chromatin and transcription. a) Chromatin polymer model and computational simulation to study the target search strategy of DNA-Binding proteins (DBPs). The model is setup with polymer (p) and anchor (a) particles, connected by harmonic springs. Binders (b) are introduced to generate bridges between anchor particles, forming loops. Finally, Tracers (t) interact non-specifically with both the polymer (p) and the anchor (a) particles[203]. **b)** A drawing that represent a model where chromatin is condensed into different states facilitated by the presence of linker histone H1. Chromatin forms compact phase-separated domains that corresponds to the clutches observed with localization-based microscopy. Adapted from [191]. **c)** A method to analyze the motion of biomolecules in a fractal environment. Left panel shows an example of a trajectory exhibiting dynamics at different time scales, with a short-lived transient immobilization event (highlighted in yellow). Right panel the x (blue) and y (yellow) frame to frame jump displacements**.** The transient interaction correspond to a decrease in the size of the displacements. Adapted from [85].

In our project, we provided a benchmark for the connection between experimental data obtained from localization-based microscopy and complex state of the art modelling of chromatin. The analysis of SMLM simulated images from the chromatin fiber models of ESCs and NPCs recapitulated the tendencies measured experimentally and allowed us to test the impact of different parameters (acetylation, levels of linker histone and nucleosome free regions) on nucleosome clutch formation. For example, we saw in the models that the nucleosomes are arranged in discrete heterogeneous groups (previously named clutches[11]) and that Nucleosome Free Regions (NFRs) are essential for the formation of those clutches. In the future, it would be interesting to validate this prediction of the model by varying NFR in a controllable manner within the chromatin fiber. Such experiments will require the development of more precise tools that can allow modifying one aspect of nucleosome organization (e.g. amount of NFRs) without affecting other aspects. Furthermore, in our models, the number of nucleosomes per clutch, which is a measure of local chromatin compaction, correlates with cell pluripotency following the same trend as the experimental

data, but the absolute values of the number of nucleosome per clutch obtained from the experiments were slightly underestimated.

In summary, the recent technical developments have allowed tracking single molecules in the nucleus of live cells with high spatial and temporal resolution. However, until now, the SMT measurements provided just a collection of sparse findings. In order to understand large and complex biological processes, like the dynamic conformation of chromatin structure and its relation with gene transcription, apart from the improvement of the experimental methods, the field still needs to establish a benchmark for quantitative and meaningful probing. From my point of view, the most important steps to achieve it are a deep characterization of chromatin at the different spatiotemporal scales and the development of a framework of standardized and robust algorithms to extract comparable information from the experimental data.

Detailed Methods

DM1.1 Frequency multiplexed Super Resolution Microscopy

Sample preparation for fm-DNA-PAINT and fm-STORM:

BSC1 cells were cultured at 37ºC with 5% CO_2. Cell culture consisted of complete growth medium (Minimum Essential Medium Eagle with Earle's salts and nonessential amino acids plus 10% (v/v) FBS, 2 mM L-glumine, and 1 mM sodium pyruvate). For the imaging experiments, cells were plated on 8-well Lab-Tek 1 coverglass chamber (Nunc) at a seeding density of 20000–50000 cells per well. After 24 hours of incubation, cells were fixed with fixation buffer consisting of 3% paraformaldehyde and 0.1% of glutaraldehyde in PBS at 37ºC during 10 minutes. The background fluorescence of glutaraldehyde was quenched by 0.1% of $NaBH_4$ solution in PBS during 7 minutes at room temperature. After fixation, blocking buffer solution was applied (3% (w/v) BSA, 0.2% TritonX-100 (Fisher Scientific) (v/v) in PBS) for 60 minutes.

For immunofluorescence, cells were labeled with the appropriate primary and secondary antibodies. For fm-DNA-PAINT, rabbit-anti-alpha-tubulin primary antibody (ab18251 Polyclonal, AbCam) at a dilution of 1:150 and mouse-anti-TOM20 primary antibody (WH0009804M1 Monoclonal, Sigma Aldrich) at a dilution of 1:150 in blocking buffer were used to label microtubules and mitochondria, respectively. For secondary antibodies, oligo-functionalized goat- anti-mouse (1:100 dilution in blocking buffer) and goat-anti-rabbit (1:100 dilution in blocking buffer) secondary antibodies included in the Ultivue-2 kit (Ultivue, Inc) were used. For fm- STORM, rabbit-anti-TOM20 (sc-11415, Santa Cruz Biotechnologies) and rat-anti-alpha-tubulin (MAB1864-I, Clone YL1/2, Merck), primary antibodies were used at a dilution of 1:150 and 1:150 in blocking buffer to label mitochondria and microtubules, respectively. Donkey-anti-rabbit conjugated with Cy3b/AF405 and donkey-anti-rat conjugated with AF647/AF405 were used as secondary antibodies. The secondary antibodies were custom labeled with the fluorophore pairs as previously described[89]. The training dataset for the cross-talk correction algorithm implemented for fm-STORM was prepared and imaged in the exact same way with the exception that only one primary and appropriate secondary antibody was used to label a single structure. fm-DNA-PAINT was performed in an imaging buffer with high ionic phosphate strength provided in Ultivue-2 kit. fm-STORM was performed in an imaging buffer containing GLOX solution as oxygen scavenging system (40 mg/mL Catalase [Sigma], 0.5 mg/ml glucose oxidase, 10% Glucose in PBS) and MEA 10 mM (Cysteamine MEA [SigmaAldrich, #30070-50G] in 360mM Tris-HCl).

Optical setup:

Imaging was performed on a custom-built inverted Nikon Eclipse Ti microscope (Nikon Instruments). The excitation module is equipped with four excitation laser lines: 405 nm (100 mW, OBIS Coherent, CA), 488 nm (200 mW, Coherent Sapphire, CA), 561 nm (500 mW MPB Communications, Canada) and 647 nm (500 mW MPB Communications, Canada). The laser beams intensities were sinewave modulated through AOMs (AA Opto Electronics MT80 A1,5Vis) at different frequencies ranging from 50 Hz to 10 Hz, depending on the modality and on the imaging conditions. The different wavelengths were combined and coupled into the microscope objective through dichroic mirrors. The same objective (Nikon, CFI Apo TIRF 100x, NA 1.49, Oil) was used for illumination and for collecting the fluorescence signal. The focus was locked through the Perfect Focus System (PFS, Nikon). Fluorescence emitted signal then passed through a notch filter "Quad Band" (ZT405/488/561/647rpc-UF2, Chroma Technology) that blocks just the excitation laser lines. Imaging was performed on an EM-CCD camera (Andor iXon X3 DU-897, Andor Technologies). The pixel size after the 100X magnification was 160 nm.

We note that chromatic aberrations affect all super-resolution multicolor approaches that use spectrally different reporter dyes, including the frequency multiplexed imaging implementation reported here. Chromatic aberrations lead to a shift in the center position of the localizations between different channels that is on the range of tens of nanometers (~ 10-40 nm), depending on the wavelengths and the imaging conditions[204]. Fiducial markers like beads can be used to correct for this offset, and typically yield alignment precisions below or comparable to the localization precision[204].

fm-DNA-PAINT imaging conditions:

Imaging for fm-DNA-PAINT modality was performed using highly inclined (HiLo) illumination[62] with an excitation intensity of ~300W/cm^2 for the 561nm and 647nm laser lines. Camera frame rate of 60 Hz was used for the experiments with a field of view of 128x128 pixels (20 μm x 20 μm). The 647 nm and 561 nm lasers were modulated with sinusoidal waves at 30 Hz and 20 Hz, respectively. For 3D imaging, a cylindrical lens was used to encode the z position of the molecules into the PSF shape[67].

fm-STORM imaging conditions:

Imaging for fm-STORM modality was performed using HiLo illumination[62] with an excitation intensity of ~1.8kW/cm^2 for the 561nm and the 647nm laser lines, and ~1kW/cm^2 for the 488nm laser line. The 405nm laser line was used in continuous illumination mode for the reactivation of the fluorophore pairs. The 405nm laser intensity follows a ramp (ranging from ~10W/cm^2 to ~25W/cm^2), in order to maintain a relatively constant density of fluorophores per frame. Camera frame rate of 90 Hz was used for the experiments with a

field of view of 128x128 pixels (20 µm x 20 µm). 647 nm and 561 nm lasers were modulated with a sinewave at 45 Hz and 22.5 Hz. For the 3-color data sets, the 647nm, 561nm and 488nm lasers were modulated at 45 Hz, 30 Hz and 15Hz, respectively.

fm-DNA-PAINT data analysis:

Demodulation of the raw data was carried out using a custom written Pyhton code (available at https://github.com/PabloAu/Excitation-multiplexed-multicolor-super-resolution-imaging-with-fm-DNA-PAINT-and-fm-STORM). For the demodulation, packages of 6 frames (frame window size, *m*) were used in order to maintain the long effective exposure time required for DNA-Paint (we chose 100 ms). The intensity evolution of each pixel from these 6 frames were transformed to the frequency domain using a one-dimensional Discrete Fourier Transform for real input:

$$X_k = \sum_{n=0}^{m-1} x_n \cdot e^{-i2\pi k \cdot \frac{n}{m}}; \quad k = 0, \dots, m-1,$$

where, X0,…,Xm-1 are the Fourier Transformed output values in the discrete frequency domain, x0,…,xm-1 are the real discrete input values from time domain, and *m* is the total number of real input values (equal to the frame window size).

The Discrete Fourier Transform presents symmetry. X0 and Xm/2 are real values. The rest of the output values from the DFT are specified by (m/2)-1 complex numbers, because the remaining output values are the conjugated ones. Therefore, a 6 frame window size (*m* = 6), will provide 3 frequency bins and thus 3 available channels (**Figure 25**). The X0 corresponds to DC component and contains no valuable information, while the AC components encode the amplitudes at which the fluorophore absorbs each excitation laser, and hence reveal the spectral characteristics of that localization.

For this calculation, we used the efficient Fast Fourier Transform algorithm (FFT). The absolute values of the amplitudes in the frequency domain were used to assign a pixel value to its channel on the demodulated data, corresponding to each frequency bin in use. With a frame window of 6 frames and a camera frame rate of F=60Hz, we had 30Hz, 20Hz and 10Hz frequency bins available. We obtained the demodulated data for two channels, corresponding to 30 Hz (for 647 nm channel) and 20 Hz (for 561 nm channel). Insight3 (a kind gift of Bo Huang, UCSF) was used to localize the fluorescent molecules in each channel of the demodulated frames by performing a simple Gaussian fitting (2D) or elliptical Gaussian fitting (3D) as previously described[67].

Given that the percentage of correct fluorophore assignment was always higher than 96% for fm-DNA-PAINT, a crosstalk correction step was not required. Nevertheless, a simple additional step can be used to further reduce the crosstalk (**Figure 23**). In this step, localizations in both color channels were identified if they appeared in the same frame within a distance of 80 nm. We computed the sum of intensity values within a 3x3 pixels subROI

around the center of each of these localizations in the demodulated data and compared the intensities between both channels. Since the integrated intensity is directly related to the amplitudes of the frequency bins in the frequency domain, we used this information to assign the localization to the correct color channel. This step further reduces the crosstalk to less than 1% in the Cy5 channel and less than 3% in the Cy3 channel (**Figure 23**).

Localization precision calculation:

We determined the localization precision in two ways. First, from the experimental data we measured the standard deviations of clusters of localizations originated from a single fluorophore[52,67]. To generate traces over several frames of the same fluorophore, a spatial threshold between consecutive frames of 55 nm was set. A minimum track length of 8 frames was set in order to have enough points to properly estimate the localization precision (**Figure 24a**). Second, we calculated the localization precision by obtaining the Cramér-Rao lower bound (CRLB) of the *x* and *y* position parameters from the Maximum Likelihood Estimation Gaussian 2D fitting of the single molecules, as previously described[63]. We used the software provided in reference[63] and followed the suggested procedure. We estimated a σ_{psf} of around 1 pixel, so we used a box size of 7x7 pixels ($2x3\sigma_{psf}$ + 1) around each localization. We calculated first σ_x and σ_y and then the x-y localization precision (**Figure 24b**) by:

$$\sigma = \sqrt{\sigma_x^2 + \sigma_y^2}$$

For fm-DNA-PAINT, 2 sine-wave modulated lasers were used with a maximum laser power of ~300W/cm^2 and an exposure time of 16 ms. For regular DNA-PAINT a continuous illumination with constant laser power of ~300W/cm^2 with an exposure time of 100 ms was used. The somewhat lower localization accuracy of fm-DNA-PAINT as compared to regular DNA-PAINT is simply due to the fact that we use modulated excitation, so that fluorophores are excited half of the duration of a single frame, and thus emit roughly half of the photons compared to continuous excitation. Note that given the low laser power excitations used for fm-DNA-PAINT, the SNR could be increased and the subsequent localization precision could be improved, simply by increasing the laser powers.

The localization precision for fm-STORM data was estimated following the first approach since it accounts for the experimental conditions and it is well-accepted in the literature[52,67].

Synthetic data:

We first generated sinewaves for each channel frequency (f), depending on camera frame rate (F) and frame window size (m). The sinewaves were then integrated within the time limits of consecutives frames to obtain an effective integrated intensity per frame (**Figure 27b**). We used this information to generate synthetic data, taking as input a 5x5 pixels subROI of a PSF from one frame of single-color experimental data. Then, 5x5 pixels stacks were generated by multiplying the PSF by the effective integrated intensity per frame over several consecutive

frames. In this way, we could simulate the emission of a fluorophore under sinewave modulated illumination. **Figure 27** shows a comparison of the intensity evolution over time of 2-color synthetic data with that of 2-color fm-DNA-PAINT experimental data, showing excellent agreement between synthetic and experimental data and validating our approach. We followed a similar procedure for generating the 5-color synthetic data (**Figure 28** and **29**). In that case, we used f_i =50Hz, 40Hz, 30Hz, 20Hz and 10Hz, F=100Hz and m=10. The 5 different types of PSFs were spatially mixed, such that spatial overlap could occur. We ranged the spatial distances between the centers of each PSF from 20 pixels (for non-overlapping conditions) to 0 pixels (i.e., full spatial overlap). Note that this synthetic data has been generated under the assumption of spectrally distinct fluorophores and have minimum overlap in their absorption spectra.

Semi-synthetic data:

A 5x5 pixels stack over 6 consecutive frames around the center of a PSF from the fm-DNA-PAINT experimental data was extracted. We performed this procedure for the two different color-fluorophores. In the experimental data, the 647nm laser was modulated at f = 30 Hz for Cy5, and the 561 nm laser was modulated at f = 20Hz for Cy3. Those 5x5 PSFs were replicated 168 times per color, and spatially distributed in order to generate semi-synthetic stacks of images. Several stacks were created, with different relative distances between the centers of the PSFs of both color channels (**Figure 31a**), ranging from +4 pixels to -4 pixels for spatially overlapping fluorophores and +5 pixels or larger (or -5 pixels or smaller) for the non-overlapping ones. An example of the semi-synthetic data is shown in **Figure 30**. In order to generate the background that also fluctuates with the sine-wave modulated lasers illumination, we took a similar 5x5 pixels stack over the same 6 consecutive frames of the experimental data on a background region, i.e., devoid of fluorophores. We then added the background associated to each frame in the corresponding synthetic frame.

The 6-frame semi-synthetic stacks were demodulated to generate 2 demodulated frames, one per channel. Then the centers of the PSFs in those demodulated frames were localized by fitting a 2D Gaussian and the distances from the retrieved localization positions (x,y) to the real, simulated positions (the pixel where the center of the PSF was positioned) was computed ($D_{relative}$ in **Figure 31**). Plots of $D_{relative}$ as a function of spatial overlap (D_{shift}) were generated to estimate the effect of Cy3 spatial overlap on the Cy5 channel (**Figure 31b**) and effect of Cy5 spatial overlap in the Cy3 channel (**Figure 31c**). Moreover, to estimate the effect of fluorophore brightness on the perturbations to the localization positions for spatially overlapping fluorophores (set to +3pixels), we generated stacks by varying the relative brightness of one color-fluorophore with respect to the other. For this, all the pixels within the 5x5 PSF corresponding to Cy3 (561nm channel) were multiplied by a reduction a factor ranging from 0.5 to 1 (**Figure 32**).

fm-STORM data analysis:

Background was subtracted using a median filter. Fluorescent molecules were localized in the raw data using Insight3 and performing a simple Gaussian fitting. Localizations were subsequently classified as single-frame or multi-frame localizations. If a fluorophore that appeared in one frame did not move by more than half a pixel (80 nm) in the subsequent frame, it was taken as the same fluorophore and classified as multi-frame. A frame window size was chosen for the demodulation, depending on the desired number of channels and imaging conditions. We used a 4 frame window size for 2-color imaging and a 6 frame window size for 3-color imaging. A 4x4xm voxel region around the centroid (x,y,f)→(x,y,f+m) coordinate of a localization was sliced from the background-suppressed camera data. First, we calculated the mean intensity value of the 16 pixels in the subROI for each raw frame within the frame window, from which we end up with a m-length vector of time-domain data. On these data we performed a one dimensional discrete real-valued Fourier Transform, which yields (m/2) AC components and 1 DC component in the frequency domain. We used the Python's rfft function from scipy.fftpack[205]. Lastly, the absolute values from the FFT for the different frequency bins on the frequency domain were calculated and recorded. Based on the natural logarithm of these values, the localizations were classified into a specific channel. We used the natural logarithms of the demodulated amplitudes rather than the raw values; the distributions of the latter are highly skewed with amplitudes clustered near the origin, while the distributions of the former are more symmetric and can be approximated to first order as rotated asymmetric normals. To perform the channel assignment, decision boundaries were generated by a machine learning algorithm based on a support vector classifier (SVC) (see below Machine learning algorithm for crosstalk correction). The performance of an SVC is typically improved with standard-scaled data that has mean=0 and standard deviation=1, but we find that scaling the amplitudes of our data using only a natural logarithm yields very good results.

Machine learning algorithm for crosstalk correction:

Training data sets were acquired using one-color biological samples, which were labeled with the same dyes used for the two-color imaging and imaged in exactly the same way as the two-color samples. The training data was demodulated and the intensities around the localizations corresponding to 4 x 4 pixels subROI were used to define 2D decision boundary regions for those two dyes. The same procedure can be applied for three or more colors. The boundary regions were defined using an SVC. In particular, we used the SVC class contained in the Scikit-learn[206] Python package, which uses libsvm and liblinear libraries[207,208] for the computations. SVC are well established supervised learning methods used for classification in high dimensional spaces, using training data points in the decision function (called support vectors) and that can use different kernel functions to construct the decision function. Therefore, it can perform multi-class classification on a dataset, taking two inputs: the training

datasets and the sample data. SVC implements the one-against-one approach[209] . We used the Radial Basis Function (RBF) as kernel function defined by the following equation:

$$K(x_i, x_j) = e^{-\gamma \cdot \|x_i - x_j\|^2},$$

where x_i and x_j are the support vectors and γ defines how large the influence of a single training example is. We used γ parameter in "auto" mode. SVC uses training datasets vectors x and an array of class labels y as inputs. The boundary regions are generated by the decision function:

$$sgn(\sum_{i=1}^{n} y_i \alpha_i K(x_i, x) + \rho),$$

where ρ is the independent term and the α_i are coefficients between 0 and C[209]. C is an input parameter that trades off misclassification against simplicity of the decision boundaries. We used a fixed value of C=1.0. For generating the boundary regions and the fluorophore classification of the multi-color images, we identify and eliminate data that correspond to localizations which appear in only a single frame in the N-frame demodulation window. These localizations are readily identified by recognizing that a single-frame event in the time domain is effectively a Dirac function, which has a uniform distribution of amplitudes across the frequency domain, and hence will appear along the equal-amplitude y=x line in a two-color measurement and the equivalent functions in higher-dimensional space. Furthermore, these single- frame events typically have low amplitudes relative to multi-frame events, and so appear in a distinct region of the log-log amplitude plot compared to multi-frame events. This undistinguishable population of localizations appeared with a circular shape centered around (6,6) on the 2D single-frame localizations diagram that plots the logarithm of the intensities. We used a rejection radius of 0.8 to reject these localizations. We also eliminate a subset of localizations that appear along the equal-amplitude line with high amplitudes. These localizations appear in both the training data and the experimental data for multiple fluorophores, and so yield no distinct information about the species of molecule underlying that localization. This last step has an additional advantage of preventing the SVC from over-fitting during training. We defined an acceptance ratio parameter that can be changed accordingly from 0 to 1, to achieve a compromise between the percentage of rejected localizations and the final crosstalk between different channels. We used an acceptance ratio of 0.96. The classifier was trained on a randomized sample of 60% of the total training data, with 20% reserved for cross-validation of the SVC and a further 20% used to generate performance scoring metrics.

fm-live:

We utilized an array of three continuous-wave lasers at 488 nm (Sapphire 150 mW, Coherent Inc.), 560 nm (500 mW, MPB Communications), and 647 nm (500 mW, MPB Communications), each modulated by its own acousto-optic modulator (all MT80-A1.5-Vis, AA Optoelectonics). The modulated beams are combined on appropriate dichroic mirrors and

relayed to the annulus of the back aperture of a 1.49NA obkective via a 400-mm focal-length lens located 400 mm from the back focal plane and a quad-band dichroic mirror (ZT405/488/561/647rpc-UF2, Chroma Inc.). This illumination configuration generates a highly oblique light sheet that is axially nearly diffraction-limited. Fluorescence from the entire objective field of view is transmitted through the major dichroic mirror and further spectrally filtered with an appropriate notch filter (ZET405/488/561/647m-TRF, Chroma Inc.) before being imaged onto a back-illuminated, cooled EMCCD (iXon Ultra 897 EMCCD, Andor Scientific). The frame clock signal from the EMCCD functions as the master clock for the AOM modulation signals.

Each AOM is driven by an 80-MHz carrier signal that is amplitude modulated at a fixed integer fraction of, and synchronized to, the camera frame clock: the 488-nm laser is modulated at f/2, the 560-nm laser is modulated at f/3, and the 647-nm laser is modulated at f/6. These frequencies are selected so that they are centered within the frequency bins generated by an FFT with a sampling rate equal to the camera frame rate clock and a number of time bins equal to twice the number of lasers. Because the data we record is purely real, by symmetry considerations the negative frequency components of the FFT are simply the complex conjugates of the positive frequency components, and so we save computational operations by only calculating the DC and positive frequency components, yielding a total of 4 frequency bins. The DC component is equivalent to the sum of all color channels, and is not used. Each other frequency bin nominally contains the signal from a single excitation laser.

We typically record living cells for up to 5 minutes per experiment at effective demodulated frame rates ranging from 15 to 25 Hz depending on the desired field of view, where a larger image size results in a slower frame rate. Significant photo-bleaching of the Mitotracker Far Red dye becomes apparent after a few minutes of imaging at the optical powers that we use, while the photobleaching in the microtubule and lysosomes channels is moderate.

The data presented thus far was recorded at low excitation powers and with maximum detected photon fluxes of fewer than 600 counts per pixel integrated over all color channels, implying that our approach is compatible with live-cell imaging. We used living BS-C-1 cells stably expressing eGFP-alpha-tubulin (microtubules) and mCherry-LAMP1 (lysosomes) and additionally labeled mitochondria with MitoTracker Deep Red FM to obtain three different colored organelles. We imaged the cells for five minutes with three excitation wavelengths (488, 561, and 640 nm) and detected the fluorescence using an EMCCD camera operating at a frame rate of 90 Hz. With $N = 3$ excitation lasers we selected blocks of $2 \cdot N = 6$ camera frames and demodulated the data on a pixel-by-pixel basis. The resulting images from each demodulated image block have a temporal resolution of 1/6 the camera hardware frame rate, which is only a factor of two slower than the limit using sequential excitation. However, the advantages gained by this frequency-domain approach are that motion discretization artefacts

are greatly limited because the data are acquired continuously, together with an additional factor of $2N/2$ less noise than an equivalent time-interleaved excitation. Representative demodulated images of microtubules, lysosomes, and mitochondria are shown in **Figure 39**, respectively, together with zoom-ins at various time-points across all three channels. The simultaneously obtained multicolor movies display the rich and different dynamics of each organelle without any visible photo-toxic effect on the cells, demonstrating full compatibility of this technique for imaging living cells with high temporal and spatial resolution over long time periods.

DM1.2 Mesoscale chromatin modelling

Mesoscale modeling of mESC and mNPC chromatin fibers:

To simulate fibers representative of chromatin in mouse embryonic stem cells (mESC) and neuronal progenitor cells (mNPC), we analyzed publicly available data to determine nucleosome positions, linker histone (LH) density, and histone-core tail acetylation levels. We consider the Oct4 genomic region, known for being upregulated in non-differentiated cells. We simulate the region of Chr17 spanning 35626358bp to 35657661bp (corresponding to mm9 reference). The Oct4 chromatin fiber length is ~31 Kbp and contains 121 nucleosomes in mESC and 151 nucleosomes in mNPC.

Nucleosome positions were obtained from the database NucMap[210], that includes the analysis of 798 experimental MNase-Seq data from 477 samples across 15 species. We used the nucleosome positions obtained with the DANPOS algorithm[211] on the MNase-Seq data of mESC and mNPC reported by Mieczkowski et al[124]. The list of linker lengths and nucleosome free regions (NFRs) for each system can be found in the Supplementary Information excel file. LH density was set to 0.5 LH per nucleosome for the mESC fibers, and to 0.8 LH per nucleosome for the mNPC fibers, as reported previously by Skoultchi and coworkers[122,128]. The LHs were distributed uniformly to fulfill these densities. That means 1 LH every 2 nucleosomes, and 4 LHs every 5 nucleosomes for mESC and mNPC, respectively. Based on immunofluorescence data (**Figure 43b**), the concentration of histone core tail acetylation of H3 and H4 was set to 10% for the mNPC systems and 15% for the mESC systems to reproduce the 1.5 ratio of acetylation levels in mESC versus mNPC. Since histone acetylation are distributed in clusters[127], we distributed the acetylated nucleosomes in both systems in two islands of similar size before and after the genes of interest. Specific positions of acetylation can be found in the Supplementary Information excel file (also shown in Supplementary Figure 1c for one of the islands).

The starting configuration of each fiber (**Figure 43b**) corresponds to the ideal zigzag conformation oriented with the fiber axis parallel to the z-axis, as we have shown this conformation to be the lowest energy[212]. We use our mesoscale chromatin model (**Figure 43a**) to simulate 30 independent trajectories of 80 million Monte Carlo (MC) steps for the Oct4 system. Briefly, our model combines nucleosomes, histone core tails, linker DNA, and linker histone by coarse-grained units at different levels of resolution to create oligonucleosome fibers. The model has evolved over 18 years and validated against growing experimental data[126,213–215]. The nucleosome core with wrapped DNA and without tails is treated as an electrostatic charged object, coarse grained from the crystal structure of the nucleosome core particle at 1.9 Å resolution[216]; its surface is represented with 300 Debye-Hückel pseudo-charges computed by our DISCO algorithm to approximate the electric field of the atomistic nucleosome obtained by the Poisson Boltzmann formulation[217]. Flexible

histone core tails are coarse grained with the Levitt-Warshel united-atom bead model[218] as 1 bead per 5 amino acids, and each bead charge is calculated by the DISCO algorithm[219]. Folded histone tails, mimicking acetylated tails, are modeled with increased stretching, bending, and torsional force constants by a factor of 100[220]. Linker DNA connecting nucleosomes is modeled by the Stigler worm-like chain model in which each bead represents ~9 bp[221]. Finally, linker histone H1E is coarse grained similar to histone tails with the Levitt-Warshel united-atom bead model and with charges calculated with DISCO[222]. The globular head is modeled with 6 beads and the C-terminal domain with 22 beads; the N-terminal domain is neglected since it has minor role in chromatin organization.

Standard energy terms and various local and global MC sampling moves are used to improve the conformational sampling. The total energy function contains stretching terms for linker DNA, histone tails, and linker histone that maintain equilibrium distances; bending terms for linker DNA, histone tails, and linker histone; twisting terms for linker DNA; electrostatic Debye-Hückel terms to represent all charge-charge interactions within chromatin; and excluded volume terms for all beads, described with a Lennard-Jones potential. The MC moves include local translation, local rotation, and global pivot rotations for linker DNA beads or nucleosomes, and a regrowth for histone tails[214]. Acceptance of the first three moves is based on the regular Metropolis criteria[223] while acceptance of the tail regrowth move is made according to the Rosenbluth criteria[224]. Full details concerning the energy terms, parameter values, and sampling can be found in Arya and Schlick[214] and in Bascom and Schlick[126].

Convergence of the systems is monitored by determining the evolution along the trajectory of global variables like the sedimentation coefficient and the root mean squared deviation of the nucleosomes with respect to the initial structure, and by monitoring local variables like the distance between the first and last nucleosome and evolution of angles formed by three adjacent (in sequence) nucleosomes. The last 100 structures of each trajectory corresponding to the last 10 million MC steps are used to analysis, producing configurational ensembles of 3000 structures for the Oct4 system.

Chromatin structure analysis of coarse-grained model:

The sedimentation coefficient ($S_{w,20}$), in units of Svedbergs, is used to describe the compaction of the fiber. It is defined by the expression:

$$S_{w,20} = \left((S_1 - S_0) * LH_{conc} + S_0\right) * \left(1 + \left(\frac{R_1}{N_C}\right)\sum_i \sum_j \frac{1}{R_{ij}}\right),$$

where S_0 is the sedimentation coefficient for a mononucleosome with LH bound (12 S)[225], S_1 is the sedimentation coefficient for a mononucleosome without LH (11.1 S)[226], LH_{conc} the

concentration of LH in the fiber, R_1 the spherical radius of a nucleosome (5.5 nm), N_C the number of nucleosomes in the fiber, and R_{ij} the distance between two nucleosomes i and j.

The radius of gyration, which describes the overall dimension of the polymer chain, is measured as the root mean squared distance of each nucleosome from the center of mass according to the relation:

$$R_g^2 = \frac{1}{Nc} \sum_{j=1}^{N} (r_j - r_{mean})^2,$$

where N_c is the number of nucleosomes, r_j the center position of the nucleosome core j, and r_{mean} the average of all core positions[227].

Fiber volumes are calculated using the AlphaShape function of Matlab, which creates a nonconvex bounding volume that envelops the nucleosomes. Surfaces are visually inspected to ensure that they represent correctly the fiber morphology. This is because non cylindrical-like shapes may not well be estimated. In that case, the AlphaShape object can be manipulated to tighten or loosen the fit around the points to create a nonconvex region.

Packing ratio is used to describe the compaction of the fiber and is measured as the number of nucleosomes contained in 11 nm of fiber. It is determined according to the relation:

$$Packing\ ratio = \frac{11 \cdot N_C}{fiber\_length},$$

where N_C is the number of nucleosomes and the fiber length is calculated using a cubic smoothing spline function native from Matlab.

Nucleosome clusters are quantified by determining the average number of nucleosomes per cluster and average number of clusters using the Density-based clustering algorithm DBSCAN[228], as implemented in Matlab. DBSCAN is designed to discover clusters in noisy data by partitioning the observations (the n-by-n internucleosome distance matrix) into clusters.

The algorithm identifies three kinds of points: core, border, and noise points, based on a threshold for a neighborhood search radius (epsilon) and a minimum number of neighbors in the given neighborhood (*minpts*). Any point x in the data set with a neighbor count greater than or equal to *minpts* is selected as a core point. Alternatively, if the number of neighbors is less than *minpts,* but the point x belongs to an epsilon neighborhood of some core point z, the point is identified as a border point. Finally, if a point is neither a core nor a border point, it is identified as a noise point and not assigned to any cluster.

The algorithm is implemented as follows:

1. From the input data set, select the observation x1 and assign it to cluster 1.

2. Find the set of points within the epsilon neighborhood of the current point.
   a. If the number of neighbors is less than minpts, label the current point as noise. Go to step
   b. Otherwise, label the current point as a core point belonging to cluster 1.
3. Iterate over each neighbor (new current point), and repeat step 2 until no new neighbors that can be labeled as belonging to the current cluster are found.
4. Select the next observation x2 as the current pint and increase the cluster count by 1.
5. Repeat steps 2-4 until all points in the input data set are assigned.

If the distance between two border points belonging to different clusters is smaller than epsilon, DBSCAN merges the two clusters into one. The *minpts* and epsilon parameters were chosen based on the heuristic provided by the algorithm developers[129]. *Minpts* was selected as 3 nucleosomes as it is recommended to be at least $\geq D + 1$, where D is the number of dimensions in the data set. However, this parameter does not significantly affect the overall results of the clustering[129]. The radius, epsilon, was selected as 20 nm based on the fiber dimensions.

Contact Probability matrices:

Nucleosome contact matrices describe the fraction of MC steps that the core, histone tails, or linker DNA of a nucleosome i are in contact (within 2 nm) with any of these elements of a nucleosome j. For a single fiber contact map, contacts are counted along the corresponding trajectory and normalized by the maximum number of contacts across all frames to determine the probabilities, which are then plotted in logarithmic scale. For the contact matrices of the 30-trajectory ensemble, all probabilities of each independent trajectory are summed before plotting.

Contact probability matrices are used to characterize fiber internal folding motifs. Specific fold patterns can be identified by the density features [117]. Local inter-nucleosome interactions ($i \pm 2, 3$), corresponding to the canonical zigzag topology, locate near the diagonal of the matrices; medium-range interactions ($i \pm 4, 5, 6$) indicative of hairpin- and sharp kinks-type folds are evidenced by regions perpendicular to the main diagonal; and long-range contacts ($i \pm 7, >7$), indicative of hierarchical looping, are evidenced by regions parallel to the main diagonal.

Zigzag geometry inside the clutches:

For representative trajectories of mESC and mNPC, we studied the zigzag geometry inside the clutches. Specifically, we calculated for consecutive nucleosomes (bonded) belonging to the same clutch the probability distribution of the dimer distance, distance between two consecutive nucleosomes (nucleosome i and nucleosome i+1); the triplet angle, angle formed by three consecutive nucleosomes (nucleosome i, nucleosome i+1, and nucleosome i+2); and the dihedral angle, angle between two planes about nucleosomes i+1 and i+2 defined by four

consecutive nucleosomes (nucleosome i, i+1, i+2, and i+3). As we are interested in the zigzag geometry, consecutive nucleosomes belonging to the same clutch but connected by a nucleosome free region instead of a typical linker DNA were not considered in the statistics. (**Figure 45**)

SMLM Image generation:

We used SuReSim software for the generation of synthetic SMLM images[130] (**Figure 46a**). We imported the final 3D nucleosome positions of each fiber obtained from the mesoscale chromatin modeling to SuReSim and generated a list of *x-y-z* positions of fluorophore labeled nucleosomes taking into account fluorophore blinking and precision in determining each fluorophore's position. We input a discrete list with the 3D coordinates of the nucleosome centers obtained from the mesoscale computational model. We generate the images using realistic parameters that resemble the experimental conditions [11]. We used a localization precision of 10 nm, an epitope length of 10 nm with a random 3D angle distribution with standard deviation of 50 º, a labeling efficiency of 75%, a localization efficiency of 80%, and a ratio of 2 fluorophores per antibody. We simulated 10.000 frames in order to obtain a number of localizations per cluster in the same range as in our experimental measurements.

We performed 1000 random 3D projections of the localizations using a custom-written Matlab code. Then we projected those images in 2D, taking into account that a maximum slice of 400 nm will be detected by the microscope. (**Figure 46a**).

Simulated SMLM images Cluster analysis:

For cluster quantification, we used a previously described method [11]. The localization lists were binned to construct discrete localization images with pixel size of 10 nm. These were convoluted with a 5x5 pixels kernel to obtain density maps and transformed into binary images by applying a constant threshold, such that each pixel has a value of either 1 if the density surpasses the threshold value and 0 if not. We used a threshold of 0.008 localizations/nm^2. The x-y coordinates in the binary image were grouped into clusters using a distance-based algorithm. Cluster sizes were calculated as the standard deviation of x-y coordinates from the centroid of the cluster. In addition, we used an estimated localization precision of 10 nm and a minimum number of molecules so that a group is consider a clutch of 10 localizations.

The synthetic super resolution images of the fibers were rendered using a custom-written software (Insight3, provided by Bo Huang, University of California). (**Figure 46a**).

DM1.3 Single Molecule Tracking

Cell culture conditions and generation of cell lines:

All mouse embryonic stem cells (mESC) were grown in a humidified incubator at 37°C - 5% CO2 and were cultured on gelatin (#ES-006-B, Merck) coated plates, with serum Lif medium [DMEM, 15% FBS, 1% penicillin/streptomycin (#15140122, Thermo Fisher), 1% GlutaMax (#35050061, Thermo Fisher), 1% sodium pyruvate (#11360070, Thermo Fisher), 1% MEM non-essential amino acid (#11140050, Thermo Fisher), 0.2% 2-Mercaptoethanol (#31350010, Thermo Fisher) and 1000 U/ml LIF ESGRO (#ESG1107, Merck)].

Neural progenitor cells (NPCs) were generated by plating 44000 cells/cm2 in gelatin coated Lab-Tek I (#155411, Nunc) chambers 24 hours prior to the start of differentiation. Cells were differentiated for 3 days in culture with Retinoic Acid containing medium (50% Neurobasal (#21103-049, Thermo Fisher), 50% DMEM/F12 (#21331020, Thermo Fisher), 1× penicillin/streptomycin, 1× GlutaMax, 2% B27 (#17504044, Thermo Fisher), 1% N2 (#17502048, Thermo Fisher), and 1 μM Retinoic Acid (#R2625, Sigma-Aldrich). Medium was changed every day. mESC H1tKO were a kind gift from Dr. Arthur Skoultchi[122]. mESC CTCF_Halotag (A7 clone) were a kind gift from Dr. Rafael Casellas (NIH, Bethesda). mESC Halotag_Oct4 were generated by our collaborator Prof. Eran Meshorer (HUJI, Israel) by inserting Halotag sequence at the 5' of endogenous Oct4 gene with CRISPR-Cas9, a single guide RNA (AAGGTGGGCACCCCGAGCCGGGG) and a donor vector carrying Halotag sequence flanked by Oct4 5' and 3' homology arms.

mESC H2B-Halotag were generated by lentiviral infection of mESC (GS1 129Sv) and mESC H1tKO[122] with a lentiviral plasmid encoding for H2B_Halotag under EF1a promoter (p1494_EF1a_H2B_Halotag) following The RNAi Consortium (TRC) low throughput viral production protocol (https://portals.broadinstitute.org/gpp/public/resources/protocols).

Transduced cells were selected for hygromycin resistance (#10687010, Thermo Fisher). Cells expressed H2B-Halotag at levels comparable or lower than endogenous H2B.

mESC H2B_Halotag + Cenpa_GFP or + Trf1_GFP were generated by lentiviral infection of mESC H2B_Halotag cells with pLENTI_Cenpa_GFP or pLENTI_Trf1_GFP as described above. Transduced cells were selected by cell sorting of GFP positive cells (FACS Aria) 96h post transduction.
Lentiviral vector expressing C-terminally Halo-tagged H2B was generated by Gibson cloning by preamplifying Halotag from pFN205K HaloTag EF1a-neo Flexi (Promega) and H2B from pSNAP-H2B (#N9179S, New England Biolabs) and cloning them into p1494 plasmid with Hygromycin resistance and EF1a promoter.

Lentiviral vectors expressing C-terminally eGFP-tagged Cenpa and Trf1 under EF1a promoter were generated by Genscript custom gene service by subcloning Cenpa ORF (#OMu00596C, NM_007681.3) and Trf1 ORF (#OMu19848C, NM_009352.3) into pLENTI-dCas9-VP64_GFP backbone.

Cell labelling for Single molecule tracking imaging:

For SMT experiments in mESC, cells were plated at a 31000 cells/cm^2 density in Lab-TekI chambers 24 hours before imaging. For SMT experiments in NPCs, cells were differentiated as described above and imaged after 3 days of differentiation. Cells were labelled with 2 pM and 5 pM of JF549-Halotag ligand (kind gift from Dr. Luke Lavis) diluted in grow or differentiating medium. Cells were incubated in presence of the dye for 30 min in the incubator and subsequently washed once in Phenol red free medium with Hoescht (1:1000 dilution) for 15 min in the incubator. Cells were finally washed once with Phenol red free medium for 5 min in the incubator.

For SMT imaging of living cells, cells were kept in Phenol Red free grow or differentiation medium. For SMT imaging of fixed cells, right after labelling, samples were fixed for 10 min at RT in PFA 4 % (#43368, Alfa Aesar), diluted in PBS, and washed 3 times in PBS. JF549-Halo ligand diluted in phenol red free resting medium for 30 min in the incubator. Cells were washed once for 15 min in the incubator with fresh medium and then once for 5 min. JF labeled ligands were kindly provided by Dr. Luke Lavis (Janelia Research Campus).

Imaging:

Imaging was performed in an N-STORM 4.0 microscope (Nikon Instruments) equipped with an Okolab cage incubator system set at 37ºC, 5%CO2 and controlled humidity. Images were taken with a 100X 1.49 oil objective and an EMCCD camera Andor iXon Ultra 897 (Oxford Instruments). This combination provides an effective pixel size of 160 nm. We used HILO illumination[62] and a quad-band beam splitter ZT405/488/561/640rpc (Chroma Technology Corporation). The Perfect Focus System (PFS) equipped on the NSTORM microscope was used during the acquisition.

Two imaging conditions were set to measure separately fast and slow dynamics. The fast dynamics experiments were perform with 15 ms of camera exposure time, a 561 nm laser power of ~ 200 W/cm^2 and 10 pM concentration of JF-549-Halo fluorophore in the labeling step. For the slow dynamics, we used 500 ms of camera exposure time, a 561 nm laser power of ~ 25 W/cm^2 and 4 pM concentration of JF-549-Halo fluorophore. For the fast SMT at 15 ms, we acquired 3000 frames (45 seconds), and for slow SMT videos at 500 ms of exposure time, 600 frames (5 minutes).

Apart from the JF, Hoesch33342 was used for staining chromatin. This allows to identify regions of more condensed chromatin and to precisely segment each cell nucleus subROI. In both cases, we imaged four frames of Hoesch33342 at the end of each SMT video, using the 405nm laser at a very low power (~ 5 W/cm^2) with 2 s of camera exposure time. In order to classify the trajectories as euchromatic or heterochromatic, the sub regions were defined by manually drawing subROIs based on Hoestch33342 fluorescence intensity, which correlates with chromatin compaction. In addition, a brightfield image of each FOV was taken before and after the imaging procedure, to control for apparent cell displacement or cell dead during the experiment. Cells were imaged on their corresponding phenol red free resting medium.

2-color imaging:

A Dual-view system based on a dichroic mirror was used for the 2-Color SMT experiments. The camera was splitted in two FOVs of 256x256 pixels (40x40 μm) each.

A calibration with fluorescent TetraSpeck Microspheres (ThermoFisher Scientific) was performed before and after the experiments to align both channels with a precision below 10 nm. A second order 2D polynomial transform function was calculated from the beads localizations of both channels[36]. Then the alignment of the trajectories on both channels was perform by using a linear affine transformation.

The H2B trajectories were divided in two groups based on their overlapping with Telomere trajectories. To do so, a maximum spatial distance of 250 nm between the positions of both trajectories (Telomeres and H2B) was set to identify telomeric H2B. Note that both trajectories should overlap also in time, meaning that they are present on the same frame.

Tracking:

TrackMate[84] was used for localization and tracking of the single molecules. For the localization step, we used the LoG detector with sub-pixel localization enabled and for the tracking step, the Simple LAP tracker with a maximum frame gap of 2 frames.

The images were segmented by manually selecting the nuclear areas from Hoesch33342 signal, corresponding to each cell nucleus. We performed this tracking procedure on each individual nucleus separately.

Different input parameters were used for each imaging condition. The intensity threshold for the localizations was defined to minimize false localizations: 150 for the 500 ms data, and 70 for the 15 ms data. In both cases the Linking max distance was set to 400 nm and the gap-closing max distance to 200 nm. The estimated blob diameter of the diffraction-limited spot was set to 800 nm (5 pixels). The list of trajectories were save as an xml file for their analysis.

Trajectory analysis:

The trajectories were analyzed using a custom written Matlab code, that makes use of some functions from @msdanalyzer[138]. It is publicly available at https://github.com/PabloAu/Single-

Molecule-Tracking-Analysis. First, it filters the trajectories based on their track length. For the analysis of the trajectories from 15ms exposure time, only those tracks longer than 4 frames were analyzed. For the 500ms data, all the trajectories were analyzed and 1 frame localizations were consider to be binding events lasting 500ms. Then it classifies the trajectories in different motion types. After having the subgroups, the code computes quantitative analysis on the trajectories for extracting multiple measures. Finally, it compares the results from the different cell conditions.

The MSD curves where obtained as a time average from the trajectories (T-MSD), assuming that the displacements at different times are equivalent fulfilling the ergodic principle[85]:

$$TMSD = \frac{1}{N-m} \cdot \sum_{i=1}^{N-m} \left(x_j\left(t_i + m \cdot t_{lag}\right) - x_j(t_i)\right)^2$$

The time ensemble average of the MSD (TE-MSD) is the average of the T-MSD computed on all the trajectories for a particular condition:

$$TEMSD = \frac{1}{T}\frac{1}{N-m} \cdot \sum_{j=1}^{T} \sum_{i=1}^{N-m} \left(x_j\left(t_i + m \cdot t_{lag}\right) - x_j(t_i)\right)^2$$

Where t_{lag} is the exposure time of the experiment, in our case 15ms.

TEMSD was plotted as a discrete bar plot showing the average and standard deviation for each time lag point (**Figure 50, 52** and **53**).

Trajectory classification:
The trajectories were classified into two different subgroups based on their motion type: Confined and Brownian/Directed. This was done by fitting a power law function to each individual TMSD curve[83]:

$$TMSD = 4 \cdot D \cdot t_{lag}^{\alpha},$$

where D is the diffusion coefficient and t_{lag} is the time lag between the different time points of the track. α is called the anomalous coefficient. Trajectories with $\alpha < 1$ were considered as Confined and with $\alpha \geq 1$ as Brownian/Directed.

In addition, a third group of trajectories performing both confined motion and free diffusion where identified and separated. First, we iterate through all the trajectories searching for frame-to-frame jumps that are bigger than the mean frame-to-frame jump of the track plus a spatial threshold multiplied by the standard deviation of the frame to frame jump of the track. We used 1.5 for that spatial threshold. In addition, the total distance travelled by butterfly trajectories must be bigger than a distance threshold multiplied by the mean frame-to-frame jump of the track. We used a value of 8 for that distance threshold. Once identified, the

butterfly trajectories were segmented into their multiple Confined and Brownian/Directed parts based on their geometrical properties. A Brownian/Directed segment must fulfill the condition that a minimum percentage of its points lie outside the polygon (convex hull) formed by the points of previous and posterior segments of the trajectory. We used a minimum percentage of outside points of 30%. In addition, we imposed a minimum linearity to the Directed/Brownian segments. Linearity was calculated by dividing the distance between the first and last point of a certain segment by the sum of displacements of all the individual jumps of that segment. We iterated using segments of 3 points and used a linearity ratio threshold of 0.8 so that a segment is considered Brownian/Directed type (see **Figure 49** and software at https://github.com/PabloAu/Single-Molecule-Tracking-Analysis)

Diffusion:
For an accurate calculation of the diffusion coefficient of the confined trajectories, only the first 3 points of each T-MSD curve corresponding to each trajectory were fitted with linear distribution[139,140]:

$$TMSD = 4 \cdot D \cdot t_{lag} + offset$$

A threshold on the coefficient of determination $R^2 \geq 0.8$ was set to filter out the bad fits. Since the distribution of the diffusion coefficients (D) follows a log-normal distribution[229], the $Log_{10}(D)$ was used for a proper visualization of the different subpopulations of trajectories. Consequently, a Gaussian Bi-modal distribution was fit of that $Log_{10}(D)$ distribution.

Circle confined diffusion model:
The radius of confinement of the whole population of trajectories was estimated by fitting a confined circle diffusion model to the time ensemble of the confined trajectories[88]:

$$TEMSD = R^2 \cdot \left(1 - e^{\frac{-4 \cdot D_{micro} \cdot t_{lag}}{R^2}}\right) + O,$$

where R is the radius of confinement and D_{micro} the diffusion coefficient at short time scales. O is an offset value that comes from the localization precision limit of SMLM techniques. In this case, we have estimated a localization precision of around 50nm from the experimental data

Residence Times:
The residence times of H2B bound to chromatin were extracted from the 500 ms data, which measures chromatin dynamics on a higher time scale. In this case, all the trajectories were analyzed, considering that a one-frame localization is a binding event which has a residence time of 500 ms. The dissociation kinetics were estimated from the track length of each individual trajectory. First, the track duration distribution is transformed into the survival fraction of molecules defined by 1 – Cumulative Distribution Function of the track lengths

(1-CDF). Then, we fit a two-component exponential decay function to the survival fraction[44,92,230]:

$$F(t) = f \cdot e^{-k_1 \cdot t} + (1 - f) \cdot e^{-k_2 \cdot t},$$

where f is the fraction belonging to each population, k_1 the short-live component associated with unspecific chromatin binding and k_2 the long-live component associated with specific chromatin binding.

In addition, a photobleaching correction was performed by fitting a double exponential to the evolution of the number of localizations over time during the experiment[92].

$$N(t) = f_b \cdot e^{-k_{b1} \cdot t} + (1 - f_b) \cdot e^{-k_{b2} \cdot t}$$

Then, the corrected residence times are obtained from the following relation:

$$k_{measured} = k_{corrected} + k_{bleaching},$$

where $k_{measured}$ is the dissociation rate constant estimated directly from the experimental data, k_b is the photobleaching kinetics constant and $k_{corrected}$ is the dissociation rate constant after correction. Note that k is in s^{-1} units and the residence times are inversely proportional.

For a further control, fixed cells were imaged under the same experimental conditions, obtaining similar values for the different cell types, which were larger than those of live cells, assuring that measured residence times are related with protein instability due to live cell activity.

References

1. Olins, D. E. & Olins, A. L. Chromatin history: Our view from the bridge. *Nature Reviews Molecular Cell Biology* (2003). doi:10.1038/nrm1225

2. Strick, R., Strissel, P. L., Gavrilov, K. & Levi-Setti, R. Cation-chromatin binding as shown by ion microscopy is essential for the structural integrity of chromosomes. *J. Cell Biol.* (2001). doi:10.1083/jcb.200105026

3. Jenuwein, T. & Allis, C. D. Translating the histone code. *Science* (2001). doi:10.1126/science.1063127

4. Bascom, G. D., Sanbonmatsu, K. Y. & Schlick, T. Mesoscale Modeling Reveals Hierarchical Looping of Chromatin Fibers Near Gene Regulatory Elements. (2016). doi:10.1021/acs.jpcb.6b03197

5. Finch, J. T. & Klug, A. Solenoidal model for superstructure in chromatin. *Proc. Natl. Acad. Sci. U. S. A.* (1976). doi:10.1073/pnas.73.6.1897

6. Woodcock, C. L. F., Frado, L. L. Y. & Rattner, J. B. The higher-order structure of chromatin: Evidence for a helical ribbon arrangement. *J. Cell Biol.* (1984). doi:10.1083/jcb.99.1.42

7. Oudet, P., Gross-Bellard, M. & Chambon, P. Electron microscopic and biochemical evidence that chromatin structure is a repeating unit. *Cell* (1975). doi:10.1016/0092-8674(75)90149-X

8. Dorigo, B. *et al.* Nucleosome arrays reveal the two-start organization of the chromatin fiber. *Science (80-.).* (2004). doi:10.1126/science.1103124

9. Maeshima, K., Hihara, S. & Eltsov, M. Chromatin structure: Does the 30-nm fibre exist in vivo? *Curr. Opin. Cell Biol.* **22**, 291–297 (2010).

10. Woodcock, C. L. & Dimitrov, S. Higher-order structure of chromatin and chromosomes. *Current Opinion in Genetics and Development* (2001). doi:10.1016/S0959-437X(00)00169-6

11. Ricci, M. A., Manzo, C., García-Parajo, M. F., Lakadamyali, M. & Cosma, M. P. Chromatin Fibers Are Formed by Heterogeneous Groups of Nucleosomes In Vivo. *Cell* **160**, 1145–1158 (2015).

12. Meshorer, E. *et al.* Hyperdynamic plasticity of chromatin proteins in pluripotent embryonic stem cells. *Dev. Cell* **10**, 105–116 (2006).

13. Stadhouders, R. *et al.* interplay between genome topology and gene regulation during cell reprogramming. *Nat. Genet.* **50**, (2018).

14. Stadhouders, R., Filion, G. J. & Graf, T. Review Transcription factors and 3D

genome conformation in cell-fate decisions. *Nature* doi:10.1038/s41586-019-1182-7

15. Popken, J. *et al.* Remodeling of the nuclear envelope and lamina during bovine preimplantation development and its functional implications. *PLoS One* (2015). doi:10.1371/journal.pone.0124619

16. Hübner, B. *et al.* Remodeling of nuclear landscapes during human myelopoietic cell differentiation maintains co-aligned active and inactive nuclear compartments. *Epigenetics and Chromatin* (2015). doi:10.1186/s13072-015-0038-0

17. Fussner, E. *et al.* Open and closed domains in the mouse genome are configured as 10-nm chromatin fibres. *EMBO Rep.* (2012). doi:10.1038/embor.2012.139

18. Ricci, M. A., Cosma, M. P. & Lakadamyali, M. Super resolution imaging of chromatin in pluripotency, differentiation, and reprogramming. *Curr. Opin. Genet. Dev.* **46**, 186–193 (2017).

19. Ohno, M., Priest, D. G. & Taniguchi, Y. Nucleosome-level 3D organization of the genome. *Biochem. Soc. Trans.* **46**, 491–501 (2018).

20. Grigoryev, S. A., Arya, G., Correll, S., Woodcock, C. L. & Schlick, T. Evidence for heteromorphic chromatin fibers from analysis of nucleosome interactions. *Proc. Natl. Acad. Sci. U. S. A.* (2009). doi:10.1073/pnas.0903280106

21. Bednar, J. *et al.* Nucleosomes, linker DNA, and linker histone form a unique structural motif that directs the higher-order folding and compaction of chromatin. *Proc. Natl. Acad. Sci. U. S. A.* (1998). doi:10.1073/pnas.95.24.14173

22. Robinson, P. J. J., Fairall, L., Huynh, V. A. T. & Rhodes, D. EM measurements define the dimensions of the '30-nm' chromatin fiber: Evidence for a compact, interdigitated structure. *Proc. Natl. Acad. Sci. U. S. A.* (2006). doi:10.1073/pnas.0601212103

23. Song, F. *et al.* Cryo-EM study of the chromatin fiber reveals a double helix twisted by tetranucleosomal units. *Science (80-.).* (2014). doi:10.1126/science.1251413

24. Horowitz, R. A., Agard, D. A., Sedat, J. W. & Woodcock, C. L. The three-dimensional architecture of chromatin in situ: Electron tomography reveals fibers composed of a continuously variable zig-zag nucleosomal ribbon. *J. Cell Biol.* (1994). doi:10.1083/jcb.125.1.1

25. Ou, H. D. *et al.* ChromEMT: Visualizing 3D chromatin structure and compaction in interphase and mitotic cells. *Science (80-.).* **357**, eaag0025 (2017).

26. Williams, S. P. *et al.* Chromatin fibers are left-handed double helices with diameter and mass per unit length that depend on linker length. *Biophys. J.* (1986). doi:10.1016/S0006-3495(86)83637-2

27. Nishino, Y. *et al.* Human mitotic chromosomes consist predominantly of irregularly

folded nucleosome fibres without a 30-nm chromatin structure. *EMBO J.* (2012). doi:10.1038/emboj.2012.35

28. Luger, K., Mäder, A. W., Richmond, R. K., Sargent, D. F. & Richmond, T. J. Crystal structure of the nucleosome core particle at 2.8 Å resolution. *Nature* (1997). doi:10.1038/38444

29. Schalch, T., Duda, S., Sargent, D. F. & Richmond, T. J. X-ray structure of a tetranucleosome and its implications for the chromatin fibre. *Nature* (2005). doi:10.1038/nature03686

30. Hübner, M. R., Eckersley-Maslin, M. A. & Spector, D. L. Chromatin organization and transcriptional regulation. *Curr. Opin. Genet. Dev.* **23**, 89–95 (2013).

31. Dixon, J. R. *et al.* Topological domains in mammalian genomes identified by analysis of chromatin interactions. *Nature* (2012). doi:10.1038/nature11082

32. Lieberman-Aiden, E. *et al.* Comprehensive mapping of long-range interactions reveals folding principles of the human genome. *Science (80-.).* (2009). doi:10.1126/science.1181369

33. Boettiger, A. N. *et al.* Super-resolution imaging reveals distinct chromatin folding for different epigenetic states. *Nature* **529**, 418–422 (2016).

34. Bintu, B. *et al.* Super-resolution chromatin tracing reveals domains and cooperative interactions in single cells. **1783**, (2018).

35. Ruiz-Velasco, M. & Zaugg, J. B. Structure meets function: How chromatin organisation conveys functionality. *Current Opinion in Systems Biology* (2017). doi:10.1016/j.coisb.2017.01.003

36. Otterstrom, J. *et al.* Super-resolution microscopy reveals how histone tail acetylation affects DNA compaction within nucleosomes in vivo. *Nucleic Acids Res.* 1–15 (2019). doi:10.1093/nar/gkz593

37. Shukron, O., Seeber, A., Amitai, A. & Holcman, D. Advances Using Single-Particle Trajectories to Reconstruct Chromatin Organization and Dynamics. *Trends Genet.* 1–21 (2019). doi:10.1016/j.tig.2019.06.007

38. Shaban, H. A., Barth, R. & Bystricky, K. Nanoscale mapping of DNA dynamics in live human cells. *Bioarxiv* 1–27 (2018).

39. Chen, H. *et al.* Dynamic interplay between enhancer–promoter topology and gene activity. *Nat. Genet.* **50**, 1296–1303 (2018).

40. Neumann, F. R. *et al.* Targeted INO80 enhances subnuclear chromatin movement and ectopic homologous recombination. *Genes Dev.* (2012). doi:10.1101/gad.176156.111

41. Chuang, C. H. *et al.* Long-Range Directional Movement of an Interphase Chromosome Site. *Curr. Biol.* **16**, 825–831 (2006).

42. Kimura, H. & Cook, P. R. Kinetics of core histones in living human cells: Little exchange of H3 and H4 and some rapid exchange of H2B. *J. Cell Biol.* (2001). doi:10.1083/jcb.153.7.1341

43. Nagai, T. *et al.* Dynamic Organization of Chromatin Domains Revealed by Super-Resolution Live-Cell Imaging. *Mol. Cell* **67**, 282-293.e7 (2017).

44. Mazza, D., Abernathy, A., Golob, N., Morisaki, T. & Mcnally, J. G. A benchmark for chromatin binding measurements in live cells. **40**, 1–13 (2012).

45. Nozaki, T., Hudson, D. F., Tamura, S. & Maeshima, K. Dynamic Chromatin Folding in the Cell. in *Nuclear Architecture and Dynamics* 101–122 (Elsevier, 2018). doi:10.1016/B978-0-12-803480-4.00004-1

46. Maeshima, K., Ide, S. & Babokhov, M. Dynamic chromatin organization without the 30-nm fiber. *Current Opinion in Cell Biology* (2019). doi:10.1016/j.ceb.2019.02.003

47. Higashi, T. *et al.* Histone H2A mobility is regulated by its tails and acetylation of core histone tails. **357**, 627–632 (2007).

48. Hansen, A. S., Pustova, I., Cattoglio, C., Tjian, R. & Darzacq, X. CTCF and cohesin regulate chromatin loop stability with distinct dynamics. 1–33 (2017). doi:10.7554/eLife.25776

49. Bryan, L. C. *et al.* Single-molecule kinetic analysis of HP1-chromatin binding reveals a dynamic network of histone modification and DNA interactions. *Nucleic Acids Res.* **45**, 10504–10517 (2017).

50. Gustafsson, M. G. L. Surpassing the lateral resolution limit by a factor of two using structured illumination microscopy. *J. Microsc.* (2000). doi:10.1046/j.1365-2818.2000.00710.x

51. Klar, T. A., Jakobs, S., Dyba, M., Egner, A. & Hell, S. W. Fluorescence microscopy with diffraction resolution barrier broken by stimulated emission. *Proc. Natl. Acad. Sci.* (2000). doi:10.1073/pnas.97.15.8206

52. Rust, M. J., Bates, M. & Zhuang, X. Sub-diffraction-limit imaging by stochastic optical reconstruction microscopy (STORM). *Nat. Methods* (2006). doi:10.1038/nmeth929

53. Betzig, E. *et al.* Imaging intracellular fluorescent proteins at nanometer resolution. *Science (80-.).* (2006). doi:10.1126/science.1127344

54. Jungmann, R. *et al.* Multiplexed 3D cellular super-resolution imaging with DNA-PAINT and Exchange-PAINT. *Nat. Methods* (2014). doi:10.1038/nmeth.2835

55. Schueder, F. *et al.* Multiplexed 3D super-resolution imaging of whole cells using spinning disk confocal microscopy and DNA-PAINT. *Nat. Commun.* **8**, (2017).

56. Bohn, M. *et al.* Localization microscopy reveals expression-dependent parameters of chromatin nanostructure. *Biophys. J.* (2010). doi:10.1016/j.bpj.2010.05.043

57. Flors, C. DNA and chromatin imaging with super-resolution fluorescence microscopy based on single-molecule localization. *Biopolymers* (2011). doi:10.1002/bip.21574

58. Galbraith, C. G. & Galbraith, J. A. Super-resolution microscopy at a glance. *J. Cell Sci.* (2011). doi:10.1242/jcs.080085

59. Bates, M., Huang, B., Dempsey, G. T. & Zhuang, X. Multicolor super-resolution imaging with photo-switchable fluorescent probes. *Science (80-.).* (2007). doi:10.1126/science.1146598

60. Oddone, A., Vilanova, I. V., Tam, J. & Lakadamyali, M. Super-resolution imaging with stochastic single-molecule localization: Concepts, technical developments, and biological applications. *Microsc. Res. Tech.* (2014). doi:10.1002/jemt.22346

61. Thompson, R. E., Larson, D. R. & Webb, W. W. Precise Nanometer Localization Analysis for Individual Fluorescent Probes. *Biophys. J.* **82**, 2775–2783 (2002).

62. Tokunaga, M., Imamoto, N. & Sakata-Sogawa, K. Highly inclined thin illumination enables clear single-molecule imaging in cells. *Nat. Methods* (2008). doi:10.1038/nmeth1171

63. Smith, C. S., Joseph, N., Rieger, B. & Lidke, K. A. Fast , single-molecule localization that achieves theoretically minimum uncertainty. doi:10.1038/nmeth.1449

64. Banterle, N., Bui, K. H., Lemke, E. A. & Beck, M. Fourier ring correlation as a resolution criterion for super-resolution microscopy. *J. Struct. Biol.* (2013). doi:10.1016/j.jsb.2013.05.004

65. Shroff, H., Galbraith, C. G., Galbraith, J. A. & Betzig, E. Live-cell photoactivated localization microscopy of nanoscale adhesion dynamics. *Nat. Methods* (2008). doi:10.1038/nmeth.1202

66. Huang, B., Wang, W., Bates, M. & Zhuang, X. Three-dimensional super-resolution imaging by stochastic optical reconstruction microscopy. *Science (80-.).* (2008). doi:10.1126/science.1153529

67. Huang, B., Wang, W., Bates, M. & Zhuang, X. Three-dimensional super-resolution imaging by stochastic optical reconstruction microscopy. *Science (80-.).* (2008). doi:10.1126/science.1153529

68. Bates, M., Blosser, T. R. & Zhuang, X. Short-range spectroscopic ruler based on a

single-molecule optical switch. *Phys. Rev. Lett.* (2005). doi:10.1103/PhysRevLett.94.108101

69. Huang, B., Babcock, H. & Zhuang, X. Breaking the diffraction barrier: Super-resolution imaging of cells. *Cell* (2010). doi:10.1016/j.cell.2010.12.002

70. Fernández-Suárez, M. & Ting, A. Y. Fluorescent probes for super-resolution imaging in living cells. *Nature Reviews Molecular Cell Biology* (2008). doi:10.1038/nrm2531

71. Lakadamyali, M. Super-resolution microscopy: Going live and going fast. *ChemPhysChem* (2014). doi:10.1002/cphc.201300720

72. Lakadamyali, M. & Pia, M. Advanced microscopy methods for visualizing chromatin structure. *FEBS Lett.* (2015). doi:10.1016/j.febslet.2015.04.012

73. Schnitzbauer, J., Strauss, M. T., Schlichthaerle, T., Schueder, F. & Jungmann, R. Super-resolution microscopy with DNA-PAINT. *Nat. Protoc.* (2017). doi:10.1038/nprot.2017.024

74. Jungmann, R. *et al.* Multiplexed 3D cellular super-resolution imaging with DNA-PAINT and Exchange-PAINT. (2014). doi:10.1038/nmeth.2835

75. Jungmann, R. *et al.* Quantitative super-resolution imaging with qPAINT. *Nat. Methods* (2016). doi:10.1038/nmeth.3804

76. Reits, E. A. J. & Neefjes, J. J. From fixed to FRAP: Measuring protein mobility and activity in living cells. *Nature Cell Biology* (2001). doi:10.1038/35078615

77. Axelrod, D. *et al.* Lateral motion of fluorescently labeled acetylcholine receptors in membranes of developing muscle fibers. *Proc. Natl. Acad. Sci.* (1976). doi:10.1073/pnas.73.12.4594

78. Magde, D., Elson, E. & Webb, W. W. Thermodynamic fluctuations in a reacting system measurement by fluorescence correlation spectroscopy. *Phys. Rev. Lett.* (1972). doi:10.1103/PhysRevLett.29.705

79. Grimm, J. B. *et al.* A general method to improve fluorophores for live-cell and single-molecule microscopy. *Nat. Methods* (2015). doi:10.1038/nmeth.3256

80. Los, G. V *et al.* HaloTag: A Novel Protein Labeling Technology for Cell Imaging and Protein Analysis. *ACS Chem. Biol.* (2008). doi:10.1021/cb800025k

81. Bancaud, A. *et al.* Molecular crowding affects diffusion and binding of nuclear proteins in heterochromatin and reveals the fractal organization of chromatin. *EMBO J.* (2009). doi:10.1038/emboj.2009.340

82. Stagge, F., Mitronova, G. Y., Belov, V. N., Wurm, C. A. & Jakobs, S. Snap-, CLIP- and Halo-Tag Labelling of Budding Yeast Cells. *PLoS One* (2013). doi:10.1371/journal.pone.0078745

83. Manzo, C. & Garcia-Parajo, M. F. A review of progress in single particle tracking: From methods to biophysical insights. *Reports Prog. Phys.* **78**, 124601 (2015).

84. Tinevez, J. *et al.* TrackMate : An open and extensible platform for single-particle tracking. *Methods* (2016). doi:10.1016/j.ymeth.2016.09.016

85. Manzo, C. *et al.* Weak Ergodicity Breaking of Receptor Motion in Living Cells Stemming from Random Diffusivity. **011021**, 1–12 (2015).

86. Metzler, R., Jeon, J. H., Cherstvy, A. G. & Barkai, E. Anomalous diffusion models and their properties: Non-stationarity, non-ergodicity, and ageing at the centenary of single particle tracking. *Phys. Chem. Chem. Phys.* (2014). doi:10.1039/c4cp03465a

87. Saxton, M. J. & Jacobson, K. Single-particle tracking: Applications to membrane dynamics. *Annual Review of Biophysics and Biomolecular Structure* (1997). doi:10.1146/annurev.biophys.26.1.373

88. Wieser, S. & Schütz, G. J. Tracking single molecules in the live cell plasma membrane — Do ' s and Don ' t ' s. *Methods* **46**, 131–140 (2008).

89. Bálint, Š., Verdeny Vilanova, I., Sandoval Álvarez, Á. & Lakadamyali, M. Correlative live-cell and superresolution microscopy reveals cargo transport dynamics at microtubule intersections. *Proc. Natl. Acad. Sci.* (2013). doi:10.1073/pnas.1219206110

90. Mueller, F., Stasevich, T. J., Mazza, D. & Mcnally, J. G. Quantifying transcription factor kinetics : At work or at play ? **9238**, 1–23 (2013).

91. Shinkai, S., Nozaki, T., Maeshima, K. & Togashi, Y. Dynamic Nucleosome Movement Provides Structural Information of Topological Chromatin Domains in Living Human Cells. *PLoS Comput. Biol.* **12**, 1–16 (2016).

92. Chen, J. *et al.* Single-Molecule Dynamics of Enhanceosome Assembly in Embryonic Stem Cells. (2014). doi:10.1016/j.cell.2014.01.062

93. Lakadamyali, M. High resolution imaging of neuronal connectivity. *J. Microsc.* (2012). doi:10.1111/j.1365-2818.2012.03638.x

94. Bates, M., Dempsey, G. T., Chen, K. H. & Zhuang, X. Multicolor super-resolution fluorescence imaging via multi-parameter fluorophore detection. *ChemPhysChem* (2012). doi:10.1002/cphc.201100735

95. Annibale, P., Scarselli, M., Greco, M. & Radenovic, A. Identification of the factors affecting co-localization precision for quantitative multicolor localization microscopy. *Opt. Nanoscopy* (2012). doi:10.1186/2192-2853-1-9

96. Dempsey, G. T., Vaughan, J. C., Chen, K. H., Bates, M. & Zhuang, X. Evaluation of fluorophores for optimal performance in localization-based super-resolution imaging. *Nat. Methods* (2011). doi:10.1038/nmeth.1768

97. Endesfelder, U. *et al.* Chemically induced photoswitching of fluorescent probes-A general concept for super-resolution microscopy. *Molecules* (2011). doi:10.3390/molecules16043106

98. Lampe, A., Haucke, V., Sigrist, S. J., Heilemann, M. & Schmoranzer, J. Multi-colour direct STORM with red emitting carbocyanines. *Biol. Cell* (2012). doi:10.1111/boc.201100011

99. Linde, S. Van De *et al.* Direct stochastic optical reconstruction microscopy with standard fluorescent probes. **6**, 34–38 (2011).

100. Auer, A., Strauss, M. T., Schlichthaerle, T. & Jungmann, R. Fast, Background-Free DNA-PAINT Imaging Using FRET-Based Probes. (2017). doi:10.1021/acs.nanolett.7b03425

101. Shechtman, Y., Weiss, L. E., Backer, A. S., Lee, M. Y. & Moerner, W. E. Multicolour localization microscopy by point-spread-function engineering. *Nat. Photonics* (2016). doi:10.1038/nphoton.2016.137

102. Zhang, Z., Kenny, S. J., Hauser, M., Li, W. & Xu, K. Ultrahigh-throughput single-molecule spectroscopy and spectrally resolved super-resolution microscopy. *Nat. Methods* (2015). doi:10.1038/nmeth.3528

103. Piatkowski, L., Gellings, E. & Van Hulst, N. F. Broadband single-molecule excitation spectroscopy. *Nat. Commun.* (2016). doi:10.1038/ncomms10411

104. Lin, Y. *et al.* Quantifying and optimizing single-molecule switching nanoscopy at high speeds. *PLoS One* (2015). doi:10.1371/journal.pone.0128135

105. McKinney, S. A., Murphy, C. S., Hazelwood, K. L., Davidson, M. W. & Looger, L. L. A bright and photostable photoconvertible fluorescent protein. *Nat. Methods* (2009). doi:10.1038/nmeth.1296

106. Huang, B., Bates, M. & Zhuang, X. Super-Resolution Fluorescence Microscopy. *Annu. Rev. Biochem.* (2009). doi:10.1146/annurev.biochem.77.061906.092014

107. Bates, M., Huang, B., Dempsey, G. T. & Zhuang, X. Multicolor super-resolution imaging with photo-switchable fluorescent probes. *Science (80-.).* (2007). doi:10.1126/science.1146598

108. Tam, J., Cordier, G. A., Borbely, J. S., Álvarez, Á. S. & Lakadamyali, M. Cross-talk-free multi-color storm imaging using a single fluorophore. *PLoS One* (2014). doi:10.1371/journal.pone.0101772

109. Dani, A., Huang, B., Bergan, J., Dulac, C. & Zhuang, X. Superresolution Imaging of Chemical Synapses in the Brain. *Neuron* (2010). doi:10.1016/j.neuron.2010.11.021

110. Beghin, A. *et al.* Localization-based super-resolution imaging meets high-content screening. *Nat. Methods* (2017). doi:10.1038/nmeth.4486

111. Garbacik, E. T., Sanz-paz, M., Borgman, K. J. E., Campelo, F. & Garcia-parajo, M. F. Frequency-Encoded Multicolor Fluorescence Imaging with Single-Photon-Counting Color-Blind Detection. *Biophysj* 1–12 (2018). doi:10.1016/j.bpj.2018.07.008

112. Chen, K. H., Boettiger, A. N., Moffitt, J. R., Wang, S. & Zhuang, X. Spatially resolved, highly multiplexed RNA profiling in single cells. *Science (80-.).* (2015). doi:10.1126/science.aaa6090

113. Beliveau, B. J. *et al.* Versatile design and synthesis platform for visualizing genomes with Oligopaint FISH probes. *Proc. Natl. Acad. Sci.* (2012). doi:10.1073/pnas.1213818110

114. Gunewardene, M. S. *et al.* Superresolution imaging of multiple fluorescent proteins with highly overlapping emission spectra in living cells. *Biophys. J.* (2011). doi:10.1016/j.bpj.2011.07.049

115. Winterflood, C. M., Platonova, E., Albrecht, D. & Ewers, H. Dual-Color 3D Superresolution Microscopy by Combined Spectral-Demixing and Biplane Imaging. *Biophys. J.* (2015). doi:10.1016/j.bpj.2015.05.026

116. Ricci, M. A., Manzo, C., García-Parajo, M. F., Lakadamyali, M. & Cosma, M. P. Chromatin Fibers Are Formed by Heterogeneous Groups of Nucleosomes In Vivo. *Cell* **160**, 1145–1158 (2015).

117. Grigoryev, S. A., Bascom, G., Buckwalter, J. M., Schubert, M. B. & Woodcock, C. L. Hierarchical looping of zigzag nucleosome chains in metaphase chromosomes. (2015). doi:10.1073/pnas.1518280113

118. Collepardo-Guevara, R. & Schlick, T. Chromatin fiber polymorphism triggered by variations of DNA linker lengths. *Proc. Natl. Acad. Sci. U. S. A.* **111**, 8061–8066 (2014).

119. Perišić, O., Collepardo-Guevara, R. & Schlick, T. Modeling studies of chromatin fiber structure as a function of DNA linker length. *J. Mol. Biol.* **403**, 777–802 (2010).

120. Portillo-Ledesma, S. & Schlick, T. Bridging chromatin structure and function over a range of experimental spatial and temporal scales by molecular modeling. *Wiley Interdiscip. Rev. Comput. Mol. Sci.* 1–20 (2019). doi:10.1002/wcms.1434

121. Bascom, G. D., Myers, C. G. & Schlick, T. Mesoscale modeling reveals formation of an epigenetically driven HOXC gene hub. *Proc. Natl. Acad. Sci. U. S. A.* (2019). doi:10.1073/pnas.1816424116

122. Fan, Y. *et al.* Histone H1 depletion in mammals alters global chromatin structure but causes specific changes in gene regulation. *Cell* **123**, 1199–1212 (2005).

123. Zeineddine, D., Hammoud, A. A., Mortada, M. & Boeuf, H. The Oct4 protein: More

than a magic stemness marker. *American Journal of Stem Cells* (2014).

124. Mieczkowski, J. *et al.* MNase titration reveals differences between nucleosome occupancy and chromatin accessibility. *Nat. Commun.* **7**, 1–11 (2016).

125. Woodcock, C. L., Skoultchi, A. I. & Fan, Y. Role of linker histone in chromatin structure and function : H1 stoichiometry and nucleosome repeat length. 17–25 (2006).

126. D. Bascom, G. & Schlick, T. Mesoscale Modeling of Chromatin Fibers. in *Nuclear Architecture and Dynamics* (2018). doi:10.1016/b978-0-12-803480-4.00005-3

127. Roh, T., Wei, G., Farrell, C. M. & Zhao, K. Genome-wide prediction of conserved and nonconserved enhancers by histone acetylation patterns. 74–81 (2007). doi:10.1101/gr.5767907.

128. Fan, Y. *et al.* H1 Linker Histones Are Essential for Mouse Development and Affect Nucleosome Spacing In Vivo. **23**, 4559–4572 (2003).

129. Ester, M., Kriegel, H.-P., Sander, J. & Xu, X. A Density-Based Algorithm for Discovering Clusters in Large Spatial Databases with Noise. in *Proceedings of the 2nd International Conference on Knowledge Discovery and Data Mining* (1996).

130. Venkataramani, V., Herrmannsdörfer, F., Heilemann, M. & Kuner, T. SuReSim : simulating localization microscopy experiments from ground truth models. (2016). doi:10.1038/nmeth.3775

131. Neguembor, M. V *et al.* (Po)STAC (Polycistronic SunTAg modified CRISPR) enables live-cell and fixed-cell super-resolution imaging of multiple genes. *Nucleic Acids Res.* **46**, e30–e30 (2018).

132. Schlesinger, S. & Meshorer, E. Open Chromatin, Epigenetic Plasticity, and Nuclear Organization in Pluripotency. *Developmental Cell* (2019). doi:10.1016/j.devcel.2019.01.003

133. Fan, Y. *et al.* Histone H1 depletion in mammals alters global chromatin structure but causes specific changes in gene regulation. *Cell* (2005). doi:10.1016/j.cell.2005.10.028

134. Shen, H. *et al.* Single Particle Tracking : From Theory to Biophysical Applications. (2017). doi:10.1021/acs.chemrev.6b00815

135. Monnier, N. *et al.* Inferring transient particle transport dynamics in live cells. *Nat. Methods* (2015). doi:10.1038/nmeth.3483

136. Izeddin, I. *et al.* Single-molecule tracking in live cells reveals distinct target-search strategies of transcription factors in the nucleus. 1–27 (2014). doi:10.7554/eLife.02230

137. Schindelin, J. *et al.* Fiji: An open-source platform for biological-image analysis. *Nature Methods* (2012). doi:10.1038/nmeth.2019

138. Tarantino, N. *et al.* TNF and IL-1 exhibit distinct ubiquitin requirements for inducing NEMO–IKK supramolecular structures. **204**, 231–245 (2014).

139. Michalet, X. Mean square displacement analysis of single-particle trajectories with localization error: Brownian motion in an isotropic medium. *Phys. Rev. E - Stat. Nonlinear, Soft Matter Phys.* (2010). doi:10.1103/PhysRevE.82.041914

140. Michalet, X. & Berglund, A. J. Optimal diffusion coefficient estimation in single-particle tracking. *Phys. Rev. E - Stat. Nonlinear, Soft Matter Phys.* (2012). doi:10.1103/PhysRevE.85.061916

141. Melcer, S. *et al.* Histone modifications and lamin A regulate chromatin protein dynamics in early embryonic stem cell differentiation. *Nat. Commun.* (2012). doi:10.1038/ncomms1915

142. Starling, J. A., Maule, J., Hastie, N. D. & Allshire, R. C. Extensive telomere repeat arrays in mouse are hypervariable. *Nucleic Acids Res.* (1990). doi:10.1093/nar/18.23.6881

143. Bandaria, J. N., Qin, P., Berk, V., Chu, S. & Yildiz, A. Shelterin protects chromosome ends by compacting telomeric chromatin. *Cell* (2016). doi:10.1016/j.cell.2016.01.036

144. Verdaasdonk, J. S. *et al.* Centromere tethering confines chromosome domains. *Mol. Cell* **52**, 819–831 (2013).

145. Schermelleh, L. *et al.* Super-resolution microscopy demystified. *Nat. Cell Biol.* **21**, (2019).

146. Balzarotti, F. *et al.* Nanometer resolution imaging and tracking of fluorescent molecules with minimal photon fluxes. *Science (80-.).* (2017). doi:10.1126/science.aak9913

147. Tenne, R. *et al.* Super-resolution enhancement by quantum image scanning microscopy. *Nat. Photonics* (2019). doi:10.1038/s41566-018-0324-z

148. Niekamp, S. *et al.* Nanometer-accuracy distance measurements between fluorophores at the single-molecule level. *Proc. Natl. Acad. Sci. U. S. A.* (2019). doi:10.1073/pnas.1815826116

149. Jungmann, R. Super-Resolution Microscopy with DNA Molecules: Towards Localizomics. *Biophys. J.* (2019). doi:10.1016/j.bpj.2018.11.064

150. Hajj, B., El Beheiry, M., Izeddin, I., Darzacq, X. & Dahan, M. Accessing the third dimension in localization-based super-resolution microscopy. *Phys. Chem. Chem. Phys.* **16**, 16340–16348 (2014).

151. Cella Zanacchi, F. *et al.* Live-cell 3D super-resolution imaging in thick biological samples. *Nat. Methods* (2011). doi:10.1038/nmeth.1744

152. Hu, Y. S., Zimmerley, M., Li, Y., Watters, R. & Cang, H. Single-molecule super-resolution light-sheet microscopy. *ChemPhysChem* (2014). doi:10.1002/cphc.201300732

153. Jones, S. A., Shim, S. H., He, J. & Zhuang, X. Fast, three-dimensional super-resolution imaging of live cells. *Nat. Methods* (2011). doi:10.1038/nmeth.1605

154. Wade, O. K. *et al.* 124-Color Super-resolution Imaging by Engineering DNA-PAINT Blinking Kinetics. *Nano Lett.* (2019). doi:10.1021/acs.nanolett.9b00508

155. Schueder, F. *et al.* An order of magnitude faster DNA-PAINT imaging by optimized sequence design and buffer conditions. *Nat. Methods* (2019). doi:10.1038/s41592-019-0584-7

156. Mao, H. *et al.* Cost-efficient nanoscopy reveals nanoscale architecture of liver cells and platelets. *Nanophotonics* **8**, 1299–1313 (2019).

157. Auer, A. *et al.* Nanometer-scale Multiplexed Super-Resolution Imaging with an Economic 3D-DNA-PAINT Microscope. *ChemPhysChem* **19**, 3024–3034 (2018).

158. Zhuang, X. *et al.* High-throughput single-cell gene-expression profiling with multiplexed error-robust fluorescence in situ hybridization. *Proc. Natl. Acad. Sci.* **113**, 11046–11051 (2016).

159. Coto-García, A. M. *et al.* Nanoparticles as fluorescent labels for optical imaging and sensing in genomics and proteomics. *Analytical and Bioanalytical Chemistry* (2011). doi:10.1007/s00216-010-4330-3

160. Johnson, C. J., Zhukovsky, N., Cass, A. E. G. & Nagy, J. M. Proteomics, nanotechnology and molecular diagnostics. *Proteomics* (2008). doi:10.1002/pmic.200700665

161. Krishhan, V. V., Khan, I. H. & Luciw, P. A. Multiplexed microbead immunoassays by flow cytometry for molecular profiling: Basic concepts and proteomics applications. *Critical Reviews in Biotechnology* (2009). doi:10.1080/07388550802688847

162. Marquette, C. A., Corgier, B. P. & Blum, L. J. Recent advances in multiplex immunoassays. *Bioanalysis* (2012). doi:10.4155/bio.12.56

163. Verdeny-Vilanova, I. *et al.* 3D motion of vesicles along microtubules helps them to circumvent obstacles in cells. *Journal of Cell Science* (2017). doi:10.1242/jcs.201178

164. Raote, I. *et al.* TANGO1 builds a machine for collagen export by recruiting and spatially organizing COPII, tethers and membranes. *Elife* (2018). doi:10.7554/eLife.32723

165. Gómez-García, P. A., Garbacik, E. T., Otterstrom, J. J., Garcia-Parajo, M. F. & Lakadamyali, M. Excitation-multiplexed multicolor superresolution imaging with fm-STORM and fm-DNA-PAINT. *Proc. Natl. Acad. Sci. U. S. A.* (2018). doi:10.1073/pnas.1804725115

166. Hell, S. W. *et al.* The 2015 super-resolution microscopy roadmap. *J. Phys. D. Appl. Phys.* **443001**, 443001 (2015).

167. Nir, G. *et al.* Walking along chromosomes with super-resolution imaging, contact maps, and integrative modeling. *PLoS Genet.* (2018). doi:10.1371/journal.pgen.1007872

168. Cardozo Gizzi, A. M. *et al.* Microscopy-Based Chromosome Conformation Capture Enables Simultaneous Visualization of Genome Organization and Transcription in Intact Organisms. *Mol. Cell* **74**, 212-222.e5 (2019).

169. Bintu, B. *et al.* Super-resolution chromatin tracing reveals domains and cooperative interactions in single cells. *Science (80-.).* **362**, (2018).

170. Moser, F. *et al.* Cryo-SOFI enabling low-dose super-resolution correlative light and electron cryo-microscopy. *Proc. Natl. Acad. Sci. U. S. A.* (2019). doi:10.1073/pnas.1810690116

171. Paez-Segala, M. G. *et al.* Fixation-resistant photoactivatable fluorescent proteins for CLEM. *Nat. Methods* (2015). doi:10.1038/nmeth.3225

172. Ohno, M. *et al.* Sub-nucleosomal Genome Structure Reveals Distinct Nucleosome Folding Motifs. *Cell* **176**, 520-534.e25 (2019).

173. Paulsen, J. *et al.* Chrom3D: Three-dimensional genome modeling from Hi-C and nuclear lamin-genome contacts. *Genome Biol.* (2017). doi:10.1186/s13059-016-1146-2

174. Odermatt, P. D. *et al.* High-Resolution Correlative Microscopy: Bridging the Gap between Single Molecule Localization Microscopy and Atomic Force Microscopy. *Nano Lett.* (2015). doi:10.1021/acs.nanolett.5b00572

175. Perkovic, M. *et al.* Correlative Light- and Electron Microscopy with chemical tags. *J. Struct. Biol.* (2014). doi:10.1016/j.jsb.2014.03.018

176. Levet, F. *et al.* SR-Tesseler: A method to segment and quantify localization-based super-resolution microscopy data. *Nat. Methods* **12**, 1065–1071 (2015).

177. Klaholz, B. P. *et al.* 3DClusterViSu: 3D clustering analysis of super-resolution microscopy data by 3D Voronoi tessellations. *Bioinformatics* **34**, 3004–3012 (2018).

178. Reinhard, S., Aufmkolk, S., Sauer, M. & Doose, S. Registration and Visualization of Correlative Super-Resolution Microscopy Data. *Biophys. J.* (2019). doi:10.1016/j.bpj.2019.04.029

179. Cella Zanacchi, F. *et al.* ADNAorigami platform for quantifying protein copy number in super-resolution. *Nat. Methods* (2017). doi:10.1038/nmeth.4342

180. Golfetto, O. *et al.* A Platform to Enhance Quantitative Single Molecule Localization Microscopy. *J. Am. Chem. Soc.* (2018). doi:10.1021/jacs.8b04939

181. Llères, D. *et al.* Quantitative FLIM-FRET Microscopy to Monitor Nanoscale Chromatin Compaction In Vivo Reveals Structural Roles of Condensin Complexes. *Cell Rep.* (2017). doi:10.1016/j.celrep.2017.01.043

182. Coleman, R. A. *et al.* Imaging transcription: Past, present, and future. in *Cold Spring Harbor Symposia on Quantitative Biology* (2016). doi:10.1101/sqb.2015.80.027201

183. Normanno, D. *et al.* Probing the target search of DNA-binding proteins in mammalian cells using TetR as model searcher. *Nat. Commun.* (2015). doi:10.1038/ncomms8357

184. Abrahamsson, S. *et al.* Fast multicolor 3D imaging using aberration-corrected multifocus microscopy. *Nat. Methods* (2013). doi:10.1038/NMETH.2277

185. Ball, D. A. *et al.* Single molecule tracking of Ace1p in Saccharomyces cerevisiae defines a characteristic residence time for non-specific interactions of transcription factors with chromatin. 1–12 (2016). doi:10.1093/nar/gkw744

186. Roy, R. *et al.* Single-molecule imaging of transcription factor binding to DNA in live mammalian cells. *Nat. Methods* **10**, 421–426 (2013).

187. Mazza, D., Mueller, F., Stasevich, T. J. & Mcnally, J. G. Convergence of chromatin binding estimates in live cells To the Editor : Many transcription factors exhibit highly dynamic. *Nat. Publ. Gr.* **10**, 691–692 (2013).

188. Chevalier, C. & Voituriez, R. Facilitated di ff usion of proteins on chromatin. 1–4 (2018).

189. Caccianini, L., Normanno, D., Izeddin, I. & Dahan, M. Single molecule study of non-specific binding kinetics of LacI in mammalian cells. *Faraday Discuss.* (2015). doi:10.1039/c5fd00112a

190. Hansen, A. S., Amitai, A., Cattoglio, C., Tjian, R. & Darzacq, X. Guided nuclear exploration increases CTCF target search efficiency. *bioRxiv* 495457 (2018). doi:10.1101/495457

191. Watson, M. & Stott, K. Disordered domains in chromatin-binding proteins. *Essays Biochem.* **63**, 147–156 (2019).

192. Nozaki, T. *et al.* Dynamic Organization of Chromatin Domains Revealed by Super-Resolution Live-Cell Imaging. *Mol. Cell* (2017). doi:10.1016/j.molcel.2017.06.018

193. Stefano, M. Di *et al.* Dynamic simulations of transcriptional control during cell

reprogramming reveal spatial chromatin caging. *bioRxiv* (2019). doi:10.1101/642009

194. Gibson, B. A. *et al.* Organization of Chromatin by Intrinsic and Regulated Phase Separation. *Cell* (2019). doi:10.1016/j.cell.2019.08.037

195. Saxton, M. J. Single-particle tracking: The distribution of diffusion coefficients. *Biophys. J.* (1997). doi:10.1016/S0006-3495(97)78820-9

196. Saxton, M. J. Single-particle tracking: Connecting the dots. *Nat. Methods* (2008). doi:10.1038/nmeth0808-671

197. Saxton, M. J. Modeling 2D and 3D diffusion. *Methods Mol. Biol.* (2007). doi:10.1385/1-59745-519-9:295

198. Saxton, M. J. Anomalous diffusion due to binding: A Monte Carlo study. *Biophys. J.* (1996). doi:10.1016/S0006-3495(96)79682-0

199. Saxton, M. J. Lateral Diffusion in an Archipelago. *Biophys. J.* (1982). doi:10.1016/s0006-3495(82)84504-9

200. Shkilev, V. P. Kinetic model for fluorescence microscopy experiments in disordered media with binding sites and obstacles. *Phys. Rev. E* (2018). doi:10.1103/PhysRevE.98.032140

201. Sibarita, J. B. High-density single-particle tracking: Quantifying molecule organization and dynamics at the nanoscale. *Histochemistry and Cell Biology* (2014). doi:10.1007/s00418-014-1214-1

202. Türkcan, S. & Masson, J. B. Bayesian decision tree for the classification of the mode of motion in single-molecule trajectories. *PLoS One* **8**, (2013).

203. Filion, G. J. Theoretical principles of transcription factor traffic on folded chromatin. *Nat. Commun.* doi:10.1038/s41467-018-04130-x

204. Erdelyi, M. *et al.* Correcting chromatic offset in multicolor super-resolution localization microscopy. *Opt. Express* (2013). doi:10.1364/OE.21.010978

205. Oliphant, T. E. SciPy: Open source scientific tools for Python. *Comput. Sci. Eng.* (2007). doi:10.1109/MCSE.2007.58

206. Pedregosa, F. *et al.* Scikit-learn: Machine Learning in Python. *J. Mach. Learn. Res.* (2012). doi:10.1007/s13398-014-0173-7.2

207. Chang, C. & Lin, C. LIBSVM : A Library for Support Vector Machines. *ACM Trans. Intell. Syst. Technol.* (2013). doi:10.1145/1961189.1961199

208. Fan, R.-E., Chang, K.-W., Hsieh, C.-J., Wang, X.-R. & Lin, C.-J. LIBLINEAR: A Library for Large Linear Classification. *J. Mach. Learn. Res.* (2008). doi:10.1038/oby.2011.351

209. Knerr, S., Personnaz, L. & Dreyfus, G. Single-layer learning revisited: a stepwise procedure for building and training a neural network. in *Neurocomputing* (1990). doi:10.1007/978-3-642-76153-9_5

210. Zhao, Y. *et al.* NucMap: A database of genome-wide nucleosome positioning map across species. *Nucleic Acids Res.* (2019). doi:10.1093/nar/gky980

211. Chen, K. *et al.* DANPOS: Dynamic analysis of nucleosome position and occupancy by sequencing. *Genome Res.* (2013). doi:10.1101/gr.142067.112

212. Sun, J., Zhang, Q. & Schlick, T. Electrostatic mechanism of nucleosomal array folding revealed by computer simulation. *Proc. Natl. Acad. Sci. U. S. A.* (2005). doi:10.1073/pnas.0408867102

213. Portillo-Ledesma, S. & Schlick, T. Bridging chromatin structure and function over a range of experimental spatial and temporal scales by molecular modeling. *Wiley Interdiscip. Rev. Comput. Mol. Sci.* (2019). doi:10.1002/wcms.1434

214. Arya, G. & Schlick, T. A tale of tails: how histone tails mediate chromatin compaction in different salt and linker histone environments. *J. Phys. Chem. A* (2009). doi:10.1021/jp810375d

215. Arya, G., Zhang, Q. & Schlick, T. Flexible histone tails in a new mesoscopic oligonucleosome model. *Biophys. J.* (2006). doi:10.1529/biophysj.106.083006

216. Davey, C. A., Sargent, D. F., Luger, K., Maeder, A. W. & Richmond, T. J. Solvent mediated interactions in the structure of the nucleosome core particle at 1.9 Å resolution. *J. Mol. Biol.* (2002). doi:10.1016/S0022-2836(02)00386-8

217. Zhang, Q., Beard, D. A. & Schlick, T. Constructing Irregular Surfaces to Enclose Macromolecular Complexes for Mesoscale Modeling Using the Discrete Surface Charge Optimization (DiSCO) Algorithm. *J. Comput. Chem.* (2003). doi:10.1002/jcc.10337

218. Levitt, M. & Warshel, A. Computer simulation of protein folding. *Nature* **253**, 694–698 (1975).

219. Arya, G. & Schlick, T. Role of histone tails in chromatin folding revealed by a mesoscopic oligonucleosome model. *Proc. Natl. Acad. Sci. U. S. A.* (2006). doi:10.1073/pnas.0604817103

220. Collepardo-Guevara, R. *et al.* Chromatin unfolding by epigenetic modifications explained by dramatic impairment of internucleosome interactions: A multiscale computational study. *J. Am. Chem. Soc.* (2015). doi:10.1021/jacs.5b04086

221. Jian, H., Vologodskii, A. V. & Schlick, T. A combined wormlike-chain and bead model for dynamic simulations of long linear DNA. *J. Comput. Phys.* (1997). doi:10.1006/jcph.1997.5765

222. Luque, A., Collepardo-guevara, R., Grigoryev, S. & Schlick, T. Dynamic condensation of linker histone C-terminal domain regulates chromatin structure. 1–8 (2014). doi:10.1093/nar/gku491

223. Metropolis, N. & Ulam, S. The Monte Carlo Method. *J. Am. Stat. Assoc.* **44**, 335 (1949).

224. Rosenbluth, M. N. & Rosenbluth, A. W. Monte carlo calculation of the average extension of molecular chains. *J. Chem. Phys.* (1955). doi:10.1063/1.1741967

225. Butler, P. J. G. & Thomas, J. O. Dinucleosomes show compaction by ionic strength, consistent with bending of linker DNA. *J. Mol. Biol.* (1998). doi:10.1006/jmbi.1998.1954

226. Garcia-Ramirez, M., Dong, F. & Ausio, J. Role of the histone 'tails' in the folding of oligonucleosomes depleted of histone H1. *J. Biol. Chem.* (1992).

227. Peri, O., Collepardo-guevara, R. & Schlick, T. Modeling Studies of Chromatin Fiber Structure as a Function of DNA Linker Length. (2010). doi:10.1016/j.jmb.2010.07.057

228. Sander, J., Ester, M., Kriegel, H. P. & Xu, X. Density-based clustering in spatial databases: The algorithm GDBSCAN and its applications. *Data Min. Knowl. Discov.* (1998). doi:10.1023/A:1009745219419

229. Nandi, A., Heinrich, D. & Lindner, B. Distributions of diffusion measures from a local mean-square displacement analysis. *Phys. Rev. E - Stat. Nonlinear, Soft Matter Phys.* **86**, (2012).

230. Ball, D. A. *et al.* Single Molecule Tracking Of Ace1p In Saccharomyces cerevisiae Defines A Characteristic Residence Time For Non-specific Interactions Of Transcription Factors With Chromatin.

List of publications

Excitation-multiplexed multicolor superresolution imaging with fm-STORM and fm-DNA-PAINT. **Pablo A. Gómez-García**, Erik T Garbacik, Jason J Otterstrom, Maria F Garcia-Parajo, Melike Lakadamyali. Published in Proceedings of the National Academy of Sciences 115-51, 2018.

Mesoscale modeling and single nucleosome tracking reveal remodeling of clutch folding and dynamics in stem cell differentiation. **Pablo A. Gomez-Garcia**, Stephanie Portillo-Ledesma, Maria Victoria Neguembor, Martina Pesaresi, Walaa Oweis, Talia Rohrlich, Stefan Wieser, Eran Meshorer, Tamar Schlick, Maria Pia Cosma, Melike Lakadamyali. Under preparation for submission.

(Po)STAC (Polycistronic SunTAg modified CRISPR) enables live-cell and fixed-cell super-resolution imaging of multiple genes. Maria V Neguembor, Ruben Sebastian-Perez, Francesco Aulicino, **Pablo A. Gomez-Garcia**, Maria P Cosma, Melike Lakadamyali. Published in Nucleic acids research 46, 2017.

Super-resolution microscopy reveals how histone tail acetylation affects DNA compaction within nucleosomes in vivo. Jason Otterstrom, Alvaro Castells-Garcia, Chiara Vicario, **Pablo A. Gomez-Garcia**, Maria Pia Cosma, Melike Lakadamyali. Published in Nucleic acids research 1–15 (2019). doi:10.1093/nar/gkz593

Diverse Chromatin Interacting Proteins Map To Different Regions of a Chromatin Mobility Landscapes. Jonathan Lerner, **Pablo A. Gomez-Garcia**, Ryan McCarthy, Zhe Liu, Melike Lakadamyali, Kenneth S Zaret. Submitted to Cell.